Precipitation Reactions in the Tungsten-Nickel-Iron Heavy Alloy System

J.B. Posthill
St. Anne's College
University of Oxford

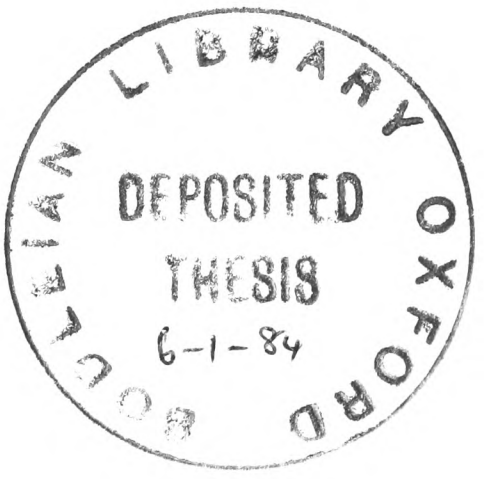

A thesis submitted for the degree of Doctor of Philosophy at the University of Oxford, Trinity Term, 1983.

John B. Posthill
St. Anne's College

D.Phil. Thesis
Trinity Term, 1983

PRECIPITATION REACTIONS IN THE TUNGSTEN-NICKEL-IRON HEAVY ALLOY SYSTEM

Abstract

This research is concerned with identifying and characterizing four solid-state precipitation reactions in the W-Ni-Fe system that can be induced by appropriate heat treatments.

Previous work in this area is reviewed, and a general overview of the research on this system that may, directly or indirectly, further the understanding of microstructure/mechanical property relationships in the W-Ni-Fe heavy alloy is presented. The many metallographic and analytical techniques that have been employed in the course of this investigation are also briefly reviewed.

The specific precipitation reactions studied in the 90W-5Ni-5Fe heavy alloy are listed and briefly described.

1) Interfacial precipitation - interfacial precipitates at the W-γ and γ-γ boundaries were found to be η-carbides. This morphology is expected to severely embrittle the alloy.
2) Matrix-phase precipitation - discontinuous precipitation of W was observed in the matrix region.
3) W-W grain boundary precipitation - W-W grain boundary allotriomorphs (γ-phase) were identified and characterized.
4) W-phase precipitation hardening - fine scale precipitation in the W-phase was found to strengthen the alloy. Deformation prior to aging significantly increased the rate of precipitate nucleation. TEM contrast analysis showed the precipitates to be plate-like with a {100} habit plane, and the strain in the W lattice normal to the precipitates was found to be tensile in nature.

Matrix-composition alloys were manufactured to simulate the γ-phase in the 90W-5Ni-5Fe alloy. Metallographic observations of these alloys furthered the understanding of reactions 1) and 2) above.

These results are discussed in terms of (a) current theories of solid-state precipitation and (b) the influence of the various morphologies on mechanical properties.

CONTENTS

ABSTRACT

ACKNOWLEDGEMENTS

PREFACE

Chapter 1 : INTRODUCTION 1

1. Tungsten Heavy Alloy 1

1.1. Commercial Manufacture 1

1.2. Basic Microstructure 2

1.3. Applications 2

2. Scope of this Study 2

3. Specific Materials Examined 3

3.1. 90W-5Ni-5Fe Commercial Alloy 3

3.2. 90W-7Ni-3Fe Commercial Alloy 3

3.3. Matrix-Composition Alloys 3

3.4. Tungsten Single Crystals 4

4. Thesis Framework 4

Figure 5

Chapter 2 : LITERATURE REVIEW 6

1. Early Work/Development of Tungsten Heavy Alloys 6

2. Previous Research Related to the Precipitation Reactions Studied in this Work 7

2.1. W-γ Interphase Precipitation 7

2.2. Precipitation in the γ-Phase 10

2.3. W-W Grain Boundary Precipitation 12

2.4. W-Phase Precipitation Hardening 13

3. Miscellaneous Tungsten Heavy Alloy Research 15

3.1. General Review Articles 15

3.2. Liquid Phase Sintering 15

3.3. Deformation/Fracture/Fatigue 16

3.4. Porosity 16

3.5. *Hydrogen Embrittlement* 17

3.6. Interfacial Segregation 18

3.7. Phase Equilibria 18

Figures 20

Chapter 3 : EXPERIMENTAL TECHNIQUES AND PROCEDURES 24

1. Materials Processing 24

1.1. Tungsten Heavy Alloys 24

1.2. Matrix-Composition Alloy Manufacture 24

1.2.1. Batch A 24

1.2.2. Batch B 24

1.3. Deformation 25

1.4. Heat Treatment 25

2. Optical Microscopy 25

3. Scanning Electron Microscopy 26

4. Transmission Electron Microscopy 26

4.1. Specimen Preparation and Storage 26

4.2. Two-Beam Contrast Analysis 27

4.3. Weak Beam Imaging 28

4.4. Stereo Microscopy 29

4.5. Convergent Beam Electron Diffraction 30

4.6. High Voltage Electron Microscopy 31

4.7. Energy Dispersive X-ray Analysis 32

5. X-ray Diffraction 32

5.1. Guinier Camera 32

5.2. Diffractometry 32

6. Electron Microprobe (X-ray Microanalysis) 33

7. Secondary Ion Mass Spectrometry (SIMS) 34

8. Laser Induced Ion Mass Analyzer (LIMA) 35

9. Mechanical Testing 35

9.1. Microhardness 35

9.2. Tensile Testing 35

Chapter 4 : EXPERIMENTAL RESULTS:
INTERPHASE (W-γ) AND MATRIX-PHASE PRECIPITATION 37

1. Interphase (W-γ) Precipitation 37

1.1. 90W-5Ni-5Fe Alloy 37

1.2. Matrix-Composition Alloy, Batch B (~ 21.5W-38.5Ni-40Fe) 38

1.2.1. Transmission Electron Microscopy 38

1.2.2. X-ray Diffraction 39

1.2.3. Microanalysis 40

2. Matrix-Phase Precipitation 42

2.1. 90W-5Ni-5Fe Alloy 42

2.2. Matrix-Composition Alloy, Batch A (19.2W-41.4Ni-39.4Fe) 43

Figures 45

Chapter 5 : DISCUSSION:
INTERPHASE (W-γ) AND MATRIX-PHASE PRECIPITATION 69

1. Interphase (W-γ) Precipitation 69

1.1. Matrix-Composition Alloy, Batch B (~ 21.5W-38.5Ni-40Fe) 69

1.2. 90W-5Ni-5Fe Alloy 70

1.2.1. Precipitate Identity 70

1.2.2. Precipitate Formation and Morphology 71

1.2.3. Effect on Mechanical Properties 72

2. Matrix-Phase Precipitation 73

2.1. Matrix-Composition Alloy, Batch A (19.2W-41.4Ni-39.4Fe) 73

2.2. Heavy Alloy (90W-5Ni-5Fe) 76

2.2.1. Morphology 76

2.2.2. Phase Equilibria 77

2.2.3. Effect on Mechanical Properties 77

Figure 78

Chapter 6 : EXPERIMENTAL RESULTS:
W-W GRAIN BOUNDARY PRECIPITATION AND W-PHASE PRECIPITATION HARDENING 79

1. W-W Grain Boundary Precipitation 79

1.1. Scanning Electron Microscopy 79

1.2. Transmission Electron Microscopy 79

1.3. Microanalysis 81

1.4. Kinetics 81

2. Precipitation Hardening in the W-phase 82

2.1. Cold Rolled Material 82

2.1.1. Microhardness 82

2.1.2. Weak Beam TEM 82

2.1.3. $\underset{\sim}{g}\cdot\underset{\approx}{R}$ Contrast Analysis (TEM) 84

2.2. Undeformed Material 85

2.2.1. Mechanical Testing 85

2.2.1.1. Microhardness 85

2.2.1.2. Tensile Testing 85

2.2.2. $\underset{\sim}{g}\cdot\underset{\approx}{R}$ Analysis (TEM) 85

2.2.3. Stereo Microscopy - Nature of the Defect Strain Field 86

2.2.4. Microanalysis and Diffraction of Precipitates 87

2.2.5. Morphology and Kinetics of Precipitation 88

2.3. 14% Hydrostatically Extruded Tungsten Single Crystal 89

2.3.1. Microhardness 89

2.3.2. Transmission Electron Microscopy 90

Figures 91

Chapter 7 : DISCUSSION:
W-W GRAIN BOUNDARY PRECIPITATION AND W-PHASE PRECIPITATION HARDENING 121

1. W-W Grain Boundary Precipitation 121

1.1. Precipitate Formation and Morphology 121

1.2. Effect on Mechanical Properties 125

2. W-Phase Precipitation Hardening 125

2.1. Precipitate Identity 126

2.2. Morphology and Kinetics 127

2.3. Effect on Mechanical Properties 133

3. Relation between W-W Grain Boundary Precipitation and W-Phase Precipitation Hardening 133

Figures 134

Chapter 8 : SUMMARY 139

1. Conclusions 139

2. Suggestions for Further Work 140

BIBLIOGRAPHY

ACKNOWLEDGEMENTS

Many people have helped me enormously in the course of this research, and I should like to express my thanks to all of them. In particular, I should like to thank the following:

Professor Sir Peter Hirsch F.R.S. and Professor J.W. Christian F.R.S. for the provision of laboratory facilities.

My supervisor Dr. David Edmonds for his advice and guidance throughout this project.

The Procurement Executive, Ministry of Defence for financial support and provision of material.

The departmental staff, especially G. Dixon-Brown, R. Doole, D.J.H. Hawes, and J. Short for their assistance.

John Speer for his insightful comments concerning phase transformations.

All the members of the DVE group for their help, encouragement, and friendship during my stay at Oxford.

Lali Gómez for performing the thankless task of typing this thesis.

John B. Posthill

August 1983

PREFACE

This thesis is an account of research carried out in the Department of Metallurgy and Science of Materials at the University of Oxford between October 1979 and August 1983. The work reported is original, and is not substantially the same as any thesis submitted in this or any other university. Where the work of other authors has been included in the text, this has been acknowledged and its source given in a list of references at the end of the thesis. Part of this work has been presented at the Modern Metallography in Metallurgy Conference and Exhibition, University of Cambridge, September 1982, and at the International Conference on Phase Transformations in Solids, Crete, Greece, June 1983.

Chapter 1

INTRODUCTION

1. Tungsten Heavy Alloy

Tungsten heavy alloys are a group of materials based on tungsten (80-95wt%) and produced by liquid phase sintering in the presence of nickel and other element(s) (e.g.Cu,Fe,Cr). The resulting microstructure basically consists of spheroidal tungsten-rich bcc grains (~20-30μm diameter) embedded in a face-centered cubic matrix (Fig.1.1). This structure leads to an interesting and technologically important combination of properties. They are:

1) High density (16-18.5 g/cm^3)

2) High tensile strength (800-1000 N/mm^2)

3) Good tensile elongation (10-30%)

This study has concentrated exclusively on the W-Ni-Fe system and particularly on a 90W-5Ni-5Fe commercial alloy.

1.1. Commercial Manufacture

The production of these alloys begins by mixing the appropriate elemental powders; tungsten, nickel, and iron; and then hydrostatically compacting the mix to give a green billet. The billet is then sintered at 1110°C for ~ 1 hour in a hydrogen atmosphere to facilitate handling. This is followed by further sintering in another furnace at a temperature high enough to melt the non-tungsten elements and dissolve some of the tungsten. This is referred to as liquid phase sintering and is generally done at T≈1440-1460°C for times of up to 3 hours, again in a hydrogen atmosphere. After slow cooling from the sintering temperature the billet is reheated in hydrogen to 1050°C, held for ~ 1 hour, and water quenched.

1.2. Basic Microstructure

Figure 1.1 shows the resulting microstructure. Spheroidal tungsten-rich grains (hereafter referred to as the W-phase) are embedded in a Ni-Fe-W fcc matrix (hereafter referred to as the γ-phase). The W grains are ~ 20-30μm in diameter while the γ grains can often surround many W grains with grain size $\gtrsim$ 100μm. Occasionally, a pore is observed at a W-γ boundary, but the porosity, in general, is low and densities $\gtrsim$ 99% of the theoretical value are obtained. It is important to note that many W-W grain boundaries are present in addition to W-γ interphase boundaries. It will be shown that the microstructure of the two phases, W and γ, and that of the two predominant types of interfaces, W-W and W-γ, can be significantly altered by appropriate heat treatments.

1.3. Applications

The tungsten heavy alloys can find application wherever a high density material is needed. Often, high strength coupled with adequate ductility is also desirable, thus making heavy alloys even more attractive. Typical applications include:

1) Static and dynamic balances (e.g. counterbalances for control surfaces in military and commercial aircraft)
2) Rotating inertia members (e.g. gyroscope rotors)
3) Projectiles (e.g. darts)
4) Radiation shielding (e.g. radioactive material storage containers).

2. Scope of this Study

This work employs a range of high resolution microanalytical techniques in an attempt to characterize and understand many of the solid-state precipitation reactions that occur in a commercially produced 90W-5Ni-5Fe alloy.

Specifically, these reactions are:

1) W-γ interphase precipitation

2) Precipitation in the γ-phase

3) W-W grain boundary precipitation

4) W-phase precipitation hardening

In addition to the scientific interest in these reactions, mechanical properties can be significantly altered by changes in microstructure which result from the various types of precipitation reactions possible in the tungsten heavy alloy systems. The microstructure/mechanical property relationships are examined and discussed where appropriate.

3. Specific Materials Examined

3.1. 90W-5Ni-5Fe Commercial Alloy

The manufacture of this alloy is described in section 1.1. As this study is primarily concerned with the 90W-5Ni-5Fe alloy, all four precipitation reactions listed above were investigated in this material.

3.2. 90W-7Ni-3Fe Commercial Alloy

The manufacture of this alloy is described in section 1.1 but with one deletion - the post-sintering heat treatment of 1050°C for ~ 1 hour has not been performed (i.e. the alloy was received in the as-sintered condition). The usefulness of this difference will become apparent when the W-W grain boundary precipitation reaction is examined in chapter 6.

3.3. Matrix-Composition Alloys

Alloys were produced to simulate the γ-phase of the 90W-5Ni-5Fe heavy alloy. They facilitated study of the interphase and γ-phase precipitation reactions. Their manufacture is described in chapter 3 section 1.2.

3.4. Tungsten Single Crystals

Deformed and heat treated high-purity tungsten single crystals were metallographically examined to provide further information concerning the precipitation hardening of the W-phase of the heavy alloy.

4. Thesis Framework

The results and discussion concerning the interphase and γ-phase precipitation reactions are presented separately from those concerning the W-W grain boundary precipitation and W-phase precipitation hardening. Though all the reactions are distinct, this division was made (a) for the convenience of the reader, and (b) because the two sections are roughly concerned with precipitation in the two separate phases, γ and W, respectively.

Before presenting any of the results of this study, however, it is appropriate to review pertinent earlier work on the subject.

Figure 1.1

Optical micrograph of the commercially supplied 90W-5Ni-5Fe heavy alloy.

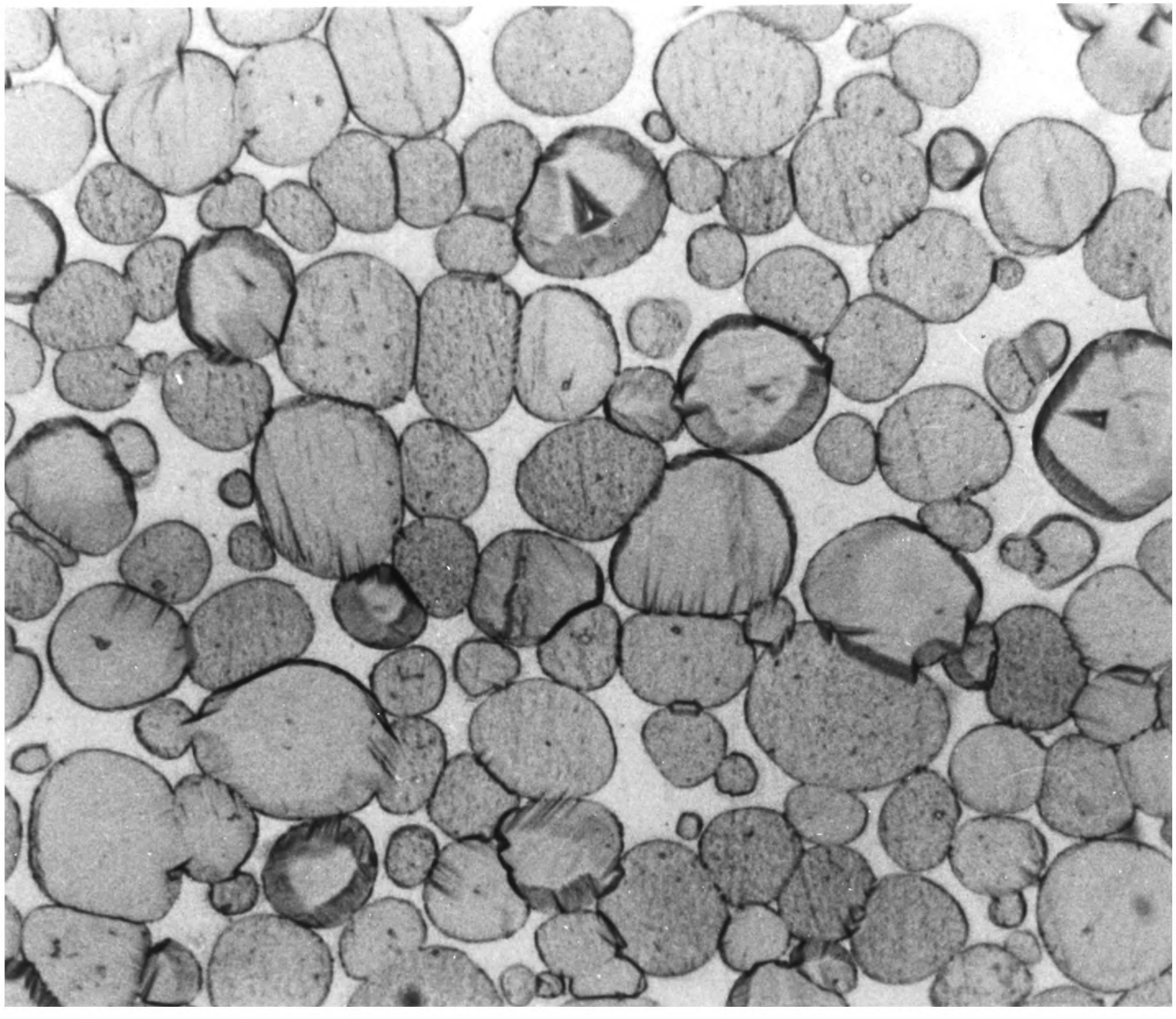
25µm

Chapter 2

LITERATURE REVIEW

1. Early Work/Development of Tungsten Heavy Alloys

In 1935, McLennan and Smithells[1] reported the development of a W-Ni-Cu alloy containing approximately 90% tungsten and produced by liquid phase sintering elemental powders at ~ 1400°C. Further investigations into this system were carried out by Price, et al.[2] They described the structure of W-Ni-Cu alloys of various compositions and produced at different sintering temperatures. Those sintered at temperatures high enough to form a liquid phase ($T \gtrsim 1350°C$) were found to consist of large rounded grains of tungsten embedded in a tungsten-saturated Ni-Cu-W matrix. For alloys with $\lesssim$90%W, near theoretical density was obtained.

Green, et al.[3] were responsible for producing the first W-Ni-Fe heavy alloys and employed the same procedure used for the W-Ni-Cu alloys. They measured the properties of a series of alloys containing 75-97 wt% tungsten with the Ni/Fe ratio maintained constant at 7:3. This choice of Ni/Fe ratio can be understood by observation of the Ni-Fe phase equilibrium diagram[4]. A minimum in the liquidus occurs at 1436°C with composition ~ 68Ni-32Fe. The authors assumed that this feature would be maintained in the ternary Ni-Fe-W so that the liquid phase would solidify without coring developing in the γ-phase.

In the last 15 years the majority of heavy alloy research has been concerned with the W-Ni-Fe system. The reason for this emphasis is that W-Ni-Fe alloys have generally been found to have superior mechanical properties (particularly tensile elongation) to the W-Ni-Cu alloys[e.g.5,6]. Additionally, researchers have tended to maintain the Ni/Fe ratio in the range of 1:1 to 7:3. Partly this was to avoid γ-phase coring, as mentioned

previously, but it was also done to prevent the formation of undesirable intermetallic compounds. For example, if the heavy alloy was produced with a very high Ni/Fe ratio, the intermetallic Ni_4W could be formed[3,7]. Likewise, if the Ni/Fe ratio was too low, the μ-phase (Fe_7W_6) would be produced[8]. The presence of either intermetallic has been associated with alloy embrittlement[8,9], and therefore appropriate nickel and iron concentrations have been chosen to avoid their occurrence.

2. Previous Research Related to the Precipitation Reactions Studied in This Work

2.1. W-γ Interphase Precipitation

This reaction was first observed by Minakova, et al.[10,11] in a series of W-Ni-Fe alloys containing 88-97 wt% tungsten with the Ni/Fe ratio maintained constant at 7:3. Various specimens were furnace cooled from the sintering temperature of 1400°C to temperatures of 1300, 1200, 1100, 1000, 900, 800, 700, and 600°C and then rapidly cooled (~ 600°C/min.) to freeze their structures. Their fracture surfaces were then examined using scanning electron microscopy. The structure of the interphase boundaries was radically altered by the aging process that occurred upon slow cooling. The authors observed precipitation starting at 1200-1300°C and noted three distinct stages of the aging sequence:

1) Formation of parallel plates extended along the grain surfaces and coherent with the W lattice.
2) Breaking of plates of the precipitate phase and formation of discreet particles.
3) Coagulation and growth of particles of the new phase.

The authors, unfortunately, were not clear about the temperatures associated with each of the stages, and the precipitate phase was not

identified. Additionally, a concurrent precipitation reaction was reported to take place in the γ-phase, but there was no mention of its morphology or identity.

Kannappan[12] observed this W-γ interfacial precipitation concurrent with precipitation of a "dendritic" configuration in the γ-phase. He produced this structure in 80W-10Ni-10Fe, 90W-5Ni-5Fe, and 97W-1.5Ni-1.5Fe alloys sintered at 1450°C and 1550°C for various times up to 27 hours and then slow cooled to room temperature. Figure 2.1 shows the results of powder X-ray diffraction of this multiphase alloy. The structure of this third phase was not determined but was said to be "complex". Electron microprobe analysis yielded a precipitate composition of 75W-10Ni-15Fe.

To establish if this precipitate phase was present during liquid phase sintering, the alloy was solution treated at 1300°C and then at 1400°C for 24 hours and quenched to room temperature. The precipitate phase was still present after solution treating at 1300°C but no trace of it was observed after heat treatment at 1400°C. It was concluded that under sintering conditions only two phases, W and liquid, existed and that the slow cool from the sintering temperature allowed the third phase to form.

W-γ interphase precipitation was also observed by Edmonds and Jones[5] after furnace cooling a 90W-5Ni-5Fe alloy from the sintering temperature of 1450°C. SEM and TEM showed that this precipitate exists as platelets ~ 0.5μm in length. Thin foil CDS microanalysis showed the precipitate composition to be 78W-10Ni-12Fe (±2 wt%). This agrees rather well with the microprobe results of Kannappan described earlier.

This precipitate phase was extracted off the fracture surface by deep etching and subjected to X-ray analysis. Figure 2.2 shows the d-spacings obtained from this procedure alongside those observed by Walsh and Donachie[13] for the intermetallic compound NiW (~75 wt%W). It is

apparent that this X-ray diffraction data is quite different from Kannappan's, but as there is reasonable agreement between the measured d-spacings and tungsten concentrations obtained in this study and those of Walsh and Donachie, the authors tentatively concluded that this precipitate was an intermetallic phase of the form (Ni,Fe)W - an isomorpth with NiW.

After this alloy was given a heat treatment at 1000°C and water quenched, the charpy impact energy increased dramatically and the fracture surfaces no longer showed the extensive W-Y separation with accompanying intermetallic precipitation. Instead, the fracture mode was primarily W-W separation with the Y matrix failing in a ductile manner. Thus it was shown that this W-Y intermetallic precipitation was responsible for embrittlement of the alloy.

Henig, et al.[8] have also observed interphase precipitation in a 90W-7Ni-3Fe alloy heat treated at < 1000°C. They claim to have identified it as an intermetallic compound of the form (Ni,Fe)W, an isomorph of NiW, in agreement with Edmonds and Jones. Discontinuous precipitation of W was also observed in the matrix upon certain heat treatments in the 800-1000°C temperature range. After a further 300 hours at temperature, the (Ni,Fe)W intermetallic was seen to form from this precipitated W.

This work also included phase equilibria research on the Fe-W binary system. A new intermetallic compound, FeW, was identified and is thought to form peritectoidally from the μ-phase (Fe_7W_6) and W at ~ 1060°C. X-ray diffraction data was almost identical to that from NiW[13]. As NiW, FeW, and (Ni,Fe)W were all thought to be isomorphic (orthorhombic structure - a_o=7.76Å, b_o=12.48Å, c_o=7.10Å) [13] the authors suggested a modified ternary phase diagram (T=800°C) incorporating the (Ni,Fe)W intermetallic with complete iron and nickel miscibility (Fig.2.3).

Muddle[14] has also recently obtained some interesting results concerning W-γ interphase precipitation in a 90W-5Ni-5Fe alloy. Numerous selected area electron diffraction patterns indicated the precipitate to have a face-centered cubic structure with $a_o \simeq 10.8\text{Å}$. Additionally, all his convergent beam electron diffraction patterns are consistent with a Fd3m (No.227) space group with $a_o \simeq 10.9\text{Å}$. Also, high resolution (~1000Å) scanning auger electron spectroscopy performed on the precipitate on a fracture surface showed a significant carbon peak - even after prolonged sputtering. The shape of the peak (i.e. the presence of two minor peaks at the low energy side) suggests that the carbon is in the form of a carbide, rather than a surface deposit. As both the ternary systems Ni-W-C and Fe-W-C have η-carbides of the form Ni_6W_6C[15] and Fe_6W_6C[16,17], both with Fd3m structure and $a_o \simeq 10.9\text{Å}$, Muddle tentatively concluded that the interfacial precipitate is an η-carbide of the form $W_6(Ni,Fe)_6C$ and not an intermetallic compound.

It is clear that there is some confusion and apparent contradiction in the literature concerning the identity of the interfacial precipitate.

2.2. Precipitation in the γ-phase

As mentioned previously, Minakova, et al.[11] observed "dispersed inclusions" in the γ-phase after slow cooling 88-97 wt%W(Ni/Fe ratio = 7:3) alloys from the sintering temperature to various intermediate temperatures and then rapidly cooling. The precipitate size was reported to be ~10-100Å but the precise morphology and identity of the phase was not ascertained.

Also described in the last section was Kannappan's[12] observation of precipitation with a dendritic configuration in 80-97 wt%W(Ni/Fe ratio = 1:1) alloys slow cooled from the sintering temperature of 1450°C. Their composition was found to be 75W-10Ni-15Fe and X-ray results are reported in Figure 2.1.

Konyukhova, et al.[6] conducted tensile tests of a 90W-7Ni-3Fe alloy at temperatures in the range 20-700°C. Raising the test temperature to 400-500°C led to a progressive increase in elongation, however, at 600°C and above the elongation decreased. The authors associated this unexpected result with observed decomposition of the γ-phase. In alloys deformed at 700°C, they observed precipitation of finely dispersed particles throughout the γ-phase, identified as tungsten by X-ray diffraction analysis.

The effect of cooling rate from the sintering temperature was studied in a 90W-7Ni-3Fe alloy by Kiparisov, et al.[18] Their results showed that slow cooling rates (~ 2°C/min.) led to a decreased γ lattice parameter compared with faster cooling rates (>160°C/min). This was thought to be caused by a decomposition of the matrix, and metallographic observation showed the γ-phase to contain a fine dispersion of W inclusions.

In the same work the effects of post-sintering heat treatment on this alloy and a 30W-49Ni-21Fe alloy were examined. After sintering, both alloys were solution treated at 1550° and 1400°C, respectively, and water quenched. Samples of both alloys were then tempered for 24 hours at temperatures in the range 200-1400°C at 100°C intervals. A reduction in the γ lattice parameter was noted for both alloys after tempering in the 400-900°C range and was associated with γ-phase decomposition. In the 90W-7Ni-3Fe alloy, the majority of precipitated tungsten was deposited on the primary W grains. That which precipitated within the γ-phase, in both alloys, assumed a lamellar morphology in the 400-600°C temperature range. Upon raising the temperature to 800°C, the W precipitates were observed to be spherical with size ~ 1-2μm. At higher temperature, their size increased to 6-7μm - with a corresponding decrease in number density.

The ultimate tensile strength of the 90W-7Ni-3Fe alloy was raised ~ 25% after a heat treatment at 800°C. This is also accompanied by an increase in elongation - from 7% to 25%. The authors attribute these changes in mechanical properties to the precipitation of W from the tungsten-saturated γ solid solution.

As described in the last section, Henig, et al.[8] observed discontinuous precipitation of W in the γ-phase of a 90W-7Ni-3Fe alloy after annealing in the 800-1000°C range. If held at temperature for ≥ 300 hours a (Ni,Fe)W intermetallic would be seen to form from the precipitated tungsten.

Muddle[14] has observed two types of precipitation within the γ-phase of a 90W-5Ni-5Fe alloy. The first is believed to have the same identity as that of the W-γ interphase precipitate (i.e. $W_6(Ni,Fe)_6C$) and is distributed in the γ-phase in widmanstatten laths. The second is W precipitated in a discontinuous, lamellar morphology.

2.3. W-W Grain Boundary Precipitation

Brandon, et al.[19] first observed precipitation at the W-W grain boundaries in a 90W-5Ni-5Fe alloy using scanning electron microscopy on fracture surfaces. The precipitate was not identified but was associated with increased W-W boundary cohesion and, therefore, alloy ductility. The authors did not state how this precipitation reaction was induced.

Another observation of this reaction was reported by Verkhovodov, et al.[20] During examination of areas of W-W separation on a fracture surface of a 90W-7Ni-3Fe alloy they noticed nickel- and iron-rich precipitation with a lamellar morphology. The authors claim that the precipitate was γ-phase and was observed on high-angle grain boundaries but both these assertions appear to be speculation rather than experimentally determined facts.

Frantsevich, et al.[21] also observed W-W grain boundary precipitation using SEM on fracture surfaces of a 90W-7Ni-3Fe alloy. No description of the precipitate morphology was given, but they claimed its presence was the result of increased sintering times (although no specific times were mentioned).

Hogwood[22] recognized this precipitation on W-W grain boundaries in a variety of alloys (e.g. 90W-5Ni-5Fe, 90W-7Ni-3Fe, 95W-3.5Ni-1.5Fe). He associated it with a post-sintering heat treatment at 1050°C for various times. The precipitate morphology varied in a nonuniform fashion - lamellar, nodular, or a combination of both morphologies could be seen on any given face of an intergranular W-W fracture.

This association of the presence of W-W grain boundary precipitation and a post-sintering heat treatment was also made by Gero and Chaiat[23]. SEM fractographs of an as-sintered 94W-4Ni-2Fe alloy showed smooth, featureless W-W separation. After the material was given an unspecified heat treatment; however, lamellar and nodular precipitates were observed on W-W intergranular facets. The authors attributed an improved ductility after the heat treatment to the presence and plastic deformation of the interfacial precipitates.

Most recently Lea, et al.[24] have used TEM to show that this W-W grain boundary precipitation is, in fact, γ-phase. It was observed in a 90W-5Ni-5Fe alloy heat treated at 1350°C for 1 hour. As this was a subsidiary result from an article concerned primarily with segregation to W-γ and W-W interfaces, the authors did not elaborate on the reaction.

2.4. W-Phase Precipitation Hardening

A certain hardening response upon aging prior deformed heavy alloy has been reported by a number of researchers. Wehr[25] measured the ultimate tensile strength of a rolled 90W-7Ni-3Fe alloy as a function

of annealing temperature in the 100-1500°C range (t=1 hour). The graph showed a significant increase in UTS after annealing in the 300-700°C range with the peak strength observed after annealing at ~ 500°C. The magnitude of strengthening is quite impressive. The UTS of as-rolled material was 190 KSI (1310 N/mm^2) compared with a UTS of material rolled and annealed at 500°C of approximately 240 KSI (1650 N/mm^2) - a 25% increase. Examination of specimens by metallographic and X-ray methods revealed no evidence of any new phase present in the specimens. As there was a peak and a subsequent decrease in UTS at higher annealing temperatures, Wehr speculated that this response was an age hardening reaction, with the precipitate possibly being an iron-tungsten intermetallic phase, beyond the detectability of the techniques used.

Jones and Munnery[26] also observed an increase in UTS of a swaged W-Ni-Cu heavy alloy upon annealing at ~ 450°C for 30 minutes. The alloy composition was 90W-7.5Ni-2.5Cu, and the increase in UTS upon annealing was ~ 10%.

A more recent observation of this phenomena has been made at R.A.R.D.E.[27] Annealing a 24% swaged 90W-5Ni-5Fe alloy at various temperatures for 1 hour yielded a hardness peak at ~ 550°C. Similarly, a UTS vs. heat treatment temperature plot showed a strength peak at ~ 600°C with a progressive decrease in UTS with rising anneal temperature. The increase in UTS induced by annealing at 600°C for 1 hour is ~ 10%. Additionally, microhardness values taken from the W and γ-phases after various anneals showed a peak in microhardness vs. heat treat temperature curve for the W-phase at ~ 550°C but only a progressive decrease for the γ-phase with increasing annealing temperature. This demonstrated that the observed alloy strengthening is due to W-phase hardening,

although, the mechanism responsible for this remains unclear.

3. Miscellaneous Tungsten Heavy Alloy Research

This section briefly describes published work on heavy alloys that is not directly related to the present study, with the purpose of providing useful background information on the tungsten heavy alloy system. Emphasis is placed on research which could have a bearing on the mechanical properties of the alloys.

3.1. General Review Articles

Larsen and Murphy[28] and Ariel, et al.[29] have presented good general reviews of tungsten heavy alloys. More recently, Ekbom[30] has reviewed work relevant to microstructure/mechanical property relationships for the W-Ni-Fe system.

3.2. Liquid Phase Sintering

An excellent review of the theoretical aspects of liquid phase sintering is given by Eremenko, et al.[31] Briefly, there are three stages of this process:

1) Rearrangement - densification results from the movement of the solid-phase particles due to various forces.
2) Solution/Reprecipitation - dissolution of some solid-phase into the liquid-phase and subsequent precipitation.
3) Coalescence - formation of a contiguous skeleton of the solid-phase accompanied by grain coarsening due to grain boundary migration.

The last two stages are primarily responsible for the large final W grain size (~ 25μm diameter) compared with the initial tungsten powder size ($\lesssim$ 2μm).

Kannappan[12], Zukas and Sheinberg[32], and Masuda and Watanabe[33,34], among others, have studied the kinetics of liquid phase sintering of heavy

alloys. In general, the size of the W-phase has been found to increase as $t^{1/3}$ (although Zukas and Sheinberg did not confirm this).

3.3. Deformation/Fracture/Fatigue

It has been known for some time that the ductility of the tungsten heavy alloy is much better than that of pure tungsten. Interestingly, Krock and Shepard[35] concluded that the deformation of the composite was governed solely by the deformation of the stronger W grains. They noted, however, that it was necessary that the γ-phase was capable of sustaining a stress level sufficient to deform the W-phase or premature fracture would result. Votava[7] found that plastic deformation started in the matrix and then proceeded through both phases. He attributed the high ductility to the crack blunting effect of the γ-phase and the high purity of the W grains.

Many authors[e.g.7,19,30] have reported fracture initiating at the W-W grain boundaries before progressing through the entire alloy. Generally, the γ-phase fails in a ductile, knife-edge manner, although investigators[5,24] have also noted a high fraction of W-γ interface separation which has been associated with poor ductility.

Only one study has been concerned with fatigue of heavy alloys. Roman and Jinchuk[36] found no difference in fatigue crack propagation rates as a function of the stress intensity range between as-sintered and forged 93W-7(Ni,Fe) alloys, although fatigue crack growth rates were much higher than normally exhibited in materials with a homogeneous structure.

3.4. Porosity

Churn and Yoon[37] have investigated porosity as a function of sintering time in W-Ni-Fe alloys in the composition range 90-96 wt%W with Ni/Fe ratio held constant at 1:1. Porosity was constant at ~0.1% for sintering

times up to 1 hour and then began to rise. A peak of ~ 1.5% porosity after 4 hours was found, and this was associated with a drastic reduction in mechanical properties. Longer sintering times showed reduced porosity but not to levels as low as it was after ≤ 1 hour.

More recently, Kaysser, et al.[38] have attempted to explain the formation and elimination of pores during liquid phase sintering of heavy alloys. Homogeneous particle rearrangement and liquid flow from larger to smaller capillaries are cited as reasons for pore formation. Longer sintering times, the authors claim, appear to negate the importance of these factors and porosity is reduced.

3.5. Hydrogen Embrittlement

Powell[39] has measured the bulk hydrogen concentration in a 95W-3.5Ni-1.5Fe heavy alloy after sintering and vacuum annealing. The as-sintered alloy was found to contain ~ 90wt ppb hydrogen, but after vacuum ($<10^{-7}$torr) degassing at 1000°C for 30 minutes the hydrogen content decreased to ~ 3 wt ppb. However, this study did not attempt to correlate this significant decrease in hydrogen concentration with mechanical properties.

Sczerzenie and Rogers[40] noticed a significant improvement in mechanical properties (particularly tensile elongation) after annealing 90W-7Ni-3Fe and 90W-7.5Ni-2.5Cu alloys at 1000°C for 1 hour in vacuo. Interestingly, the mechanical properties of a 90W-5Ni-5Fe alloy were unaffected by this vacuum heat treatment. SEM fractography of an as-sintered and hydrogen-charged 90W-7Ni-3Fe alloy showed significant interfacial (W-Y and W-W) separation. These results led to the conclusion that hydrogen was responsible for embrittling the interfaces, particularly the W-Y interfaces, and hence caused the poor mechanical properties.

Similar results were obtained by Guisen, et al.[41] for a 95W-3.5Ni-1.5Fe alloy. Also, an ion microprobe was used to examine the distribution

of hydrogen in the microstructure. From this analysis, the authors showed that in specimens with higher hydrogen content the hydrogen is concentrated at the interfaces, thus accounting for the observed interfacial failure.

Lux, et al.[42] and Yoon, et al.[43] have also noticed an improvement of mechanical properties for both 90W-6.7Ni-3.3Fe and 96W-2.8Ni-1.2Fe alloys with vacuum annealing. Additionally, Lux, et al. observed the same improvement of mechanical properties when the heavy alloy was slow cooled after sintering. They attributed the improvement of mechanical properties to a reduction of hydrogen content due to vacuum annealing or slow cooling from the sintering temperature.

3.6 Interfacial Segregation

In the previous section various works were cited that presented evidence for the segregation of hydrogen to the W-Y interphase boundaries. The two other works in this area are due to Muddle and Edmonds[44] and Lea, et al.[24] Both papers studied the distribution of impurity elements on the fracture surfaces of 90W-5Ni-5Fe and 90W-7.5Ni-2.5Cu heavy alloys using scanning Auger electron spectroscopy. In both alloys, slow cooled from the sintering temperature, phosphorus and sulfur were observed to be segregating to the W-Y interfaces. This segregation was associated with brittle, interfacial failure on impact loading. Furthermore, Lea, et al. detected a monolayer of nickel at the W-W grain boundaries, which would contribute to the embrittlement of these boundaries.

3.7. Phase Equilibria

The first W-Ni-Fe phase diagram was constructed by Winkler and Vogel[45] (Fig.2.4). Henig, et al[8] revised this diagram to include a ternary (Ni,Fe)W intermetallic phase and made some changes to the location of

certain phase boundaries (Fig.2.3). Raynor and Rivlin[46,47] have recently reviewed W-Ni-Fe phase equilibria and the three relevant binary systems: Ni-Fe, Ni-W, and Fe-W.

Figure 2.1

d-spacings from the X-ray results of Kannappan[12].

d(Å)	
6.456	*
6.309	
3.945	*
3.862	
2.793	*
2.731	
2.563	*
2.556	
2.277	*
2.224	$(110)_W$
2.150	*
2.103	
2.026	$(111)\gamma$
1.976	*
1.930	

* - Reflections that could be due to an η-carbide with $a_o \simeq 11.18$Å (this is referred to in chapter 5 section 1.2.2).

Figure 2.2

X-ray results from the NiW intermetallic[13] alongside those obtained for the interfacial precipitate in the tungsten heavy alloy[5].

NiW

hkl	^{d}Observed	^{d}Calculated
020	6.24	6.24
200	3.88	3.88
002	3.55	3.55
112	3.13	3.119
230	2.82	2.837
202	2.74	2.715
310	2.51	2.53
042	2.31	2.344
321	2.27	2.264
250	2.11	2.10
302	2.08	2.09
242	2.01	2.006
322	1.96	1.944
400	1.93	1.938
233	1.82	1.818
170	1.72	1.738
440	1.64	1.646
450	1.53	1.531
502	1.42	1.421
105	1.40	1.397
343	1.36	1.373
205	1.33	1.334
404	1.31	1.309
602	1.22	1.214
335	1.19	1.193
016	1.18	1.179
720	1.09	1.090
712	1.05	1.054
624	1.03	1.030
426	0.996	0.9973
615	0.952	0.9531
812	0.934	0.9323
822	0.924	0.9246
466	0.9088	0.0988
780	0.907	0.9031
407	0.8991	0.8990
803	0.898	0.8968
386	0.8846	0.8859
912	0.8346	0.8352
328	0.833	0.8322
537	0.832	0.8320
068	0.8157	0.8163

Interfacial Precipitate

hkl	d-spacing, Å	
	Observed for NiW in Ref(13)	Measure in Preser Work
200	3.88	3.83
002	3.55	3.35
202	2.74	2.68
310	2.51	2.46
250	2.11	2.13
400	1.93	1.91
450	1.53	1.51
105	1.40	1.39
404	1.31	1.31
720	1.09	1.09
712	1.05	1.05
615	0.952	0.953
812	0.934	0.936

Figure 2.3

Ni-Fe-W ternary phase diagram after Henig, et al.[8] (T = 800°C).

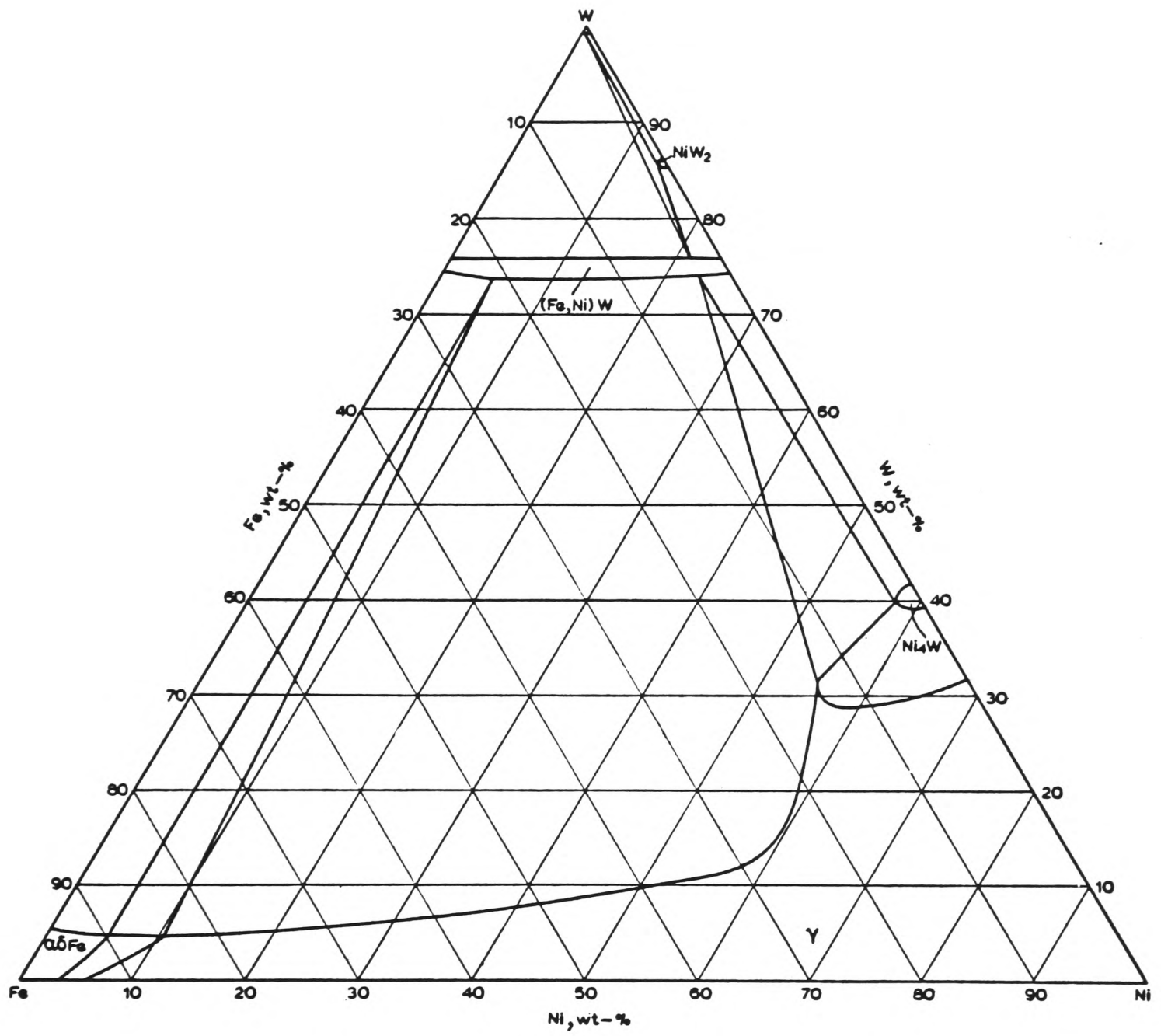

Figure 2.4

Ni-Fe-W ternary phase diagram after Winkler and Vogel[45].

Room Temperature

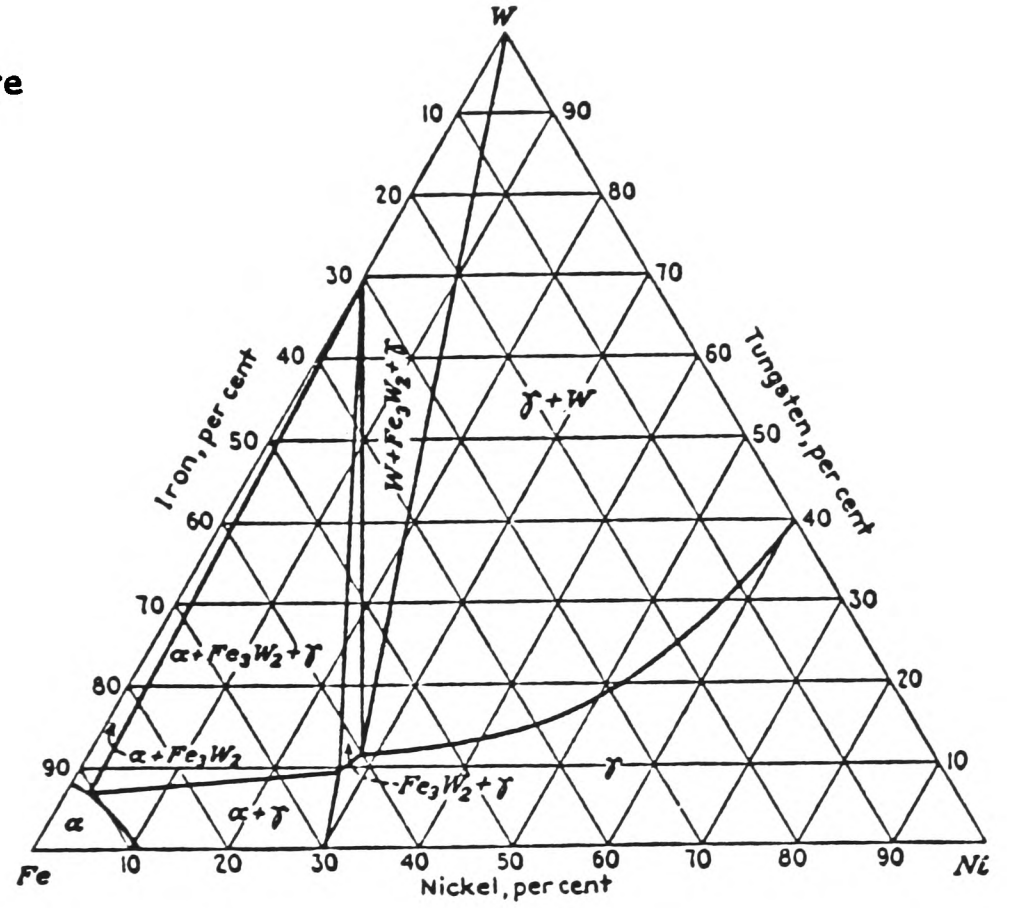

T = 1400°C

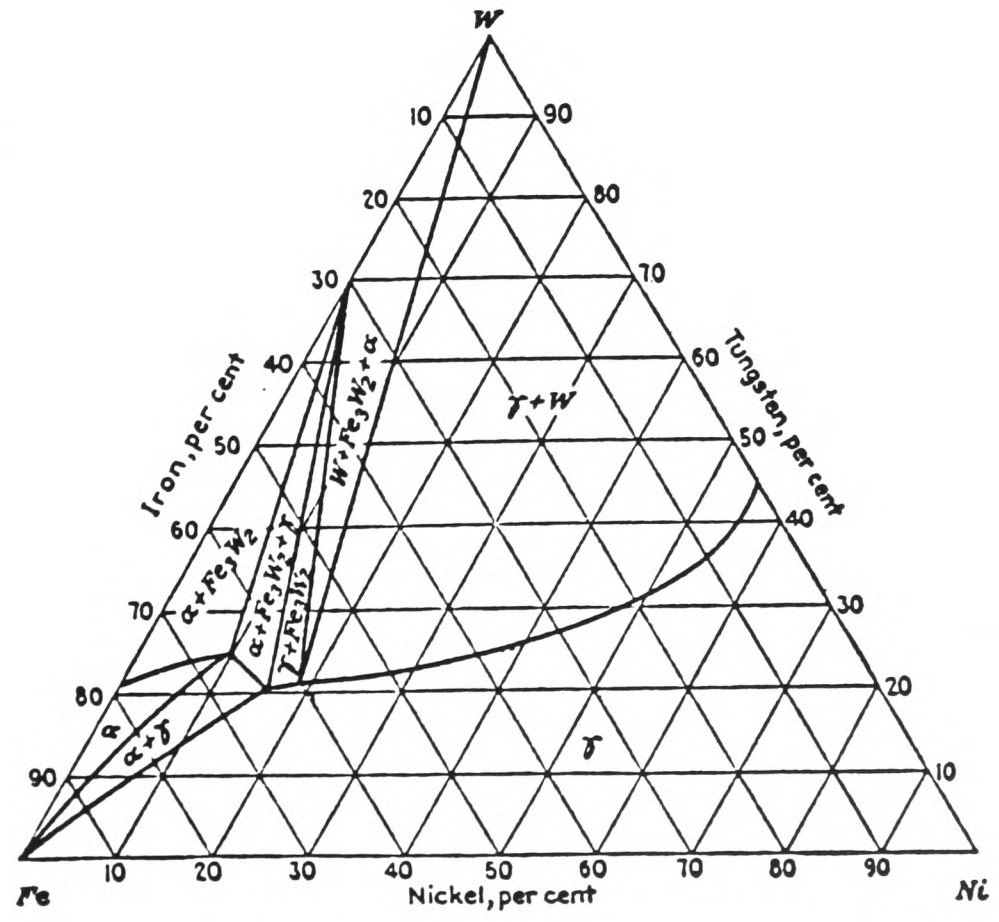

Chapter 3

EXPERIMENTAL TECHNIQUES AND PROCEDURES

1. Materials Processing

1.1. Tungsten Heavy Alloys

These alloys were commercially produced as outlined in chapter 1 section 1.1.

1.2. Matrix-Composition Alloy Manufacture

Two batches of these alloys were produced for examination.

1.2.1. Batch A

Appropriate measures of tungsten, nickel, and iron powders were mixed in a rotating mixing drum for approximately 16 hours. The powder was then arc-melted to form an ingot. The ingot was then homogenized at 1390°C for 50 hours. After grinding off the rough outer layer, the ingot was swaged to 3 mm rod - with intermediate and final annealing at 1350°C for 1 hour after every ~ 50% reduction in area. Random samples from the length of the rod were taken to check for compositional homogeneity with the electron microprobe.

1.2.2. Batch B

The processing was similar to batch A except for the following:

1) After the powder was mixed it was hydrostatically compressed into a green compact.
2) Before arc-melting, the green compact was sintered at 1000°C for 2 hours in a dry hydrogen atmosphere to remove residual water and oxygen.
3) Homogenization was carried out at 1150°C for 50 hours.

4) At an intermediate step in the swaging, the rod was given a solution treatment at 1350°C for 10 hours.

5) After swaging to 3mm rod, the alloy was given a further solution treatment at 1390°C for 20 hours.

The above procedure was used in the hope of eliminating inclusions (thought to be oxides) observed in batch A; in this the treatment was successful; however, this batch had other unusual features that will be discussed in the next chapter.

1.3. Deformation

Deformation of the relevant materials was accomplished in three ways:

1) Rolling

2) Swaging

3) Hydrostatic extrusion

All deformation was done at ambient temperature. The amount of deformation is reported in the usual way (i.e. % reduction in thickness for rolling and % reduction in cross-sectional area for swaging and hydrostatic extrusion).

1.4. Heat Treatment

Materials were heat treated in silica tubes under an argon atmosphere. The temperature was carefully monitored and a tolerance of ± 5°C should be assumed for the reported temperatures. After heat treatment, specimens were quenched into water at ambient temperature.

2. Optical Microscopy

Standard bright field optical microscopy was performed using a Zeiss metallograph. The specimens were compression molded in 1 inch diameter plastic mounts, progressively ground with finer grit silicon carbide papers, and polished with diamond paste down to ¼μm. It was essential to use

very thin polishing cloth to minimize relief polishing. Depending on requirement, a γ-Al_2O_3 suspension in distilled water was used for a final polish. The etching conditions used were:

To etch the W-phase - 10g potassium ferri-cyanide
10g NaOH
500ml H_2O
time ≈ 2 minutes

To etch the γ-phase - 10g ammonium persulfate
100ml H_2O
time ≈ 4 minutes

More general information concerning optical metallographic practice is provided by Kehl[48].

3. Scanning Electron Microscopy

Scanning electron microscopy was used to examine fracture surfaces. The specimens were obtained either by simple impact or from previously broken tensile testing bars. A Cambridge S1-80 SEM was used at an electron accelerating voltage of 20kV, utilizing secondary electrons for imaging. Typical magnifications were 1000X and 5000X. Goldstein and Yakowitz[49] provide various articles reviewing the theoretical details of this technique.

4. Transmission Electron Microscopy

4.1. Specimen Preparation and Storage

3 mm diameter discs were taken from material to be examined. Heavy alloy and tungsten discs were ground to approximately 100μm thickness using 400 and 600 grit silicon carbide paper. However, the matrix-composition alloy specimens were carefully ground to $\lesssim$ 50μm to minimize the deleterious imaging effects that a highly magnetic foil produces in the TEM. Specimens were electrochemically thinned using a Fischione twin-jet electropolishing unit with the following solution and conditions:

Electrolyte[50]	500ml methanol 46ml H_2SO_4 29ml lactic acid 12ml HF
Conditions (Heavy alloy and tungsten)	Voltage = 55V dc Current = 95 mA Temperature ≈ -30°C (with the specimen totally immersed in electrolyte)
Conditions (Matrix-composition alloy)	Voltage = 40V dc Current = 40 mA Temperature ≈ -30°C (with the specimen not immersed in electrolyte - only jet streams contacting the specimen)

Specimens were washed thoroughly after perforation using methanol and ethanol baths and then dried under a stream of warm air. Any specimens not examined immediately were stored in vacuum at ~ 10^{-6} torr.

4.2. Two-Beam Contrast Analysis

Hirsch, et al.[51], Thomas and Goringe[52], and Edington[53] have written general reviews of electron diffraction contrast theory; however, a brief summary of the essential concepts and parameters follows.

Assuming only two beams exist (i.e. the forward scattered beam and one diffracted beam) and that the column approximation is valid, the Darwin-Howie-Whelan equations for plane wave electron diffraction in a perfect crystal are

$$\frac{d\phi_o}{dz} = \frac{i\pi}{\xi_o}\phi_o + \frac{i\pi}{\xi_g}\phi_g \exp(2\pi isz)$$

$$\frac{d\phi_g}{dz} = \frac{i\pi}{\xi_g}\phi_o \exp(-2\pi isz) + \frac{i\pi}{\xi_o}\phi_g$$

When modified for the presence of a defect, the equations become

$$\frac{d\phi_o}{dz} = \frac{i\pi}{\xi_o}\phi_o + \frac{i\pi}{\xi_g}\phi_g \exp(2\pi isz + 2\pi i\underset{\sim}{g}\cdot\underset{\sim}{R})$$

$$\frac{d\phi_g}{dz} = \frac{i\pi}{\xi_g}\phi_o \exp(-2\pi isz - 2\pi i\underset{\sim}{g}\cdot\underset{\sim}{R}) + \frac{i\pi}{\xi_o}\phi_g$$

where $\phi_o = \phi_o(z)$ = amplitude of the forward scattered beam

$\phi_g = \phi_g(z)$ = amplitude of the diffracted beam

z = depth in the foil

ξ_o, ξ_g = constants (ξ_g is specifically referred to as the extinction distance for reflection g)

s = deviation parameter representing the deviation from the exact Bragg angle

$\underset{\sim}{g}$ = a vector normal to the diffracting plane (hkl) such that $|\underset{\sim}{g}| = \frac{1}{d_{hkl}}$

$\underset{\sim}{R} = \underset{\sim}{R}(z)$ = a displacement vector associated with the defect.

It is apparent that the transmitted intensity, $I_o = |\phi_o|^2$, and the diffracted intensity, $I_g = |\phi_g|^2$, are dependent on the parameter $\underset{\sim}{g} \cdot \underset{\sim}{R}$. Thus, for a given displacement vector $\underset{\sim}{R}$, characteristic of the defect in question, the image intensity will be a function of $\underset{\sim}{g}$ (s remaining constant). This leads to the invisibility criterion of $\underset{\sim}{g} \cdot \underset{\sim}{R} = 0$, where there will be no contrast from the defect. Experimentally it is possible to change $\underset{\sim}{g}$ by specimen tilting, thereby changing the image contrast due to the defect. By obtaining certain no-contrast ($\underset{\sim}{g} \cdot \underset{\sim}{R} = 0$) conditions with known $\underset{\sim}{g}$, then $\underset{\sim}{R}$, or certainly the direction of $\underset{\sim}{R}$, can be deduced. It is this method that has been used on the JEOL 100B electron microscope to characterize the direction of precipitate strain fields in the W-phase.

4.3. Weak Beam Imaging

The elegant technique of weak beam imaging has been used extensively for high resolution diffraction contrast studies of dislocation dissociation in fcc materials[54], fine precipitate structure[55], and heterogeneous precipitation nucleation[56], etc. In this study weak beam imaging was

used initially to observe an age hardening reaction in the W-phase. The theoretical development of the technique is discussed elsewhere[57]. In a simple sense, the technique acts as a "lattice strain probe"[58] where regions of high elastic strain appear brighter than a much suppressed background intensity.

Experimentally all weak beam images were taken at a film magnification of 50,000X using the $\underset{\sim}{g}/3\underset{\sim}{g}(\underset{\sim}{g} = \{211\}_W)$ technique described elsewhere [59]. Under these conditions $s \simeq 2.2\times10^{-2}$ $\mathring{A}^{-1}$ and $w = s\xi_g \simeq 5.6$ which, according to calculations by Cockayne for the core of a dislocation[59,60], should insure a high resolution (15-20$\mathring{A}$ half-width) image within ~ 20$\mathring{A}$ of the strain core. Exposure times were kept to less than 15 seconds to minimize the effects of stage instability.

4.4. Stereo Microscopy

Stereo microscopy was used to determine the depth of individual precipitates from the top of the foil. Thin foil samples were prepared in the manner described in section 4.1 and then very small (~ 20$\mathring{A}$ dia.) gold islands were evaporated onto one side of the foil. The foil was put into the microscope with the gold-sputtered side upwards - defining the top of the foil. A stereo pair of dark field micrographs (with accompanying selected area diffraction patterns) was obtained, separated by an angle of ~ 25°. Both micrographs were taken with the same diffracting conditions (i.e. the same two-beam $\underset{\sim}{g}(200)$ condition). Later, the exact tilt angle was ascertained by indexing the diffraction patterns using the Kikuchi lines. Knowing the exact magnification of the printed micrographs it was then possible, using a calibrated stereoviewer, to measure the parallax, Δp, between two features in the micrographs. Using simple geometry, Diepers[61] showed that the height difference, Δh, between these

two features in the foil is

$$\Delta h = \frac{\Delta p}{2M \sin(\phi/2)}$$

where M is the print magnification, ϕ is the angle of tilt, and Δp is the parallax between two features viewed in stereo on prints.

In this study a Zeiss stereoscope interfaced with an Apple computer was used to determine Δh between the top of the foil, defined by the gold islands, and a number of precipitates. For each precipitate the zero was set at the top foil surface and then four separate measurements were made of the precipitate depth. Finally, the zero was checked by measuring the height of the gold islands (which should be zero). In this way it was possible to minimize the severe random errors occurring due to the difficulty of judging 'depth' in stereo. An accuracy of ~ ± 15Å was obtained, which was sufficient for this work.

4.5. Convergent Beam Electron Diffraction

Convergent beam electron diffraction (CBED) can provide significantly more structural information about a crystal than the more commonly used selected area diffraction. By choosing appropriate zone axes and obtaining high quality CBED patterns it is possible to deduce the point and space group of an unknown phase. For the theoretical basis of the relationships between CBED symmetries and point and space group symmetries reference can be made to Buxton, et al.[62]

Briefly stated, CBED patterns are experimentally obtained by focussing a convergent electron beam onto the area of interest in the image mode and then switching over to diffraction mode. A selected area aperture is not necessary as only the area illuminated is contributing to the pattern. Instead of diffraction spots, diffraction discs are obtained, whose diameter is a function of the incident probe convergence angle, which, in turn, is

a function of the condenser lens currents and the condenser aperture size. When the crystal is tilted to a high symmetry zone axis, certain symmetries characteristic of the crystal point group should be immediately apparent. A more detailed description of the experimental procedure to obtain high quality CBED patterns has been presented by Steeds and Vincent [63]. Their paper also considers the more complicated task of space group determination using this technique.

CBED was used in the present work to help establish the point group of a precipitate phase with unknown crystal structure. Both JEOL 100C and Philips EM400 electron microscopes were used for this purpose but the EM400 was preferred as the pole piece construction allowed significantly more reciprocal space to be observed. The JEOL 100C only permitted observation of the zero order Laue zone, while the EM400 allowed many high order Laue zones (HOLZ) to be viewed. This is important as the HOLZ reflections are quite useful in helping to determine the precise whole pattern symmetry.

4.6. High Voltage Electron Microscopy

An AEI EM 7 operated at 1000kV or 900kV was used whenever standard 100kV microscopy proved difficult or impossible. The extra electron penetration afforded by the HVEM was essential for the study of the discontinuous and interphase precipitation reactions in the heavy alloy as larger areas of a specimen could be examined. Higher quality SAD patterns were obtainable with the HVEM making indexing much easier and measurements of d-spacings more accurate. Additionally, the HVEM enabled higher spatial resolution SAD patterns than otherwise possible with a 100kV machine (~ 0.2μm uncertainty for 1000kV as compared to ~ 0.8μm uncertainty for 100kV) [52].

4.7. *Energy Dispersive X-ray Analysis*

X-ray microanalysis of thin foils was done using suitably equipped JEOL 100C and HB-5 microscopes. The theory and application of this technique has been reviewed elsewhere [e.g.49,64]. Briefly, X-rays characteristic of the elements present are generated from the area of the specimen where the electron beam is focussed. The X-rays are detected and the results can be displayed in spectra form. Besides this identification of elements present it is also possible to arrive at an estimate of the relative concentrations of the various elements, although in the present study EDX thin foil microanalysis has only been used qualitatively.

5. X-ray Diffraction

Nearly all X-ray diffraction work was done on powder samples of extracted precipitate phase. The precipitate was extracted electrochemically using the solution described in section 4.1. The current applied was ~ 5mA dc and the process was carried out at room temperature. The resulting powder was thoroughly washed in ethanol, dried, and loaded into a Guinier camera or diffractometer for analysis as soon as possible.

5.1. *Guinier Camera*

X-ray powder photographs were obtained using a Stoe Guinier camera. Cu $K\alpha$ radiation was produced from a copper tube operated at 40kV and 30mA. Exposure times ranged from 1½ to 3 hours. After developing the film the lines were measured using a film-measuring device and converted to angles, θ. The d-spacings were then calculated using the Bragg equation. The patterns were indexed using methods described elsewhere [65].

5.2. *Diffractometry*

X-ray diffraction data was also obtained using a Philips diffractometer.

Monochromated Cu Kα radiation was used and the machine was operated with the following parameters:

1) Cu tube operated at 45kV and 32mA

2) Chart speed, 1 mm = 1°

3) Time constant = 1.0 seconds

4) Nickel filter used

5) Full scale was varied from sample to sample.

The powder specimen was floated onto a glass slide with acetone. The acetone quickly evaporated leaving the powder loosely adhering to the slide (attaching the powder with transparent adhesive tape proved unsuccessful as the tape produced large diffuse peaks at 2θ ≈ 12°and 21°- obliterating that part of the spectrum). Scans were made in the range 2θ = 10° to 95° and d-spacings were directly calculable using the Bragg equation.

6. Electron Microprobe (X-ray Microanalysis)

A Cameca Camebax electron microprobe was used to obtain quantitative compositional data from polished bulk specimens mounted in conducting mounts. Once spectra of pure metal standards were obtained and stored, it was possible to obtain spectra from the specimen being analyzed and then compute the relative concentrations using a ZAF correction program. The theory and application of this technique are described in more detail elsewhere[49,64]. The specific experimental parameters used are listed below:

Element	Line	Crystal
W	Mα	TAP
Ni	Kα	LIF
Fe	Kα	LIF

Accelerating Voltage = 20kV

Take off angle = 40°

Counting time = 15 or 20 seconds
(with usually
2 repeats)

Dead time = 2 μseconds

7. Secondary Ion Mass Spectrometry (SIMS)

SIMS was performed on precipitates suspected of containing small quantities of light elements (i.e. C,N, and B) not measurable with the electron microprobe. An Atomika ionprobe A-DIDA3000 was used in an attempt to verify this.

A detailed description of this technique is available elsewhere[49]. Briefly, a primary beam of ions (in this case, $^{16}O^-$) bombards the area of the specimen of interest thereby sputtering off surface atoms. Most of these sputtered atoms will be neutral and thus undetectable, but some will remain ions and thus will be detectable with a suitable mass spectrometer. This ion yield is a complicated function involving many factors (e.g. primary ion species and work function of specimen, etc.) and varies quite markedly from element to element.

The various isotopes can be counted and displayed in spectra form. Though precise quantification of results can be quite difficult, the tremendous sensitivity of this technique, sometimes in the parts per billion range, for all elements in the periodic table makes it a very powerful analytical tool. Because of this sensitivity, an ultra-high vacuum is a prerequisite. The spatial resolution of the Atomika machine is claimed to be ~ 1μm, which is the same order of the size of the precipitates (~ 3μm diameter) examined in this work.

8. Laser Induced Ion Mass Analyzer (LIMA)

LIMA was performed on the same alloy containing precipitates suspected of containing carbon, nitrogen, and/or boron. This micro-analytical technique was used in addition to the previously discussed SIMS technique. A Cambridge Mass Spectrometry Ltd. LIMA 2A machine was used for analysis. A more detailed description of the technique and the machine is found elsewhere[66].

Essentially, LIMA utilizes a short pulse (10nsec) of focussed laser radiation to ionize a small area of the sample. Unlike the SIMS technique, the relative concentrations of ions produced are much more representative of the bulk composition, making quantitative analysis much easier and quicker. A time-of-flight mass spectrometer is used to identify all the ions within a very short period of time (~100μsec). Spatial resolution is claimed to be in the 5μm range as 'craters' with this diameter have been viewed optically after analysis.

9. Mechanical Testing

9.1. Microhardness

Microhardness measurements were made on polished and etched specimens using a Reichert microhardness tester. A minimum of 10 indentations were obtained from each specimen using a 50g load. From these, vickers hardness numbers were calculated. The technique was used exclusively on the W-phase of the heavy alloy and tungsten single crystals to monitor hardening response as a function of aging treatment.

9.2. Tensile Testing

Tensile specimens were made to No. 15 Hounsfield specifications (gauge length = 25.2 mm, dia.≃ 5.05 mm, double shouldered) and given an

appropriate heat treatment. The gauge length was then polished to a mirror finish with 1μm diamond paste. All tests were performed on an Instron 1195 machine operating at a crosshead speed of 1mm/min.

Yield strength was determined using a standard 0.2% offset graphical method and the ultimate tensile strength was readily available from the chart. This technique was used to monitor precipitation hardening of the W-phase in the heavy alloy.

Chapter 4

EXPERIMENTAL RESULTS:

INTERPHASE (W-γ) AND MATRIX-PHASE PRECIPITATION

1. Interphase (W-γ) Precipitation

The materials examined in this section are the 90W-5Ni-5Fe heavy alloy (described in chapter 1 section 3.1) and a matrix-composition alloy (batch B - described in chapter 3 section 1.2). The matrix-composition alloy was intended to be a single phase simulation of the γ-phase in the 90W-5Ni-5Fe alloy with composition presented in Figure 4.1. However, even after solution treating at 1390°C for 20 hours, dispersed particles (~2.5μm diameter) of a second phase were observed (Fig.4.2). It will be shown that these precipitates bear a crystallographic similarity with the interphase precipitation observed in the 90W-5Ni-5Fe alloy, and therefore it is appropriate to present the analysis of both consecutively.

1.1. 90W-5Ni-5Fe Alloy

HVEM revealed precipitation at the W-γ boundaries when the heavy alloy was subjected to the following heat treatment sequence:

1) Solution treated at 1350°C for 1 hour and water quenched.

2) Annealed at 750-850°C for 100 hours and water quenched (Fig.4.3).

When the alloy was solution treated and annealed at a lower temperature (550°C) or a higher temperature (950°C) for 100 hours, no interphase precipitation was observed.

The size of the precipitates was $\lesssim$ 0.4 μm in thickness making them observable by TEM only. Additionally, the reaction was found to be very sporadic and nonuniform, and therefore the HVEM, which allowed examination

of significantly more area, was essential in this study.

Numerous selected area diffraction patterns were obtained from the interfacial precipitate (Fig. 4.4) and all could be indexed consistently with an fcc Bravais lattice. Using the W-phase as an internal standard (assuming $a_{W\text{-phase}} = a_W = 3.165\text{Å}$), the lattice parameter of the precipitate phase was found to be, $a_o = 10.96 \pm 0.04\text{Å}$.

This same phase was also observed at γ-γ grain boundaries in material heat treated as previously described (Fig. 4.5). This morphology was very infrequently observed as there are relatively few γ-γ grain boundaries - with only a very low percentage of them showing precipitation. An interface appears to be a prerequisite for the nucleation of this phase in the heavy alloy. Therefore, it is of interest that both stacking faults and annealing twins have been observed in the γ-phase (Fig. 4.6) under different conditions. These represent other possible nucleation sites for this precipitation reaction, although no precipitation was ever observed on them.

1.2. Matrix-Composition Alloy, Batch B (~ 21.5W - 38.5Ni - 40Fe)

1.2.1. Transmission Electron Microscopy

Figure 4.7 shows a typical HVEM micrograph of the undissolved precipitate. All SAD patterns obtained were consistent with a fcc Bravais lattice (Fig. 4.8). As there was no internal standard in these specimens, it was not possible to measure accurately the lattice parameter using electron diffraction, although it was estimated to be, $a_o \simeq 11\text{Å}$.

Convergent beam electron diffraction (CBED), as described in chapter 3 section 4.5, was utilized in an attempt to ascertain the point group of the precipitate. An appropriate condenser aperture was chosen that would allow the diffraction discs to overlap - thereby making the high order Laue

zones (HOLZ) more visible. Figure 4.9 shows [111] and [110] zone axes CBED patterns obtained from the precipitate in this manner. Unfortunately, the 'deficient' HOLZ lines in the forward scattered beam (referred to as "bright field" by Buxton, et al.[62]) were unobtainable. Nevertheless, certain symmetries are visible in both patterns.

Examining the [111] pattern first, it can be seen that the apparent whole pattern symmetry† is 3m. Utilizing the tables of Figure 4.10 due to Buxton, et al., the only possible diffraction groups are: 3m, $3m1_R$, and 6_Rmm_R. Since we know the crystal is cubic we can restrict ourselves to the five cubic point groups (Fig.4.10 b). This leaves two possible point groups: m3m and $\bar{4}3m$. Turning now to the [110] pattern, which has whole pattern symmetry of 2mm, the possible diffraction groups are: 2mm, $2mm1_R$, and 4_Rmm_R. From a [110] cubic zone axis this is quickly narrowed down to diffraction group $2mm1_R$, which corresponds to the m3m point group. Thus, it is concluded that the point group of the precipitate phase in the matrix-composition alloy is m3m.

1.2.2. X-ray Diffraction

Powder X-ray diffraction of the extracted precipitate phase was accomplished using both a Guinier camera and a diffractometer, as described in chapter 3 section 5. Figures 4.11 and 4.12 show a typical X-ray powder photograph and diffractometer trace, respectively. The d-spacings can be indexed according to a diamond cubic-type lattice with lattice parameter, $a_o \simeq 11.18\text{Å}$.

---

† 'Apparent' whole pattern symmetry refers to the entire pattern symmetry (including the HOLZ lines) except for the direct beam. Strictly speaking, the whole pattern symmetry must include the bright field symmetry. However, the direct beam always contains equal or more symmetry elements as the whole pattern *(63)* (exclusive or inclusive of the direct beam) - thereby not restricting the whole pattern symmetry. Thus, the apparent whole pattern symmetry is the same as the whole pattern symmetry.

Since the point group is m3m there are ten possible space groups (Nos. 221-230)[68]. Numbers 221-224, 229, and 230 can be ruled out immediately as they are primitive and body-centered cubic structures. Space groups 225 and 226 have only the diffraction condition that the structure factor is not equal to zero (i.e. the reflection is permissible) for h, k, and l all even or all odd[68]. This means that many reflections that were not experimentally observed would have been expected for either of these two space groups (e.g. 200, 311, 222, 420, etc.). Thus, space groups numbers 225 and 226 are very unlikely possibilities - particularly as the {111} reflection was experimentally observed but not the {222} reflection.

The choice is narrowed to space groups 227 and 228. Figure 4.13 lists the nonforbidden reflections for both space groups alongside the reflections that were observed experimentally. There are discrepancies for both possibilities, but in the case of space group No. 228, there are certain reflections that are not expected but are observed experimentally (e.g. 111, 331, 511/333, 711/551, and 733). In particular, the 511/333 reflection is the most intense observed experimentally but is forbidden for space group No. 228. The discrepancy between the experimental and S.G. No. 227 is only that certain reflections were not observed that are not forbidden for this space group. It is quite possible that these nonforbidden reflections have zero or very low intensity, rendering them experimentally nondetectable. Consequently, it is concluded that the space group of the precipitate phase is Fd3m (No. 227).

1.2.3. Microanalysis

Electron microprobe analysis, as described in chapter 3 section 6, was performed on a polished bulk specimen of matrix-composition alloy. The analysis showed the average composition of the precipitate phase to be:

	wt%	at% (±0.3 at%)
W	76.5	50.2
Ni	10.0	20.6
Fe	13.5	29.2

A detailed scan through the energy spectrum using the crystal spectrometers to look for X-rays characteristic of additional elements (esp. carbon and silicon) showed no other element to be present in any significant quantity (i.e. $\gtrsim$ 0.1 wt%), even though a very small Si Kα peak was observed (Fig. 4.14). However, this result was not completely trusted as the electron microprobe was thought to be unsuitable for detecting the presence of small quantities of light elements in a high average atomic number compound because the high bremsstrahlung would be expected to obscure X-ray peaks.

Secondary Ion Mass Spectrometry (SIMS), as described in chapter 3 section 7, was then used in an attempt to detect the presence of light elements (e.g. C, N, and B) in a precipitate. Unfortunately, experimental difficulties prevented high spatial resolution from being realized, and therefore it was not possible to obtain elemental data from just the precipitate. Spectra obtained from relatively large areas of the specimen (~200μm^2) did show the presence of carbon, boron, and nitrogen. Although no attempt was made to quantify precisely their concentrations, it was believed to be in the parts per million range.

LIMA microanalysis, as described in chapter 3 section 8, was also used to attempt detection of light elements in the precipitate. Figure 4.15 shows spectra obtained from a region with a precipitate and a region of surrounding matrix. A tiny carbon peak and two seemingly spurious peaks on the low atomic mass side of the calcium and sodium peaks are observed in the precipitate spectrum but not in the matrix spectrum. The 'spurious' peaks, unfortunately, remain unexplained, but the carbon peak is thought

to be genuine since (a) it is not accompanied by hydrogen from hydrocarbons, and (b) the Na, K, and Ca signals are not larger from the precipitate region indicating that the general contamination is not greater at the precipitate. Because of the high ionization potential of carbon compared to nickel, iron, and tungsten, LIMA will be much less carbon-sensitive, and therefore a rough estimate of the carbon level would be ~ 1-2 at %[69].

It must be remembered that spectra are obtained from a region ~5μm diameter while the precipitates are only about 2.5μm diameter. Using these values it is easy to show that a typical precipitate only contributes to ~ 25% of a 'precipitate region' spectrum while the balance is due to the surrounding matrix. This changes the estimate of the precipitate carbon concentration to $\lesssim$ 8 at %.

2. Matrix-Phase Precipitation

The materials examined in this section are the 90W-5Ni-5Fe heavy alloy and a matrix-composition alloy (batch A - described in chapter 3 section 1.2). This matrix-composition alloy is essentially single phase (γ-fcc) but contains dispersed inclusions (Fig. 4.16). Electron microprobe results showed the average alloy composition to be, 19.2W-41.4Ni-39.4Fe. The inclusions were found to contain a substantial amount of titanium and, due to the nature of alloy manufacture, are thought to be complex oxides.

2.1. 90W-5Ni-5Fe Alloy

A discontinuous precipitation reaction occurring in the γ-phase was observed concurrently with the interfacial precipitation described earlier (Fig. 4.17). This reaction could also be observed optically, although the reaction product lamellae could not be properly resolved (Fig. 4.18). Again, this reaction is very irregular and nonuniform. Prior solution

treating at 1350°C and water quenching was essential as just annealing for 100 hours at 800°C showed no discontinuous precipitation. Considering isochronal (t=100 hours) heat treatments, the discontinuous reaction was only observed after solution treating and annealing at 750-850°C. With annealing at 850°C precipitation could be observed after 5 hours (Fig. 4.19), but no precipitation was observed after solution treating and annealing at 950°C for 200 hours. Longer anneal times (t>100 hours) were not attempted at lower temperatures.

Selected area electron diffraction using the HVEM consistently showed the identity of the lamellae to be tungsten and tungsten-depleted γ (Fig. 4.20). Although the characteristic boundary of the cellular reaction was observed (see Fig. 4.17a), it was not possible to establish at which microstructural feature the reaction had nucleated.

2.2. Matrix-Composition Alloy, Batch A (19.2W - 41.4Ni - 39.4Fe)

The initial processing of this alloy included solution treating at 1350°C for 1 hour. Figure 4.21 shows a series of optical micrographs taken from specimens aged 100 hours in the temperature range 750-1250°C. The specimens annealed at 750-950°C show a morphology typical of a discontinuous precipitation reaction product. In specimens aged for shorter times (e.g. 10 hours), discontinuous precipitation can clearly be seen to nucleate at the grain boundaries and grow into one (or sometimes both) adjacent grains (Fig. 4.22). No precipitation was observed after annealing at ≤ 650°C for 100 hours. As the aging temperature was raised above 950°C the morphology changes from discontinuous to predominantly grain boundary precipitation at 1250°C.

TEM shows the precipitate morphology at higher resolution (Figs. 4.23 -4.25). After aging at 850°C for 100 hours various morphologies can be observed (Fig. 4.23). Clearly, discontinuous precipitation is present,

but the W lamellae appear to be broken up in some areas. In other regions, a Widmanstatten morphology is observed. After heat treating at the lower temperature of 750°C for 100 hours the morphology is essentially all discontinuous, while aging at the higher temperature of 1050°C for 100 hours the precipitation is widmanstatten (Fig. 4.24). At still higher aging temperatures (i.e. 1250°C) precipitation is observed almost exclusively on the grain boundaries. Selected area electron diffraction showed the precipitates, whatever their morphology, to be tungsten. Also, in the case of the alloy aged at 1250°C for 100 hours, a Nishiyama-Wassermann bcc/fcc orientation relationship was observed between the grain boundary allotriomorph and one adjacent grain (Fig. 4.25)

Powder X-ray diffraction of precipitate extracted from alloy aged at various temperatures verified the identity of the precipitate as tungsten. Additionally, the lattice parameter of unaged matrix-composition alloy was measured to be, $a_o = 3.605 \pm 0.005$ Å (Fig. 4.26).

Figure 4.1

Bulk chemical analysis results for the 90W-5Ni-5Fe alloy and the matrix-composition alloy (batch B). (weight per cent)

	90W-5Ni-5Fe	Matrix-Composition Alloy (batch B)
W	89.70	21.21
Ni	4.36	38.08
Fe	4.77	39.70
C	0.004	0.10
Si	0.73	0.72
S	0.003	0.005
P	< 0.01	< 0.01
K	0.05	0.02
Ca	0.14	0.02
B	< 0.0005	0.0014
N	< 0.01	< 0.01
Na	0.21	0.05

Performed by S.G.S. Inspection Services Ltd., Birmingham, 27th July 1983.

Figure 4.2

Optical micrograph of the matrix-composition alloy (batch B) showing dispersed precipitates.

Figure 4.3

HVEM micrographs showing W-Y precipitation in the heavy alloy.

a) Solution treated and aged at 750°C for 100 hours.

b) Solution treated and aged at 850°C for 100 hours (some of the precipitate has been polished away).

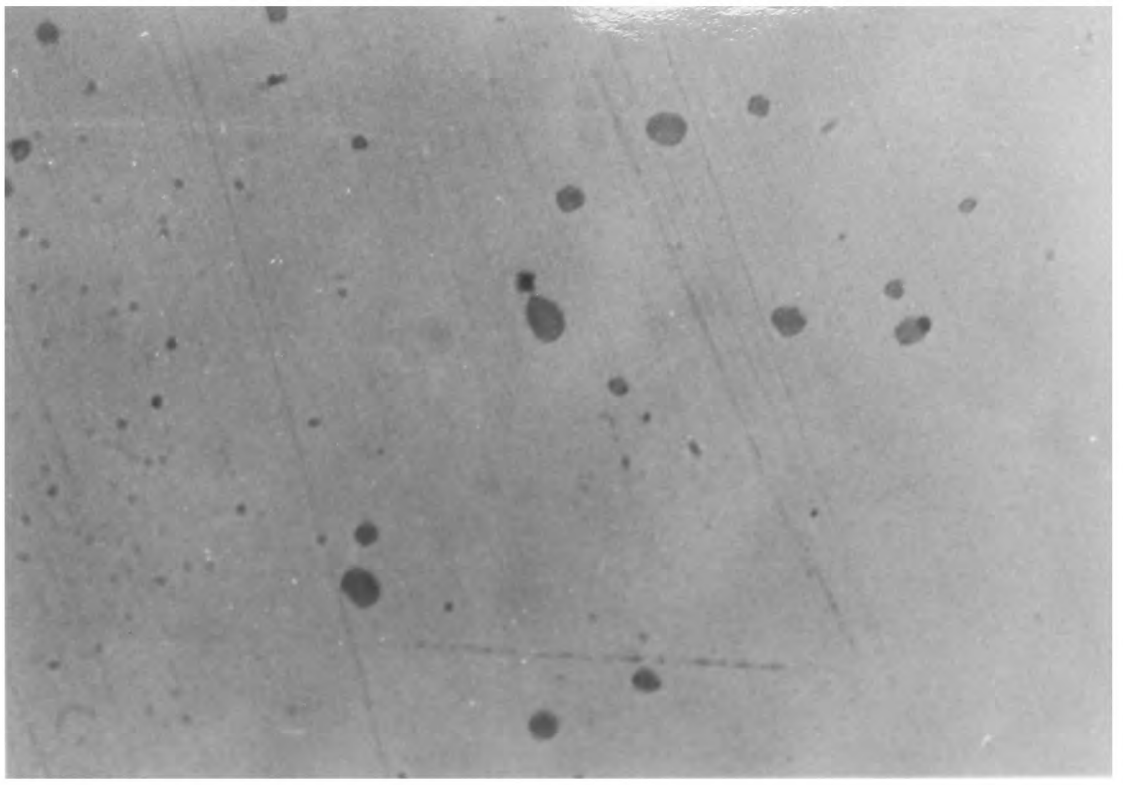

-25μm-

a

b

-0.5μm-

Figure 4.4

Typical SAD patterns obtained from the interfacial precipitate in the heavy alloy. All can be indexed according to an fcc lattice with $a_o \simeq 10.96\text{Å}$.

a) $z \simeq [01\bar{5}]$

b) $z \simeq [011]$

c) $z \simeq [\bar{5}\underline{1}07]$

d) $z \simeq [16\bar{9}]$

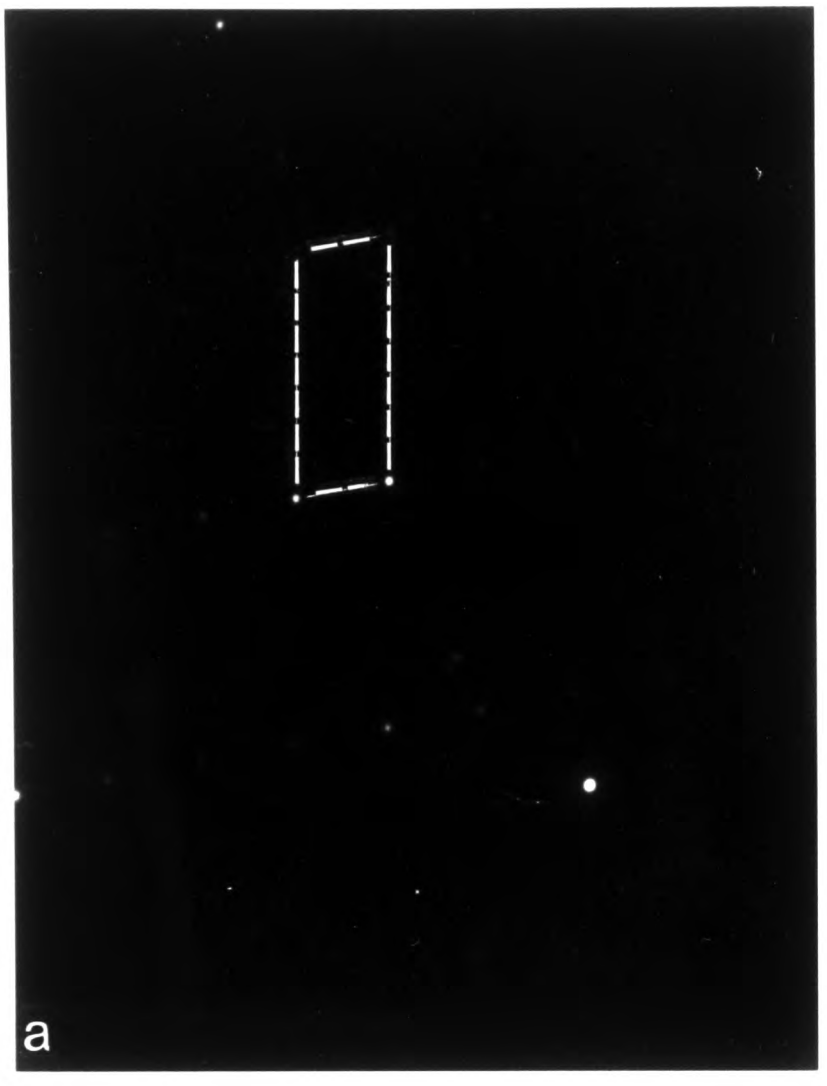
a

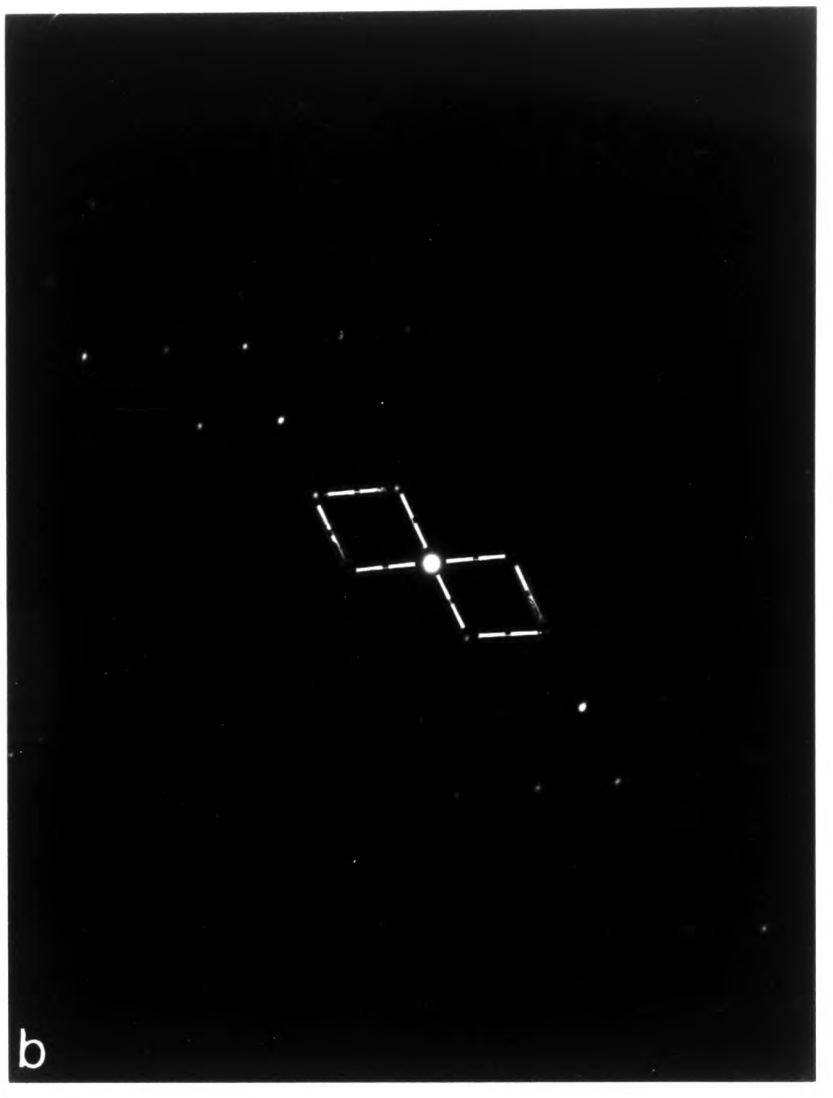
b

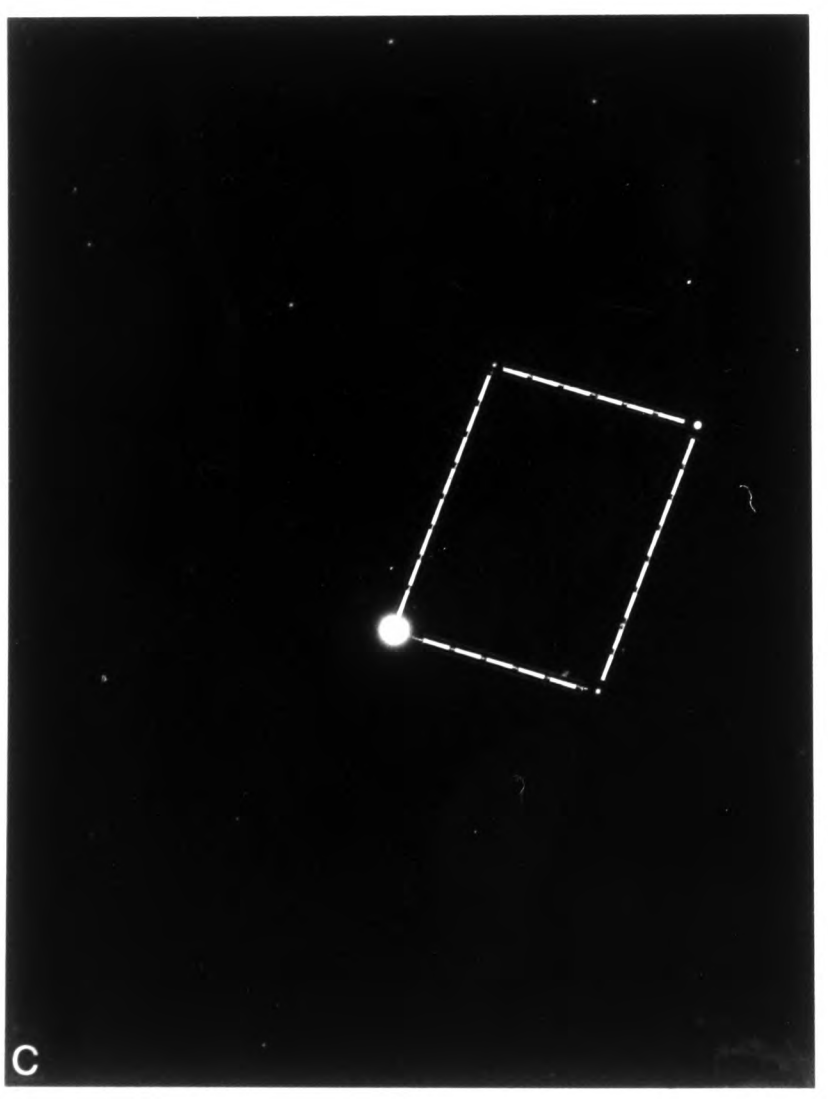
c

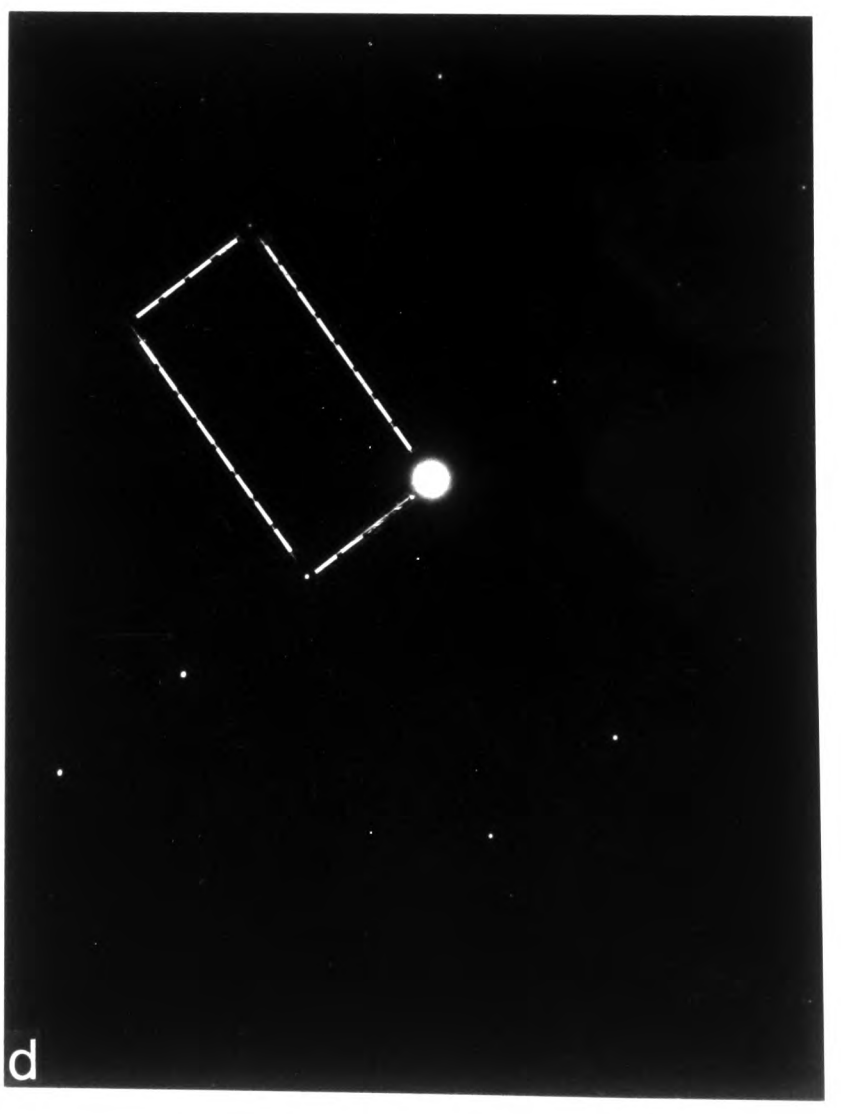
d

Figure 4.5

HVEM micrograph of heavy alloy that has been solution treated and aged at 750°C for 100 hours - showing precipitation on a γ-γ grain boundary.

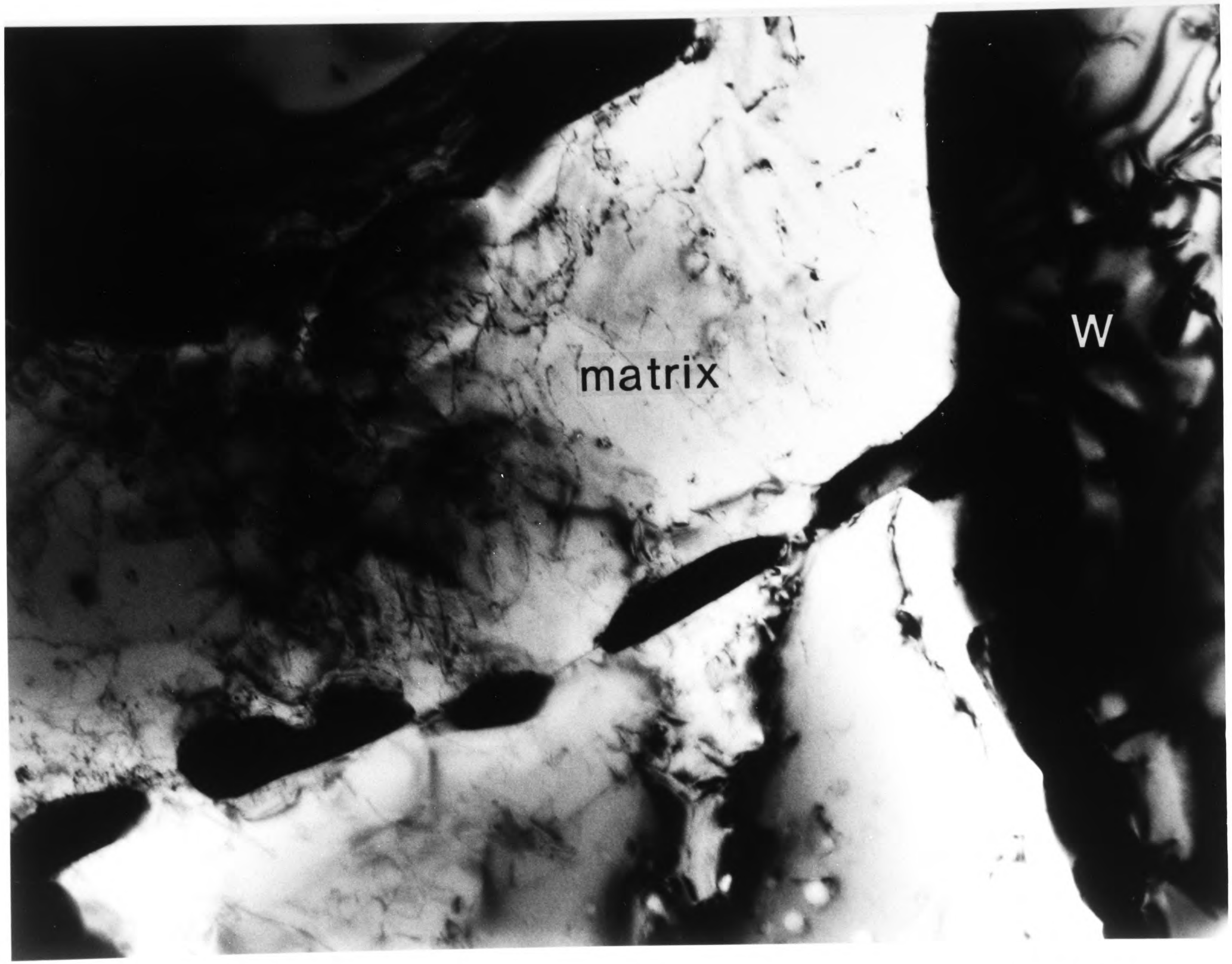
matrix
W
0.5μm

Figure 4.6

a) Dark field TEM micrograph of 90W-5Ni-5Fe alloy aged at 1050°C for 1 hour ($\underset{\sim}{g}(111)$ and $s \simeq 0$). Because $(111)_{fcc}$ is a class B reflection and $\underset{\sim}{g}$ is pointing from the light outer fringe to the dark outer fringe, the stacking fault is intrinsic[67].

b) TEM micrograph of the 90W-5Ni-5Fe alloy aged at 900°C for 100 hours showing a $[\bar{1}\bar{1}1]$ fcc annealing twin in the matrix.

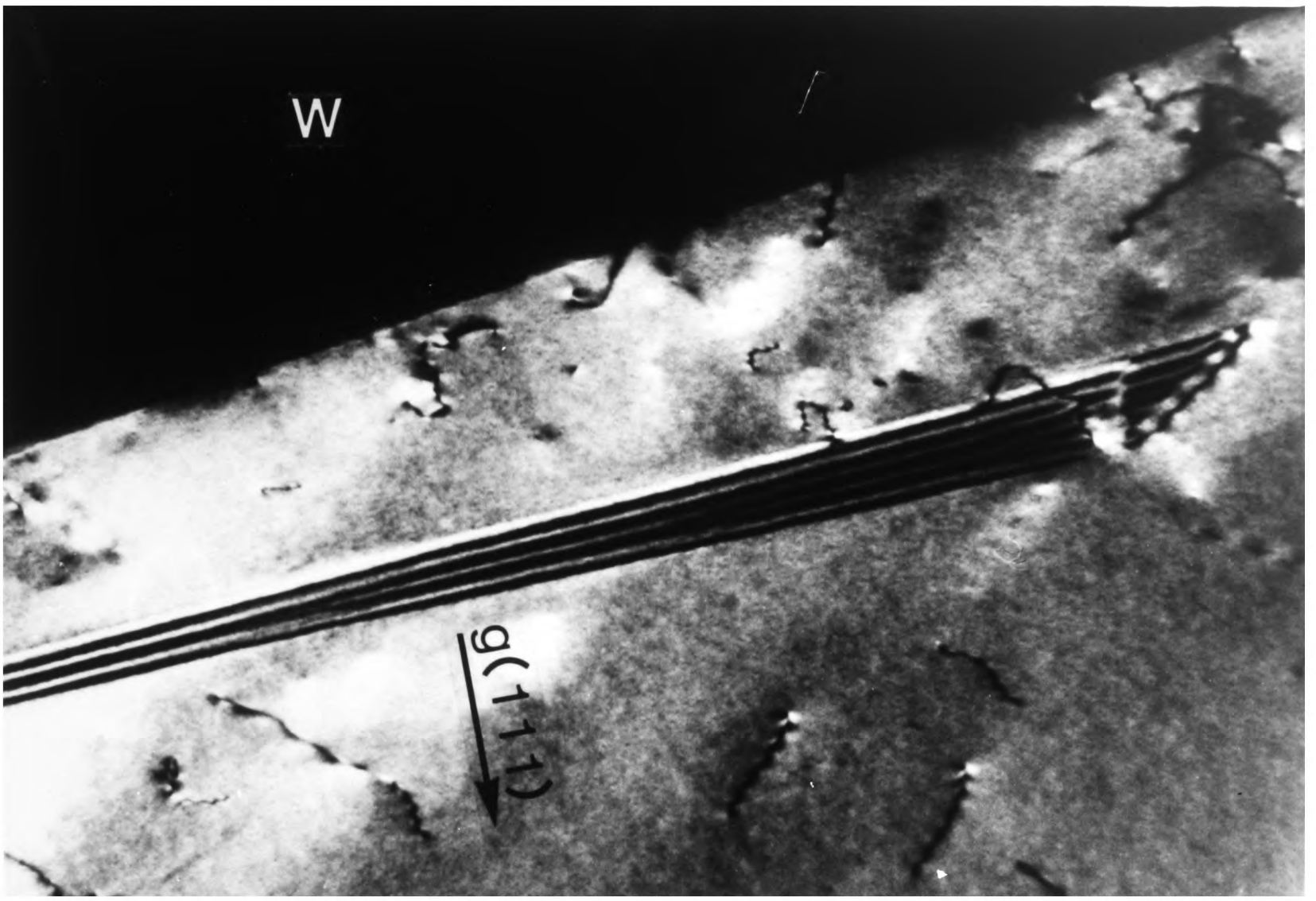
W
g(1 1 1)

a

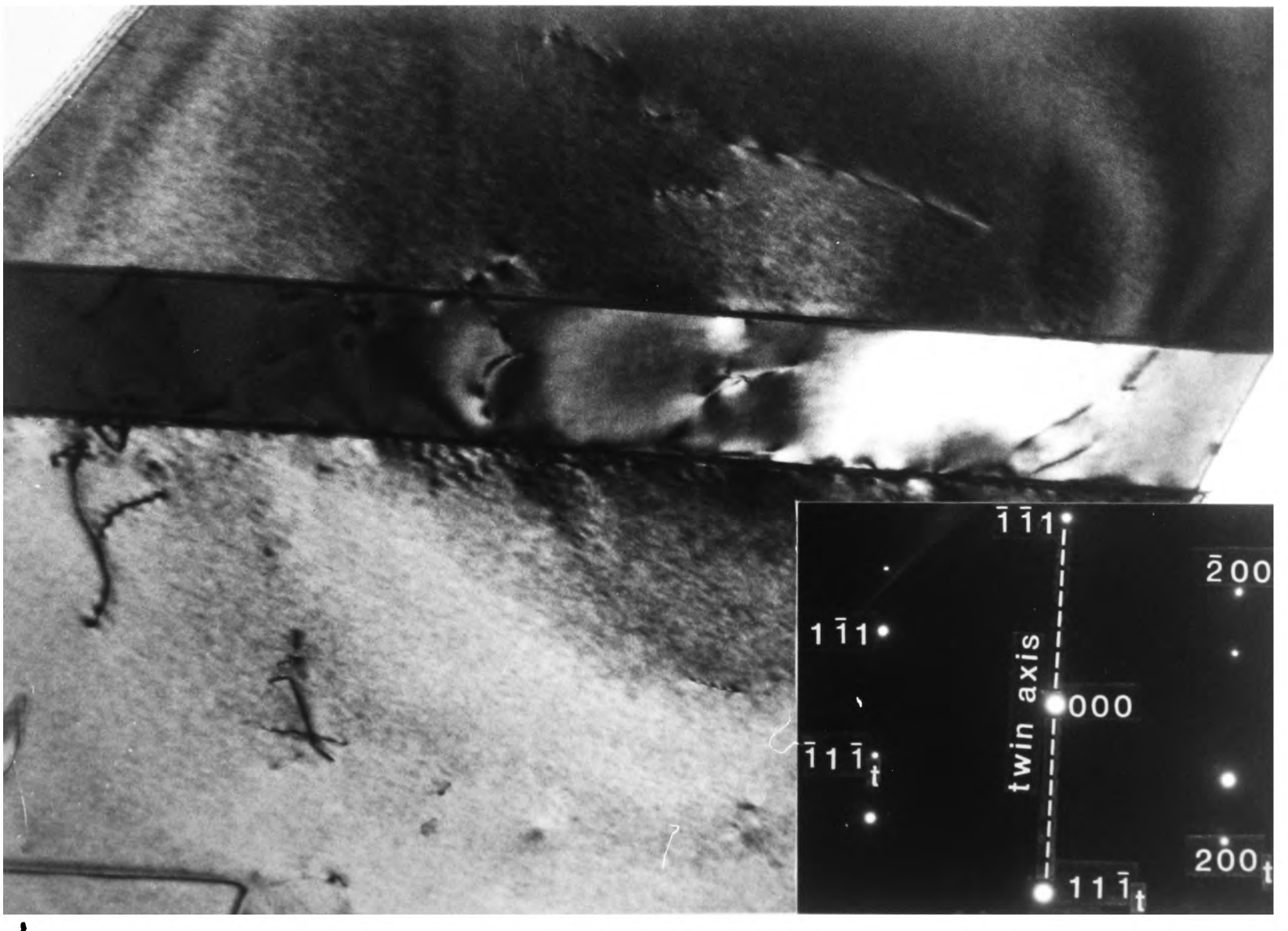
$\bar{1}\bar{1}1$
$\bar{2}00$
$1\bar{1}1$
twin axis
000
$\bar{1}1\bar{1}_t$
200_t
$11\bar{1}_t$

b

-0.2μm-

Figure 4.7

HVEM micrograph of the undissolved precipitate in the matrix-composition alloy (batch B).

Figure 4.8

Typical SAD patterns from the undissolved precipitate in the matrix-composition alloy (batch B). All patterns could be indexed consistent with an fcc lattice with $a_o \simeq 11\text{Å}$.

a) z = [111]

b) z = [345]

c) z = [325]

d) z = [974]

e) z = [365]

f) z = [554]

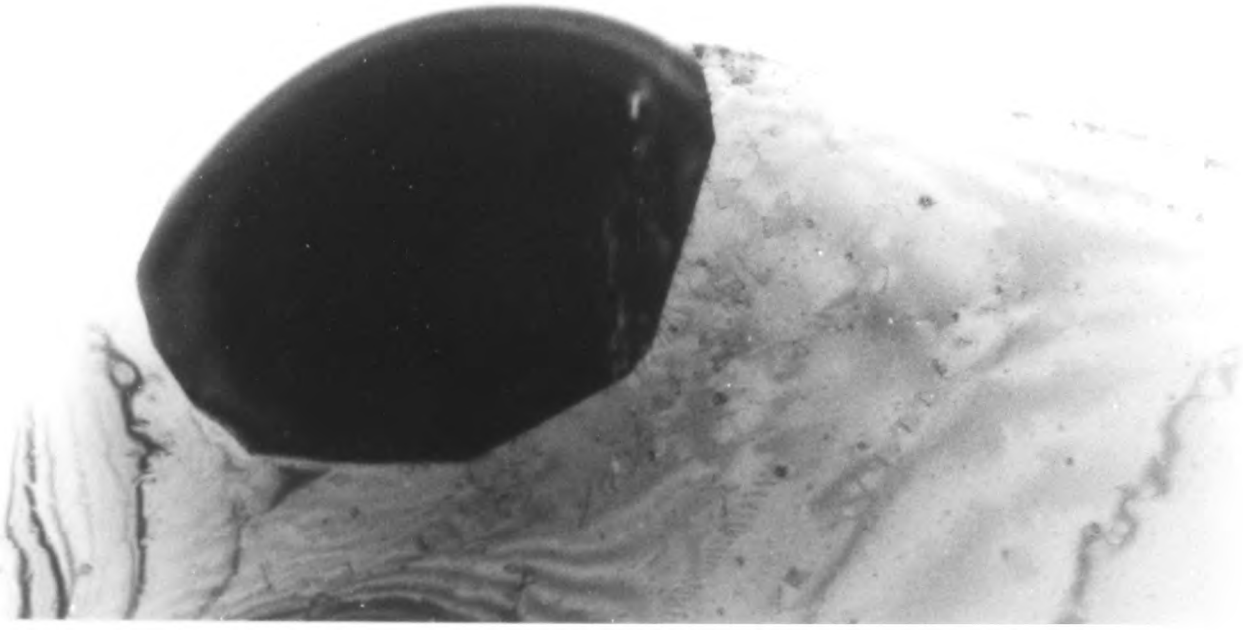

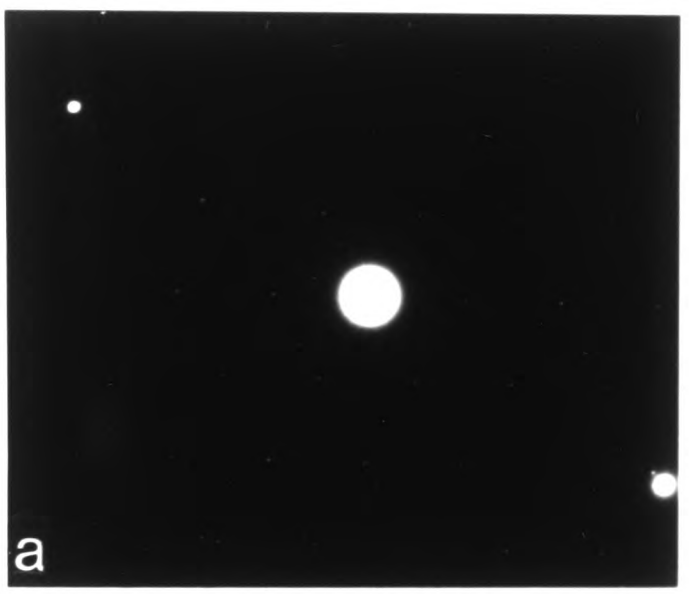
a

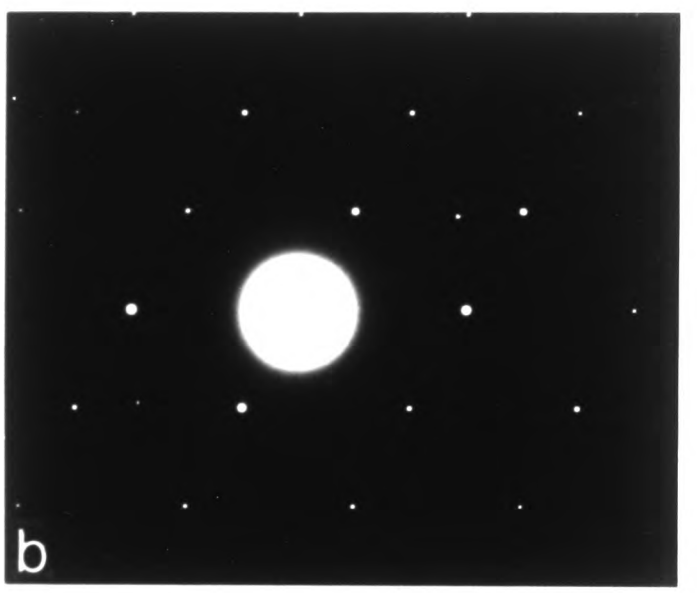
b


c

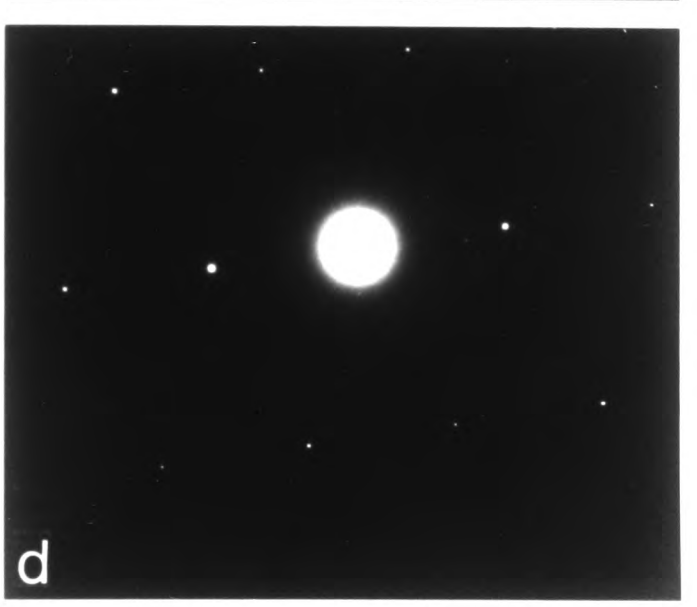
d


e


f

Figure 4.9

CBED patterns from the undissolved precipitate in the matrix-composition alloy (batch B).

a) z = [111] showing 3m symmetry.

b) z = [110] showing 2mm symmetry.

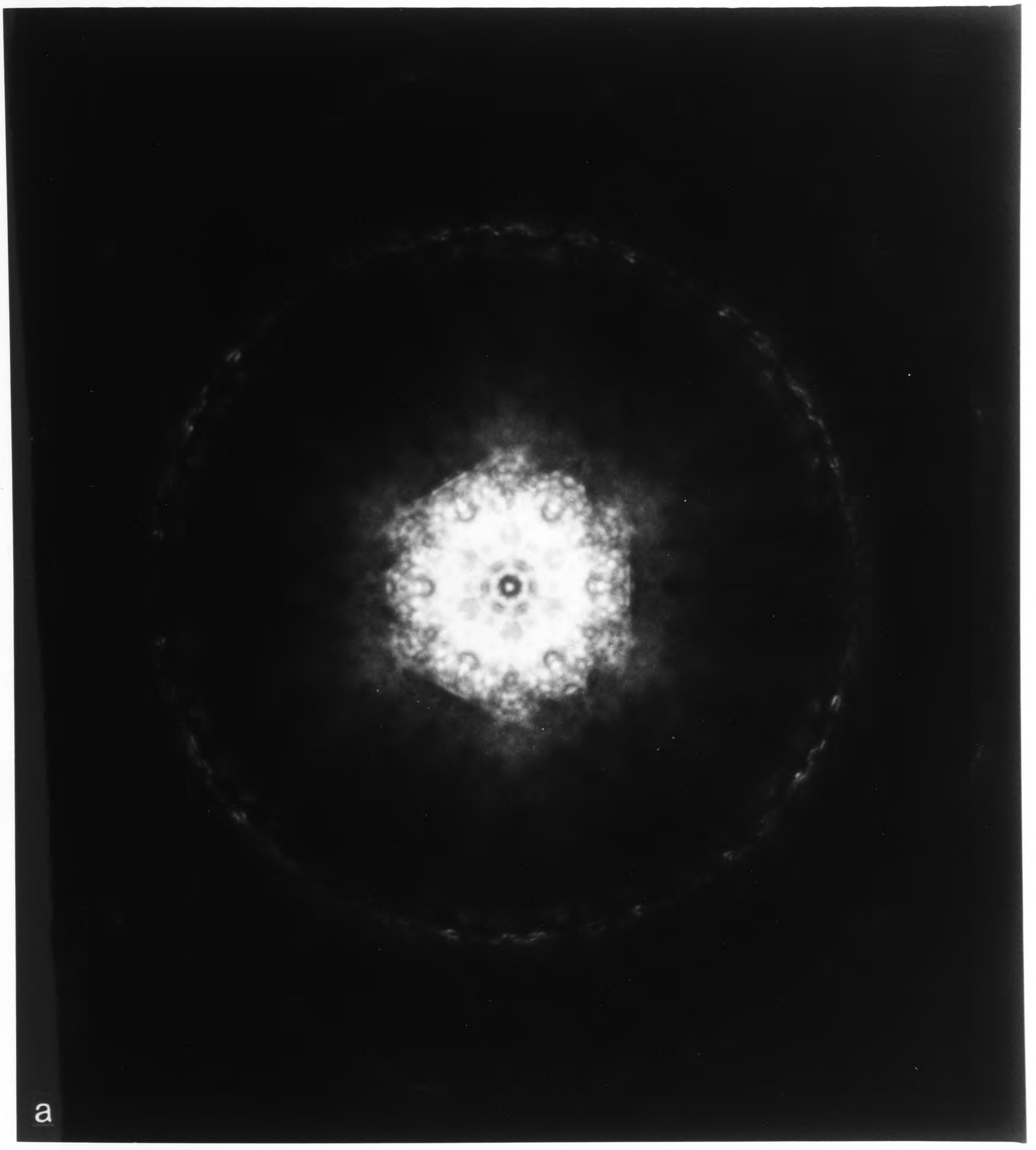
a

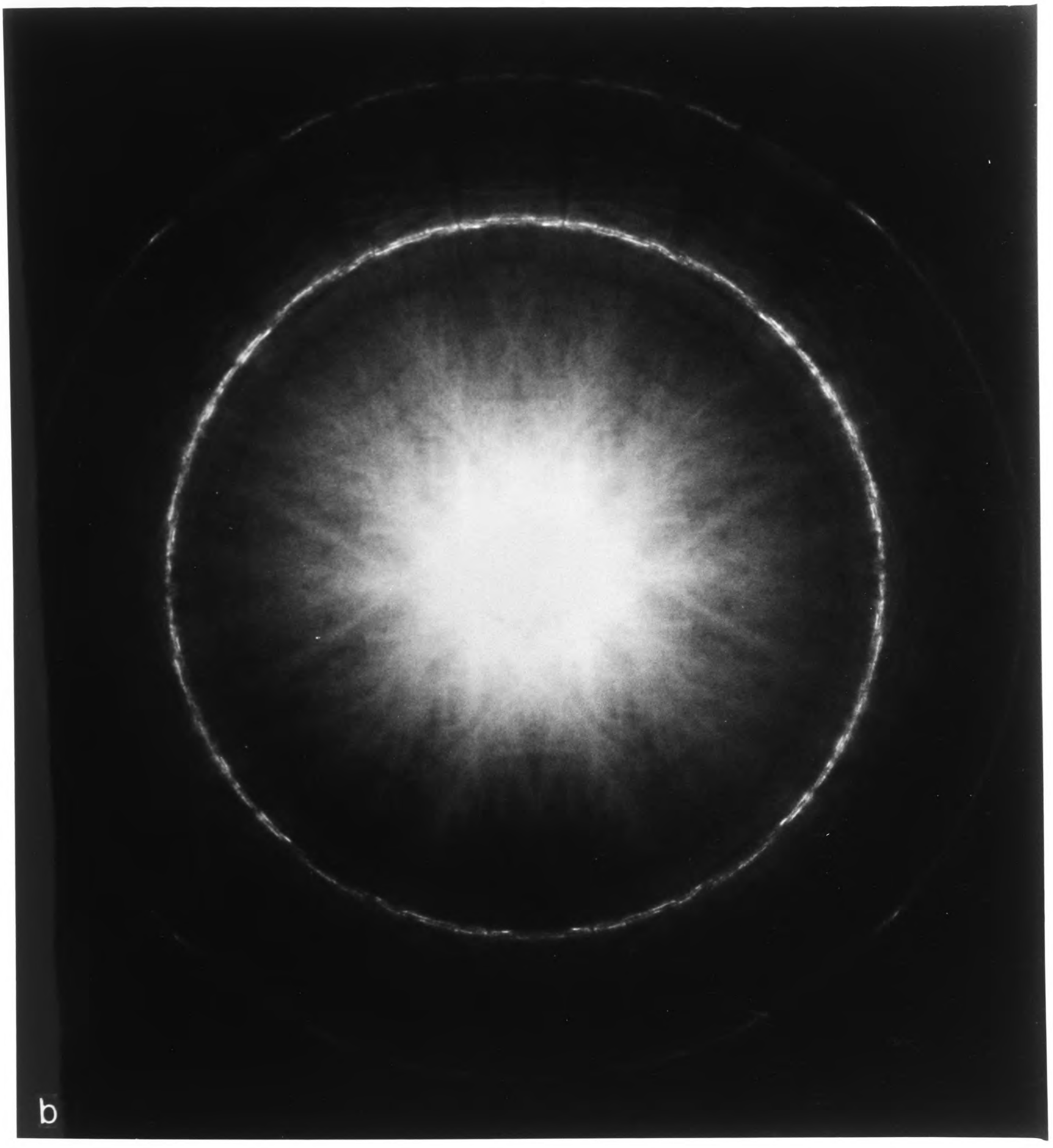
b

Figure 4.10

Convergent Beam Symmetry Tables (after Buxton, et al.[62]).

a) Pattern symmetries for the various diffraction groups.

b) Zone axis symmetries for the cubic point groups.

a)

diffraction group	bright field	whole pattern	dark field		±G		projection diffraction group
			general	special	general	special	
1	1	1	1	none	1	none	1_R
1_R	2	1	2	none	1	none	
2	2	2	1	none	2	none	21_R
2_R	1	1	1	none	2_R	none	
21_R	2	2	2	none	21_R	none	
m_R	m	1	1	m	1	m_R	$m1_R$
m	m	m	1	m	1	m	
$m1_R$	2mm	m	2	2mm	1	$m1_R$	
$2m_Rm_R$	2mm	2	1	m	2	—	$2mm1_R$
2mm	2mm	2mm	1	m	2	—	
2_Rmm_R	m	m	1	m	2_R	—	
$2mm1_R$	2mm	2mm	2	2mm	21_R	—	
4	4	4	1	none	2	none	41_R
4_R	4	2	1	none	2	none	
41_R	4	4	2	none	21_R	none	
$4m_Rm_R$	4mm	4	1	m	2	—	$4mm1_R$
4mm	4mm	4mm	1	m	2	—	
4_Rmm_R	4mm	2mm	1	m	2	—	
$4mm1_R$	4mm	4mm	2	2mm	21_R	—	
3	3	3	1	none	1	none	31_R
31_R	6	3	2	none	1	none	
$3m_R$	3m	3	1	m	1	m_R	$3m1_R$
3m	3m	3m	1	m	1	m	
$3m1_R$	6mm	3m	2	2mm	1	$m1_R$	
6	6	6	1	none	2	none	61_R
6_R	3	3	1	none	2_R	none	
61_R	6	6	2	none	21_R	none	
$6m_Rm_R$	6mm	6	1	m	2	—	$6mm1_R$
6mm	6mm	6mm	1	m	2	—	
6_Rmm_R	3m	3m	1	m	2_R	—	
$6mm1_R$	6mm	6mm	2	2mm	21_R	—	

b)

point group	⟨111⟩	⟨100⟩	⟨110⟩	⟨*vvo*⟩	⟨*uuu*⟩	[*uvw*]
m3m	6_Rmm_R	$4mm1_R$	$2mm1_R$	2_Rmm_R	2_Rmm_R	2_R
$\bar{4}3m$	3m	4_Rmm_R	$m1_R$	m_R	m	1
432	$3m_R$	$4m_Rm_R$	$2m_Rm_R$	m_R	m_R	1

point group	⟨111⟩	⟨100⟩	⟨*uuo*⟩	[*uvw*]
m3	6_R	$2mm1_R$	2_Rmm_R	2_R
23	3	$2m_Rm_R$	m_R	1

Figure 4.11

Guinier powder X-ray photograph of the phase extracted from the matrix-composition alloy (batch B). The measured d-spacings are listed and are indexed according to a diamond cubic-type lattice with $a_o \simeq 11.18\text{Å}$.

Line No.	d(Å)	{hkl}
1	6.559	111
2	3.991	220
3	2.807	400
4	2.574	331
5	2.287	422
6	2.156	511,333
7	1.979	440
8	1.866	600,442
9	1.768	620
10	1.687	622
11	1.566	711,551
12	1.457	731,553
13	~ 1.40 (v.wk.)	800
14	1.366	733
15	1.318	660,822
16	1.291	555,751
17	~ 1.23 (v.wk.)	753,911
18	~ 1.19 (v.wk.)	664
19	1.124	755,771,933
20	1.096	862,1020

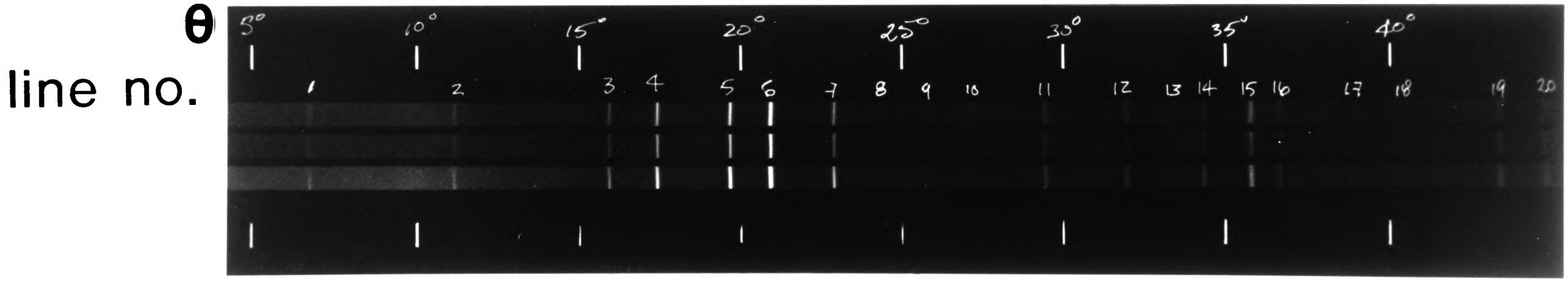
θ
5°
10°
15°
20°
25°
30°
35°
40°
line no.
1
2
3
4
5
6
7
8
9
10
11
12
13
14
15
16
17
18
19
20

Figure 4.12

X-ray diffractometer trace of the extracted precipitate. See Figure 4.11 for d-spacings.

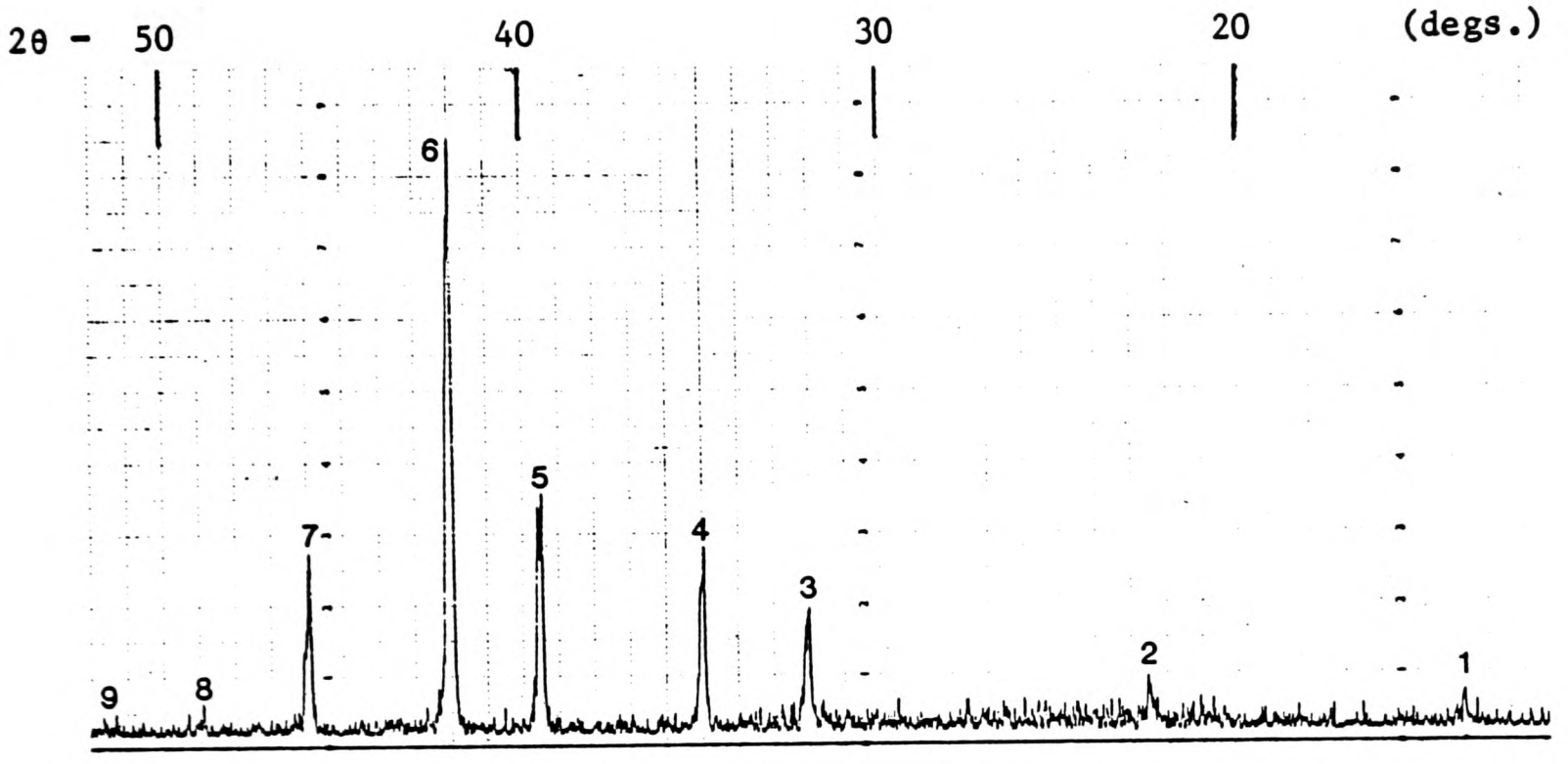

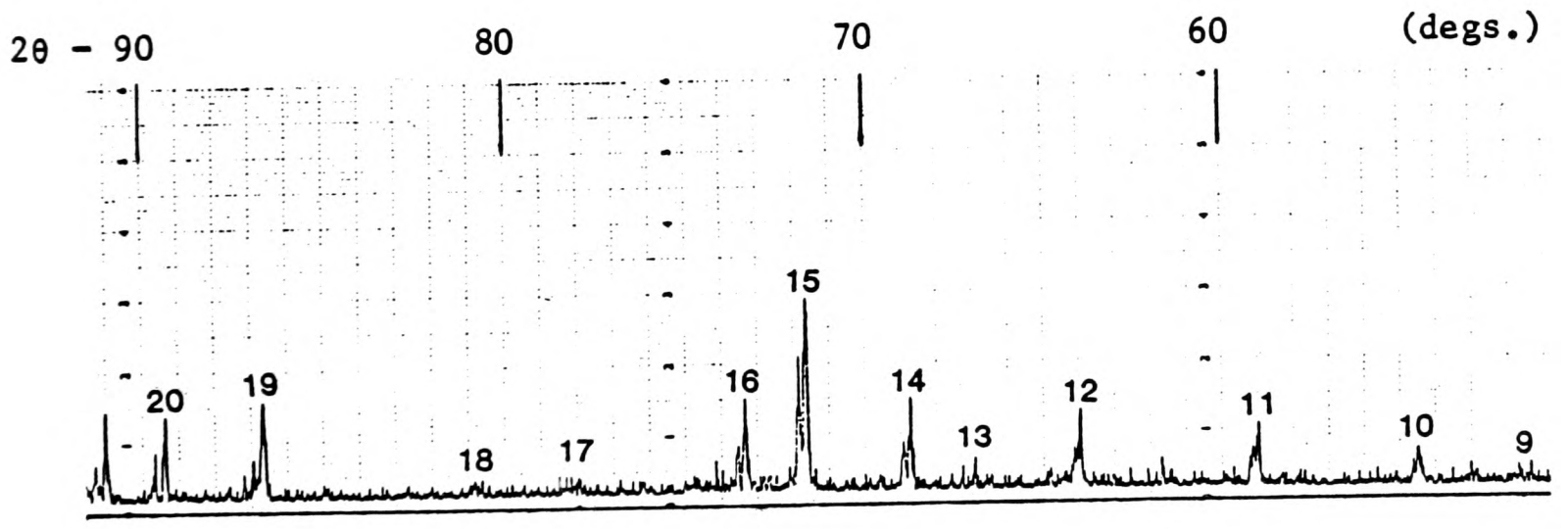

Figure 4.13

Experimentally observed X-ray reflections alongside the nonforbidden reflections for space group numbers 227 and 228 (X denotes either observed or nonforbidden).

$\{hkl\}_{fcc}$	Experimental	No. 227	No. 228
111	X	X	
200			
220	X	X	X
311		X	
222		X	X
400	X	X	X
331	X	X	
420			
422	X	X	X
511,333	X	X	
440	X	X	X
531		X	X
600,442	X	X	X
620	X	X	X
533		X	
622	X	X	X
444		X	X
711,551	X	X	
640			
642		X	X
731,553	X	X	X
800	X	X	X
733	X	X	
644,820		X	X
660,822	X	X	X
555,751	X	X	X
662		X	X
840		X	X
753,911	X	X	X
842		X	X
664	X	X	X
931		X	X
844		X	X
933,755,771	X	X	
860,$\overline{1}000$			
862,$\overline{10}20$	X	X	X

Figure 4.14

A portion of the electron microprobe spectrum of the precipitate phase showing a small Si Kα peak.

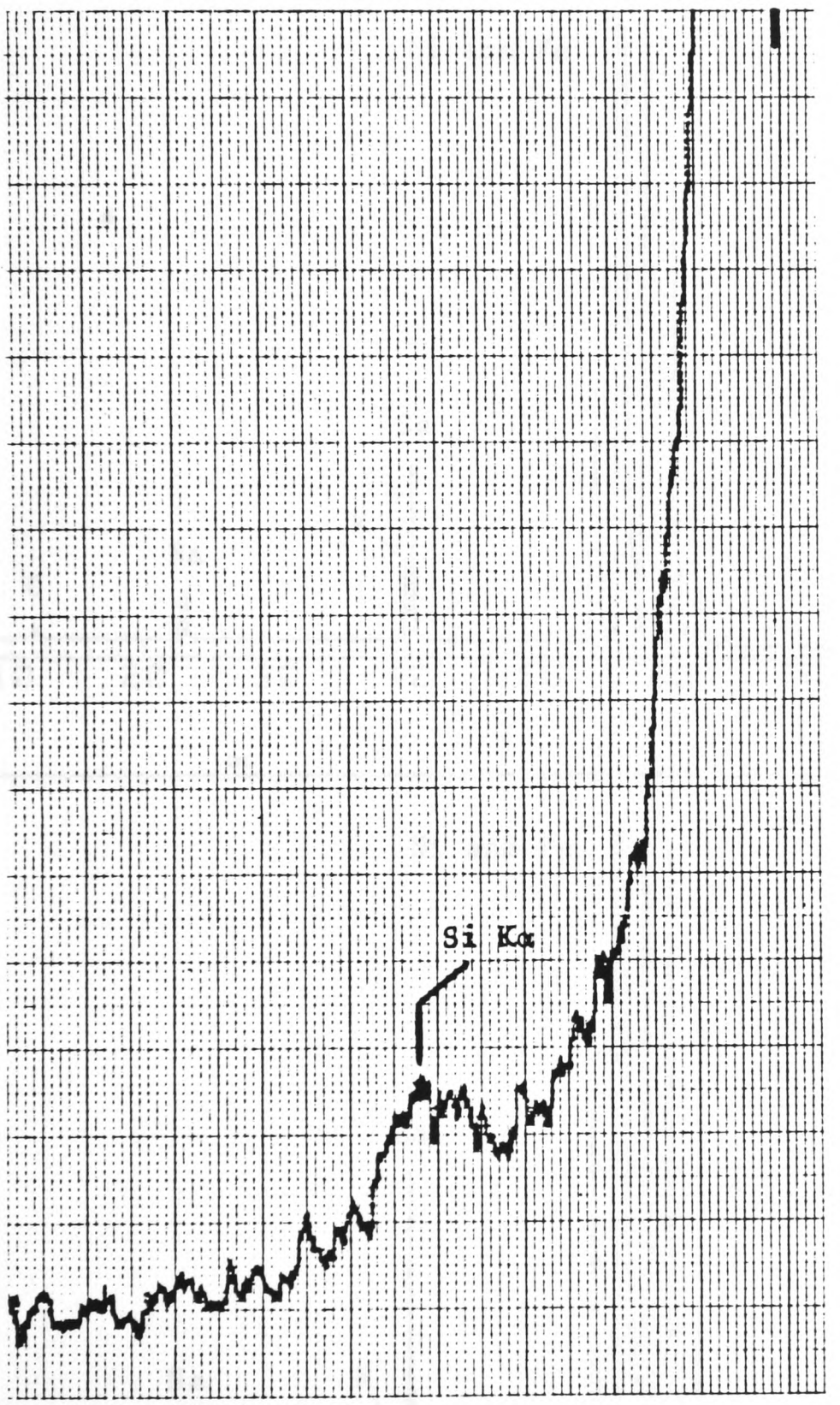

Figure 4.15

LIMA spectra taken from the matrix-composition alloy (batch B).

a) Precipitate region spectrum.

b) Bulk, matrix spectrum.

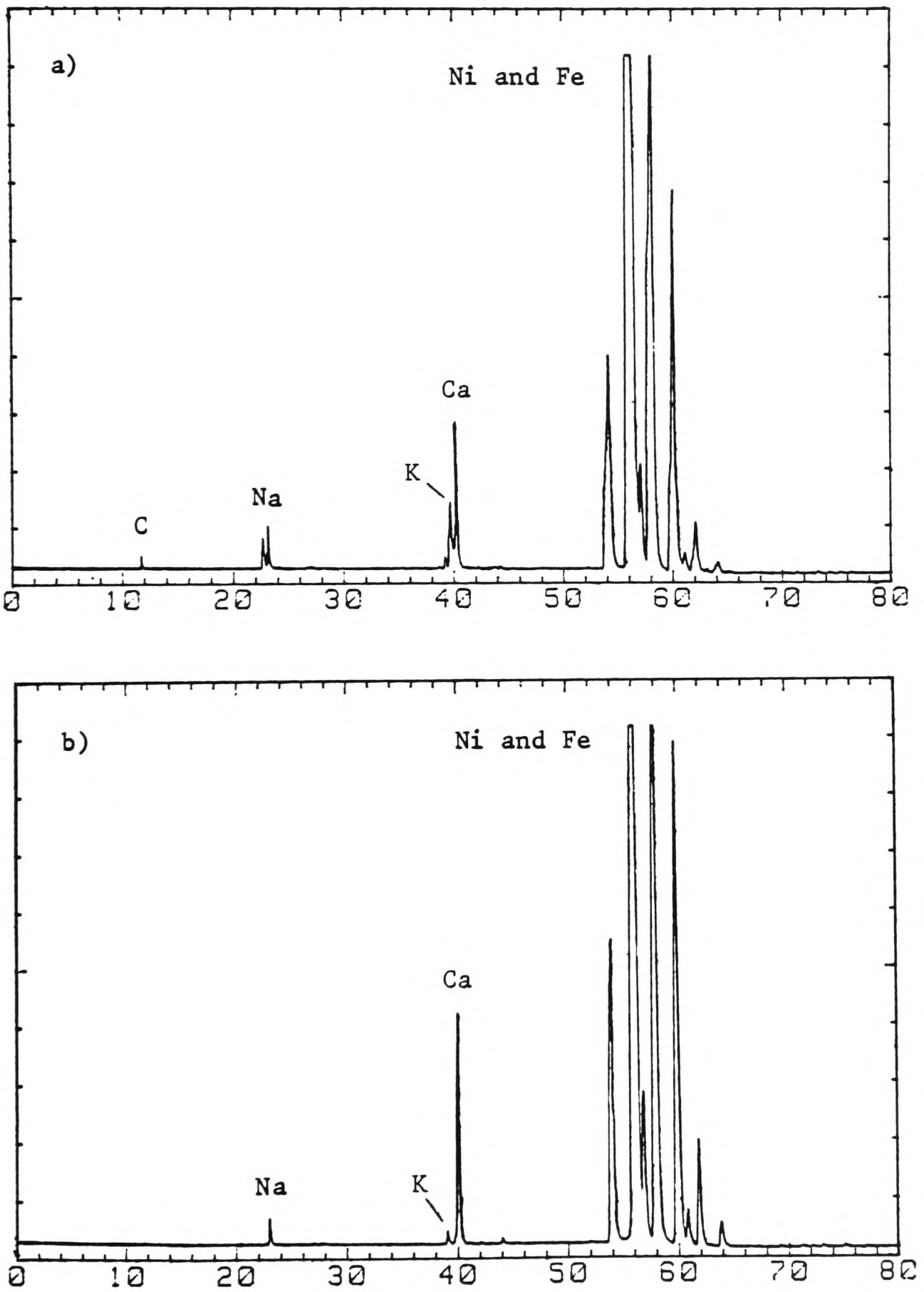

Figure 4.16

Optical micrograph of the matrix-composition alloy (batch A) showing dispersed inclusions (thought to be oxides).

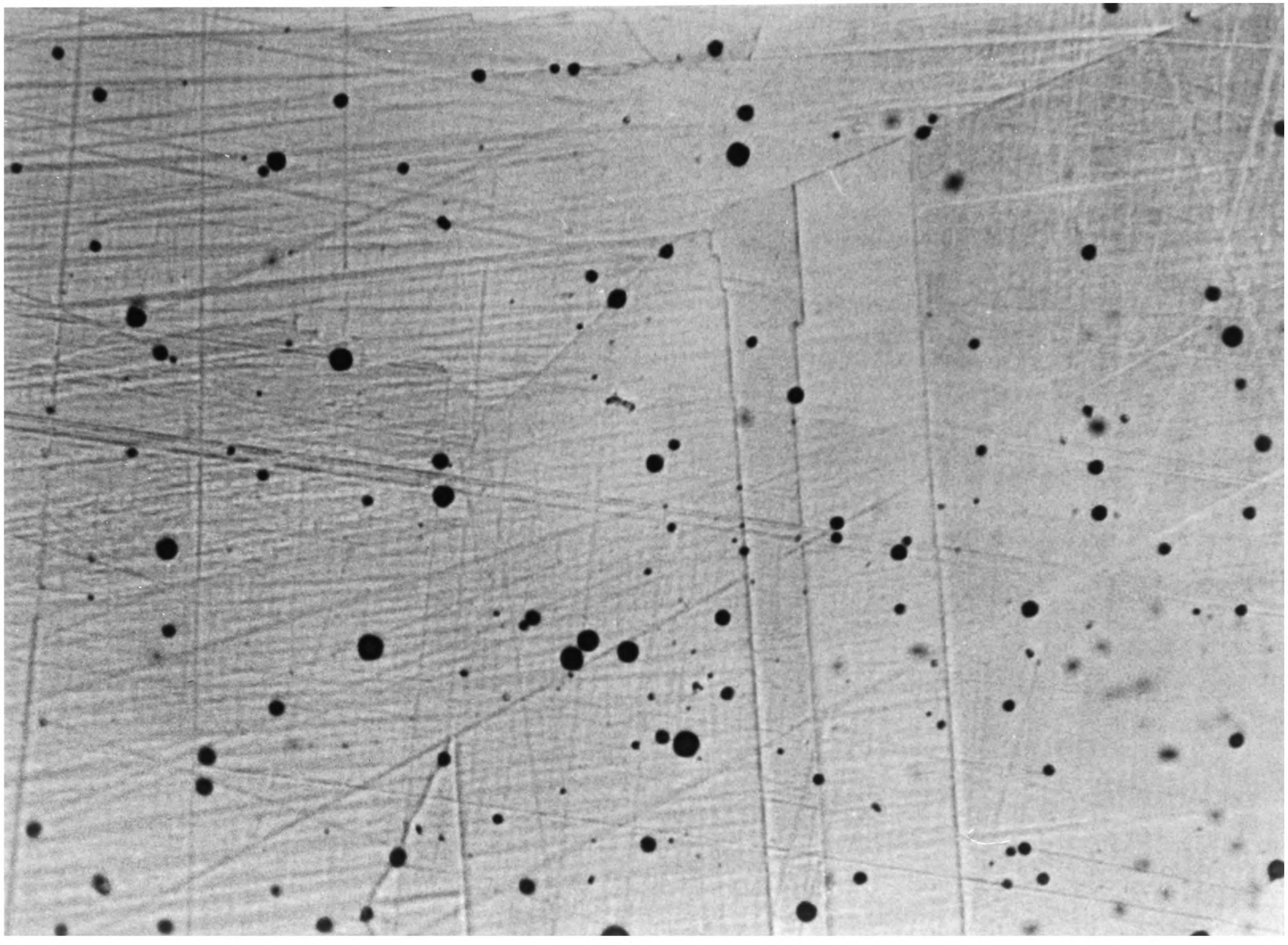

25μm

Figure 4.17

HVEM micrographs showing discontinuous precipitation of W in the γ-phase.

a) Solution treated and aged at 750°C for 100 hours.

b) Solution treated and aged at 850°C for 100 hours.


a
1 µm


b
0.5µm

Figure 4.18

Optical micrograph showing discontinuous precipitation of W in the γ-phase after solution treating and aging at 850°C for 100 hours.

Figure 4.19

Optical micrograph showing discontinuous precipitation of W in the γ-phase after solution treating and aging at 850°C for 5 hours.

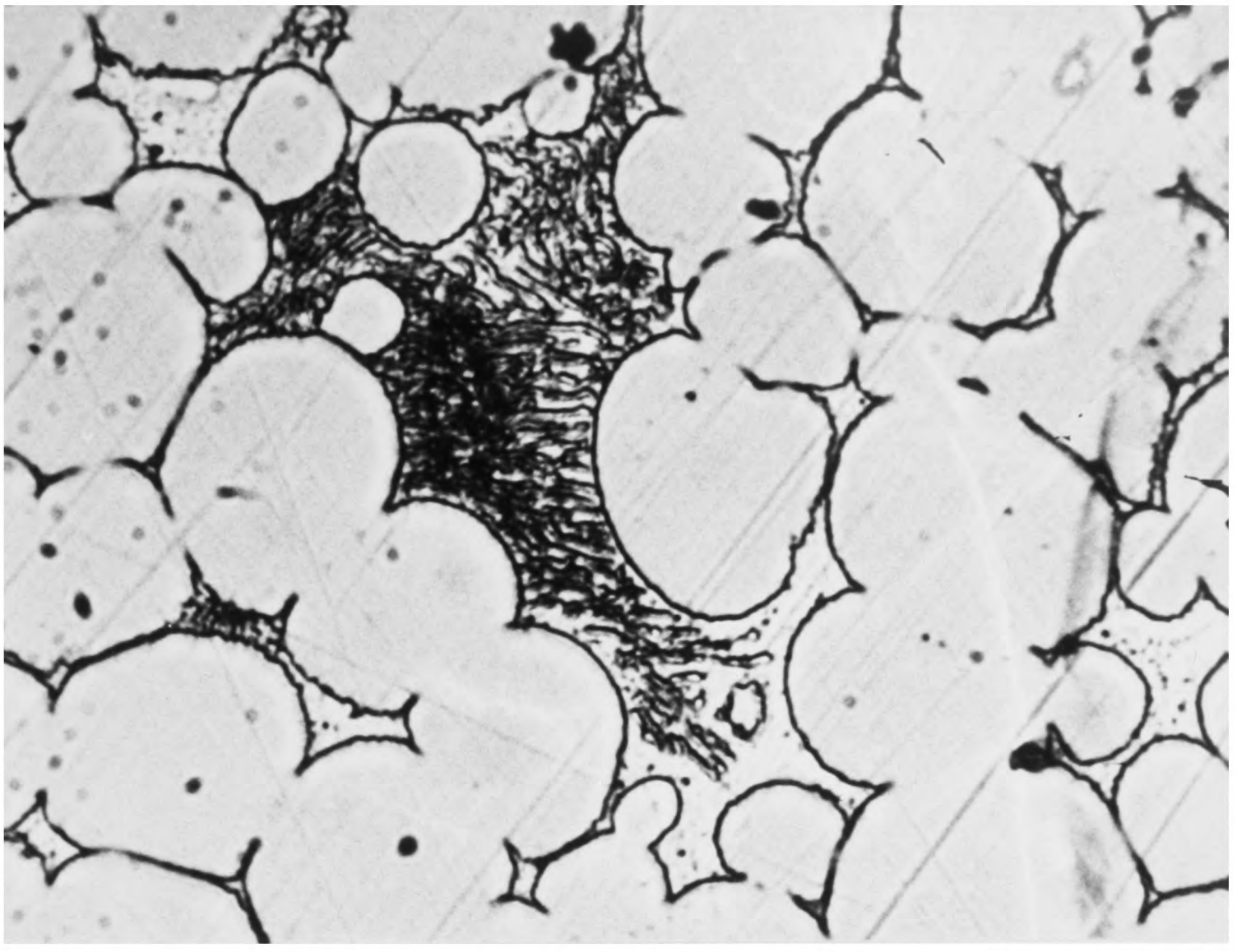

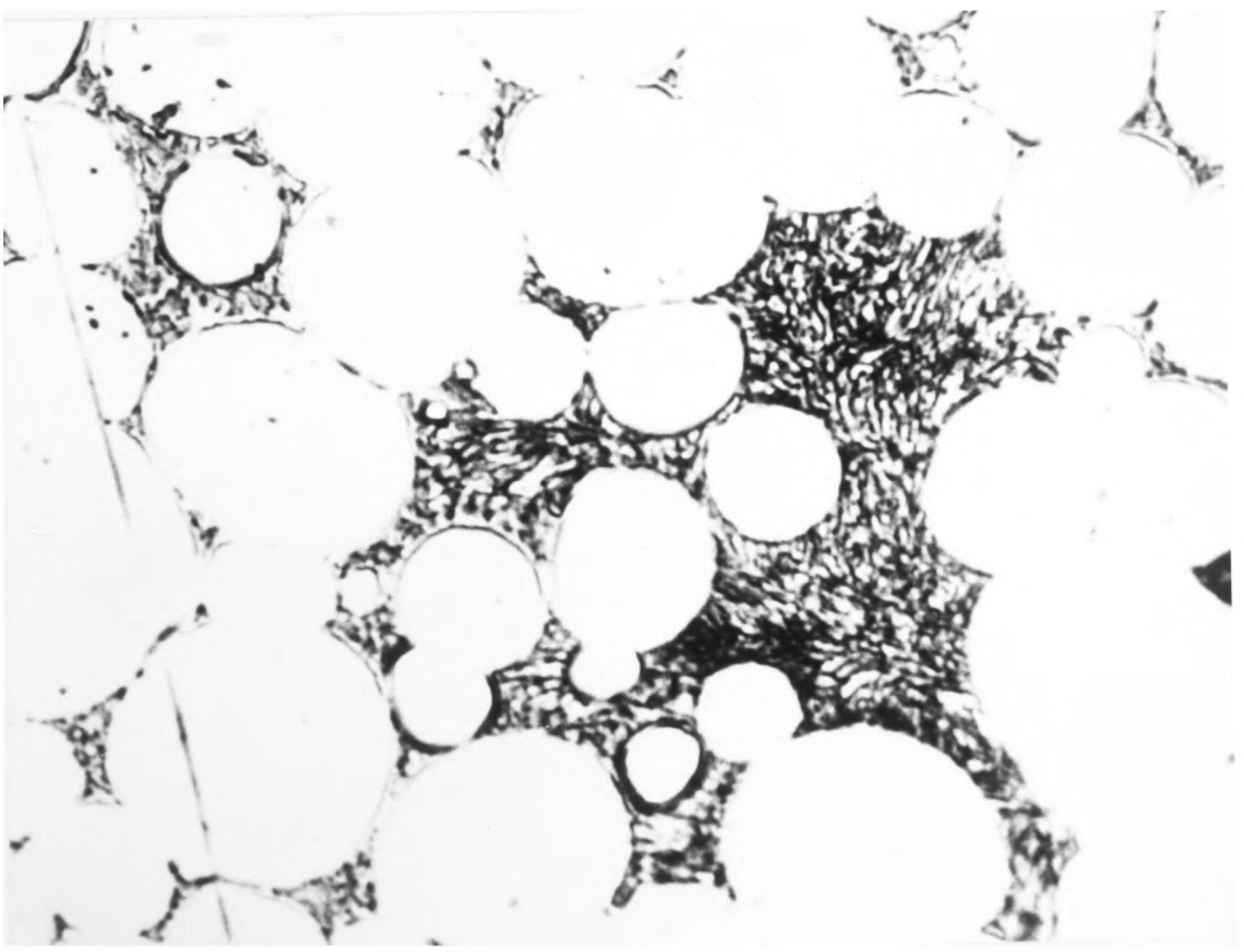

20µm

Figure 4.20

HVEM micrographs of heavy alloy that has been solution treated and aged at 750°C for 100 hours showing discontinuous precipitation of W in the γ-phase.

a) Bright field.

b) Dark field using $\underset{\sim}{g}_W(110)$.

c) SAD pattern.

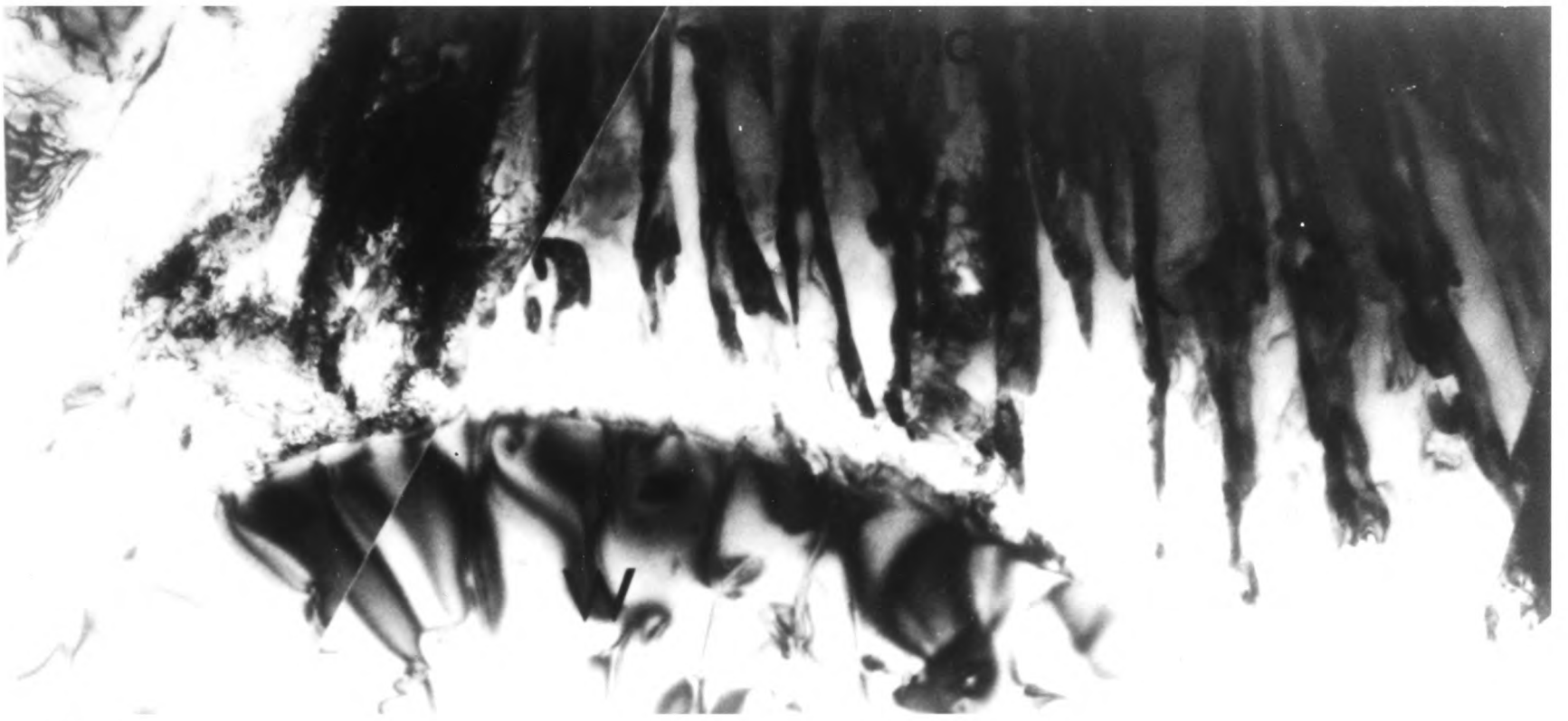

a

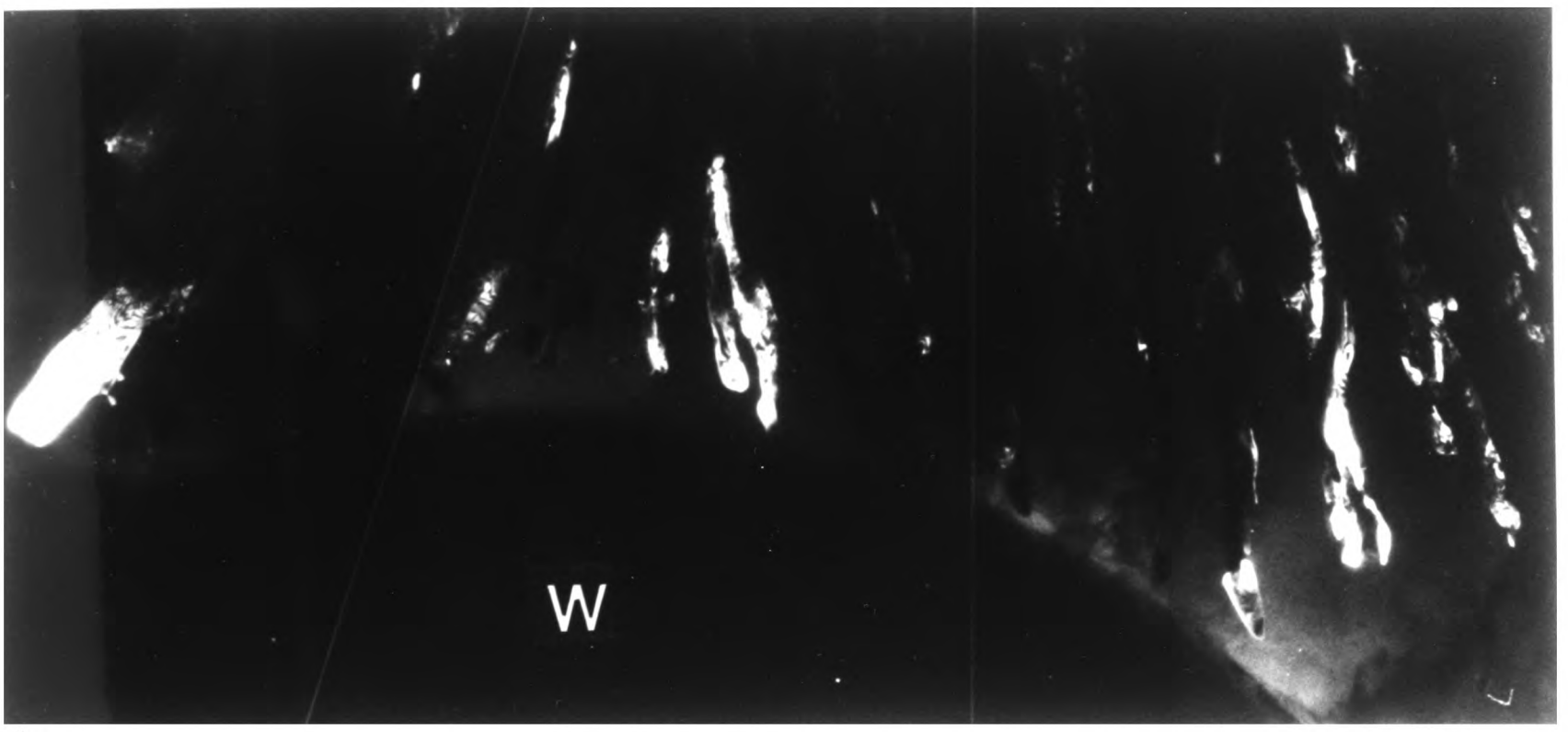

b

-1 µm-

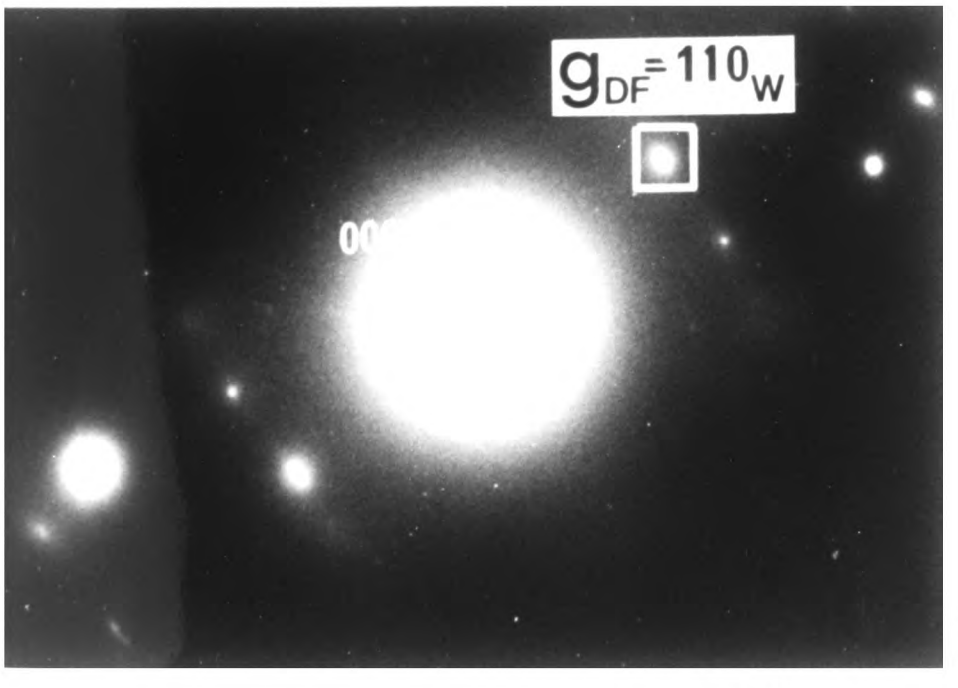

C

Figure 4.21

Optical micrographs of the matrix-composition alloy (batch A) after different heat treatments. Note the change in precipitate (W) morphology with aging temperature.

a) 750°C for 100 hours.

b) 850°C for 100 hours.

c) 950°C for 100 hours.

d) 1050°C for 100 hours.

e) 1150°C for 100 hours.

f) 1250°C for 100 hours.

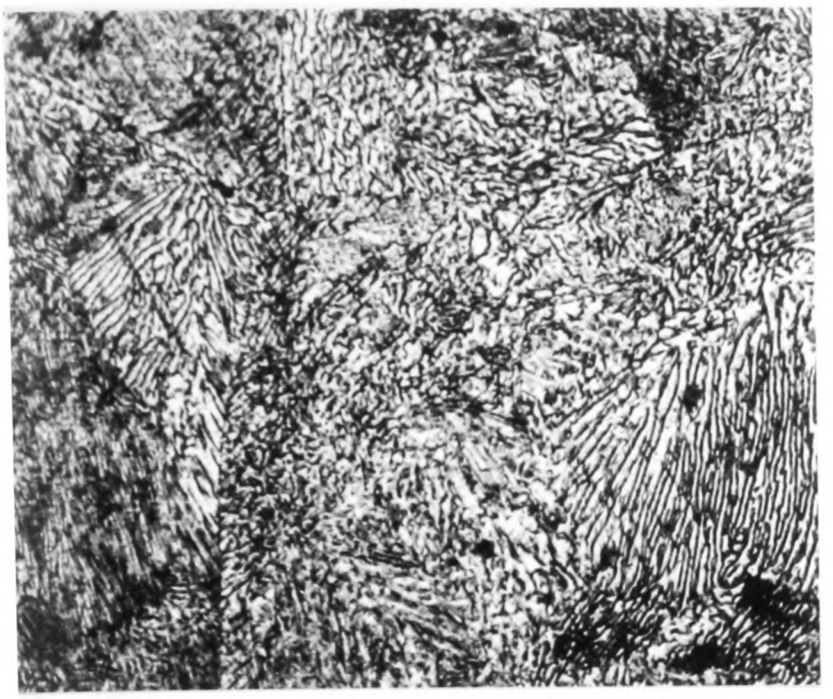

a

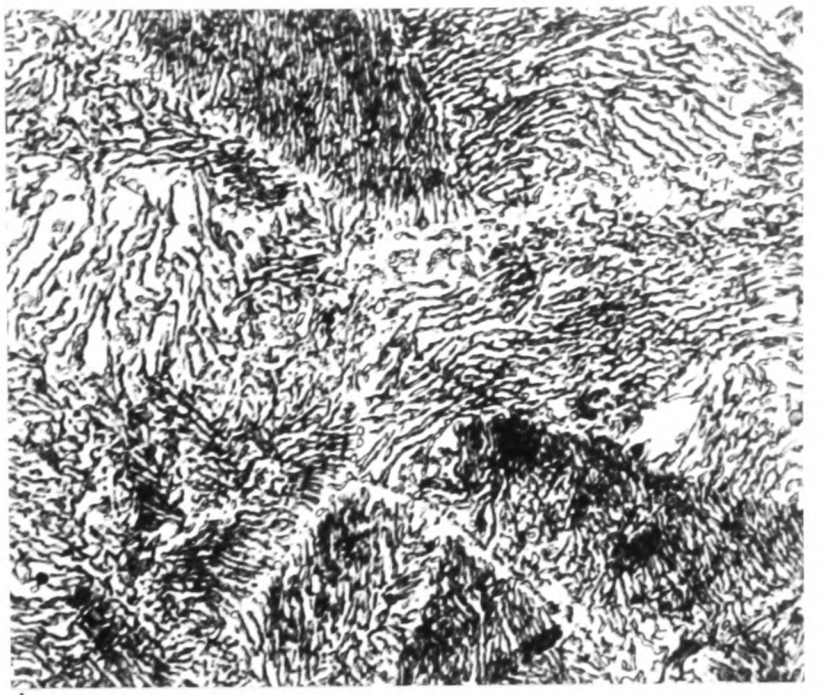

b

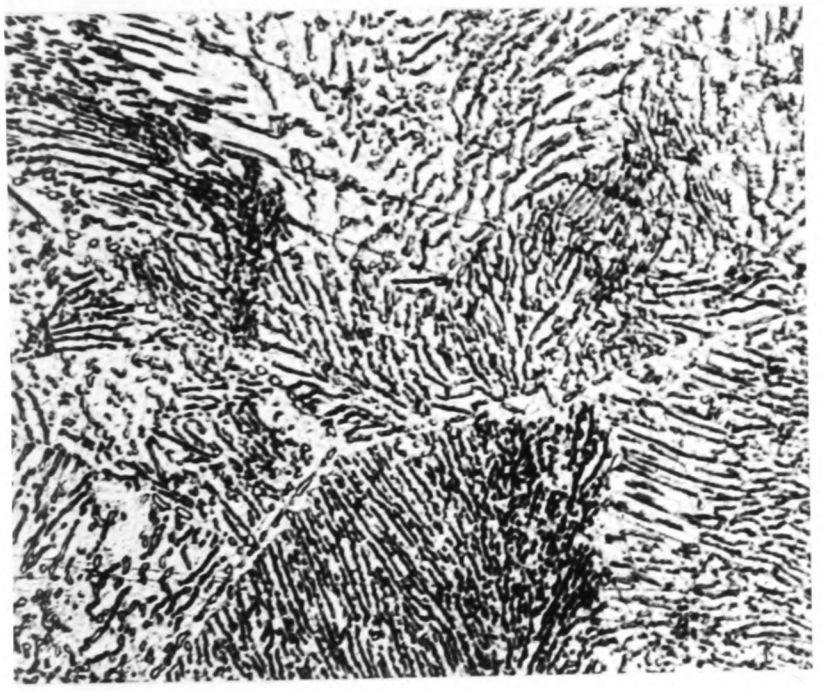

c

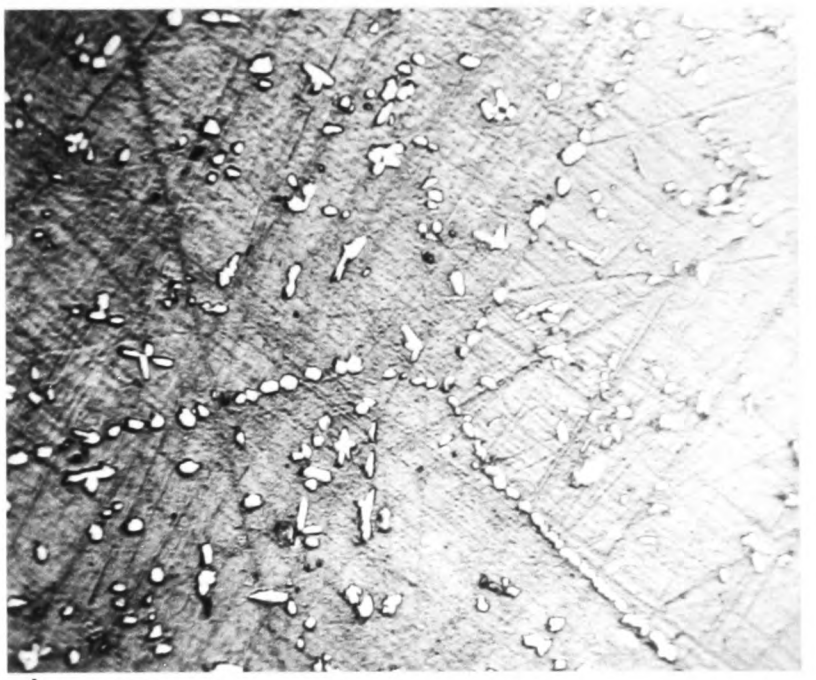

d

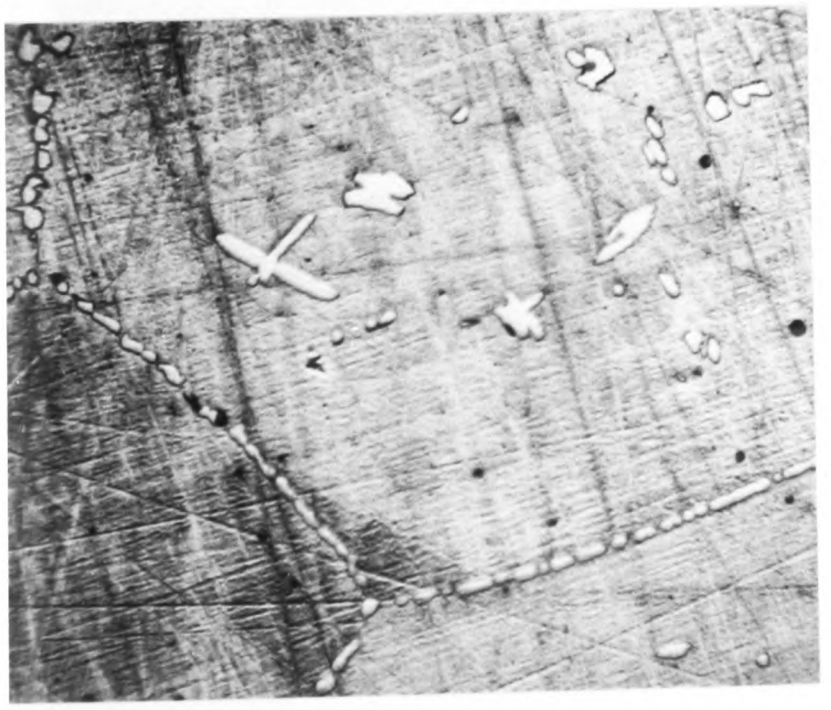

e

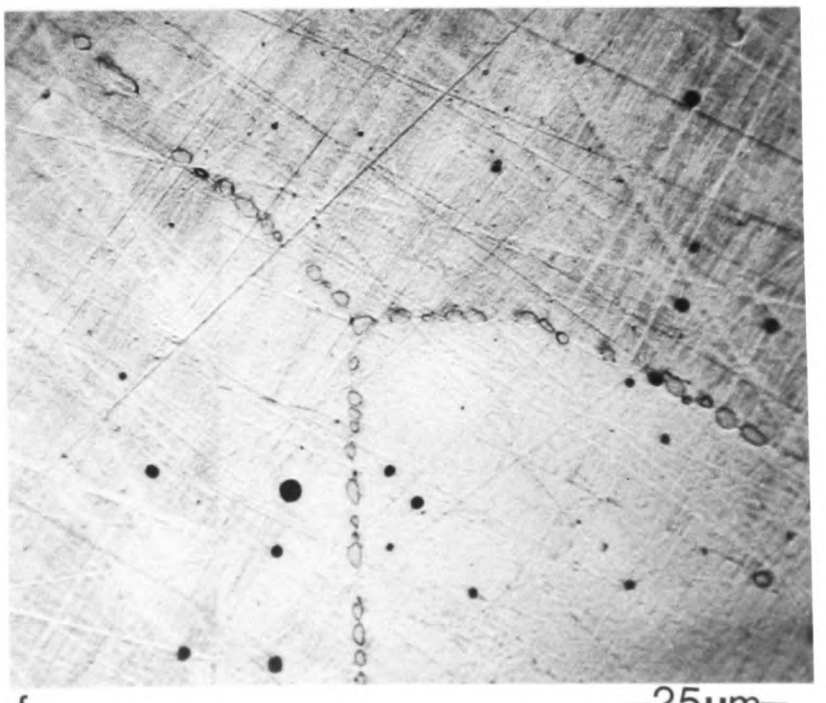

f

Figure 4.22

Optical micrographs of the matrix-composition alloy (batch A) after different heat treatments.

a) 750°C for 10 hours (note the 'double seam' reaction front in one area).

b) 850°C for 10 hours.

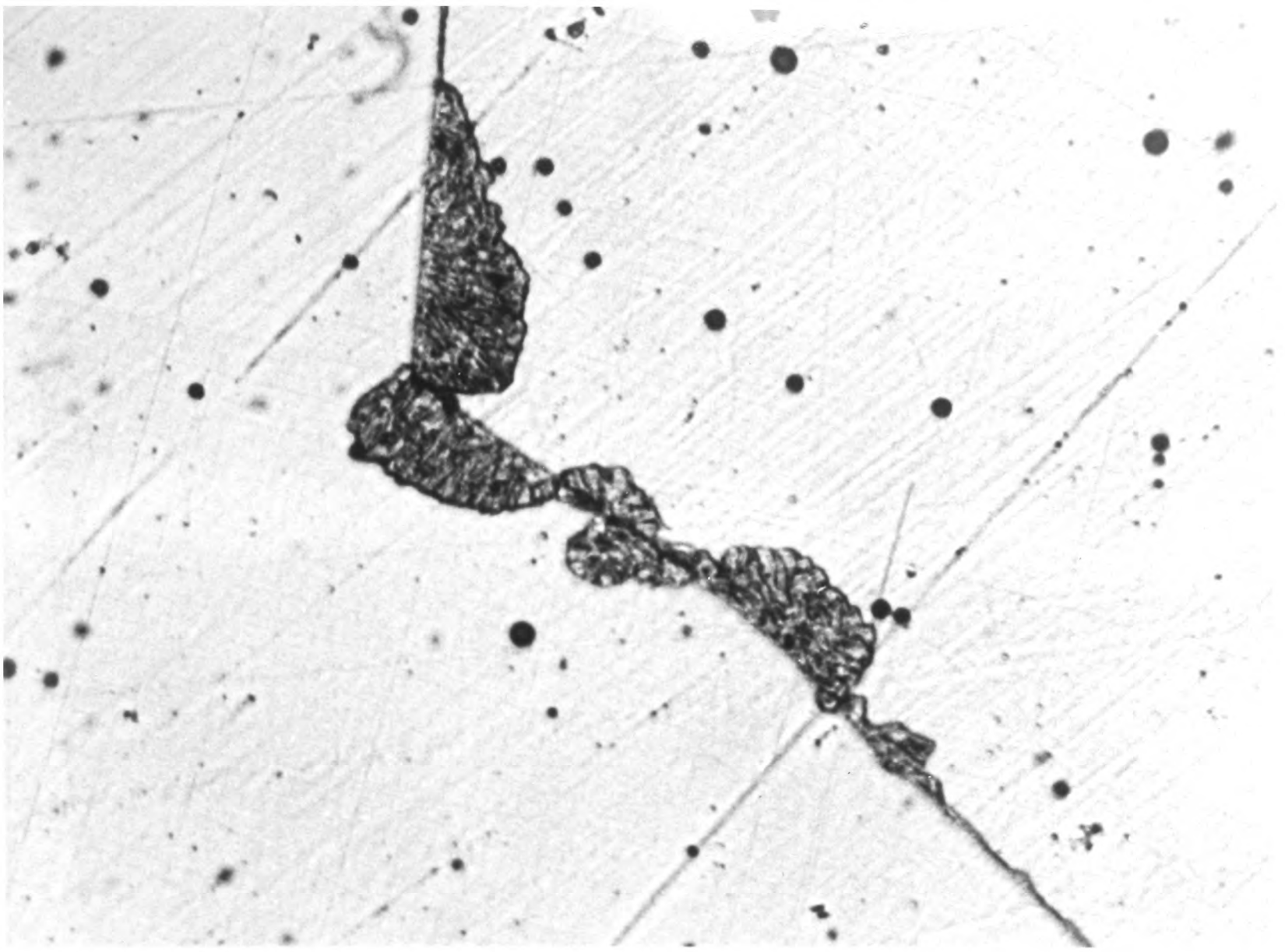

a

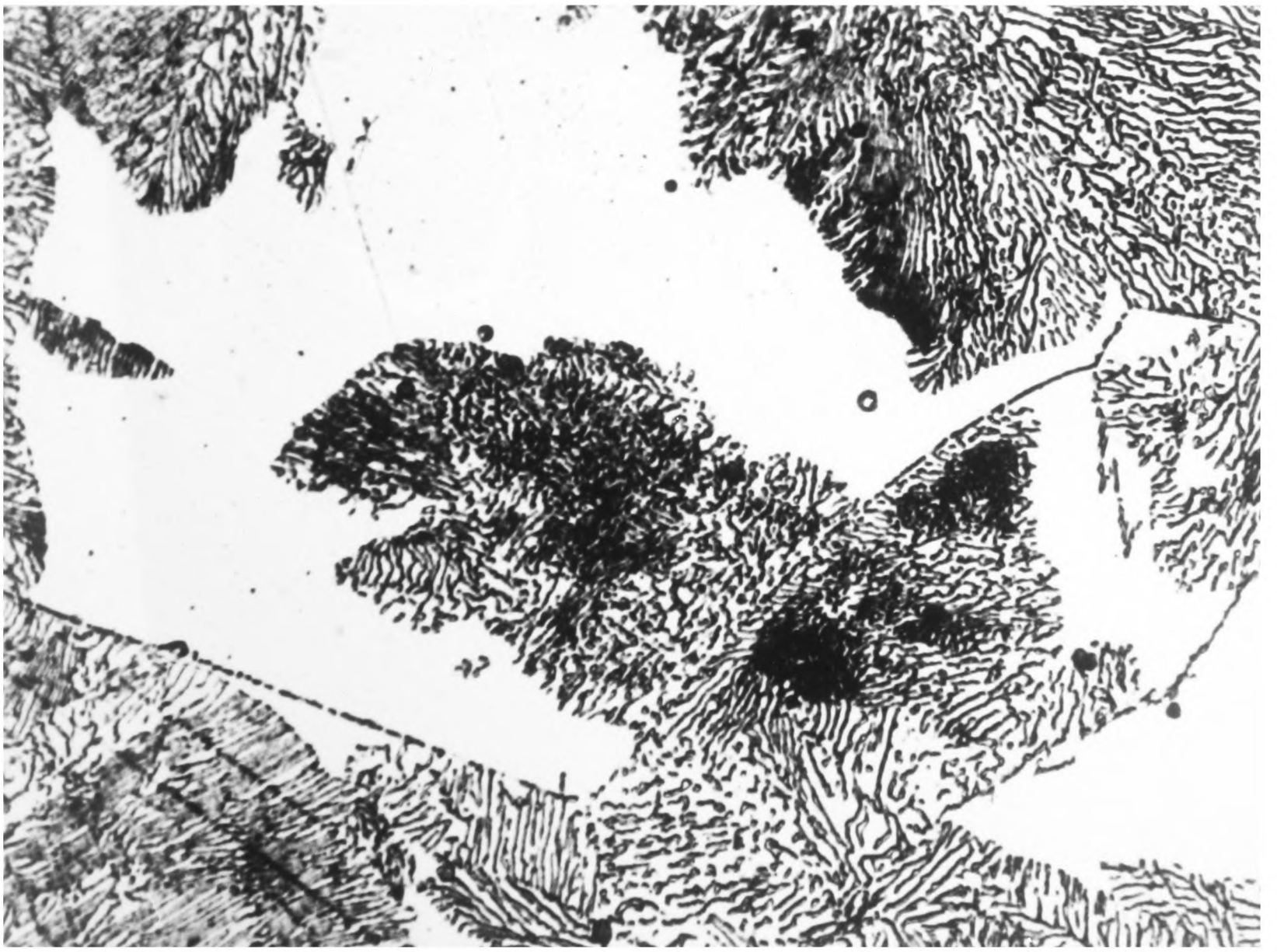

b

25μm

Figure 4.23

HVEM micrographs of the matrix-composition alloy (batch A) after aging at 850°C for 100 hours. Different areas of the same specimen are shown.

a) Lamellar discontinuous morphology.

b) 'Particle' discontinuous morphology.

c) Widmanstatten morphology.

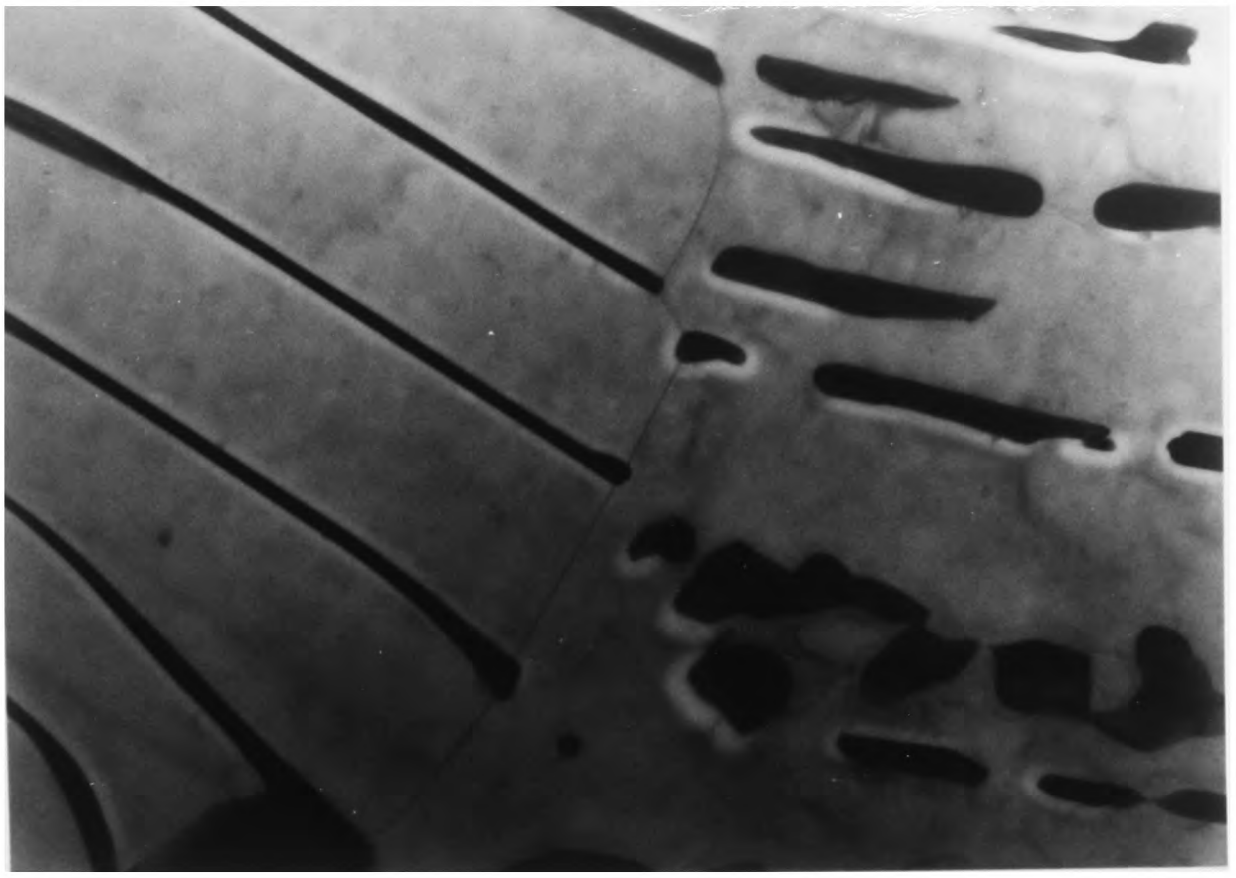

a

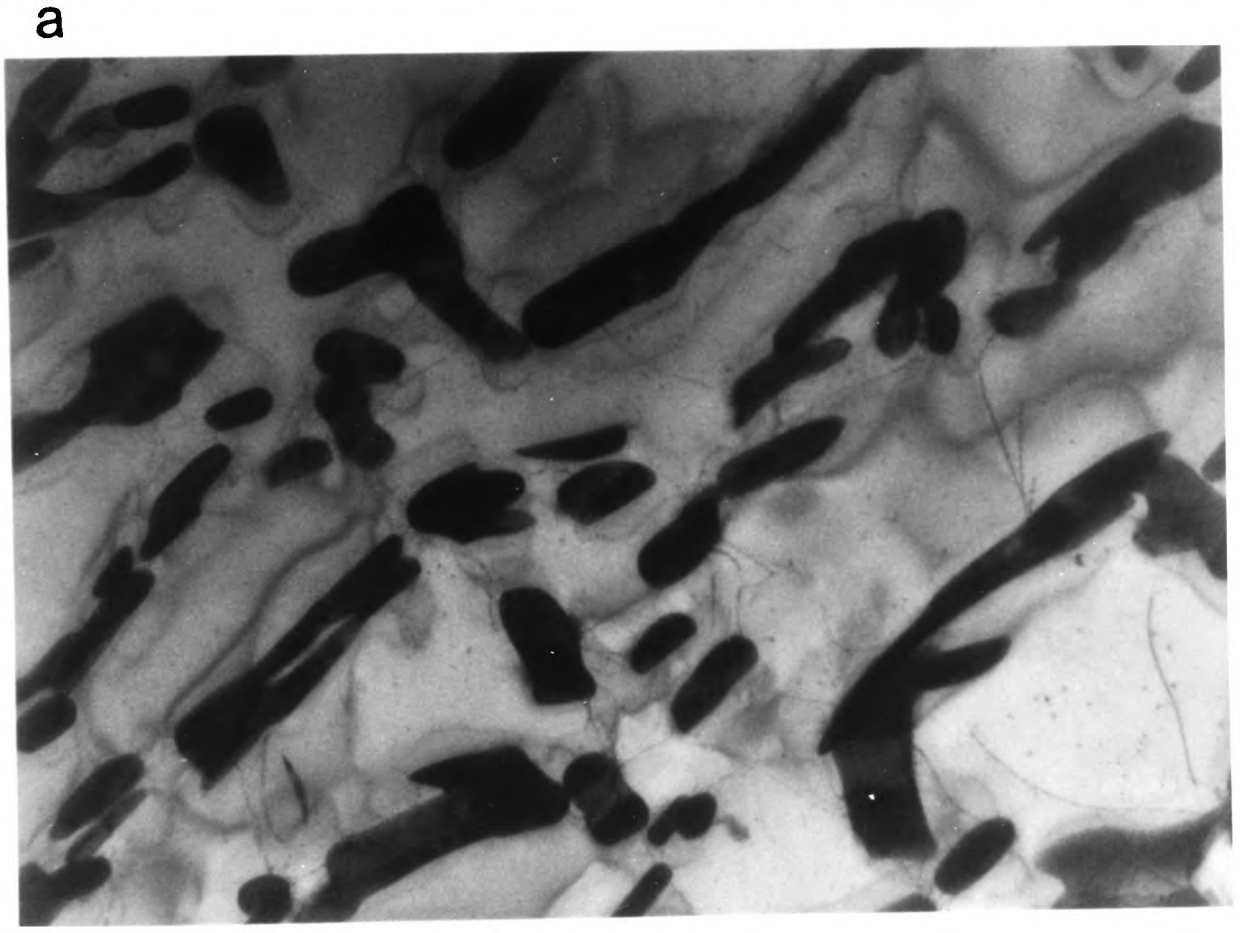

b

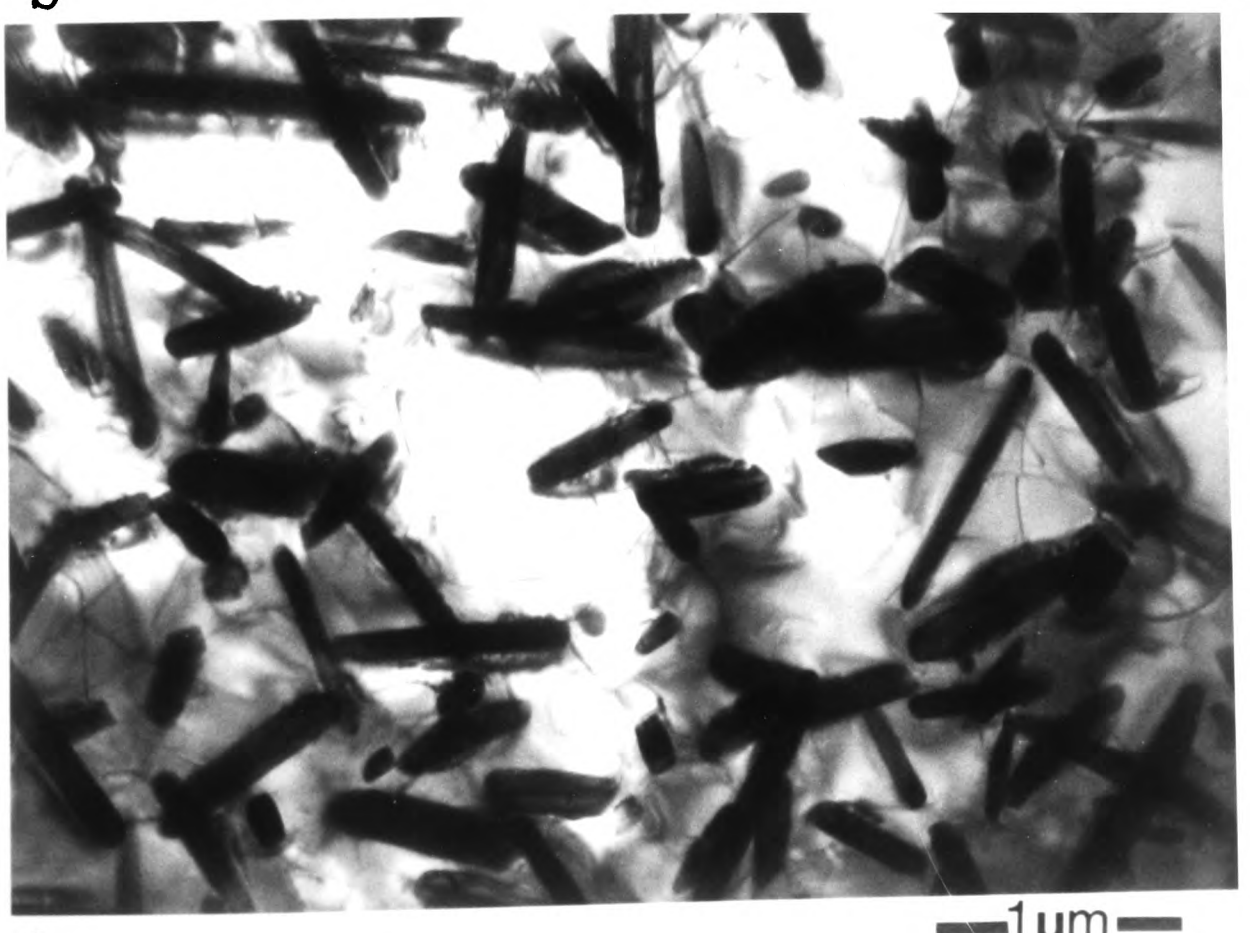

c

Figure 4.24

HVEM micrographs of the matrix-composition alloy (batch A) aged at different temperatures.

a) 750°C for 100 hours - discontinuous morphology.

b) 1050°C for 100 hours - Widmanstatten morphology.

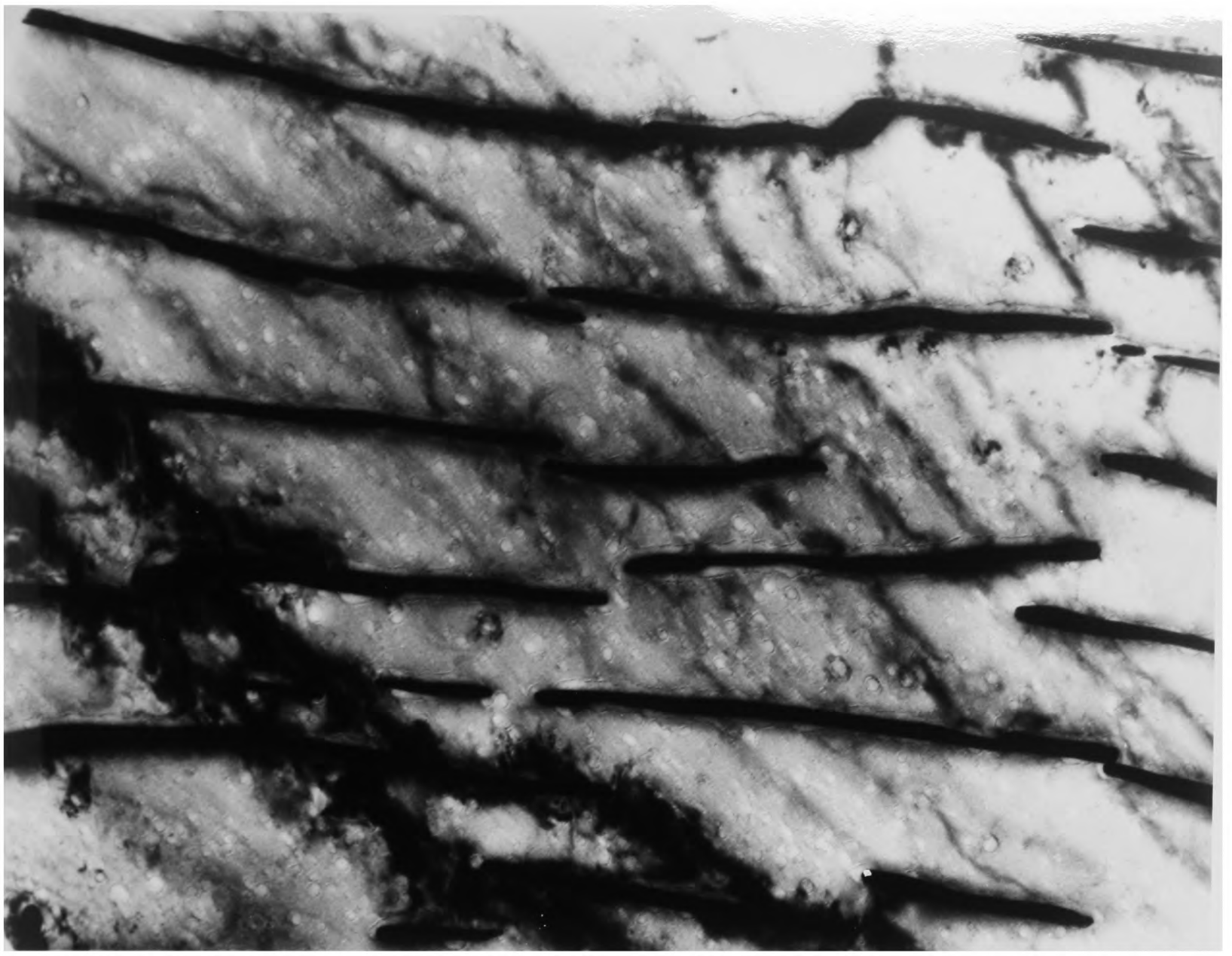

b

0.5µm

Figure 4.25

HVEM micrographs from the matrix-composition alloy (batch A) aged at 1250°C for 100 hours.

a) Bright field showing a W-phase grain boundary allotriomorph.

b) SAD pattern (from a different area) showing an N-W orientation relationship between the W precipitate and one γ grain.

i.e.

W(bcc)		γ(fcc)	
001	//	001	(zone axes)
$1\bar{1}0$	//	$11\bar{1}$	
$\bar{1}\bar{1}0$	//	$2\bar{1}1$	

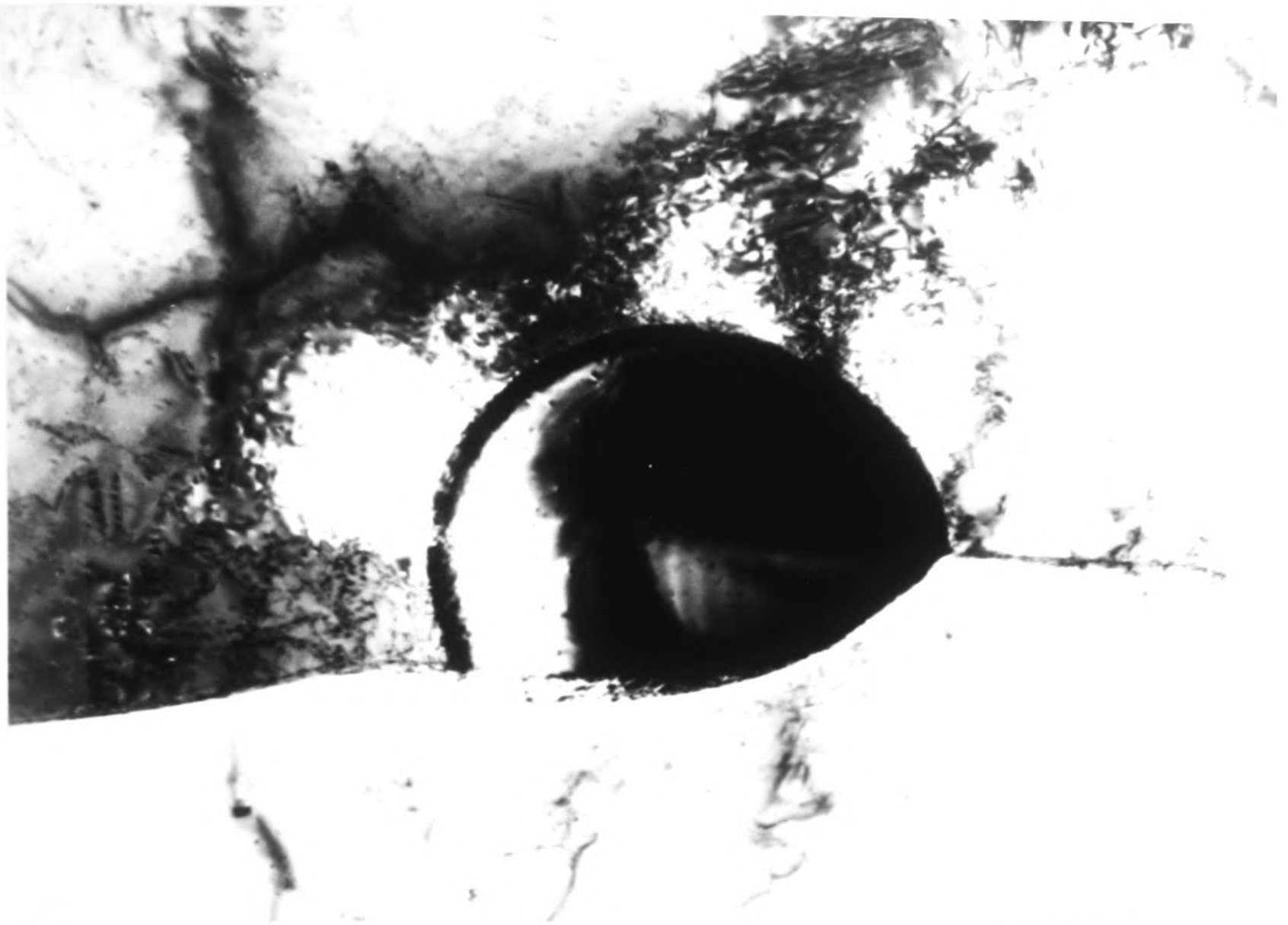

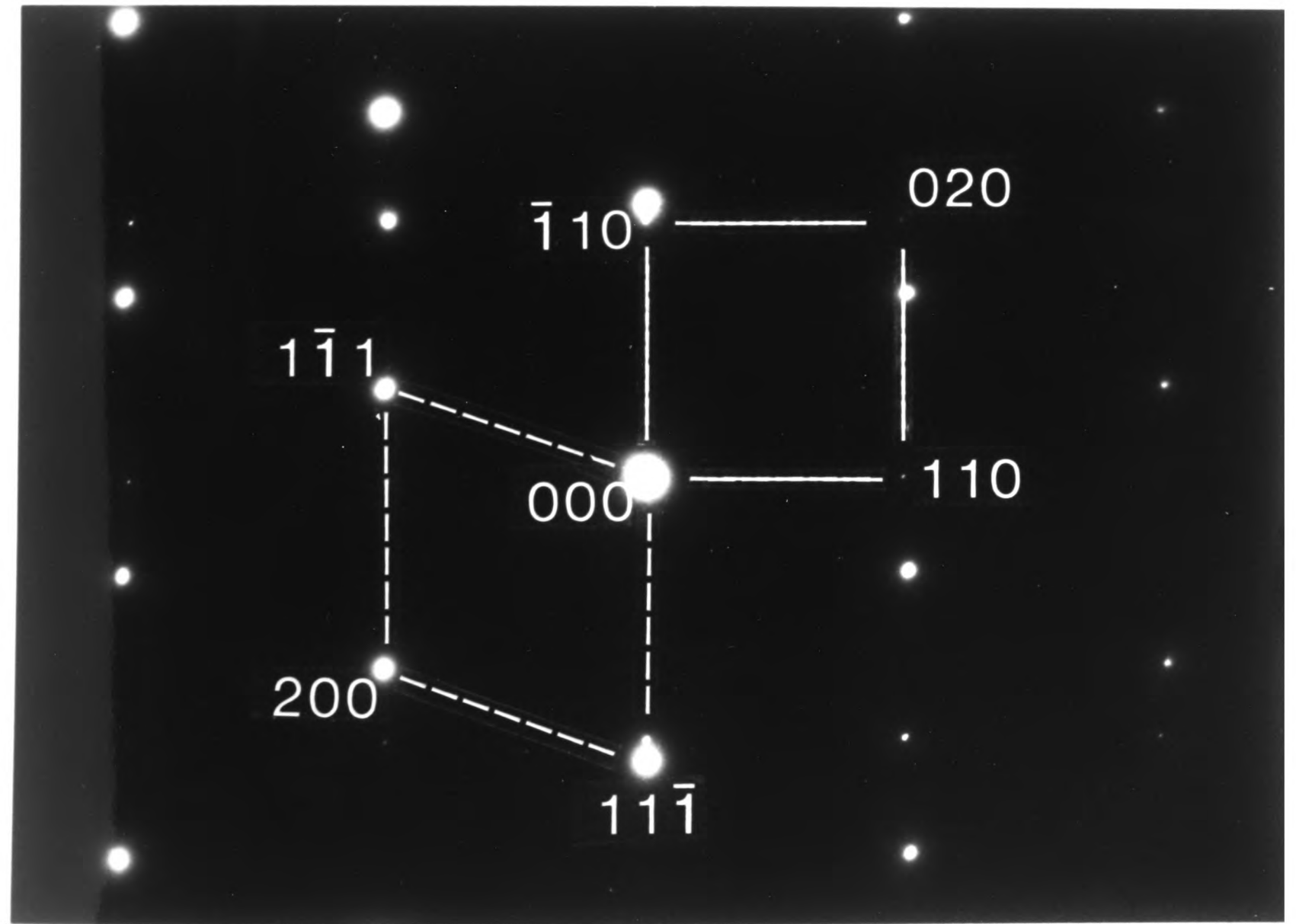

b

Figure 4.26

Guinier powder X-ray diffraction patterns.

a) Extracted precipitate (W) from the matrix-composition alloy (batch A) aged at 750°C for 100 hours.

b) Extracted precipitate (W) from the matrix-composition alloy (batch A) aged at 850°C for 100 hours.

c) Pure tungsten for comparison.

d) Matrix-composition alloy (batch A) as manufactured (unaged).


a
b
c
d
θ
10
20
30
40
(degrees)

Chapter 5

DISCUSSION:

INTERPHASE (W-γ) AND MATRIX-PHASE PRECIPITATION

1. Interphase (W-γ) Precipitation

It is appropriate to discuss the results obtained for the matrix-composition alloy (batch B) before those of the heavy alloy.

1.1. Matrix-Composition Alloy, Batch B (~21.5W - 38.5Ni - 40Fe)

The existence of the so-called η-carbides in both the Ni-W-C and Fe-W-C ternary systems is well-established[*e.g.15,16,17*]. Typically, they occur in two forms, M_6C and $M_{12}C$ (M = Ni or Fe, and W) in both systems[*15, 70*]. Whatever their stoichiometry, the η-carbides are characterized by having an Fd3m (No. 227) space group with a lattice parameter, $a_o \simeq 11\text{Å}$. More specifically, the measured lattice parameters for the relevant compounds are:

	η-Carbide	a_o(Å)	Reference
($M_{12}C$)	Fe_6W_6C	10.957±0.001	70
	Ni_6W_6C	10.900±0.004	15
(M_6C)	Fe_3W_3C	11.124±0.022	70
	Ni_3W_3C	11.242±0.022	15

The large errors in the measured lattice parameters for the M_6C compounds are thought to be due to their greater range of nonstoichiometry[*15*].

The CBED and X-ray diffraction results clearly show the undissolved precipitates in the matrix-composition alloy to have an Fd3m structure with a_o = 11.18Å. Additionally, electron microprobe results showed the atomic ratio of W:(Ni,Fe) to be ~ 1.01, and a LIMA result suggests that the precipitate contains $\lesssim$ 8 at%C. It appears that this compound is,

in fact, an η-carbide, however, the above results are somewhat contradictory.

If the carbon content is $\lesssim$ 8 at%, then we would expect the carbide to have the form, $M_{12}C$ - with a corresponding lattice parameter close to those measured for the Fe_6W_6C and Ni_6W_6C compounds (i.e. $a_o \simeq 10.90\text{-}10.95\mathring{A}$). This is not the case - in fact, the measured lattice parameter corresponds more closely with the higher carbon M_6C(~ 14 at%C) compounds. Further experiments are necessary to resolve this discrepancy, but as no ternary W-Ni-Fe intermetallics with a cubic Fd3m structure have ever been identified, it must be tentatively concluded that the precipitates observed in this matrix-composition alloy are η-carbides.

1.2. 90W-5Ni-5Fe Alloy

1.2.1. Precipitate Identity

This study has shown the interfacial precipitate to have a face-centered cubic structure with $a_o = 10.96 \pm 0.04\mathring{A}$; however, no attempt was made to determine the chemical composition of the precipitate. Other workers[5,12] have measured the 'heavy' element concentrations in an interfacial precipitate to be, ~ 51 at%W - 21 at%Ni - 28 at%Fe, and Muddle[14] has shown that the precipitate contains carbon by using scanning Auger electron microscopy. However, there is not universal agreement on the identity or crystal structure of this phase.

Edmonds and Jones[5] have presented X-ray diffraction evidence showing this interfacial precipitate to be a ternary intermetallic of the form (Ni,Fe)W - an isomorph with orthorhombic NiW[13]. Also, the results of Henig, et al.[8] appear to substantiate this conclusion - particularly as they have identified a new binary intermetallic, FeW (also an isomorph with NiW), and therefore there is thought to be complete nickel and iron

miscibility in the ternary (Ni,Fe)W intermetallic. In contrast, Muddle's [14] convergent beam electron diffraction evidence indicates that the precipitate has an Fd3m structure with $a_o \simeq 10.9\mathring{A}$. In addition to the Auger electron spectroscopy results, this is consistent with the precipitate being an η-carbide.

The current work, both on the heavy alloy and the matrix-composition alloy, tends to substantiate the results of Muddle, and therefore it must be concluded that the interfacial (W-γ and γ-γ) precipitate observed in the heavy alloy during this study is an η-carbide - possibly $W_6(Ni,Fe)_6C$. Nevertheless, it must be borne in mind that all the groups working on this alloy system are probably using different material - with, presumably, different impurity contents. It is quite conceivable that η-carbide precipitation is mainly observed in 'dirty' alloys, while intermetallic precipitation is more dominant in 'clean' alloys. It would be worthwhile for experimentalists to measure and report the bulk impurity concentrations (esp. carbon) when presenting results regarding the identity of this phase.

Figure 4.1 shows the results of bulk chemical analysis for the commercially-supplied 90W-5Ni-5Fe alloy examined in this work (the analysis was only done for twelve elements). The carbon concentration was measured to be 0.004 wt%. Further experiments are essential to establish (a) if the (Ni,Fe)W intermetallic and the η-carbide phases can coexist in tungsten heavy alloy, and (b) what conditions (i.e. sintering, impurity content, post-sintering heat treatment, etc.) are necessary to induce the formation of one or both phases.

1.2.2. Precipitate Formation and Morphology

The current work showed the η-carbide to be induced upon solution treating at 1350°C (water quenching) and subsequent aging in the temperature range 750-850°C for 100 hours. It was not ascertained whether or not the

initial solution treatment was, in fact, necessary to produce the precipitate. TEM observations also showed that an interface (i.e. a W-γ or γ-γ boundary) was the preferred nucleation site for the η-carbide. However, Muddle[14] has also observed widmanstatten laths of η-carbide in the γ-phase in appropriately heat treated material. Additionally, Kannappan[12] observed interfacial W-γ precipitation concurrent with precipitation of a "dendritic" configuration (as described in chapter 2 section 2.1) upon slow cooling heavy alloy from the sintering temperature. His X-ray results, while not completely explicable, show certain reflections that could have come from an η-carbide with a_o = 11.18Å (see Fig.2.1). This "dendritic" morphology would initially appear to imply that the η-carbide (if it actually is η-carbide) has precipitated directly from the liquid phase upon cooling. However, this is contradicted by the fact that this third (and possibly fourth) phase goes into solution when annealed at 1400°C for 24 hours. Again, it appears that properly controlled experiments are necessary to establish the preferred precipitate morphology as a function of alloy processing and impurity concentration.

1.2.3. Effect on Mechanical Properties

No systematic work was done in this study to attempt to relate the presence of this interfacial η-carbide with a change in mechanical properties. However, Edmonds and Jones[5] associated the appearance of an interfacial precipitate with a drastic reduction in Charpy impact energy. Their SEM fractography showed that a significant proportion of the fracture surface consisted of W-γ interfaces containing this brittle phase. This morphology, whether the precipitate is an intermetallic or a carbide, is obviously embrittling and should be avoided if alloy ductility or impact resistance is desired.

2. Matrix-Phase Precipitation

2.1. Matrix-Composition Alloy, Batch A (19.2W - 41.4Ni - 39.4Fe)

The progression of the tungsten precipitate morphology with increasing aging temperature is most clearly shown in the matrix-composition alloy (batch A). After 100 hour heat treatments, the predominant morphologies are:

Precipitate Morphology	Aging Temperature (°C)
Discontinuous	750
Widmanstatten	1050
Grain boundary	1250

The fact that grain boundary precipitation predominates at higher aging peratures is a well-established phenomenon *(e.g.71)*. Obviously, the chemical driving force for precipitation at higher temperature is reduced, and therefore the energy barrier for nucleation (i.e. the critical free energy, ΔG^*) is higher. Since a nucleus can minimize its strain and/or surface energy by location at a defect, heterogeneous nucleation at grain boundaries would be expected in this case. Because the solute (tungsten) supersaturation level is low at temperatures just below the solution treatment temperature (1350°C), the growth of the nuclei also requires long-range diffusion of solute. Typically, this results in slow grain boundary precipitate growth, and as allotriomorphs grow more quickly along the boundary than normal to it *(71)*, they tend to remain on the boundary with time at the annealing temperature.

The increased chemical free energy, Δg_c, at some lower aging temperature leads to a decreased critical free energy, ΔG^*, ($\Delta g_c \propto (\Delta G^*)^{-2}$) *(e.g. 72)* and consequently heterogeneous nucleation becomes less important. Qualitatively, this helps explain the Widmanstatten precipitation of W observed after aging at 1050°C.

In some systems precipitate nucleation at grain boundaries can grow into one or both grains behind the migrating grain boundary. This is known as cellular or discontinuous precipitation and results in a lamellar precipitate morphology. A high solute supersaturation level and a high grain boundary mobility are generally required for this transformation to occur; however, all the conditions necessary for discontinuous precipitation to prevail over continuous precipitation are not fully understood[73].

This reaction is observed most clearly at lower aging temperature (750°C) in the matrix-composition alloy and is a type 1 discontinuous precipitate reaction described by

$$\gamma' \rightarrow \gamma + W$$

where γ' is the tungsten-supersaturated Ni-Fe-W fcc phase, which is being transformed to a more thermodynamically stable mixture of alternating W precipitate and tungsten-depleted γ lamellae (Fig. 5.1). Certainly, the tungsten supersaturation level is higher at this lower aging temperature, but there is no detailed knowledge concerning the grain boundary mobility.

Another consideration that may help understand why discontinuous precipitation would be preferred at lower aging temperatures is the fact that the rate of atomic diffusion required for W precipitation would be enhanced along a migrating grain boundary thereby making discontinuous precipitation kinetically more favorable. Naturally, this assumes that all or most of the solute segregation occurs at the grain boundary, and this has not been established for discontinuous precipitation in this system. However, Porter and Edington[74] used EELS thin foil microanalysis to show that the elemental partitioning necessary for discontinuous precipitation in the magnesium-aluminium system occurs not in the matrix preceeding the reaction front but within ~ 100Å (essentially at) the grain

boundary. In spite of this, no current models exist that adequately explain why discontinuous precipitation is favored over continuous precipitation, and therefore, the present observation cannot be completely understood.

Nevertheless, certain other morphological features are worthy of note. The lamellar spacing in the discontinuously transformed regions increases with increasing aging temperatures (decreasing the supercooling from the equilibrium temperature). Qualitatively, this is consistent with the lamellar spacing, S, being inversely proportional to the supercooling, ΔT ($S \propto \Delta T^{-1}$)[72]. Furthermore, in some areas that have precipitated discontinuously, long lamellae are no longer distinguishable (see Fig. 4.23b). This observation could be due to the cross-sectioning of fibrous rod-like precipitates or could, in fact, be rows of particulate precipitates rather than unbroken lamellae. The latter possibility has been observed for discontinuous precipitation of vanadium carbide from an austenitic Fe-Mn-V-C alloy by Ainsley, et al.[75] They also associated the occurrence of particulate discontinuous precipitation with the presence of high-angle grain boundaries of low-coincidence lattice site density (i.e. high Σ). It is conceivable that different grain boundaries in the matrix-composition alloy could yield either fibrous or particulate discontinuous precipitate morphologies depending on the structure of the individual boundary.

A grain boundary allotriomorph, formed at high aging temperature (1250°C) was observed to have a Nishiyama-Wassermann bcc/fcc orientation relationship with one adjacent grain. To have a rational or near-rational orientation relationship with one grain is characteristic of grain boundary precipitates - as they can be more easily nucleated[71,76]. Growth then

proceeds along the boundary and into the grain with which the allotriomorph has the irrational orientation relationship.

2.2. Heavy Alloy (90W - 5Ni - 5Fe)

2.2.1. Morphology

The irregular and sporadic nature of the discontinuous precipitation in the matrix of the heavy alloy can in part be understood by considering the nucleation of the reaction. Discontinuous nucleation and growth generally requires a mobile interface - normally a grain boundary. In this case a W-γ interphase boundary would be unsuitable as this would not actually be nucleation per se but would instead be a W grain developing protrusions (lamellae) into the γ-phase. Additionally, a mobile grain boundary would have to be created so the reaction could proceed. A more plausible scenario for tungsten in γ-phase supersaturation very near a W grain is for it to precipitate uniformly on the W grain as was observed by Kiparisov, et al.[18]

Other possible nucleation sites would be an inclusion-γ interface or a γ-γ grain boundary - both of which are very infrequently observed. The inclusion-γ possibility suffers from the same problem as the W-γ interface in that a mobile grain boundary would have to be created for growth to occur. Therefore, it seems most likely for the reaction to require a γ-γ grain boundary for nucleation and growth. If this is so, then this might help explain the nonuniformity of the reaction. However, direct evidence for the nucleation site of this reaction is required before making any conclusions, and the possibility of chemical inhomogeneity cannot be ruled out either. It should be noted that other researchers (see summary in chapter 2 section 2.2) who have observed this morphology have either not observed this sporadic distribution or have not commented on it.

The Widmanstatten and grain boundary precipitation of W were not observed in the heavy alloy matrix (e.g. in material solution treated and aged at 950°C for 200 hours). At the higher temperatures needed for these morphologies to predominate, the diffusivity would be higher, thus leading to tungsten precipitation directly onto W grains. This conflicts with the results of Henig, et al.[8] who observed precipitation of W (albeit discontinuously) after annealing as high as 1000°C. However, Henig, et al. solution treated at a higher temperature (1400°C) and the time required before the reaction was observed was not specifically mentioned.

2.2.2. Phase Equilibria

The results of Henig, et al., as discussed above and in chapter 2 section 2.2, included observations of discontinuous precipitation of W in the γ-phase of the heavy alloy upon annealing in the 800-1000°C range. They also claim that if held at temperature for ≥ 300 hours a (Ni,Fe)W intermetallic would be seen to form from the precipitated W. The current work can neither confirm nor deny this as all annealing times were ≤ 200 hours.

2.2.3 Effect on Mechanical Properties

No systematic study was done to determine the effect of the observed discontinuous precipitation on heavy alloy (or matrix-composition alloy) mechanical properties. It must be remembered that W-γ interphase precipitation can occur concurrently, which is expected to be severely embrittling. Additionally, Henig, et al.[8] discussed the results of Kang[77] which showed little change in heavy alloy tensile strength and elongation after aging to produce discontinuous precipitation in the matrix.

Figure 5.1

Type 1 discontinuous precipitation, $\gamma' \rightarrow \gamma + W$.

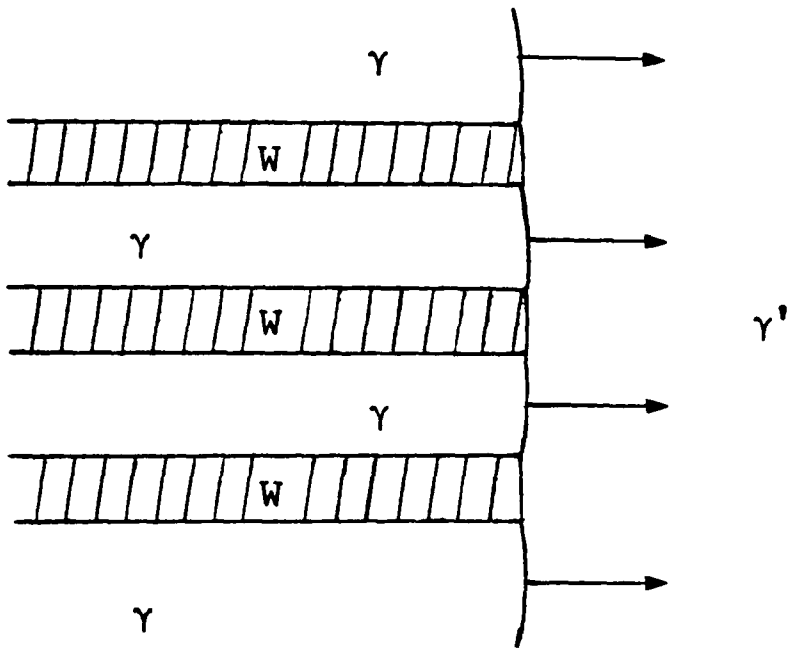

Chapter 6

EXPERIMENTAL RESULTS: W-W GRAIN BOUNDARY PRECIPITATION AND W-PHASE PRECIPITATION HARDENING

1. W-W Grain Boundary Precipitation

The materials examined in this section are the 90W-5Ni-5Fe and 90W-7Ni-3Fe commercially produced alloys. They differ not only in composition, but in their post-sintering treatment. As described in chapter 1 section 3, the 90W-5Ni-5Fe has been given a heat treatment at 1050°C for ~ 1 hour while the 90W-7Ni-3Fe alloy was not given any post-sintering heat treatment.

1.1. Scanning Electron Microscopy

SEM of fracture surfaces of heavy alloy heat treated at 1050°C for various lengths of time first showed that a W-W interfacial precipitation reaction occurs [78] . Normally, a large fraction of the fracture surface shows W-W intergranular separation which appear as smooth, featureless islands surrounded by matrix that has failed in a ductile manner (Fig.6.1). However, when grain boundary precipitation is present, the smoothness of the intergranular fracture is gone (Fig. 6.2). The precipitation morphology can be quite varied; lamellar precipitation with a precipitate free zone (PFZ) near the edges (Fig. 6.2), nodular nonlamellar particles (Fig. 6.3), and a combination of these (Fig. 6.4) can be observed on the same specimen.

1.2. Transmission Electron Microscopy

The precipitate structure was analyzed using TEM. It was difficult to produce thin foils which contained even one W-W grain boundary precipitate - nevertheless TEM analysis was possible. Figure 6.5 shows typical

bright field/dark field images with a SAD pattern. Operating at 100kV it was not possible to obtain complete, indexable SAD patterns from the precipitate phase although all diffraction spots from many different precipitates were consistent with an fcc structure having lattice parameter $a_o \simeq 3.60\text{Å}$ (equivalent to the fcc matrix phase). Higher quality SAD patterns obtained using HVEM confirmed this result (Fig.6.6).

Extensive use of the HVEM was made in an attempt to establish precisely the precipitate (fcc) - W(bcc) orientation relationship without success. However, convergent beam electron diffraction (CBED) on the JEOL 100C eventually yielded a result. Figure 6.7 shows CBED patterns taken from a precipitate and both adjacent W grains. The orientation relationship between the fcc precipitate and the first W grain is:

W (bcc)		Precipitate (fcc)
$[011]$	//	$[111]$
$[2\bar{1}1]$	//	$[1\bar{2}1]^{\dagger}$
$[11\bar{1}]$	~//	$[10\bar{1}]$
		(off by $\phi \simeq 3^{\circ}$ towards $[1\bar{2}1]_{fcc}$)

This does not correspond exactly to either of the well-known Kurdjumov-Sachs (K-S) or Nishiyama-Wassermann (N-W) bcc-fcc orientation relationships. Rather, it falls between the two as illustrated in Figure 6.8. Determination of the orientation relationship between the precipitate and the second W grain was less accurate due to experimental difficulties. It is:

W (bcc)		Precipitate (fcc)
$[010]$	~8°from	$[010]$
$[100]$	~//	$[10\bar{1}]$

which is near to the N-W orientation relationship (compare with Fig.6.8b).

---

† See note at Figure 6.8

It appears that there is no unique orientation relationship between the fcc precipitate and the bcc W-phase. However, in the cases examined all were found to be in the K-S / N-W region - generally closer to N-W.

1.3. Microanalysis

Thin film energy dispersive X-ray microanalysis was used to verify the presence of large nickel and iron concentrations in the W-W grain boundary precipitates. This was substantiated as can be seen from the spectra in Figure 6.9. Quantitative data was unobtainable, as it was not certain as to whether the X-rays produced were coming exclusively from the precipitate. Possible stage instability and/or beam spreading could have caused the surrounding tungsten grains to contribute to the W peaks.

1.4. Kinetics

The kinetics of this reaction were characterized using SEM since large areas could be searched quickly. Examining the series of heat treatments given to the commercial 90W-5Ni-5Fe alloy, there seemed to be no clear progression to the reaction as a function of temperature (Fig. 6.10). It appears that there is more precipitation present after heat treatments in the 600-900°C (t = 100 hours) temperature range than outside it; however, the as-received material also showed significant precipitation. As previously mentioned, this material was given a post-sintering heat treatment at 1050°C for ~ 1 hour, and it is suspected that this was sufficient to initiate W-W grain boundary precipitation - thus obscuring the exact effects of any further heat treatment.

The other commercial alloy, 90W-7Ni-3Fe, supplied without post-sintering heat treatment, was given a series of heat treatments and examined in the same manner (Fig. 6.11). In the as-received (as-sintered) material absolutely no precipitation was visible. This fracture surface also was

unique in having a high proportion of W-matrix separation. This is associated with poor impact toughness[5] and perhaps impurity segregation to the W-matrix boundary. There is essentially no W-W grain boundary precipitation at 450°C after 100 hours and precipitation is just barely beginning at 600°C, also after 100 hours. The maximum observed amount appears in the range 750-900°C after 100 hours, and the precipitates appear much coarser after a heat treatment for 100 hours at 1050°C. No attempt was made to quantify these results as the extent of the reaction, when present, was sporadic and irregular.

2. Precipitation Hardening in the W-Phase

2.1. Cold Rolled Material

The material examined in this section is the commercial 90W-5Ni-5Fe alloy described in chapter 1 section 3.1. It was cold-rolled to a reduction in thickness of 10.1%.

2.1.1. Microhardness

A hardening reaction was obtained in the material under investigation. Figure 6.12 shows the change in microhardness of the W-phase of the deformed alloy as a function of heat treatment. Peak hardness is obtained after annealing at ~ 600°C for 1 hour. This is qualitatively similar to results obtained by R.A.R.D.E.[27]

2.1.2. Weak Beam TEM

Preliminary bright field TEM failed to identify any microstructural changes that would be responsible for the hardening. It has been suggested that impurity interstitials such as carbon or oxygen segregate to dislocations upon annealing, forming Cottrell atmospheres, and thus inhibiting slip [27].

In the classical sequence of strain aging, the interstitial impurity atoms diffuse rapidly to and along the dislocation core and may eventually form very fine precipitates there[80]. Unless these precipitates grow to a fairly large size ($\gtrsim$ 75Å) they cannot be readily observed using conventional two-beam TEM imaging because of the relatively long range ($\sim \xi_g/3$ half-width) and complicated contrast of the superimposed dislocation.

To minimize this obscuring effect, weak beam TEM has been employed in this study. As described in chapter 3 section 4.3., the weak beam technique produces high resolution diffraction contrast at regions of high elastic strain making it ideal for the study of dislocations. Therefore, it was hoped that contrast effects due to very fine precipitates lying at or near a dislocation core could be observed, as demonstrated in the Al-Zn-M system by Allen and Vander Sande[56].

Figure 6.13 shows bright field and weak beam dark field micrographs of the W-phase in the rolled 90W-5Ni-5Fe alloy after different heat treatments. The most immediate and striking change in microstructure is the appearance of a fine dispersion of strain fields in the material heat treated at 600°C for 1 hour. Appearing as small black 'dots' in the bright field image, they could easily be mistaken for surface contamination or overlooked altogether, but because they give sharp strain contrast in the weak beam image they represent small defects (~ 20Å) that have an elastic strain field surrounding them. After aging at a higher temperature, 750°C for 1 hour, similar defects were observed, but were larger in size (~ 40Å) and had decreased in number density. In material heat treated at 900°C for 1 hour, similar image contrast was not found, nor was anything else observed that might be characteristic of the aging sequence.

Some defects can be observed in close association with dislocations (arrowed in Fig. 6.13b), but the majority of defects appear to have

precipitated homogeneously in the bulk of the W-phase. Nevertheless, all of the observed defects should inhibit dislocation slip because of their elastic strain fields.

2.1.3. $\underset{\sim}{g}\cdot\underset{\sim}{R}$ Contrast Analysis (TEM)

Two beam $\underset{\sim}{g}\cdot\underset{\sim}{R}$ analysis was used to characterize the direction of the defect displacement vector, $\underset{\sim}{R}$. The basis of this technique has been described in chapter 3 section 4.2. Figure 6.14 shows a series of micrographs taken from the W-phase in material rolled and aged at 750°C for 1 hour using different $\underset{\sim}{g}$ vectors about $z \simeq [001]$. By comparing the observed invisibilities with those that are possible (see $\underset{\sim}{g}\cdot\underset{\sim}{R}$ table accompanying Fig. 6.14) for low index displacement vectors, $\underset{\sim}{R} = K\langle 111\rangle$ (K = constant) can be ruled out immediately. The distinction between $\underset{\sim}{R} = K\langle 100\rangle$ and $\underset{\sim}{R} = K\langle 110\rangle$ is vague because of the $\underset{\sim}{g}$ vectors used in this case. However, from examination of another area, this time with $z \simeq [011]$, it is apparent from the images and the $g\cdot\underset{\sim}{R}$ table that $R = K\langle 110\rangle$ is not possible (Fig. 6.15). Consequently, it is concluded that the direction of the displacement due to the defects is in the $\langle 100\rangle$ directions of the tungsten lattice - with each defect exhibiting a single $\langle 100\rangle$ variant.

These defects could either be small dislocation loops resulting from agglomerating point defects (due to the plastic deformation), or small precipitates. The majority of dislocation loops in bcc metals, including tungsten, have Burgers vectors, $\underset{\sim}{b} = \frac{1}{2}\langle 111\rangle$. For a screw dislocation the parameter $\underset{\sim}{R}$ is proportional to $\underset{\sim}{b}$ and the simplified invisibility criterion becomes $\underset{\sim}{g}\cdot\underset{\sim}{b} = 0$[†]. Since $\underset{\sim}{R} = K\langle 100\rangle_W$, these defects are clearly not

---

[†] This is not strictly true for edge or mixed dislocations. In this case the parameter $\underset{\sim}{R}$ becomes more complicated and $g\cdot\underset{\sim}{b}$, $g\cdot\underset{\sim}{b}_e$, and $g\cdot\underset{\sim}{b}\times\underset{\sim}{\mu}$ (where $\underset{\sim}{b}_e$ is the edge component of the Burgers vector and $\underset{\sim}{\mu}$ is a unit vector along the dislocation line) must all equal zero for complete invisibility. However, in practice, only faint residual contrast occurs when $g\cdot\underset{\sim}{b} = 0$ and $g\cdot\underset{\sim}{b}_e$, $g\cdot\underset{\sim}{b}\times\mu \neq 0$. This leads to the $g\cdot\underset{\sim}{b} = 0$ effective invisibility criterion which means the above criterion is valid.

dislocation loops but instead are probably small precipitates with a misfit strain in <100>$_W$ directions. We could then expect that this reaction would also take place in undeformed material.

2.2. Undeformed Material

The material examined in this section is the commercial 90W-5Ni-5Fe alloy described in chapter 1 section 3.1.

2.2.1. Mechanical Testing

2.2.1.1. Microhardness

Figure 6.16 shows a subtle change in W-phase microhardness with aging for the longer time of 100 hours. However, the trend of the graph does not clearly show a hardening response. Because of the scatter inherent in this technique[81], it was decided to search for age hardening by measuring tensile strength as a function of annealing temperature.

2.2.1.2. Tensile Testing

The change of yield strength (YS) and ultimate tensile strength (UTS) with annealing temperature is much more well defined (Fig. 6.17). The change in UTS is higher than the YS change which shows that an increase in the work hardening rate also occurs with precipitation. These tests show a definite strengthening response in the unworked heavy alloy after annealing in the 500-600°C range for 100 hours.

2.2.2. $\underset{\sim}{g}\cdot\underset{\sim}{R}$ Analysis (TEM)

Again, $\underset{\sim}{g}\cdot\underset{\sim}{R}$ analysis was used to characterize the displacement direction due to the defects. The same result as obtained under the conditions of deformation plus aging was found in this (aged-only) condition (Fig. 6.18). The abundance of these $\underset{\sim}{R}$ = K<100> defects shows that prior deformation is not essential for their appearance - leaving little doubt that they are

precipitates.

2.2.3. Stereo Microscopy - Nature of the Defect Strain Field

It is readily apparent from the $\underset{\sim}{g}(200)$ dark field micrographs of precipitates in the W-phase presented so far (Figs. 6.14, 6.15, 6.18), that the vector $\underset{\sim}{\ell}$, defined as joining the black to the white lobe on a black/white defect image, is either parallel or antiparallel to $\underset{\sim}{g}(200)$ for a given defect. Figure 6.19 illustrates how $\underset{\sim}{\ell}$ is defined along with the two possible relationships with $\underset{\sim}{g}(200)$ for a $\underset{\sim}{R}$ = K[100] defect. When both conditions are observed simultaneously for various defects in a single micrograph there can be only three possible reasons:

1) The defects are of mixed nature - i.e. some have a compressive strain field and some have a tensile strain field.
2) The defects are of a single nature and are small enough for the sense of $\underset{\sim}{\ell}$ in relation to $\underset{\sim}{g}$ to oscillate with defect depth in the foil.
3) A combination of the above.

The presence or absence of this black/white contrast reversal with depth is influenced by the dimensionless misfit parameter, P, which is defined as[82]

$$P = \frac{|\underset{\sim}{g}|\Delta V}{\xi_g 2\pi}$$

where $|\underset{\sim}{g}| = \frac{1}{d}$ is the magnitude of diffraction vector, ΔV is the volume misfit of the defect, and ξ_g is the extinction distance for reflection $\underset{\sim}{g}$.
If P<<1 then the black/white contrast oscillates with defect depth in the manner described by Rühle[83,84] and illustrated in Figure 6.20. For P>>1 the depth oscillations are suppressed and the Ashby-Brown rules[85,86] are applicable.

Assuming that the precipitates are platelets, then ΔV is given by:

$$\Delta V = |\underset{\sim}{R}| r^2 \pi$$

where $|\underset{\sim}{R}|$ is the magnitude of the displacement vector and r is the platelet radius. From $\underset{\sim}{g}(200)$ images we can see that $r_{max} \simeq 50\mathring{A}$ and we can estimate that $|\underset{\sim}{R}|$ would not be more than one atomic distance in the $\langle 100 \rangle_W$ direction (i.e. $|\underset{\sim}{R}| \lesssim d_{100} = a_W \simeq 3.165\mathring{A}$). Since $\underset{\sim}{g}$ is (200) and $\xi_{200} \simeq 222\mathring{A}$, an approximate upper limit for P would be, $P_{max} \simeq 0.10 << 1$, and contrast oscillation with depth (as depicted in Figure 6.20) would be theoretically expected, which is in fact observed.

Stereo microscopy, as described in chapter 3 section 4.4, was used to determine the depth of individual precipitates from the top of the foil - thus establishing which layer in the foil (L_1, L_2, or L_3 [Fig. 6.20]) each precipitate was located in. Then the relative sense of $\underset{\sim}{\ell}$ and $\underset{\sim}{g}$ were deduced from the micrograph and compared with Figure 6.20 to finally determine whether the strain field was tensile or compressive in nature.

Figure 6.21 shows a typical stereo pair taken from material aged at 700°C for 100 hours. When observed with a stereo viewer the contrast reversal with depth is evident. When accurately measured and compared with Figure 6.20, all precipitates were found to have a tensile strain field. Figure 6.22 shows the results of analyzing a number of precipitates.

2.2.4. Microanalysis and Diffraction of Precipitates

Since electron microprobe measurements have shown that the W-phase does contain measurable amounts of the principle γ-phase elements, nickel and iron, to the extent of 0.1 at% and 1.1 at%, respectively, the observed precipitate could be due to one or both of these elements precipitating from supersaturated solid-solution upon aging. To explore this possibility EDX microanalysis of thin foils of material aged at 700°C for 100 hours

was performed. An HB-5 STEM was used in order to obtain a small (~20Å dia.) focussed probe. Typical spectra are shown in Figure 6.23.

Unfortunately, the W Lℓ peak (7.386keV) overlaps the Ni Kα peak (7.477keV) making nickel determination impossible. However, it was possible to ratio other W peaks to the Fe Kα peak and to compare this ratio for spectra taken from precipitates and spectra taken from the W matrix. The results are displayed in Figure 6.24. It can be seen that there is essentially no change in W:Fe peak ratios between spectra obtained from precipitate regions and areas without a precipitate.

Selected area diffraction from regions of precipitation in materials with various aging treatments (up to 800°C) revealed no extra diffraction spots that might be expected from a second phase. Consequently, many attempts were made to observe fine structure (e.g. streaking) in the diffraction pattern but none was found.

Material aged at 900°C for 100 hours was also examined. Very infrequently, a round ~0.1μm diameter 'precipitate' would be observed in the W-phase (Fig. 6.25). Assuming this to be precipitation at higher temperature, comparative spectra were obtained (Fig. 6.26). Again, there was essentially no change in W:Fe peak ratios between 'precipitate' spectra and the surrounding W spectra. In this case, however, the 'precipitate' spectra had fairly substantial Ca Kα and Kβ peaks at 3.690keV and 4.012keV, respectively.

A list of possible d-spacings of this phase has been generated using electron diffraction (Fig. 6.25). It was not possible to correlate this information with any known compound containing calcium[87].

2.2.5. Morphology And Kinetics of Precipitation

Figure 6.27 shows a series of TEM micrographs taken from the W-phase of the 90W-5Ni-5Fe alloy aged at different temperatures. The average size

of the precipitates, as measured normal to $\underset{\sim}{\ell}$ on a $\underset{\sim}{g}(200)$ micrograph, increases from ~ 40Å after 500°C for 100 hours to ~ 70Å after 700°C for 100 hours. However, one important feature of this precipitation reaction not shown by these micrographs is the localized nature of precipitation - i.e. while precipitation is readily visible and abundant in one W grain, an adjacent grain may have little or no precipitation. This situation makes quantitative information (e.g. precipitate density) difficult to obtain and interpret.

An attempt was made to establish the kinetics of this precipitation reaction by examining material heat treated at different times and temperatures. Obviously, this was both difficult and inexact owing to the problem explained above. Nevertheless, by examining many foils at each heat treatment, a precipitation C-curve was constructed as illustrated in Figure 6.28. One interesting fact to emerge from this exercise is the very limited precipitation observed at 600°C for 1 hour (Fig. 6.29). The amount, or number density, of precipitates in this case (essentially nil) contrasts with the extensive precipitation observed in material deformed and aged at 600°C for 1 hour (Fig. 6.13b).

2.3. 14% Hydrostatically Extruded Tungsten Single Crystal

To shed light on the possibility of nickel and/or iron being responsible for precipitation hardening it was decided to examine cold deformed and aged pure tungsten single crystals. Since no nickel or iron was present in this material, this effectively eliminates that variable and provides a comparison with the W-phase in the heavy alloy.

2.3.1. Microhardness

Since microhardness is orientation dependent[81], it was decided to measure the microhardness of each individual specimen before and after aging

to get a proper comparison. Specimens were repolished after aging but much care was taken to maintain the same orientation of the specimen relative to the indentor used before aging. The results are shown in Figure 6.31. There is no discernible hardness increase occurring after any of the heat treatments.

2.3.2. Transmission Electron Microscopy

No precipitation was observed in unaged material or in material heat treated at 700°C for 1 hour (Fig. 6.30). Therefore, it is concluded that the precipitation observed in the W phase of the heavy alloy is not present in pure, deformed and aged tungsten.

Figure 6.1†

SEM fractograph showing featureless W-W separation.

Figure 6.2†

SEM fractograph showing lamellar W-W precipitation with a PFZ.

Figure 6.3†

SEM fractograph showing nodular W-W precipitation.

Figure 6.4†

SEM fractograph showing both nodular and lamellar W-W precipitation.

---

† Taken from various W-Ni-Fe heavy alloys (courtesy of Hogwood *(78)*).

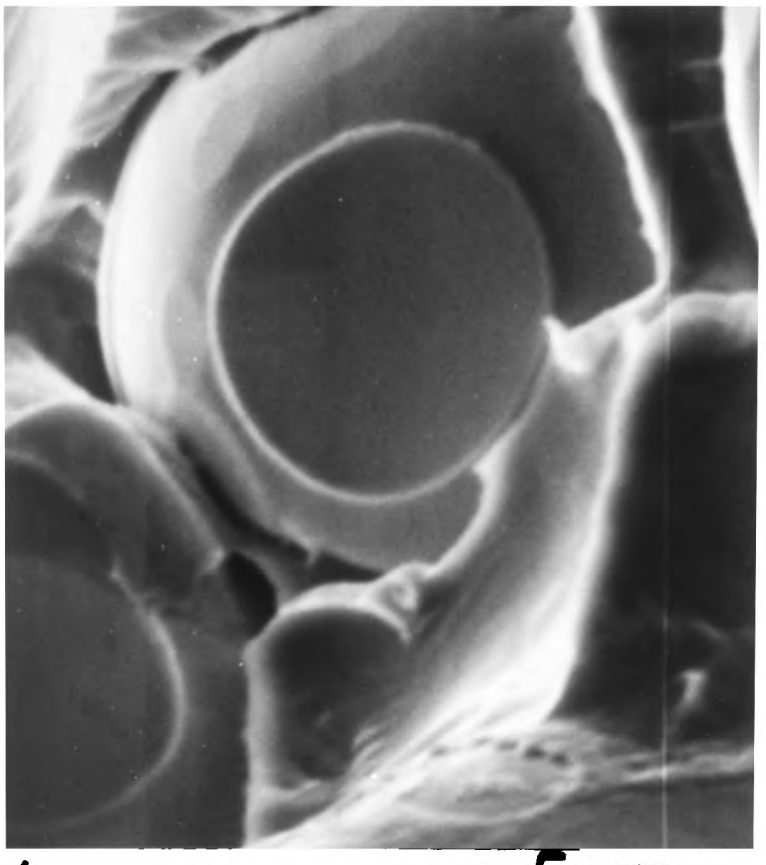

1 —5µm—

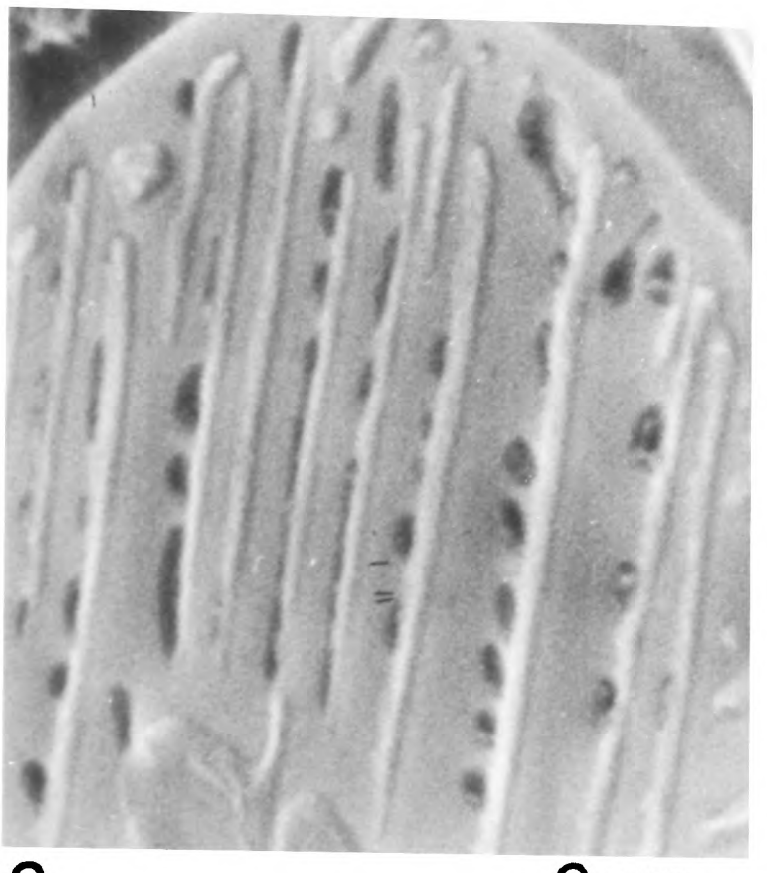

2 —2µm—

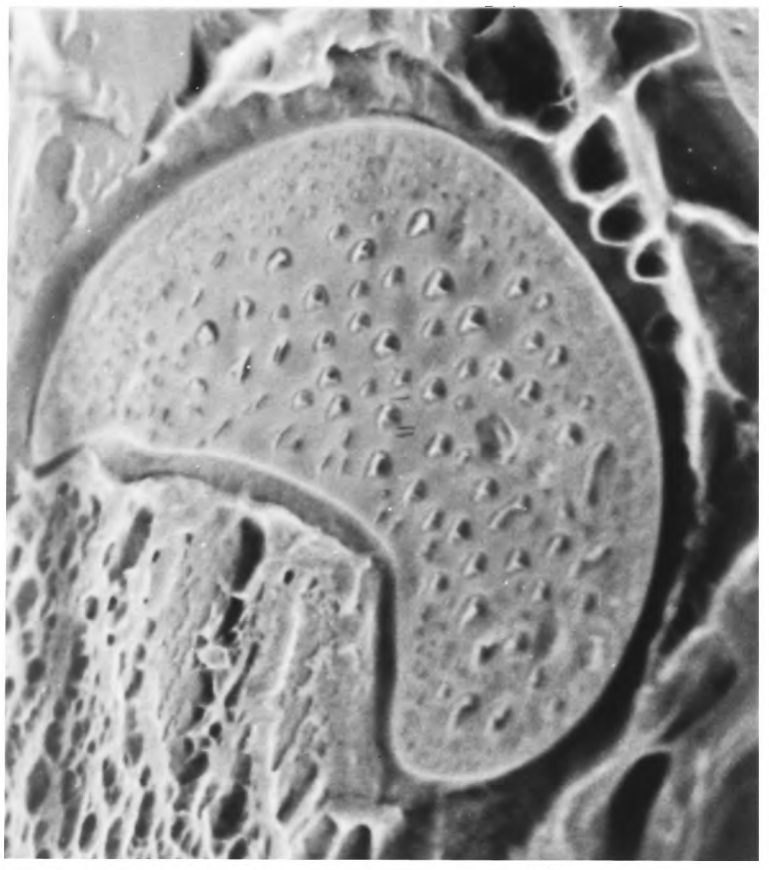

3 —5µm—

4 —5µm—

Figure 6.5

Typical TEM (100keV) micrographs showing W-W grain boundary precipitates in heavy alloy aged at 1050°C for 1 hour.

a) Bright field.

b) Dark field, using $(311)_{fcc}$ reflection.

c) SAD pattern; $z_W \simeq [1\bar{3}5]$ and reflection used for dark field.

a

b

-0.2μm-

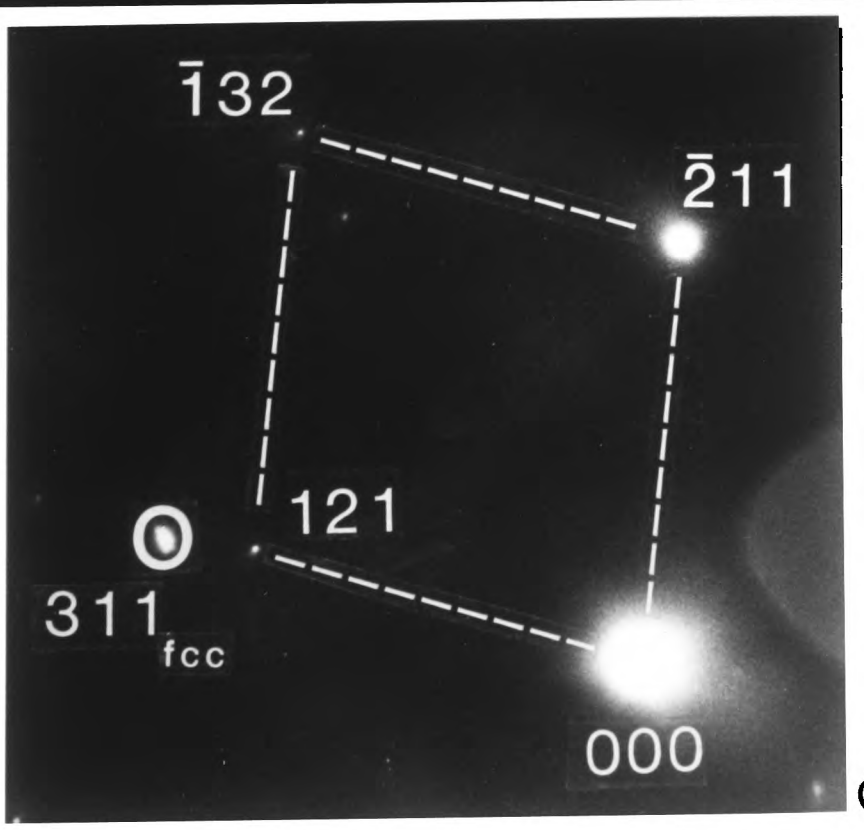

c

Figure 6.6

HVEM micrographs of material aged at 1050°C for 1 hour.

a) Bright field showing W-W grain boundary precipitate.

b) SAD pattern from the same area, $z_{fcc} \simeq [011]$ (major pattern) with some W reflections and double diffracted beams.

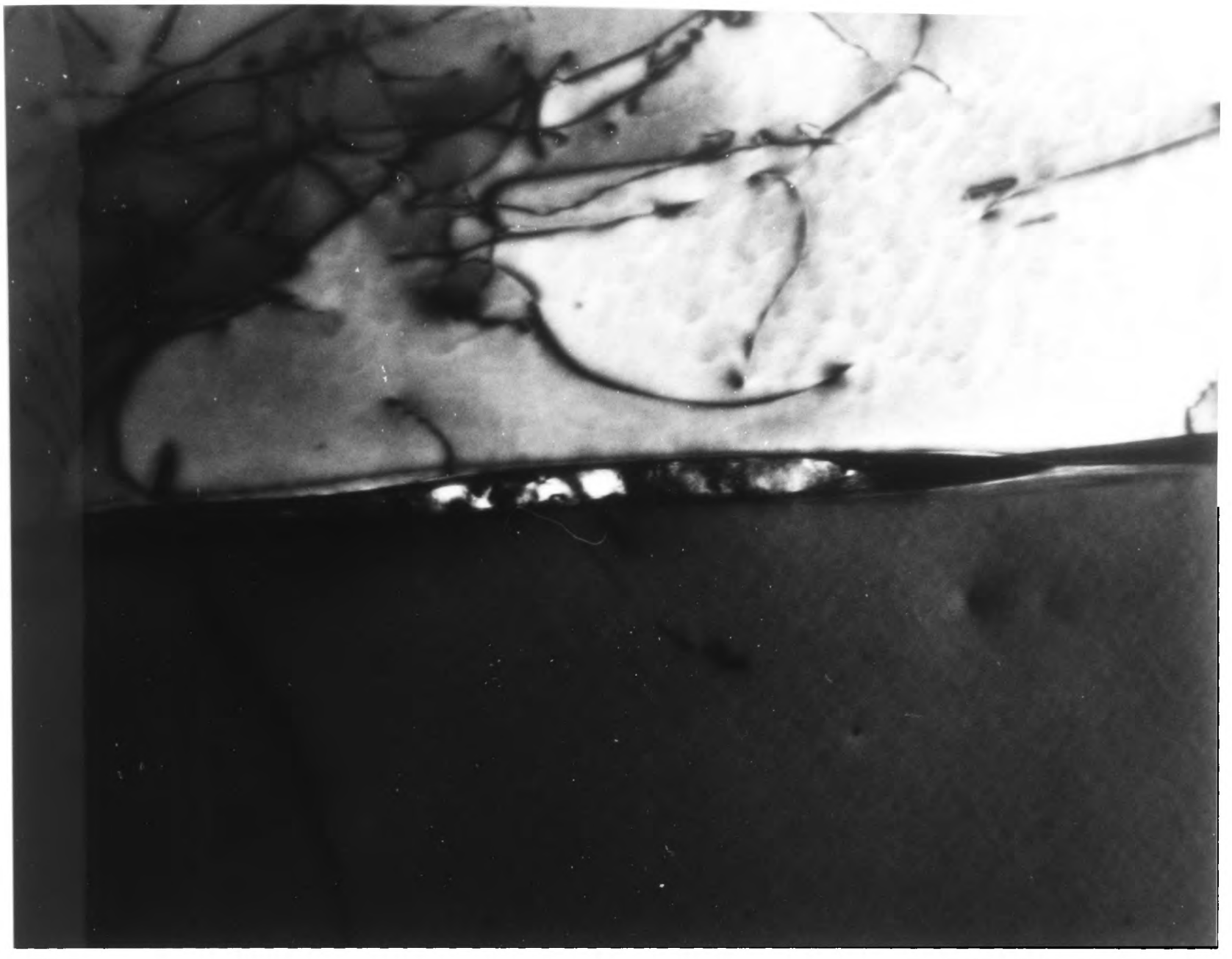
a
0.3µm

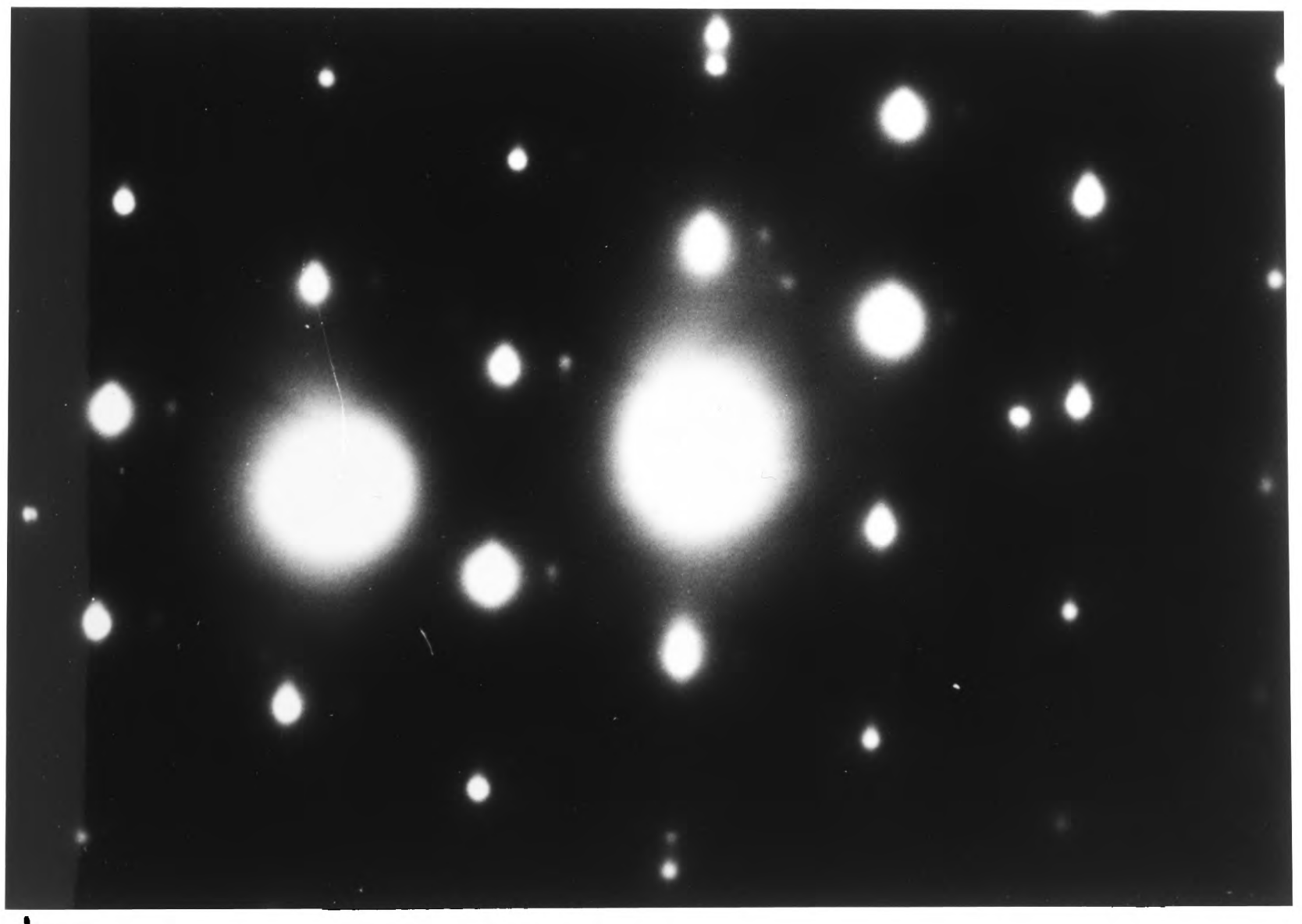
b

Figure 6.7

CBED patterns from material aged at 1050°C for 1 hour showing the bcc/fcc orientation relationships described in the text.

a) $z_{fcc} \simeq [\bar{1}01]$ (approximately $\phi \simeq 3^\circ$ from the zone axis).

b) $z_{W1} = [\bar{1}\bar{1}1]$.

c) $z_{W2} = [\bar{1}00]$ (but was tilted slightly [~2°] away from the other two before photographing).

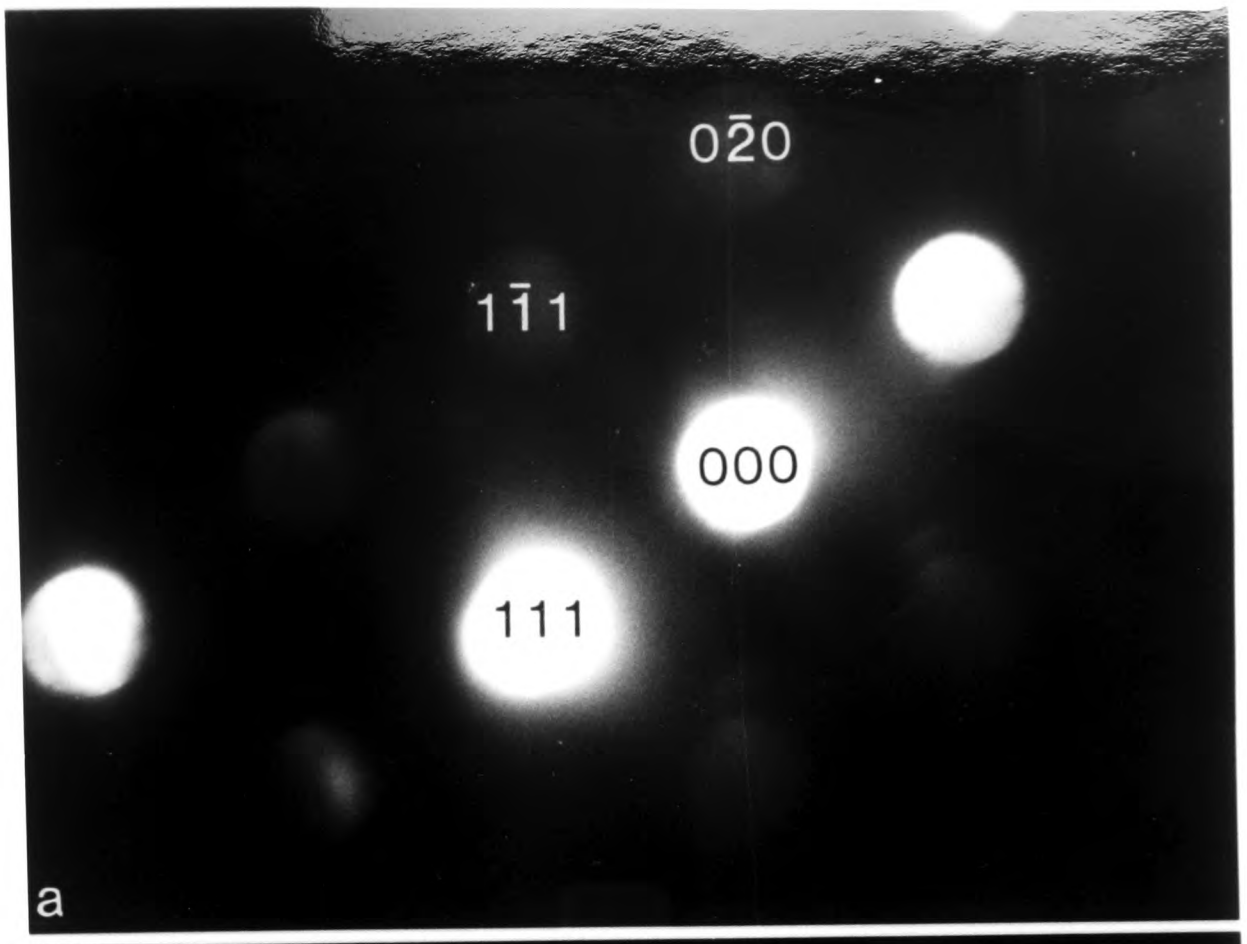
0$\bar{2}$0
1$\bar{1}$1
000
111
a

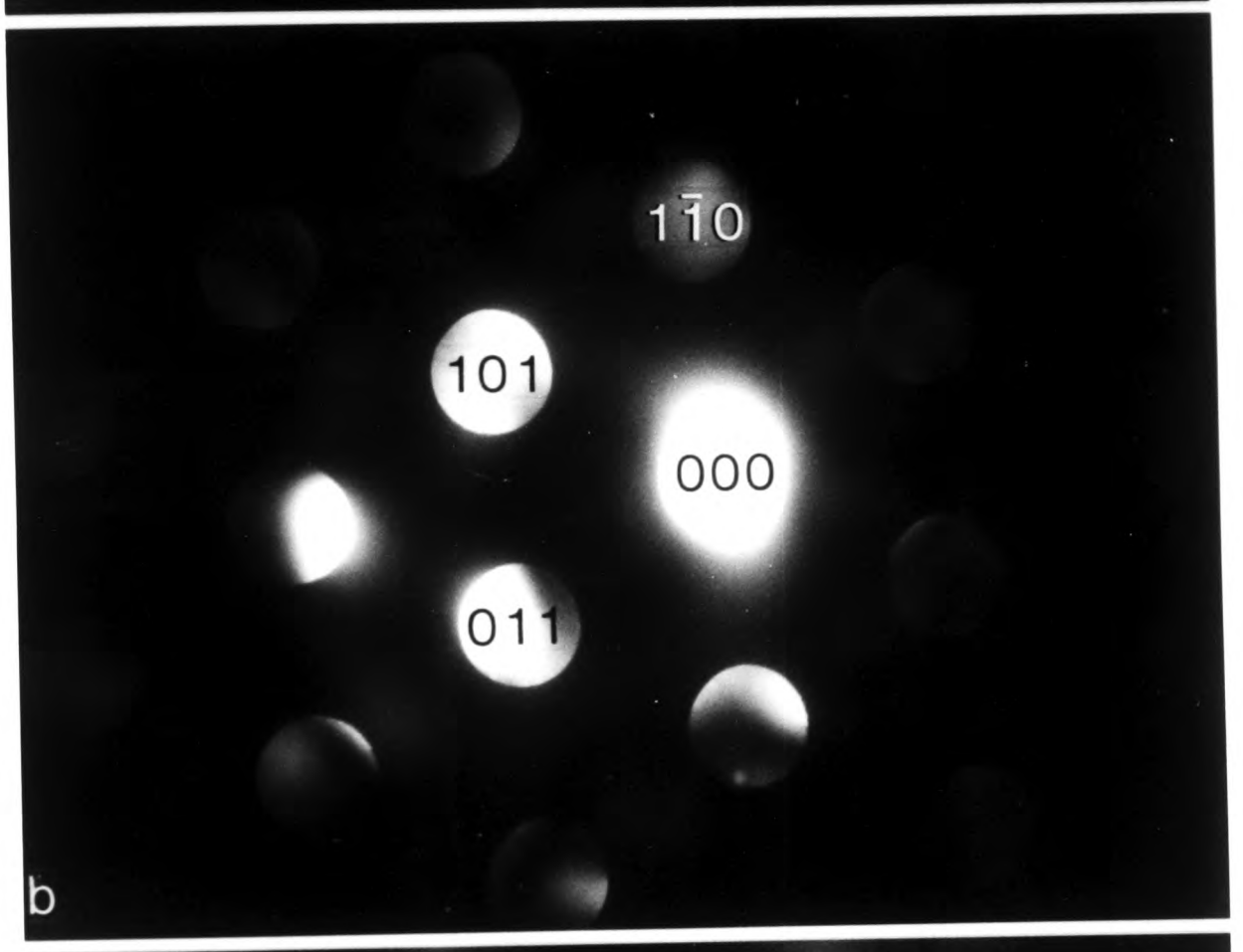
1$\bar{1}$0
101
000
011
b

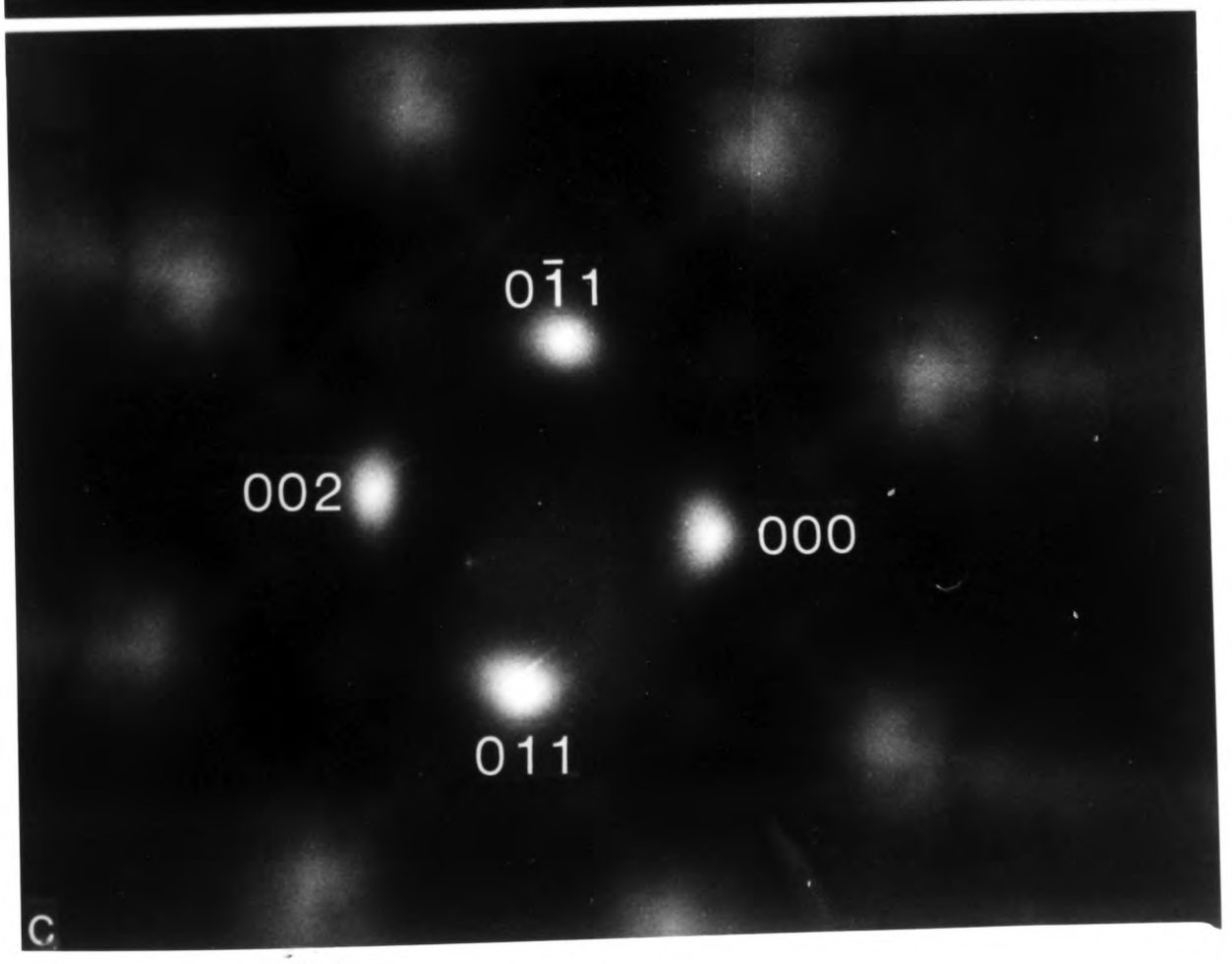
0$\bar{1}$1
002
000
011
c

a)

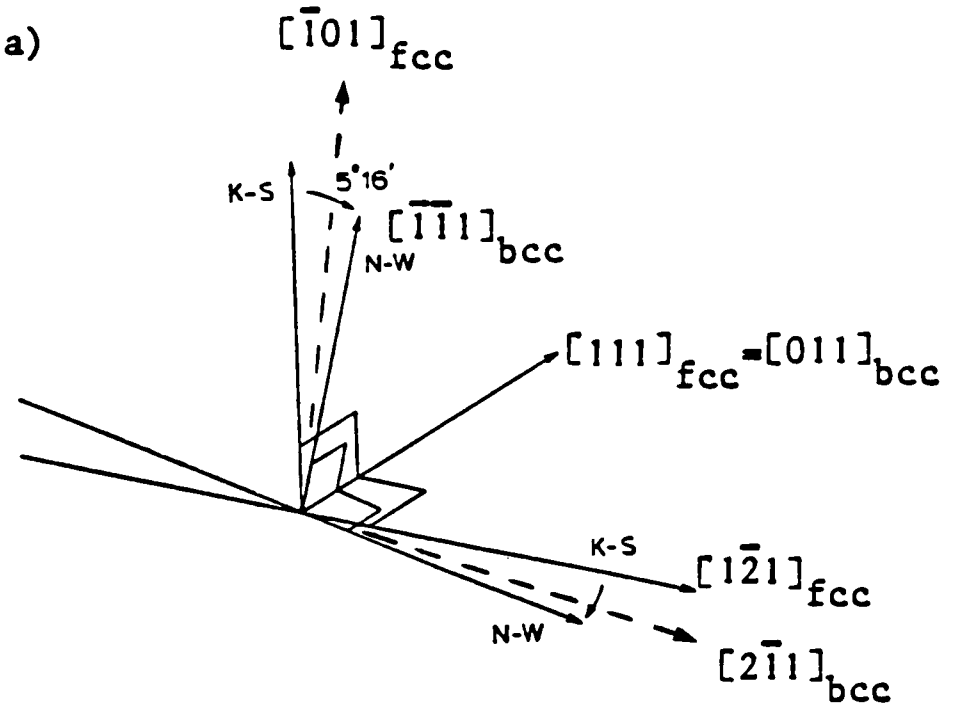
$[\bar{1}01]_{fcc}$
K-S
5°16'
N-W
$[\bar{1}\bar{1}\bar{1}]_{bcc}$
$[111]_{fcc}=[011]_{bcc}$
K-S
$[1\bar{2}1]_{fcc}$
N-W
$[2\bar{1}1]_{bcc}$

b)

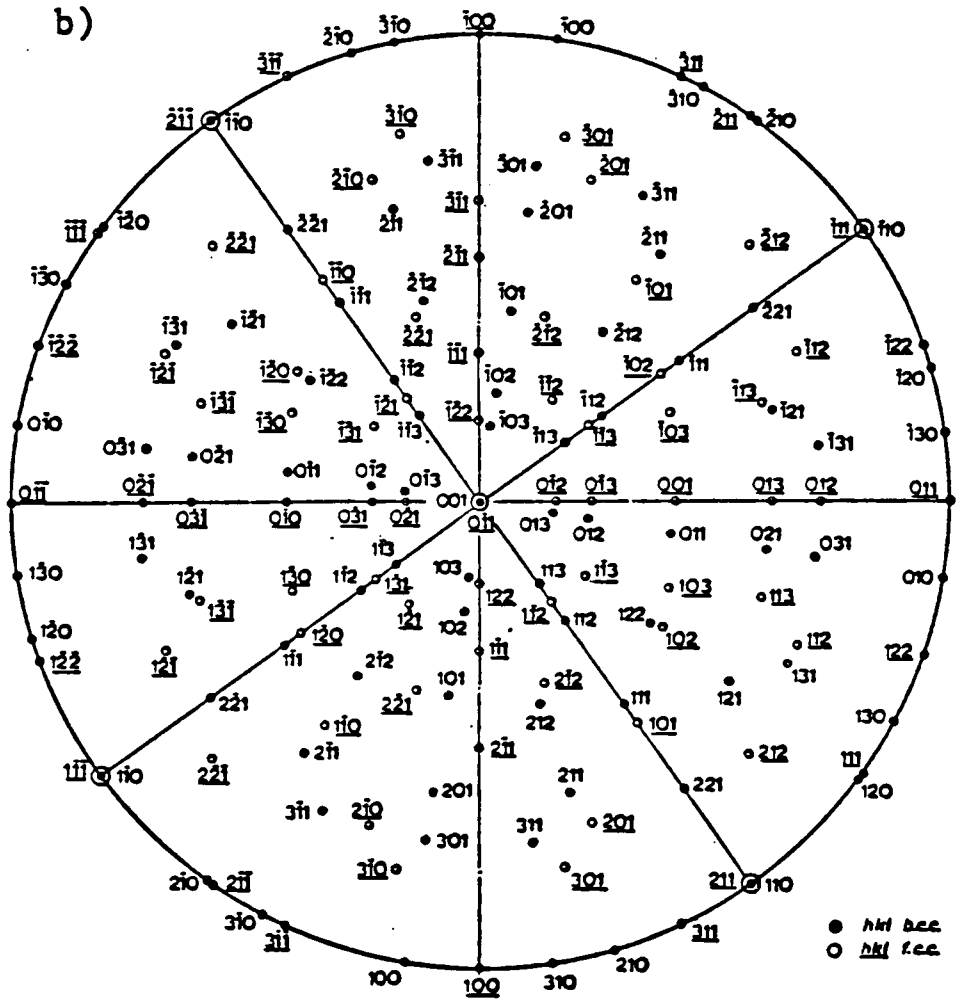
● hkl bcc
○ hkl fcc

c)

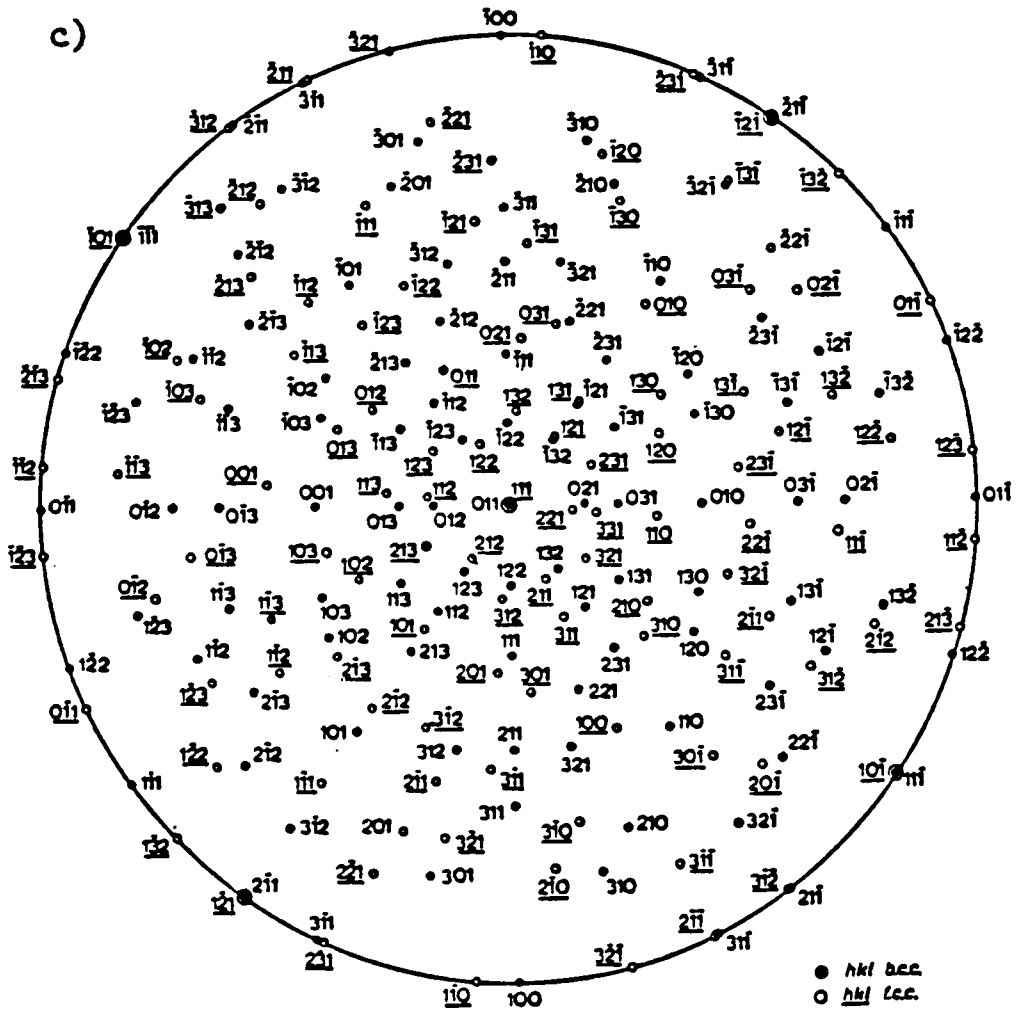
● hkl bcc
○ hkl fcc

Figure 6.8

a) Schematic diagram illustrating the observed W_1-Y orientation relationship falling between K-S and N-W (rotated about $[111]_{fcc} - [011]_{bcc}$). As it is the zone axes that are slightly tilted from one another ($\phi \approx 3^\circ$), the $(1\bar{2}1)_{fcc}$ and $(2\bar{1}1)_{bcc}$ reflections are not parallel as they appear to be in the plane of the diffraction pattern.

b) Stereographic projection† showing the Nishiyama-Wassermann orientation relationship.

i.e.	bcc		fcc
	(001)	//	$(0\bar{1}1)$
	$(\bar{1}10)$	//	$(\bar{1}11)$
	(110)	//	(211)

This projection can be used for comparison with the experimentally determined W_2-Y orientation relationship only if the indices are changed to a different (but equivalent) variant.

i.e.	bcc		fcc
	(100)	~ 8° from	(100)
	(001)	~ //	$(0\bar{1}1)$

c) Stereographic projection† showing the Kurdjumov-Sachs orientation relationship.

i.e.	bcc		fcc
	(011)	//	(111)
	$(11\bar{1})$	//	$(10\bar{1})$
	$(\bar{2}1\bar{1})$	//	$(\bar{1}2\bar{1})$

---

† After Andrews, et al.[79]

Figure 6.9

EDX spectra taken from material aged at 1050°C for 1 hour.

a) W-phase.

b) Matrix (γ-phase).

c) W-W boundary precipitate (showing substantial Ni Kα and Fe Kα peaks).

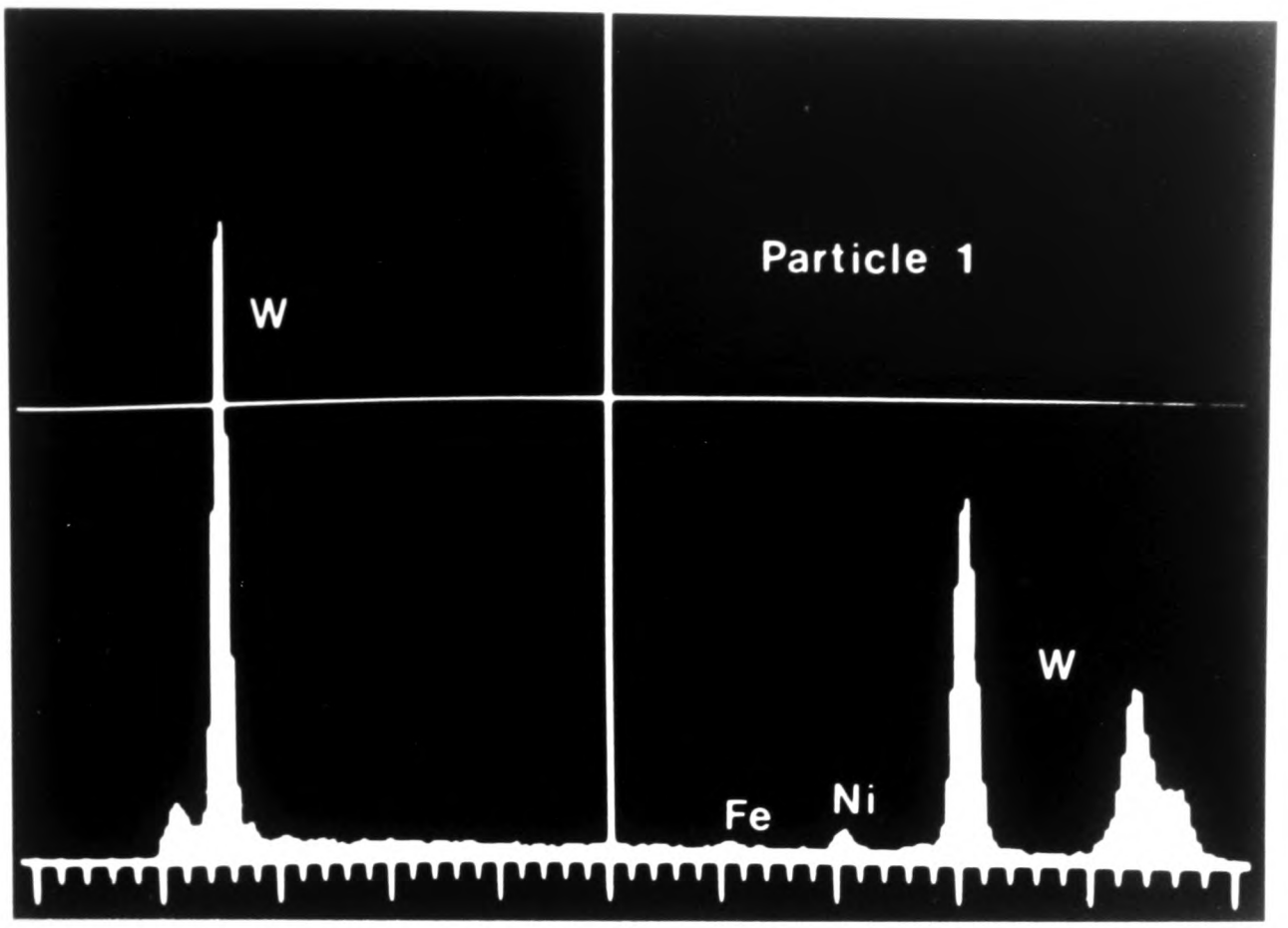

a

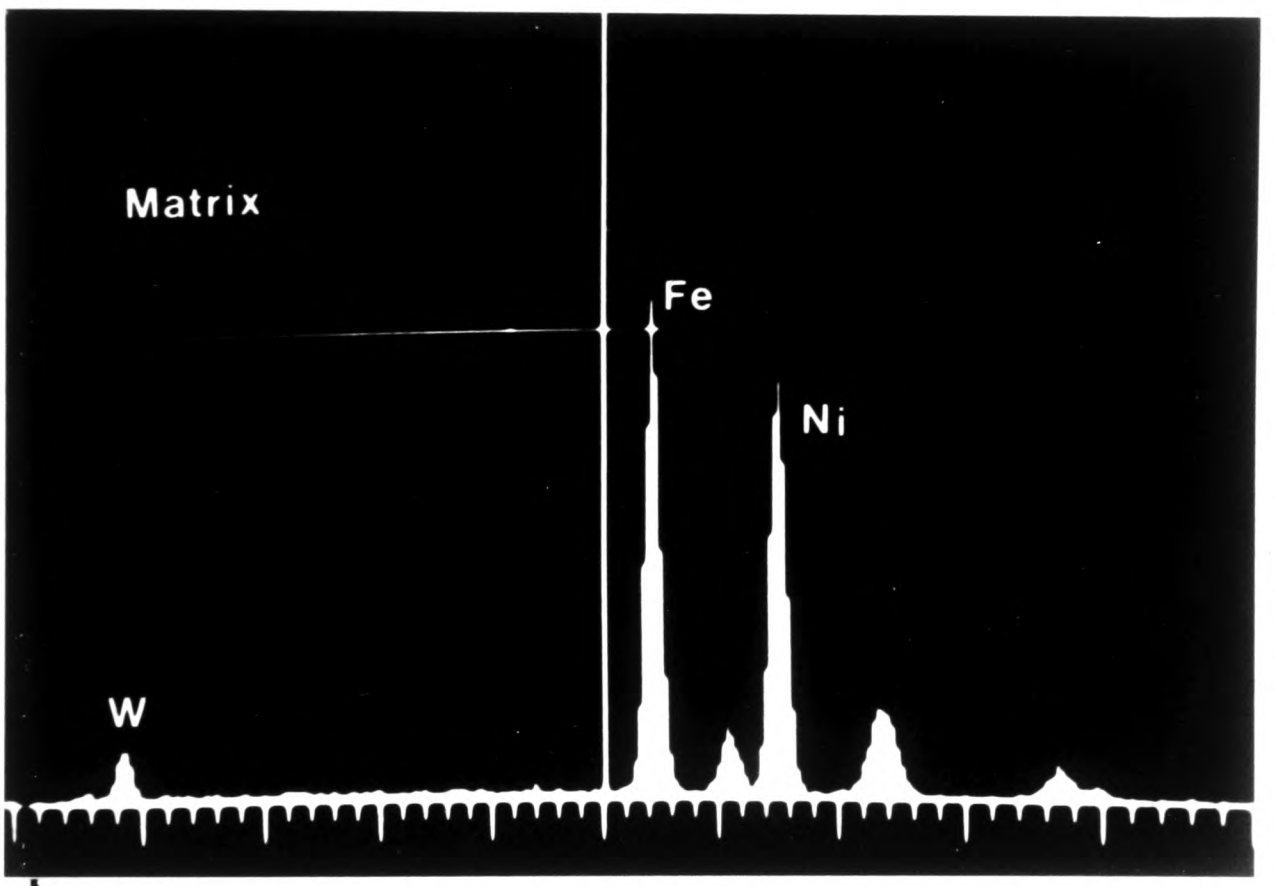

b

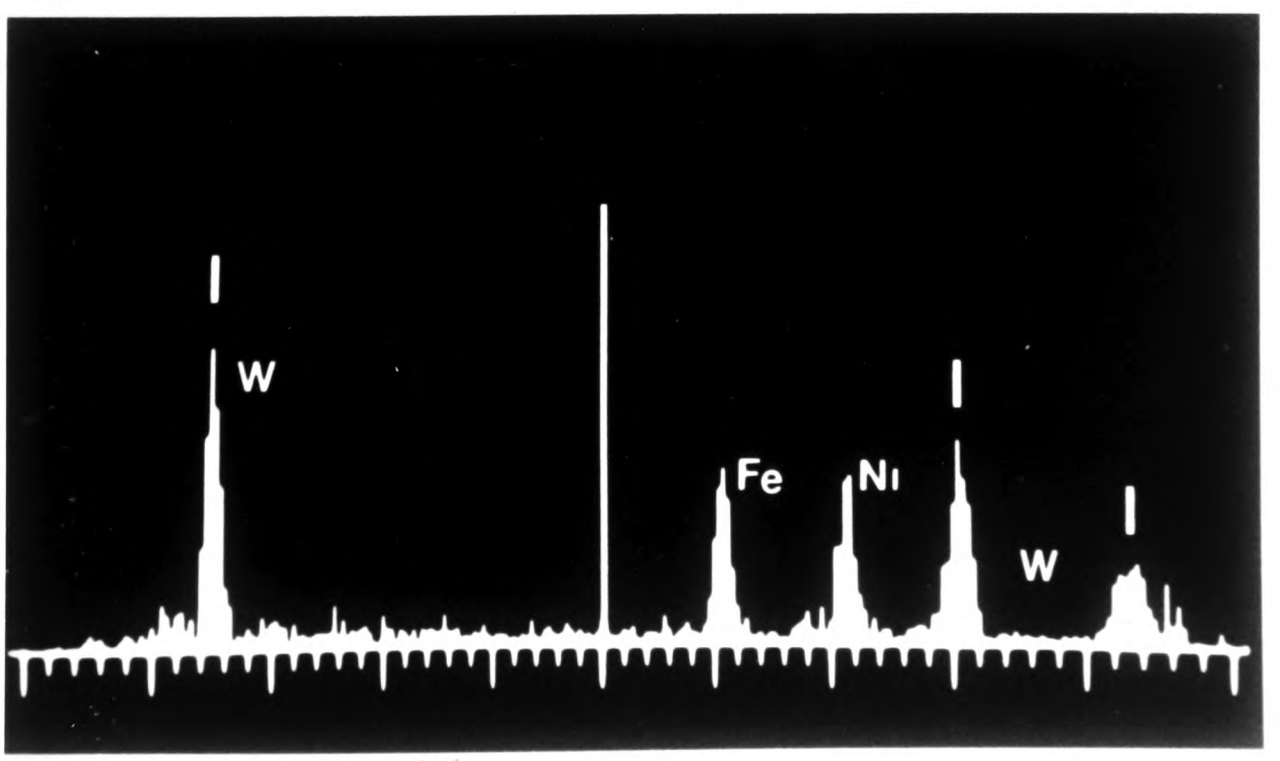

C

Figure 6.10

SEM fractographs of 90W-5Ni-5Fe heavy alloy after different heat treatments.

a) As received.

b) 500°C for 100 hours.

c) 600°C for 100 hours.

d) 700°C for 100 hours.

e) 800°C for 100 hours.

f) 900°C for 100 hours.

g) 1000°C for 100 hours.

h) 1100°C for 100 hours.

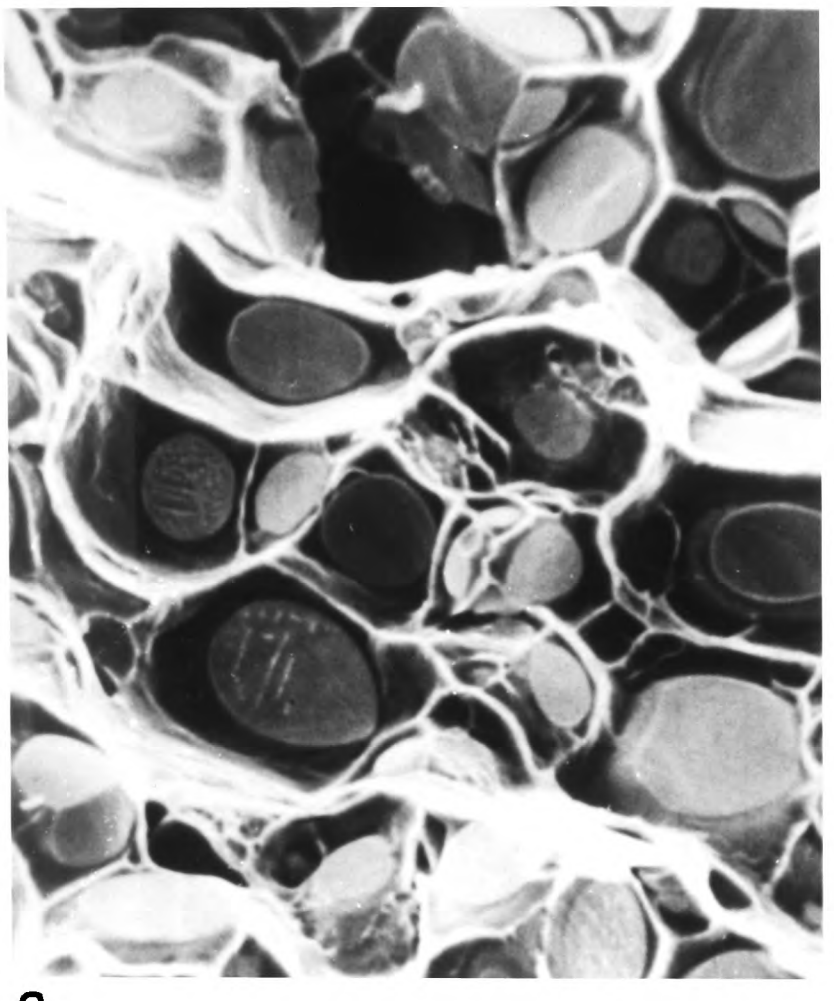

a

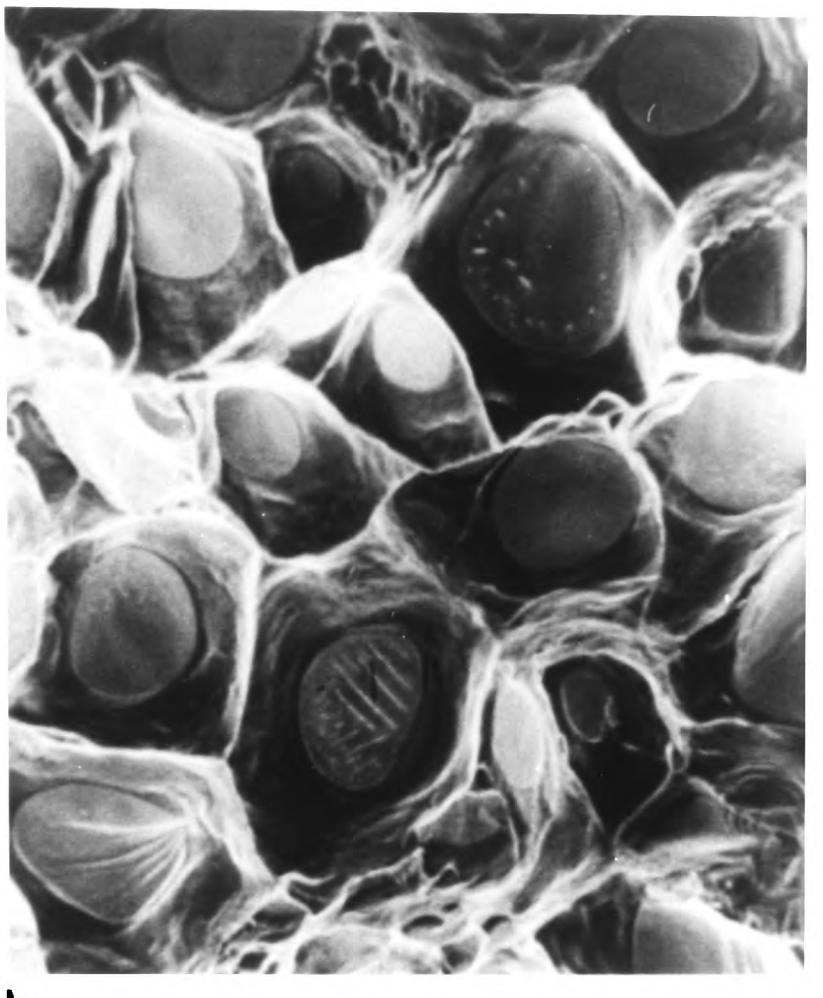

b

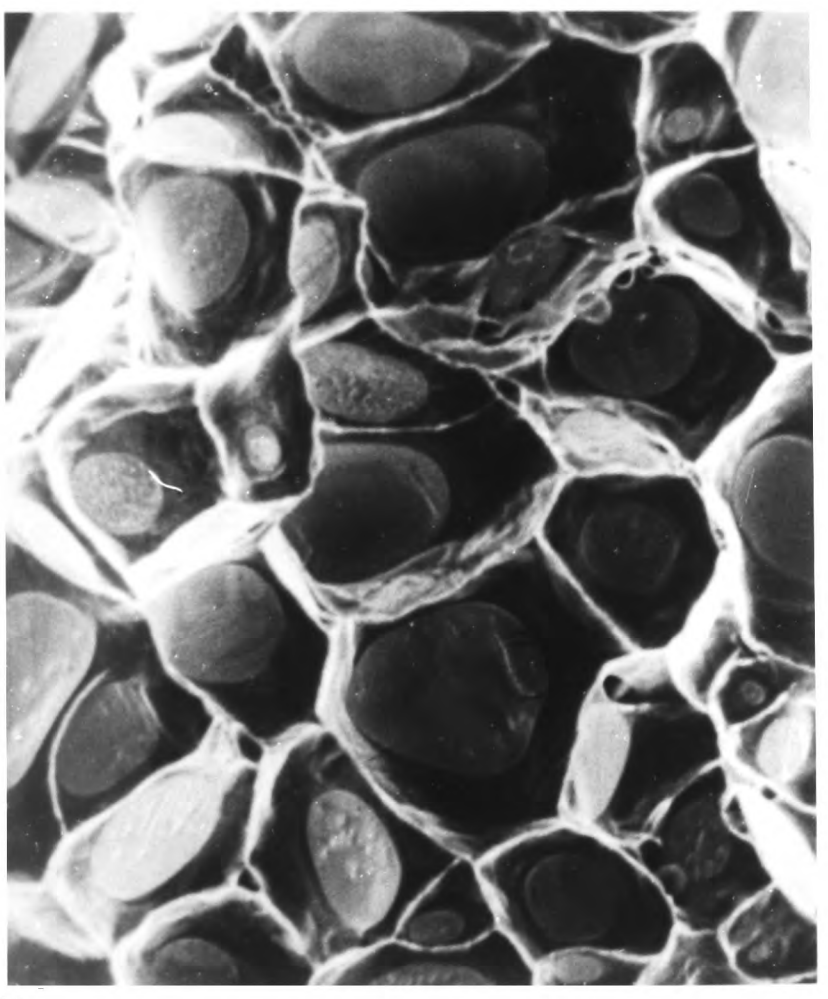

c

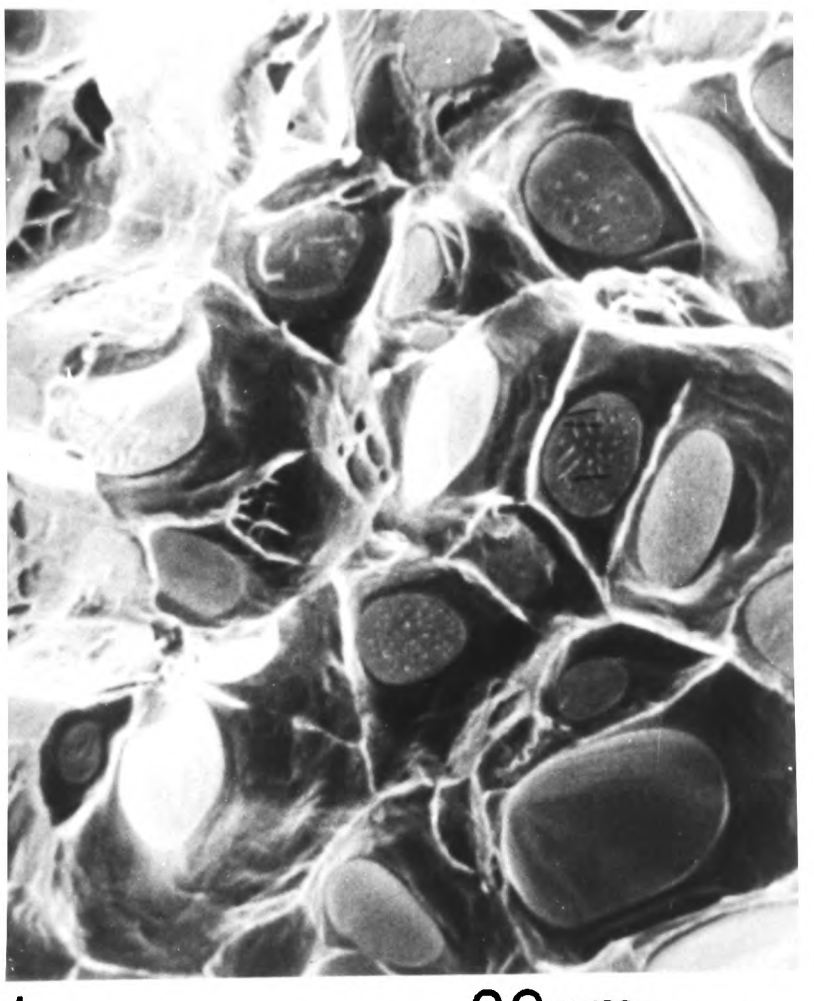

d

20µm

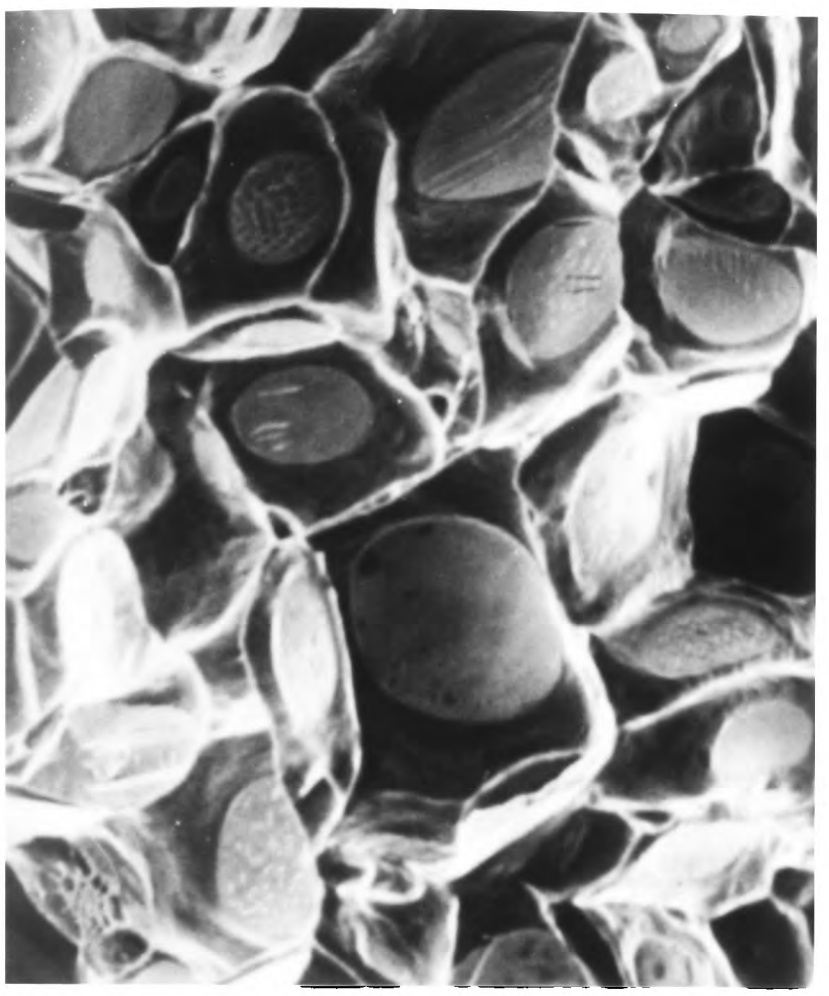

e

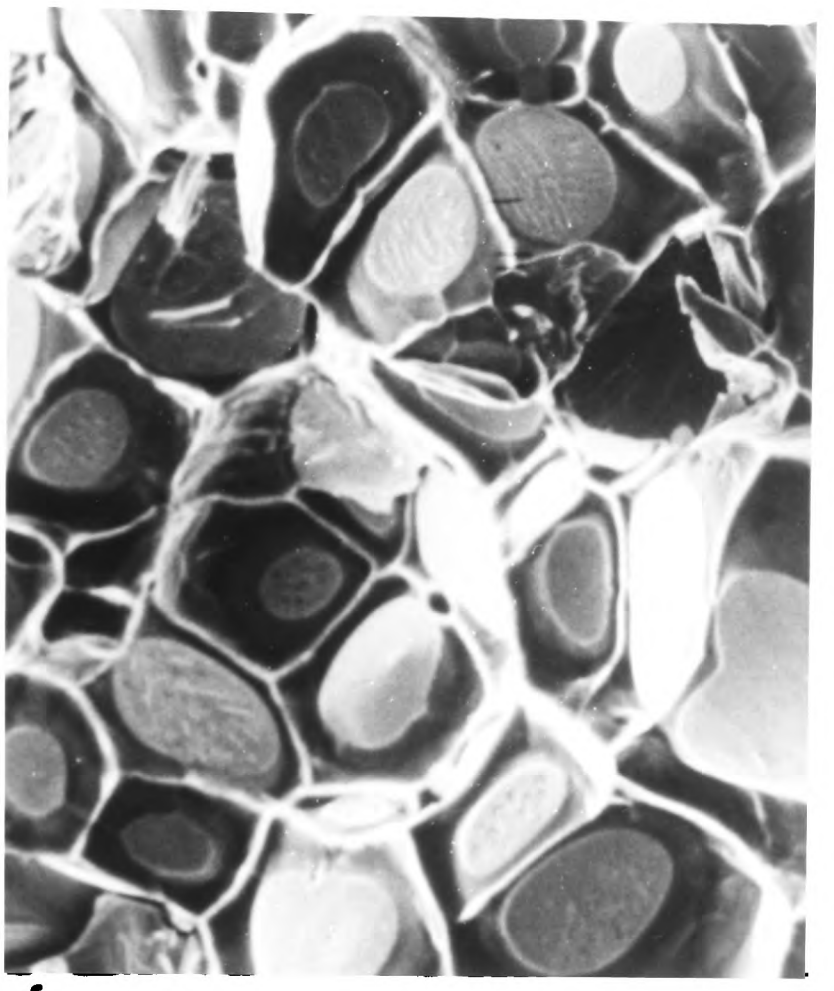

f

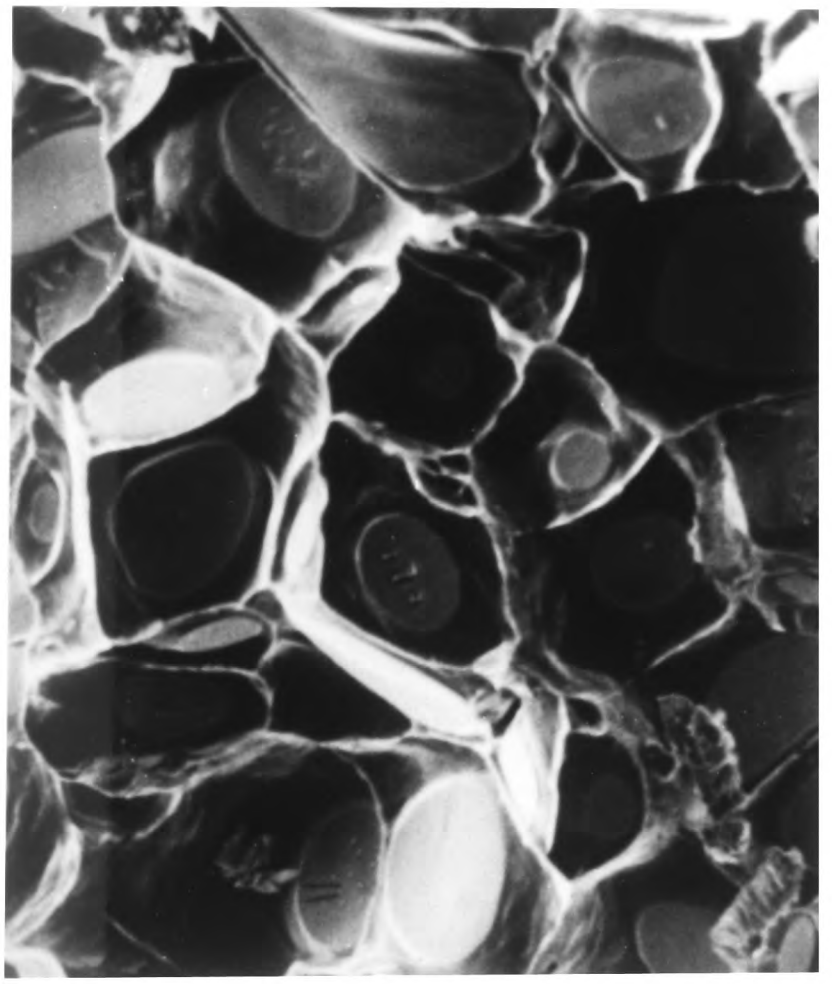

g

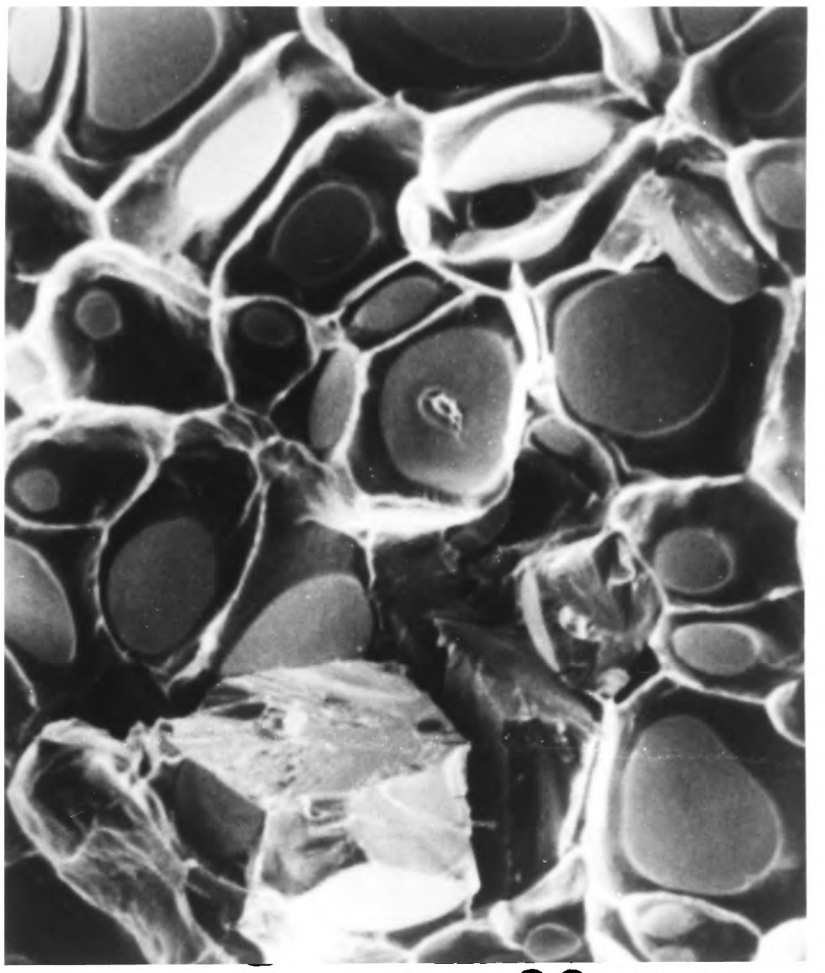

h

20µm

Figure 6.11

SEM fractographs of 90W-7Ni-3Fe heavy alloy (without the commercial post-sintering heat treatment) after different heat treatments.

a) As received (note the significant amount of W-Y separation).

b) 450°C for 100 hours.

c) 600°C for 100 hours.

d) 750°C for 100 hours.

e) 900°C for 100 hours.

f) 1050°C for 100 hours.

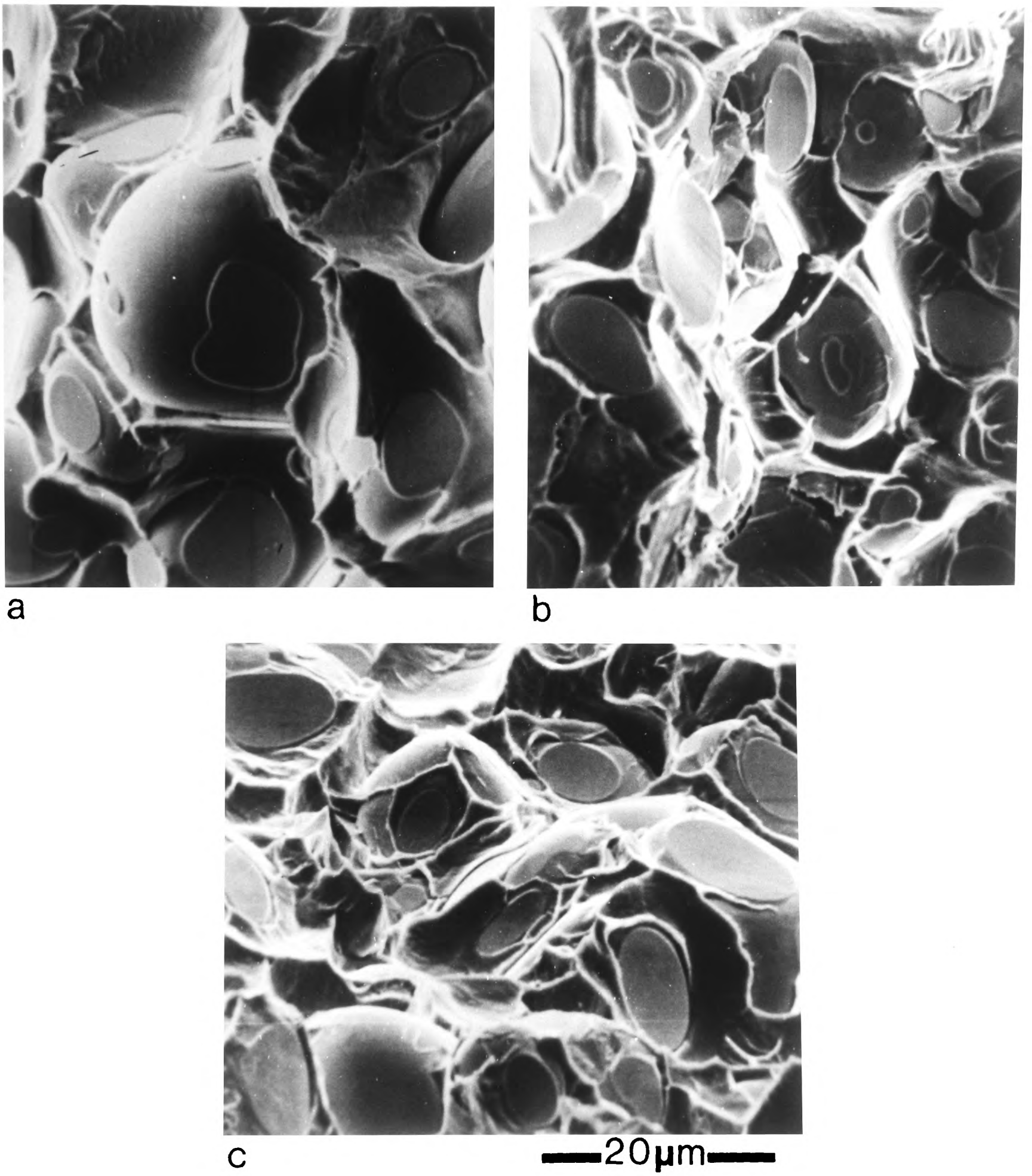
a
b
c
20µm

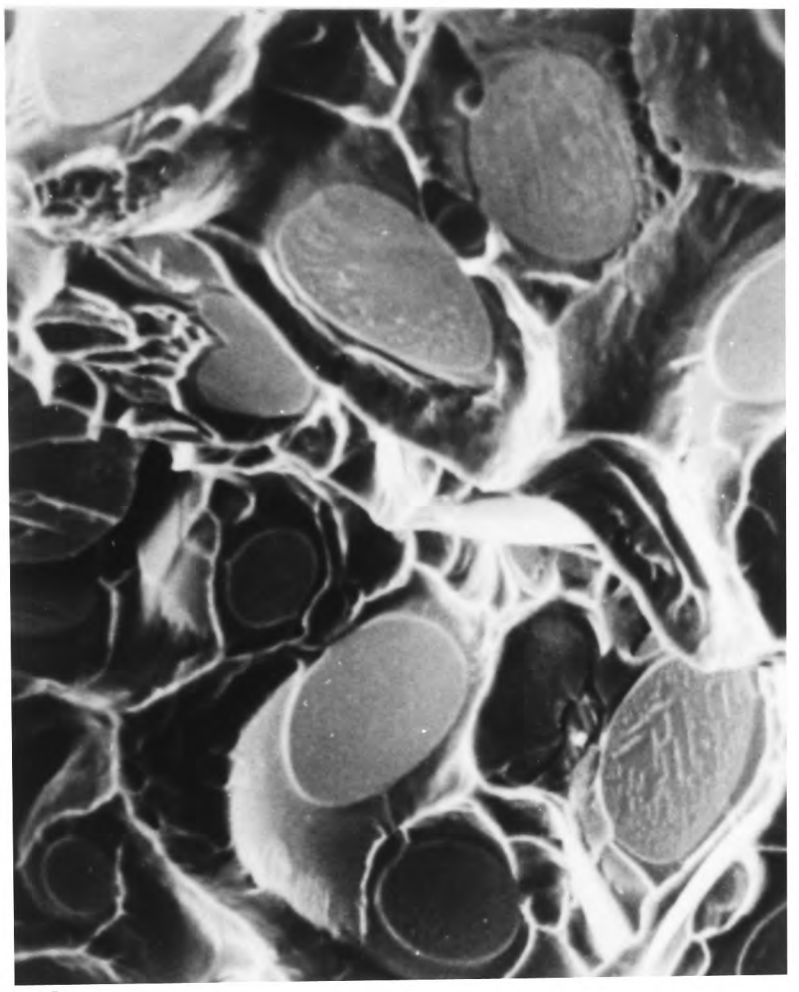

d

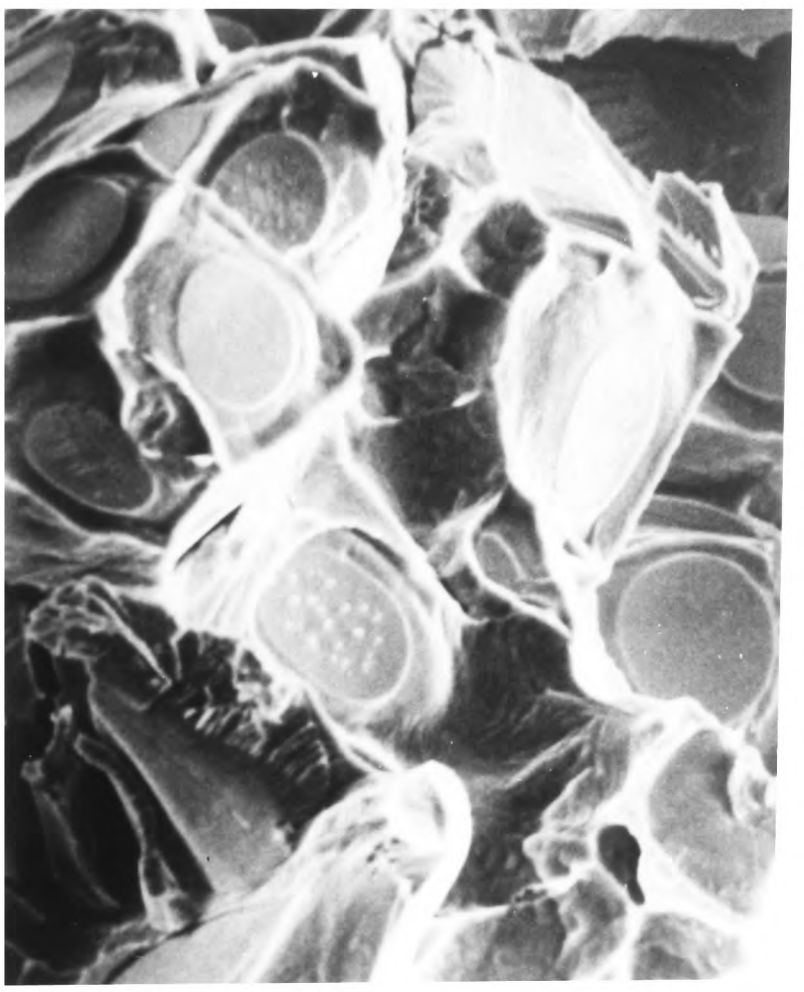

e

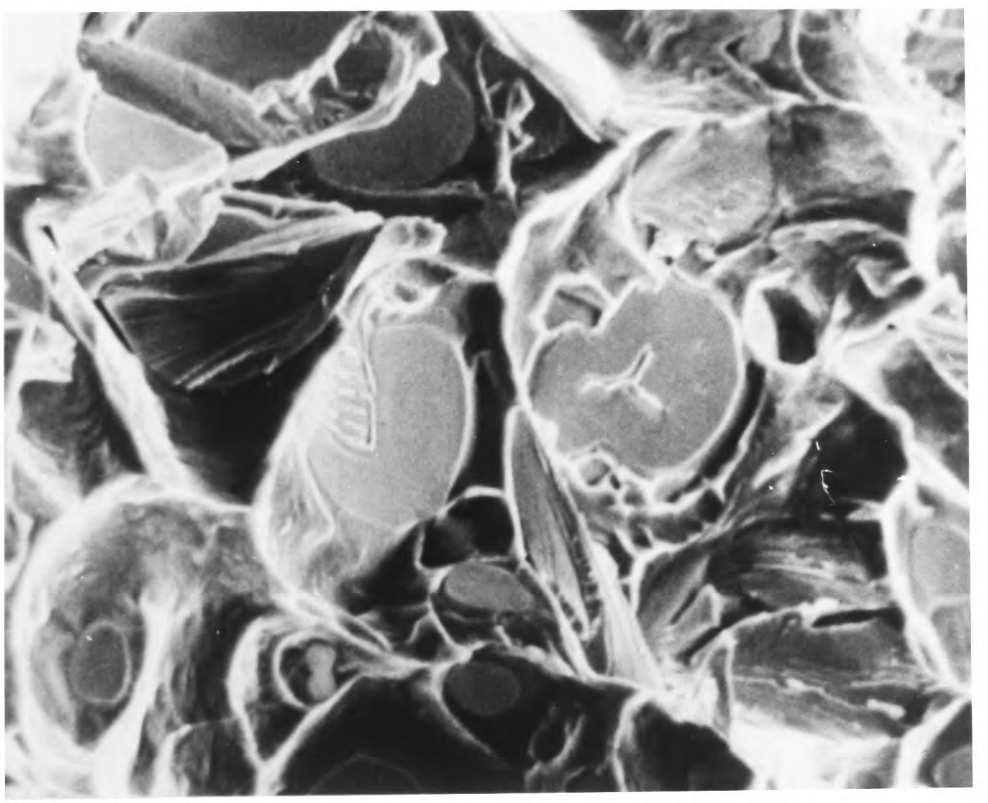

f

20µm

Figure 6.12

Microhardness of the W-phase in 10.1% rolled heavy alloy as a function of aging temperatures (t = 1 hour). Each point represents the average of 10 indentations.

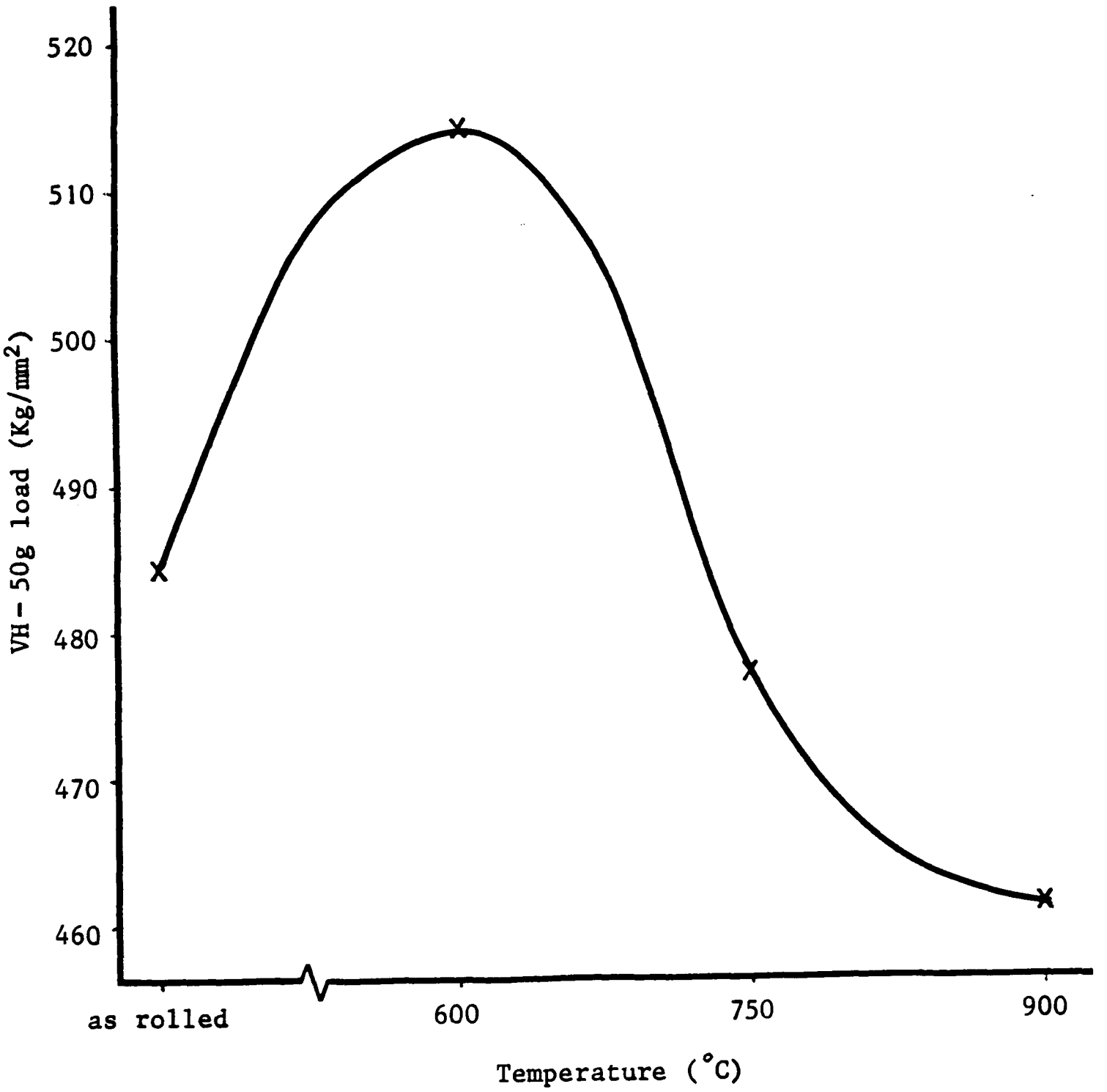

Figure 6.13

Bright field and weak beam micrographs of the W-phase in 10.1% rolled heavy alloy after different heat treatments.

a) As rolled.

b) 600°C for 1 hour (the arrows point to defects interacting with a dislocation).

c) 750°C for 1 hour.

d) 900°C for 1 hour.

a

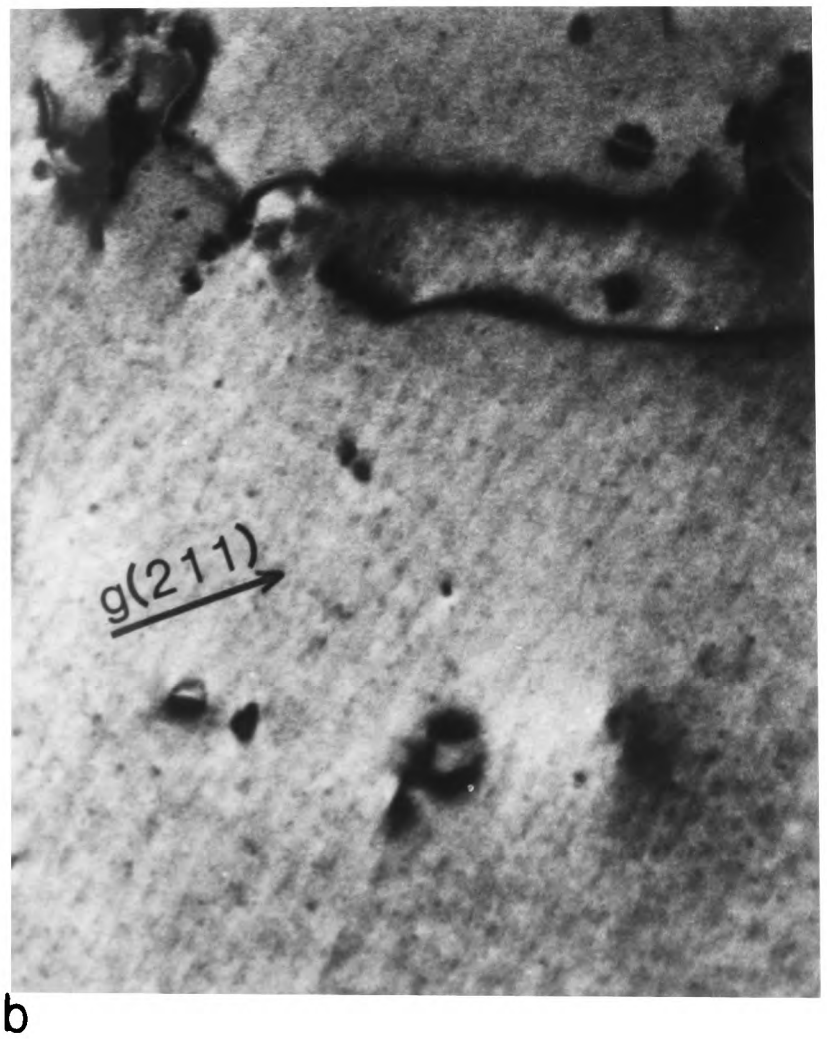

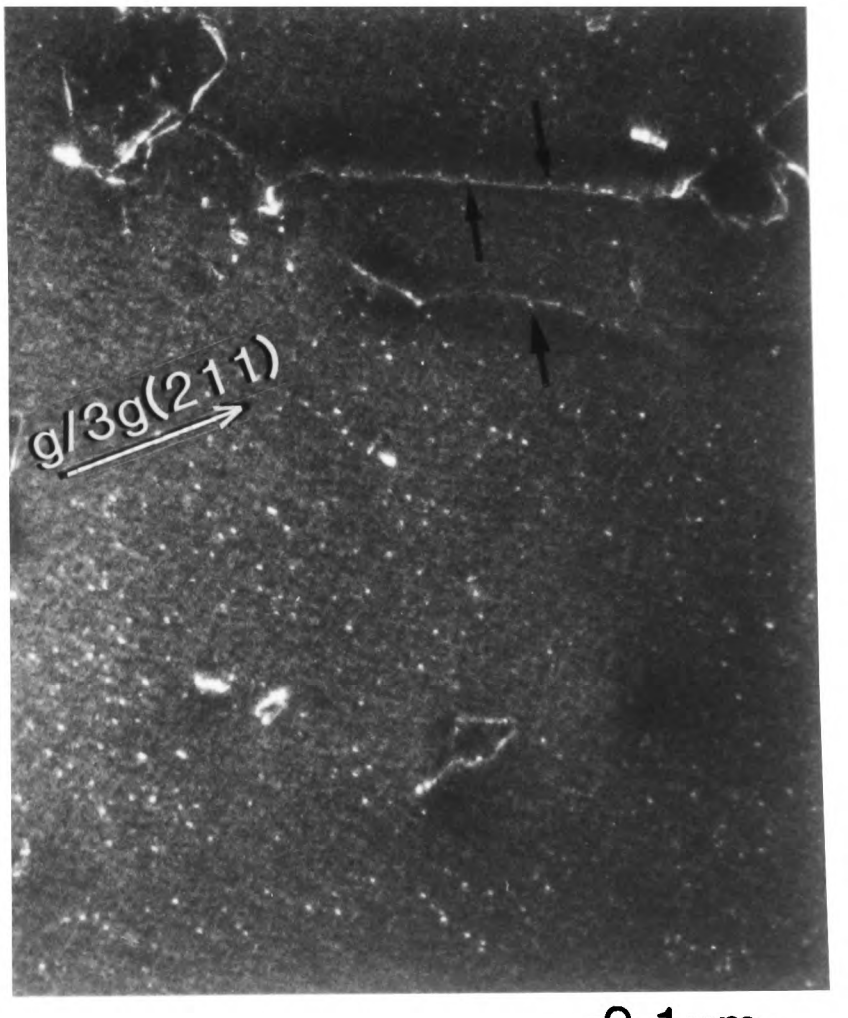

b

▪0.1µm▪

C

d

0.1μm

Figure 6.14

Contrast analysis of defects in the W-phase in material rolled and aged for 1 hour at 750°C($z \simeq [001]$ and $s \simeq 0$).

a) $\underset{\sim}{g}(1\bar{1}0)$, note defects labeled A and B are visible.

b) $\underset{\sim}{g}(200)$, only defects A are visible.

c) $\underset{\sim}{g}(020)$, only defects B are visible.

This is characteristic of $\underset{\sim}{R}_A = K[100]$ and $\underset{\sim}{R}_B = K[010]$.

d) $|\underset{\sim}{g}\cdot\underset{\sim}{R}|$ visibility criteria (zero denotes invisibility).

$\underset{\sim}{g}$ \ $\underset{\sim}{R}$	111	$\bar{1}11$	$1\bar{1}1$	$11\bar{1}$	100	010	001	110	$1\bar{1}0$	011	$01\bar{1}$	101	$10\bar{1}$
110	2	0	0	2	2	2	0	2	0	1	1	1	1
$1\bar{1}0$	0	2	2	0	2	2	0	0	2	1	1	1	1
011	2	2	0	0	0	2	2	1	1	2	0	1	1
$01\bar{1}$	0	0	2	2	0	2	2	1	1	0	2	1	1
101	2	0	2	0	2	0	2	1	1	1	1	2	0
$10\bar{1}$	0	2	0	2	2	0	2	1	1	1	1	0	2
200	2	2	2	2	2	0	0	2	2	0	0	2	2
020	2	2	2	2	0	2	0	2	2	2	2	0	0
002	2	2	2	2	0	0	2	0	0	2	2	2	2

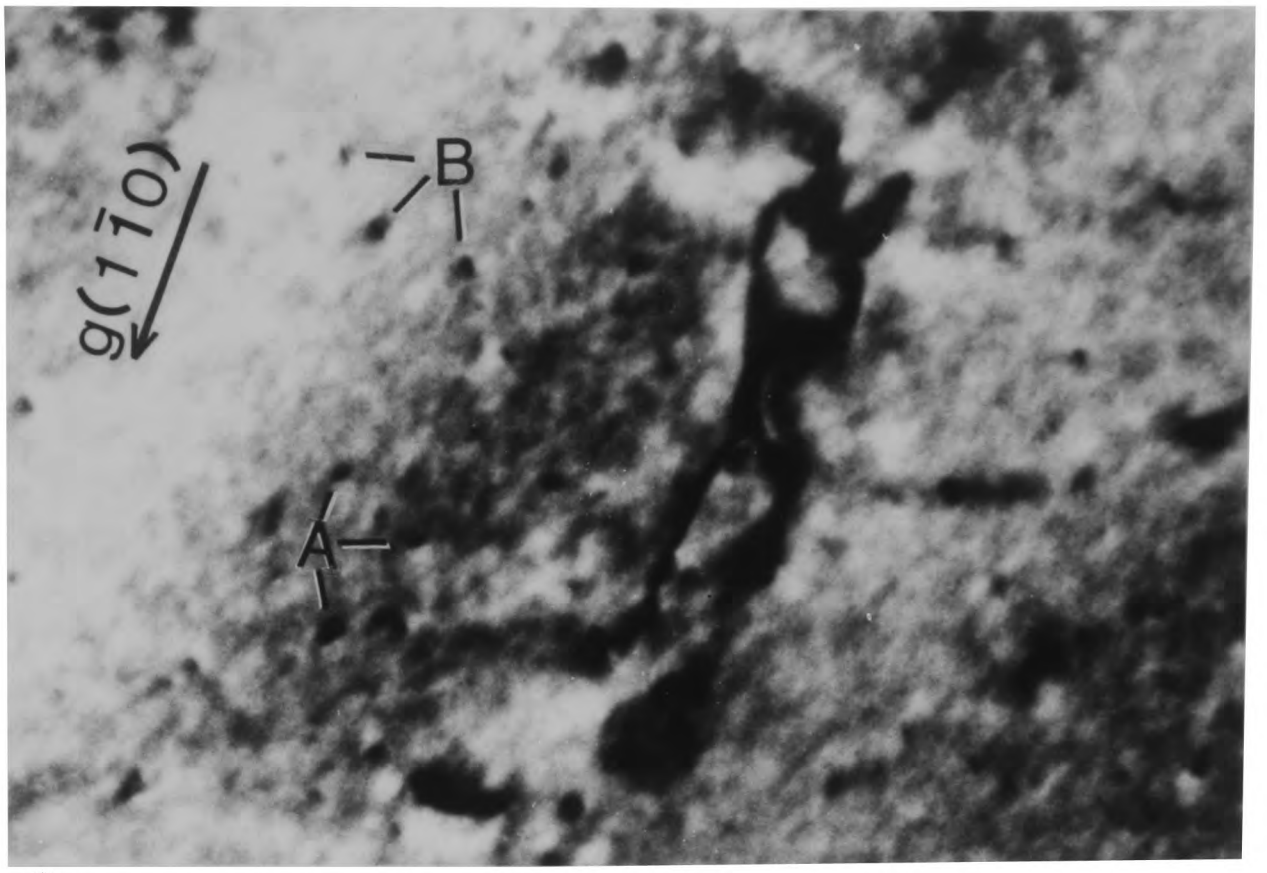

a

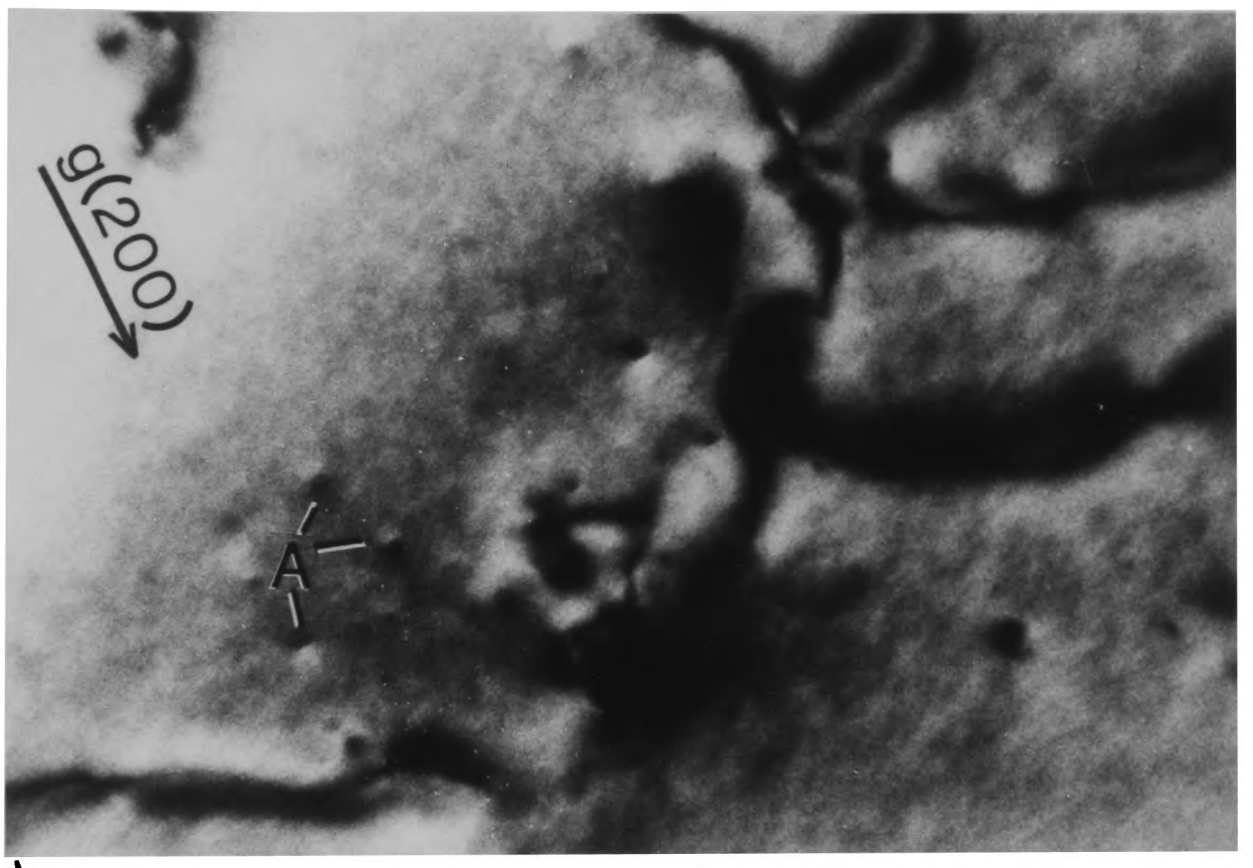

b

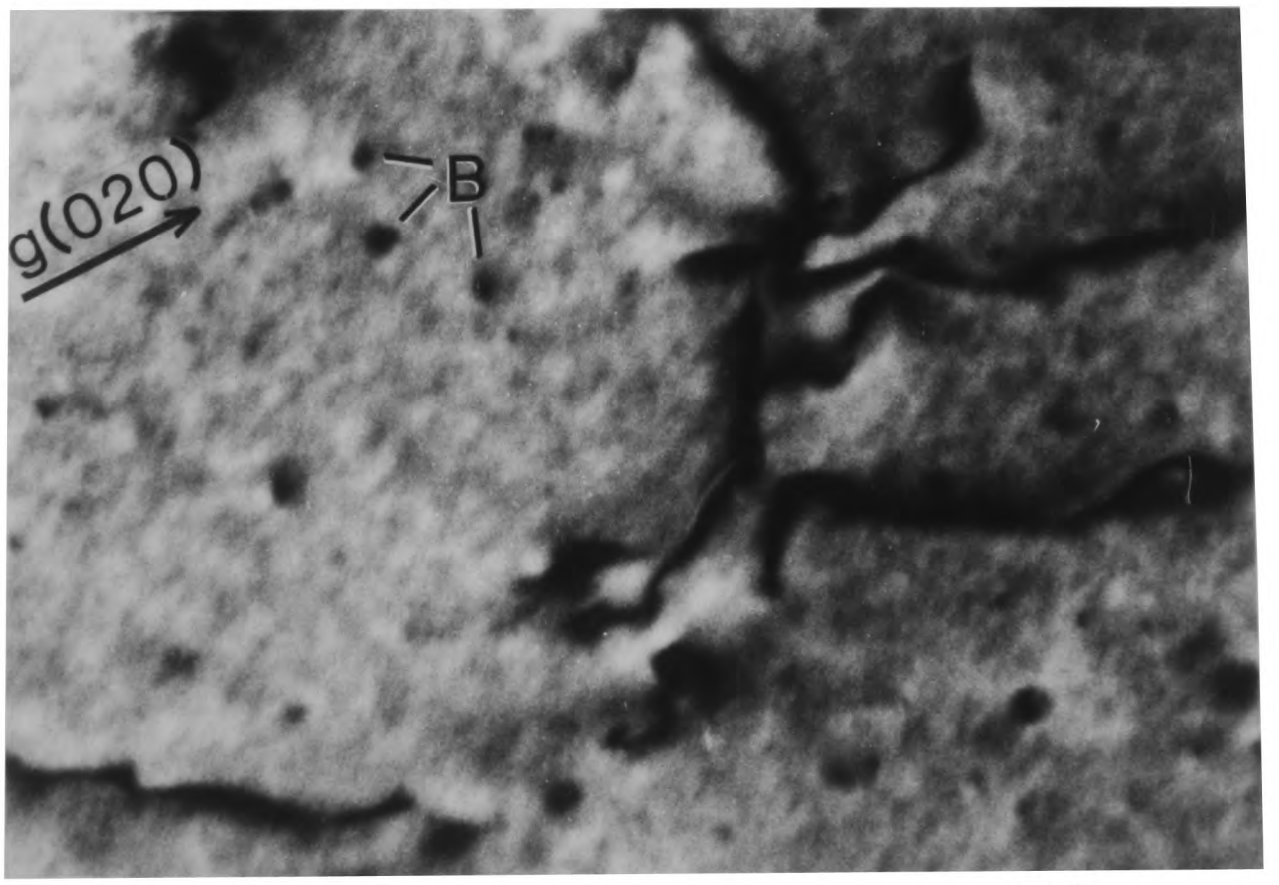

c

▪50nm▪

Figure 6.15

Contrast analysis of defects in the W-phase in material rolled and aged for 1 hour at 750°C ($z \simeq [011]$ and $s \simeq 0$).

a) $\underset{\sim}{g}(0\bar{1}1)$

b) $\underset{\sim}{g}(200)$

Individual defects are visible in either micrograph but not in both. This is consistent with the defects having a displacement vector, $\underset{\sim}{R}$ = K<100>(see $|\underset{\sim}{g}\cdot\underset{\sim}{R}|$ chart at Fig. 6.14).

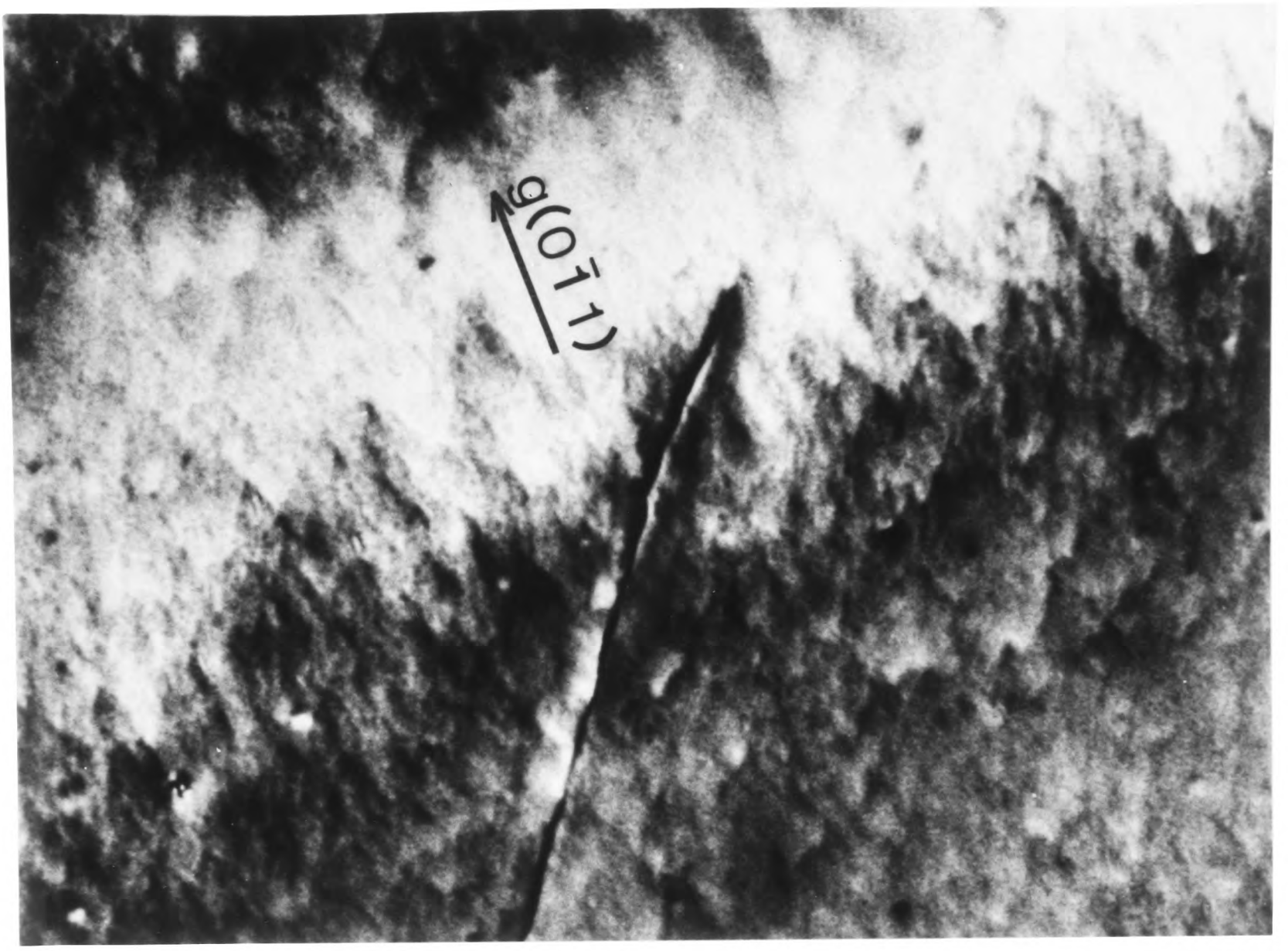

a

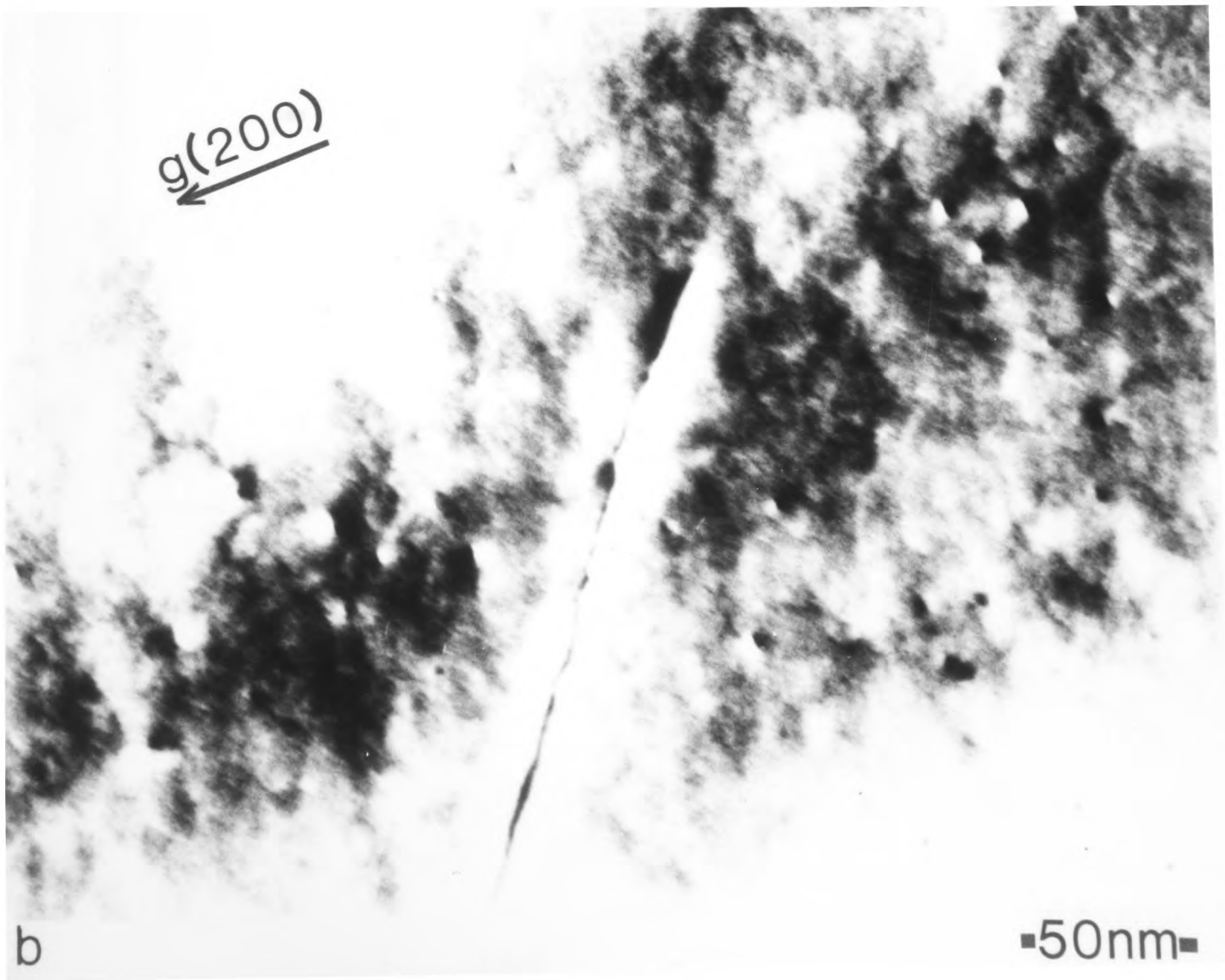

Figure 6.16

Microhardness of the W-phase in undeformed heavy alloy as a function of aging temperature (t = 100 hours). Each point represents the average of 10 indentations (no curve is fitted).

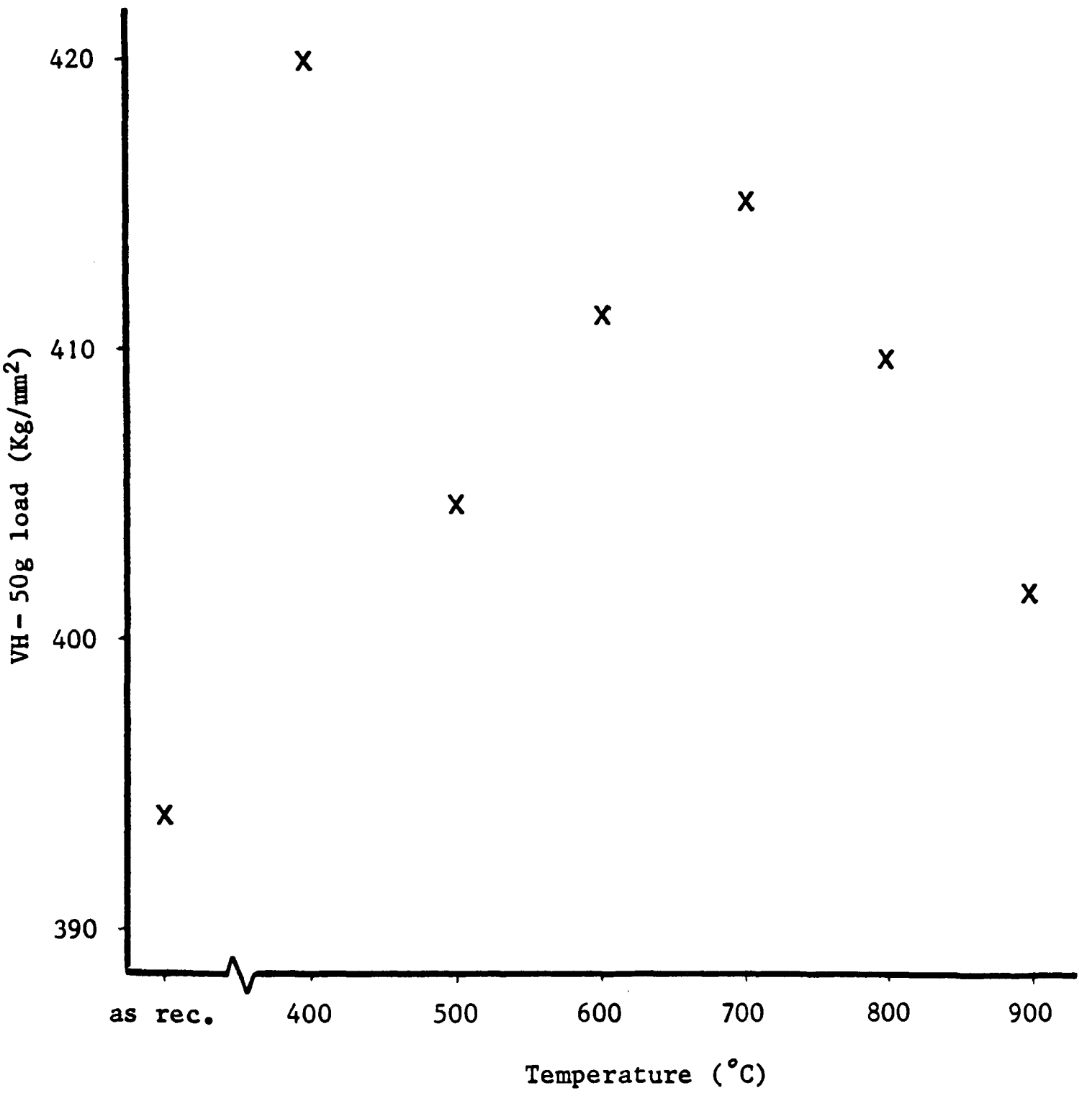

Figure 6.17

Yield and ultimate tensile strength of the heavy alloy as a function of aging temperature (t = 100 hours).

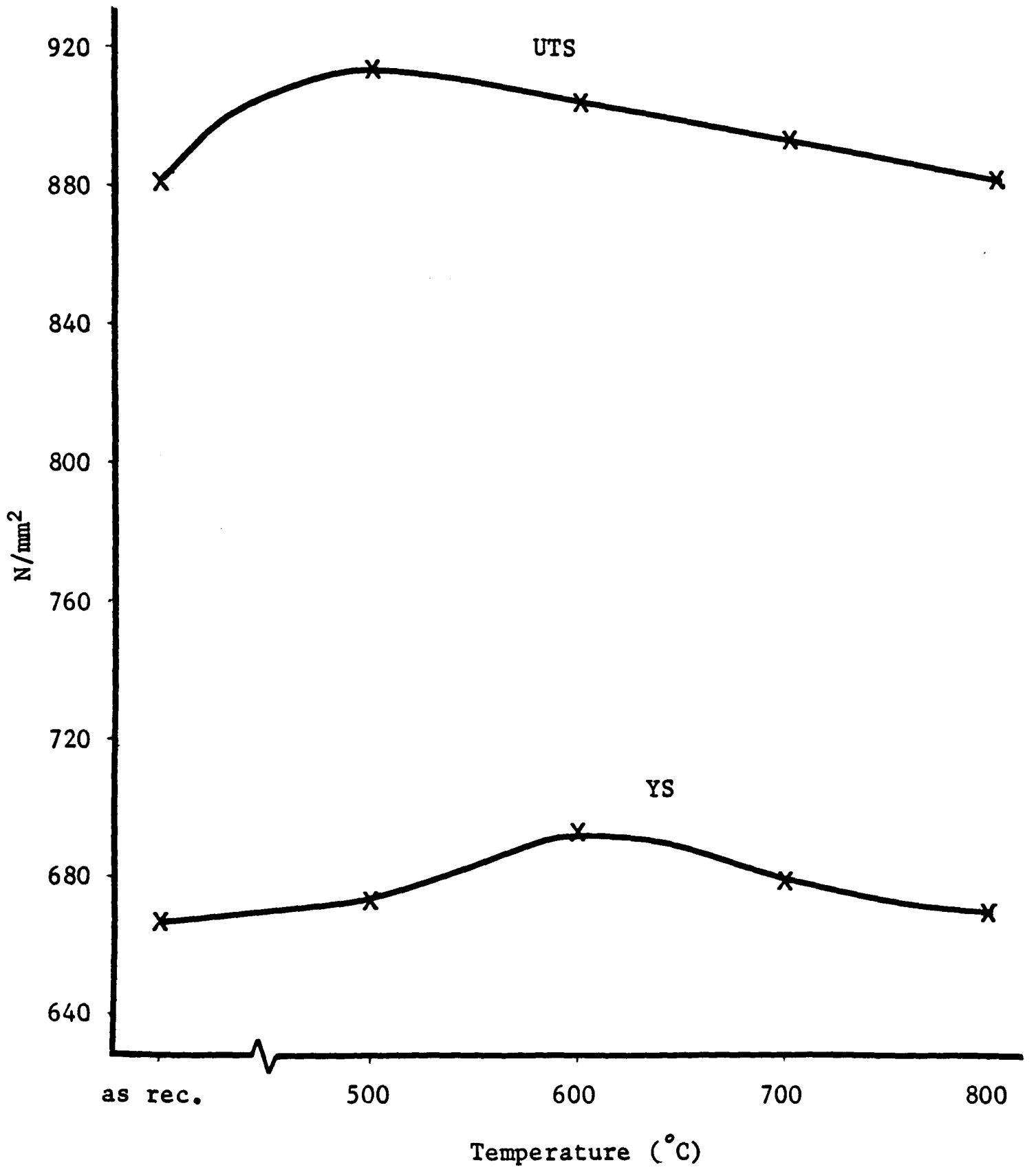

Figure 6.18

Contrast analysis of defects in the W-phase in undeformed material aged at 700°C for 100 hours ($z \simeq [001]$ and $s \simeq 0$). The area shown is at the edge of the foil.

a) $\underset{\sim}{g}(110)$ showing two defect variants.

b) $\underset{\sim}{g}(020)$ showing only one defect variant.

c) $\underset{\sim}{g}(200)$ showing the other defect variant.

Again, this is consistent with $\underset{\sim}{R} = K\langle 100\rangle$.

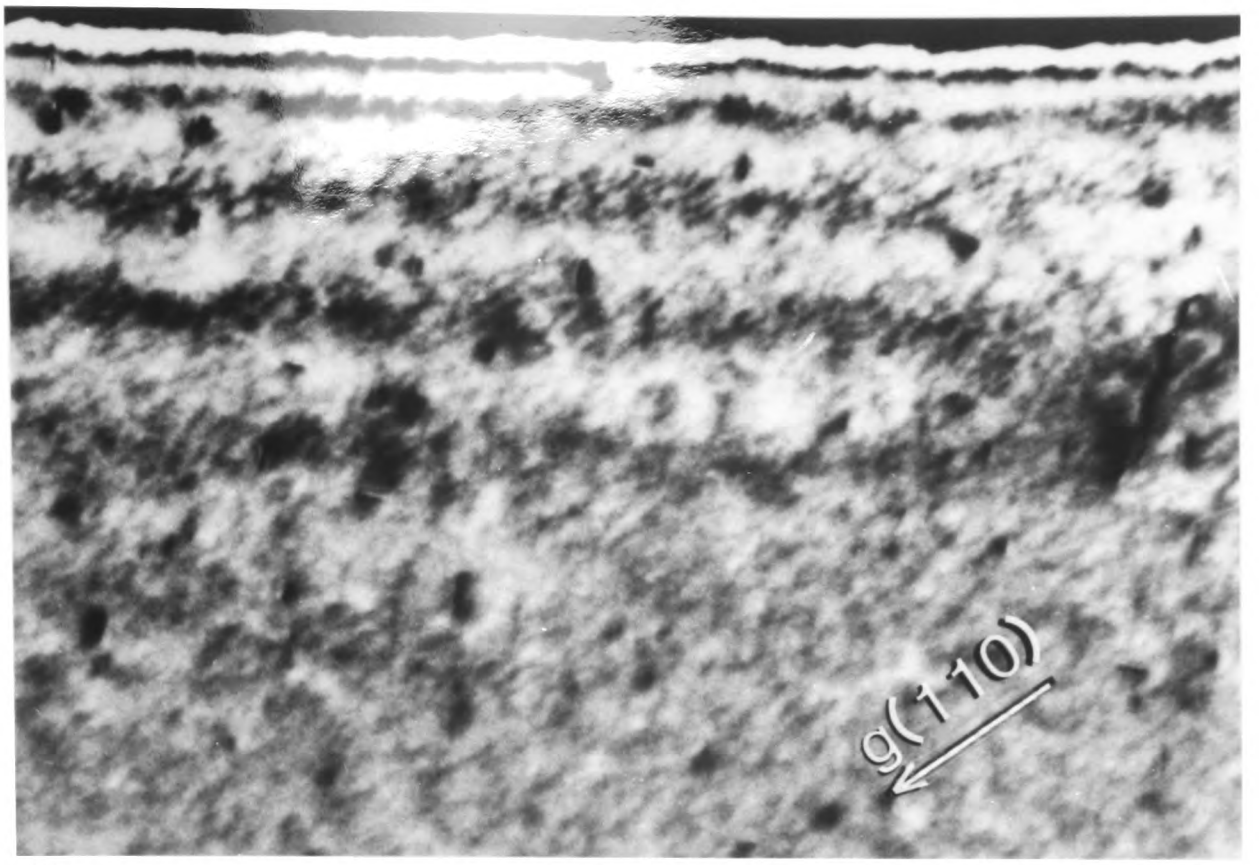

a

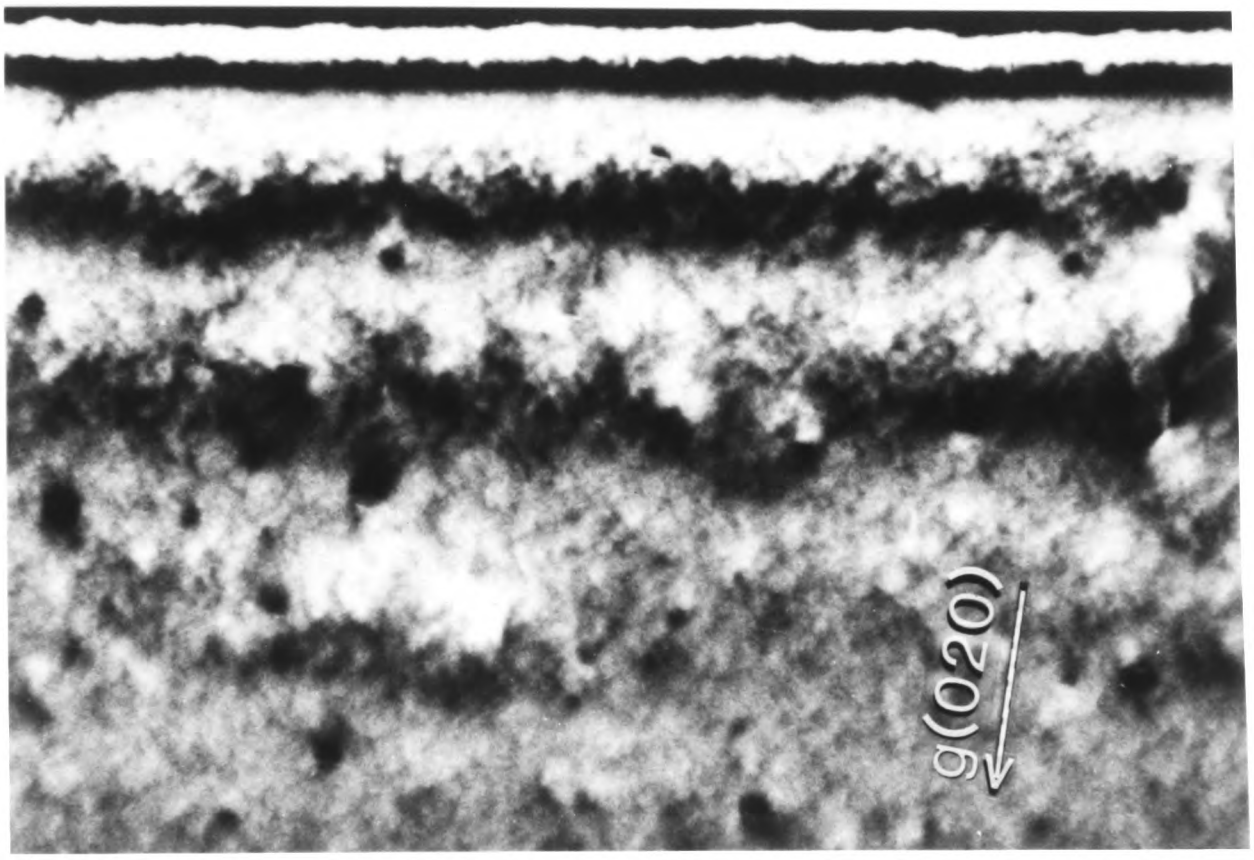

b

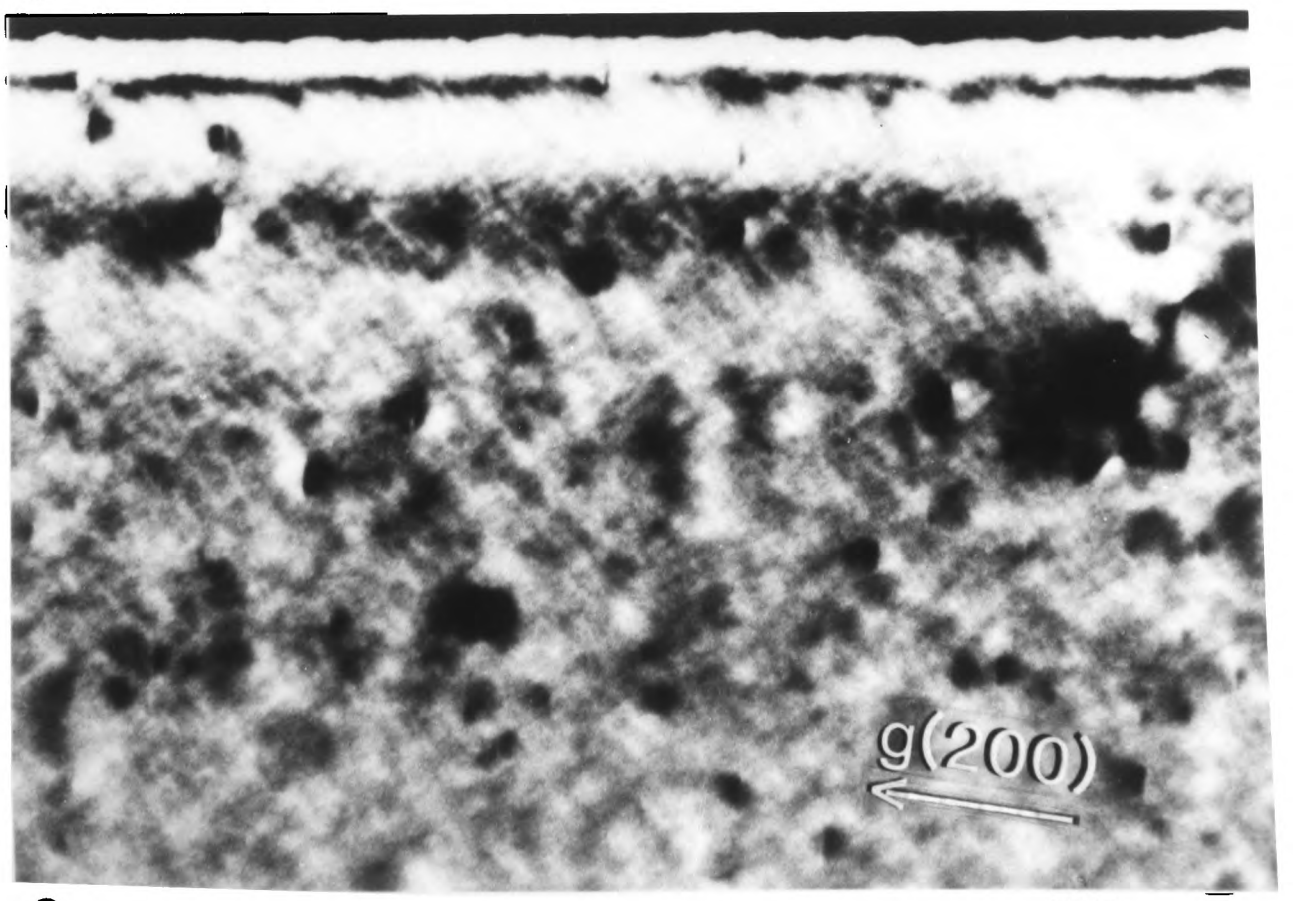

c

50nm

Figure 6.19

The two possible relationships $\underset{\sim}{\ell}$ can have with $\underset{\sim}{g}(200)$ for a $\underset{\sim}{R} = K[100]$ defect.

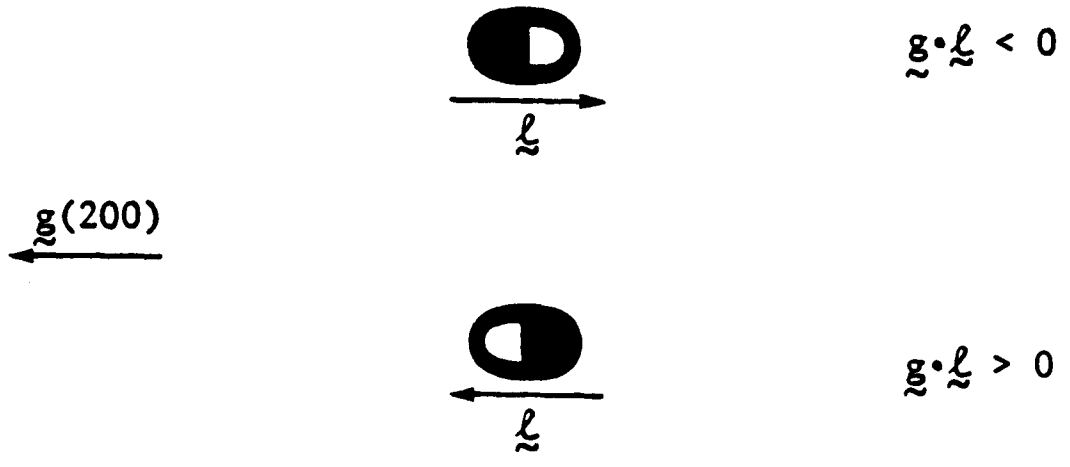

Figure 6.20

Schematic diagram illustrating the reversal of black/white image contrast as a function of depth in the foil for small defects. Note the definition of the layers L_1, L_2, and L_3 from the top of the foil (after Rühle[83,84] and Edington[53]).

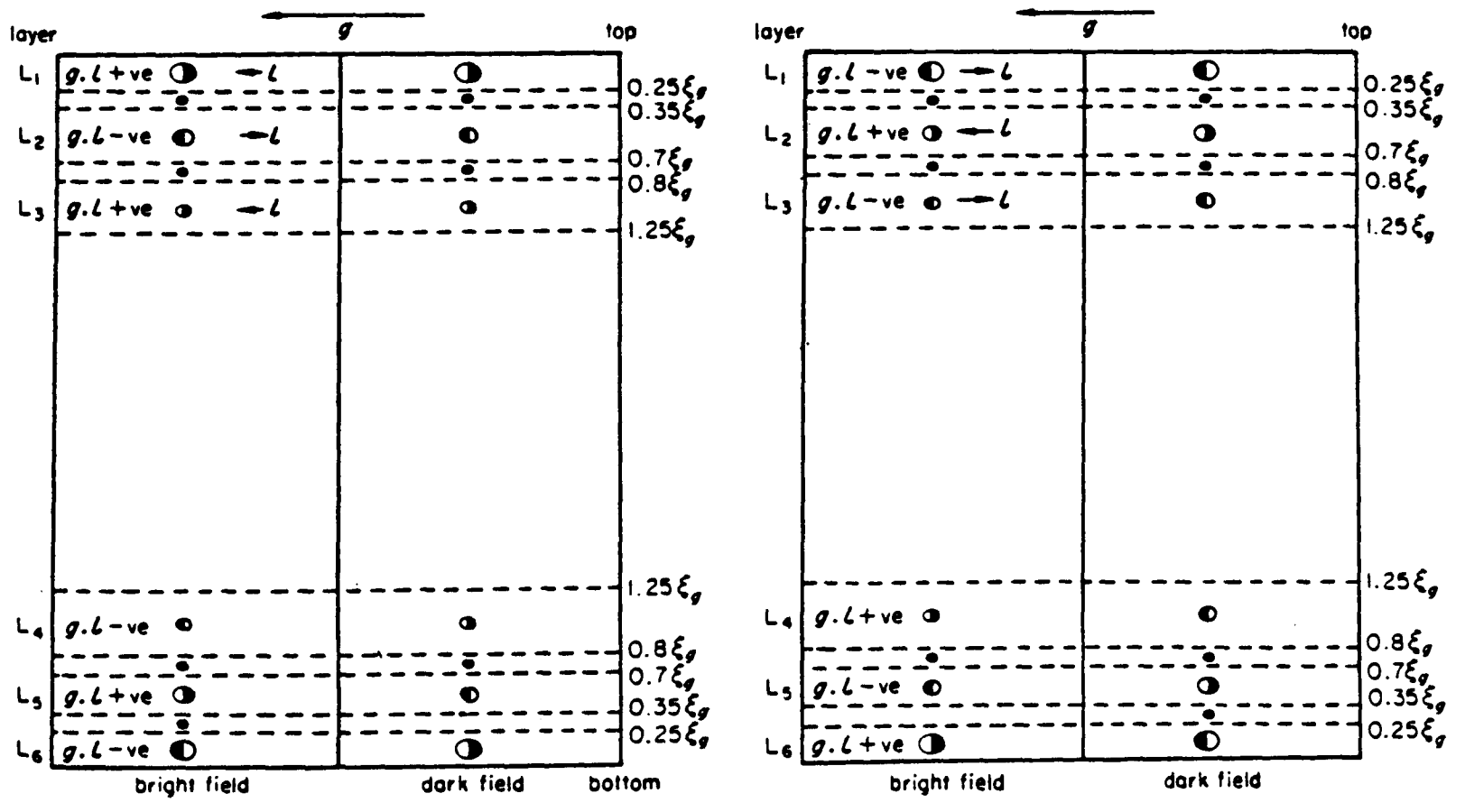

Figure 6.21

a) Dark field $\underset{\sim}{g}(200)$ stereo pair showing black/white contrast reversal with defect depth in the foil. Note the labeled defects in layers L_1, L_2, and L_3. The small (~ 15Å) dark spots are the gold islands that define the top of the foil.

b) Unit triangle showing the tilt between the two micrographs.

c) From the same area as in a) but at higher magnification (note the end of the dislocation in the lower section of the micrographs). [$s \simeq 0$]

tilt axis

a

b)

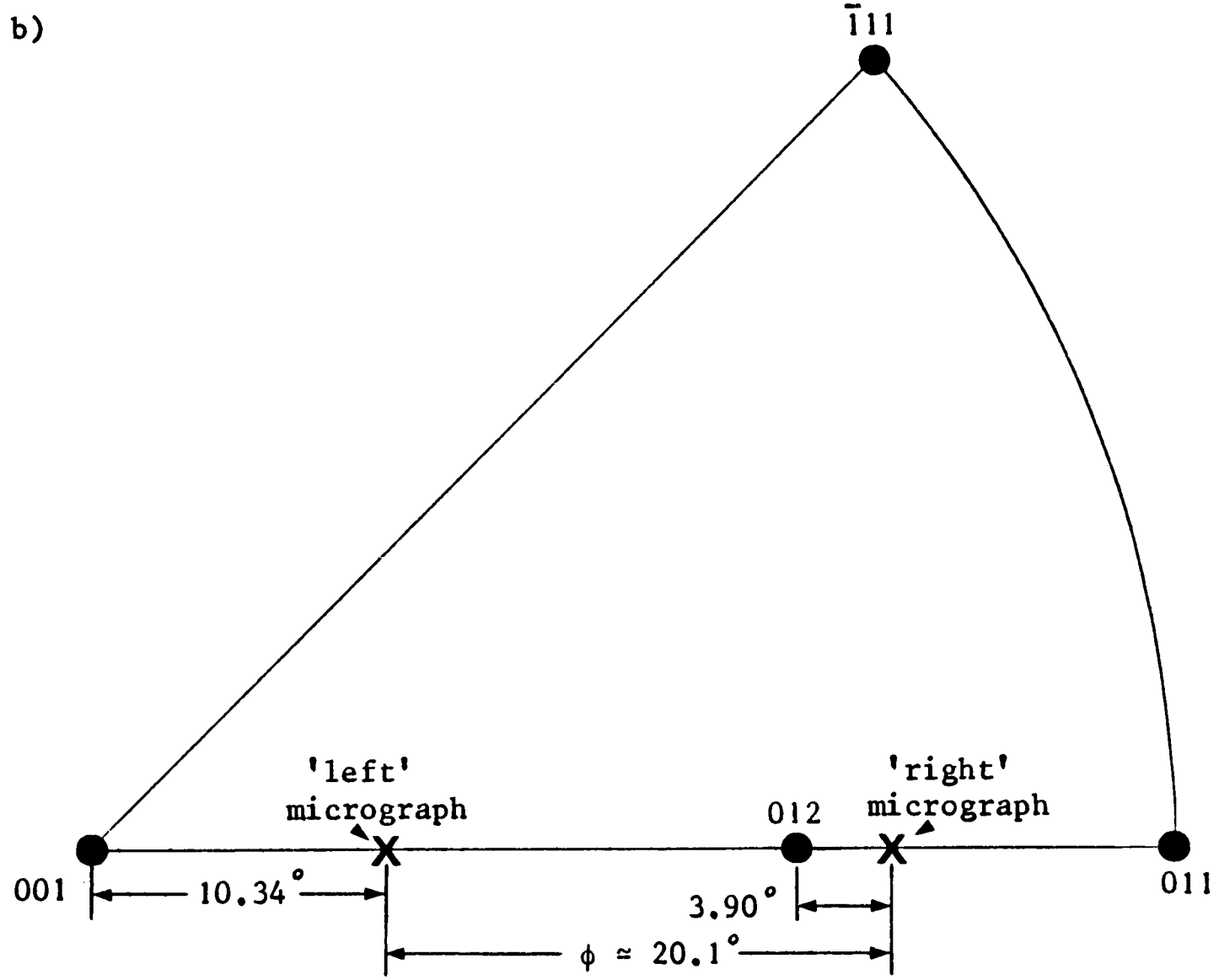
$\bar{1}11$
'left'
micrograph
012
'right'
micrograph
001
10.34°
3.90°
011
$\phi \simeq 20.1°$

tilt axis

111

g(200)

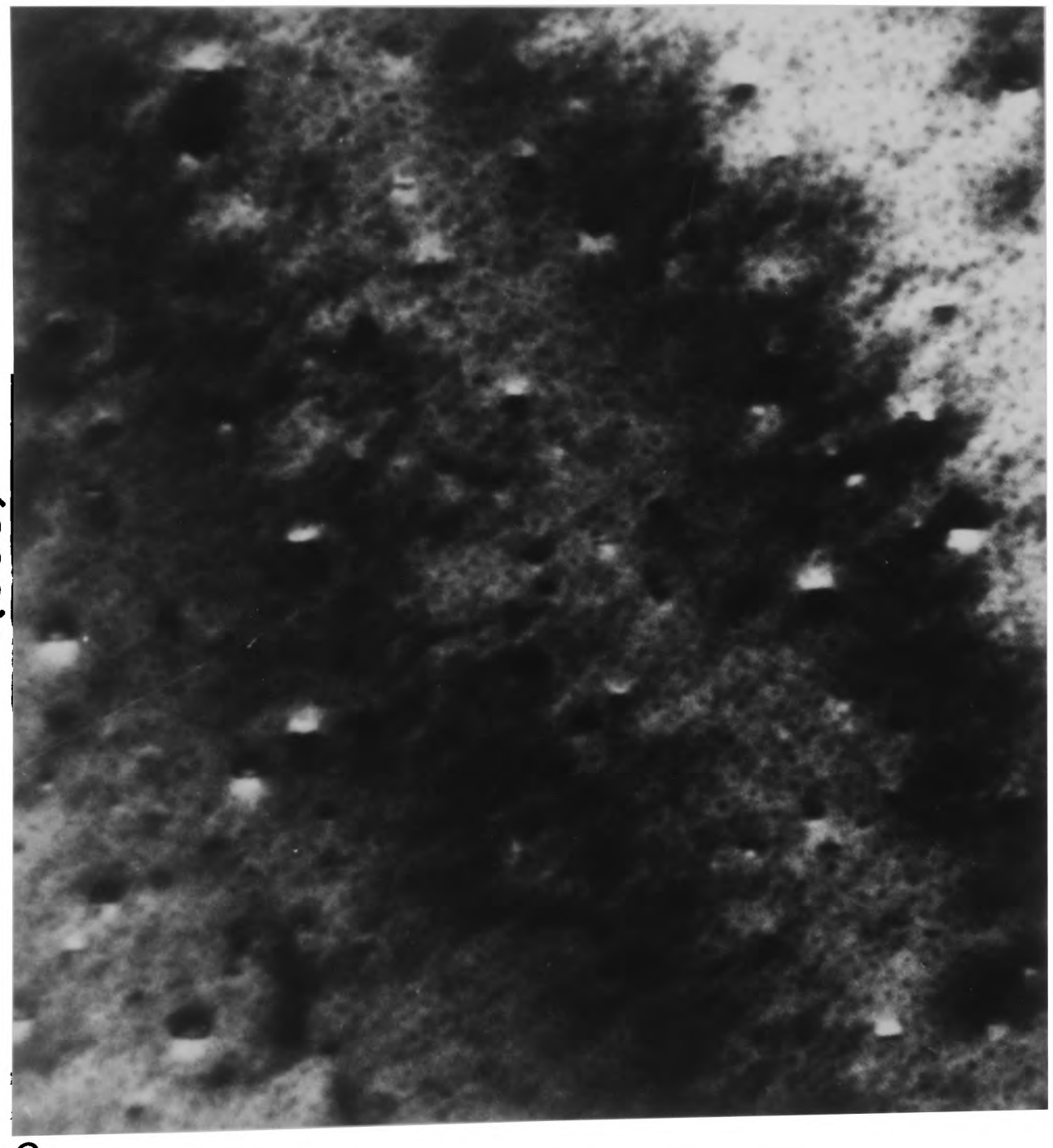

c

50nm

Figure 6.22

Compiled results from the stereo microscopy. The strain field of the defects is tensile in nature.

Measured Depth Δh(Å)[$\pm$15Å]	Sign of $\underset{\sim}{g}\cdot\underset{\sim}{\ell}$	Layer†
60	+	L_1
55	+	
47	+	
~ 10	+	
52	+	
54	+	
42	+	
54	+	
59	+	
24	+	
49	+	
60 *	-	
87	-	L_2
129	-	
148	-	
118	-	
91	-	
110	-	
109	-	
91	-	
111	-	
129	-	
157	-	
103	-	
156	-	
101	-	
94	-	
105	-	
102	-	
102	-	
101	-	
89	-	
96	-	
156	-	
159 *	+	
259	+	L_3
205	+	
207	+	

† For $\underset{\sim}{g}$(200) in tungsten,

$L_1 \simeq 0 - 0.25\xi_{200} \simeq 0 - 55$Å

$L_2 \simeq 0.35\text{-}0.7\xi_{200} \simeq 78\text{-}155$Å

$L_3 \simeq 0.8\text{-}1.25\xi_{200} \simeq 178\text{-}278$Å

* These defects did not have contrast consistent with a tensile strain field. However, both defects were found to be in between layers and therefore a small error in measurement could explain this contradictory result.

Figure 6.23

Typical EDX spectra from heavy alloy aged at 700°C for 100 hours.

a) From small precipitate in the W-phase

b) From surrounding W.

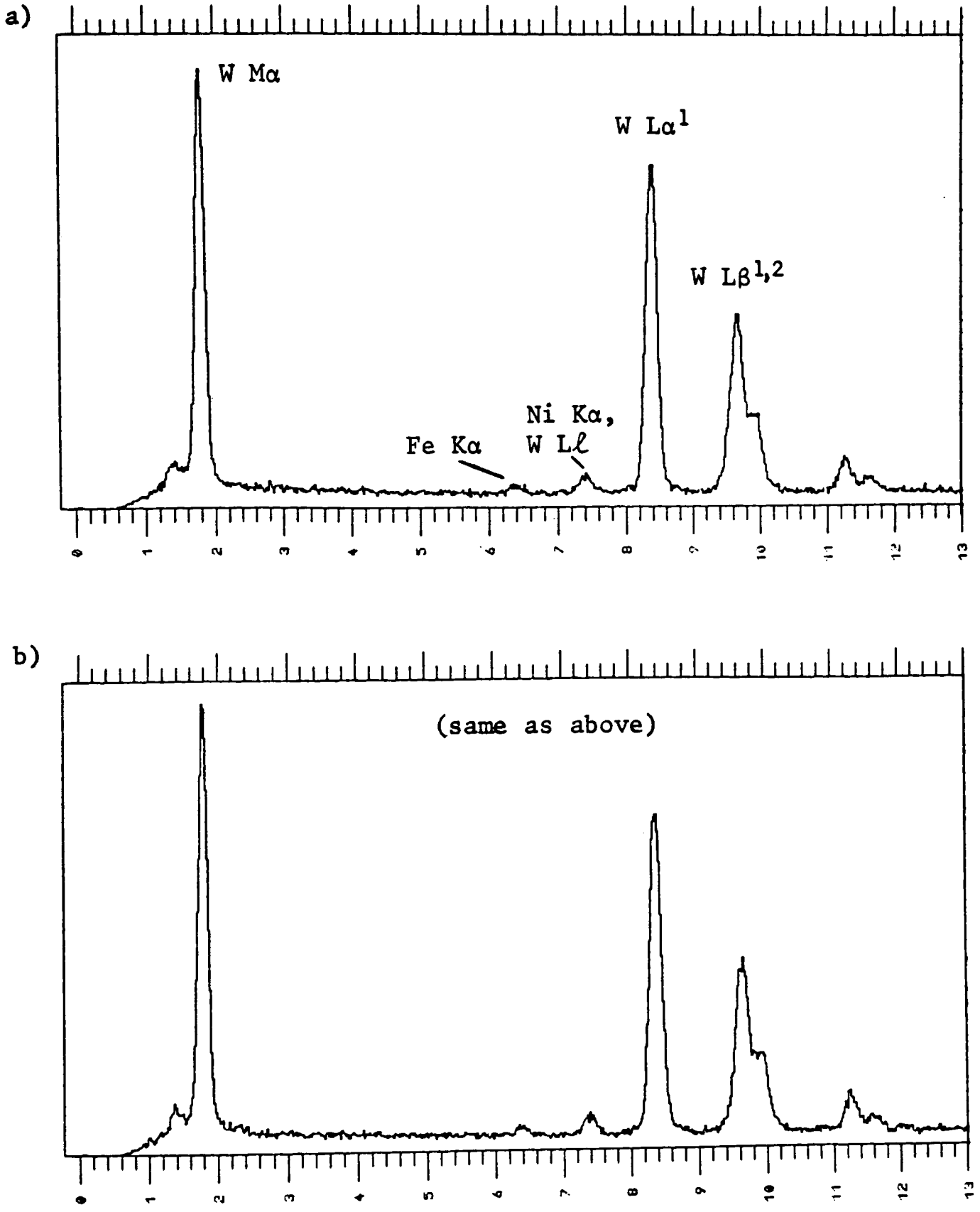

Figure 6.24

EDX ratio results (for iron only). Using the ratios

$$W{:}Fe(1) = \frac{\text{net integral } (W\ L\alpha^1)}{\text{net integral } (Fe\ K\alpha)}$$

$$W{:}Fe(2) = \frac{\text{net integral } (W\ L\beta^1 + W\ L\beta^2)}{\text{net integral } (Fe\ K\alpha)}$$

and averaging the results of a number of measurements,

	Precipitate (23)	Surrounding W(16)
W:Fe(1)	66.8 ± 13.4	65.8 ± 11.5
W:Fe(2)	58.6 ± 11.9	57.8 ± 10.6

there is essentially no difference.

Figure 6.25

TEM of 'precipitate' in W-phase in heavy alloy aged at 900°C for 100 hours.

a) Bright field

b) Dark field using 'precipitate' reflections

c) Selected area diffraction pattern, z_W=[011]. 'Precipitate' is oriented between zones (dashed lines).

d) Compiled d-spacings as measured from many SAD patterns.

d(Å)
5.87
4.68
4.62
4.56
4.16
4.04
3.99
3.84
3.61
2.77
2.64
2.41
2.34
2.16
1.78
1.72
1.54
1.48
1.39
1.32
1.23

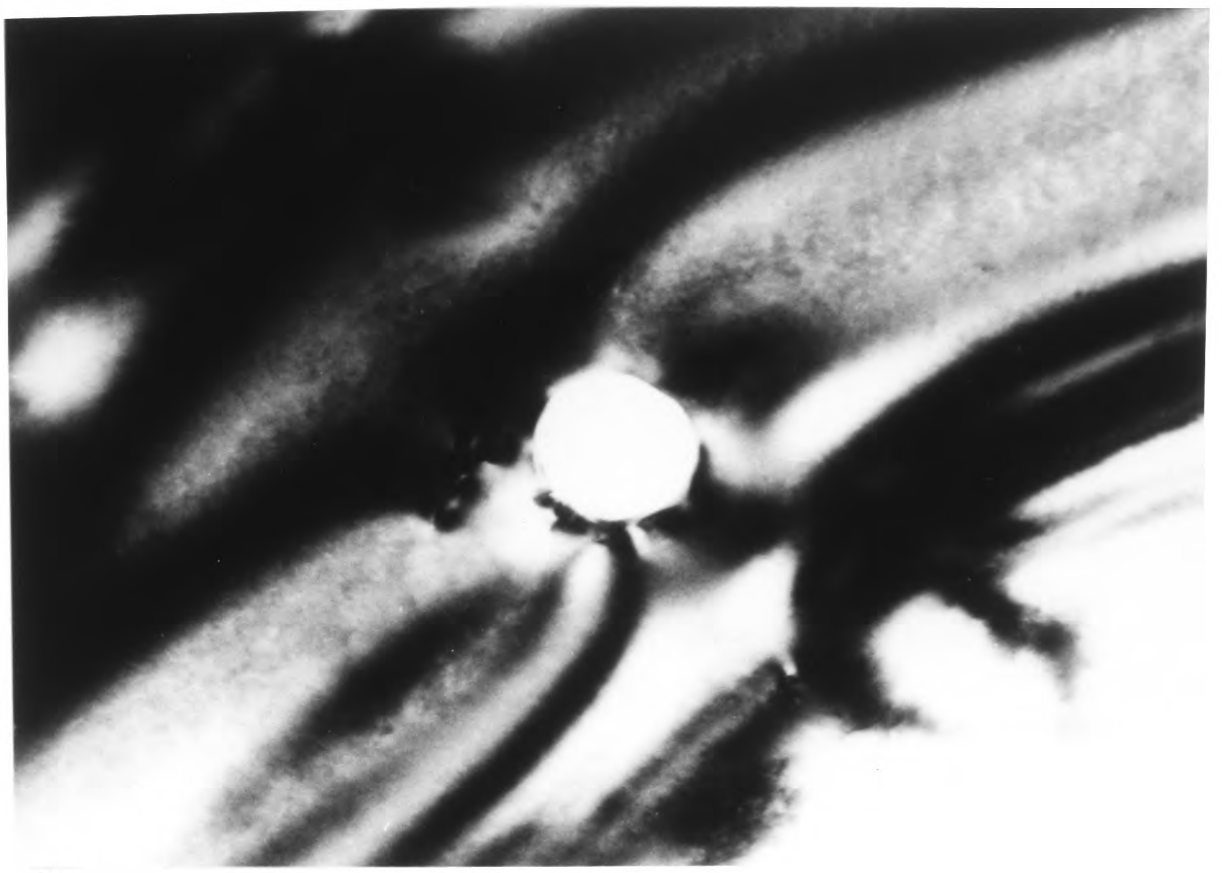

a

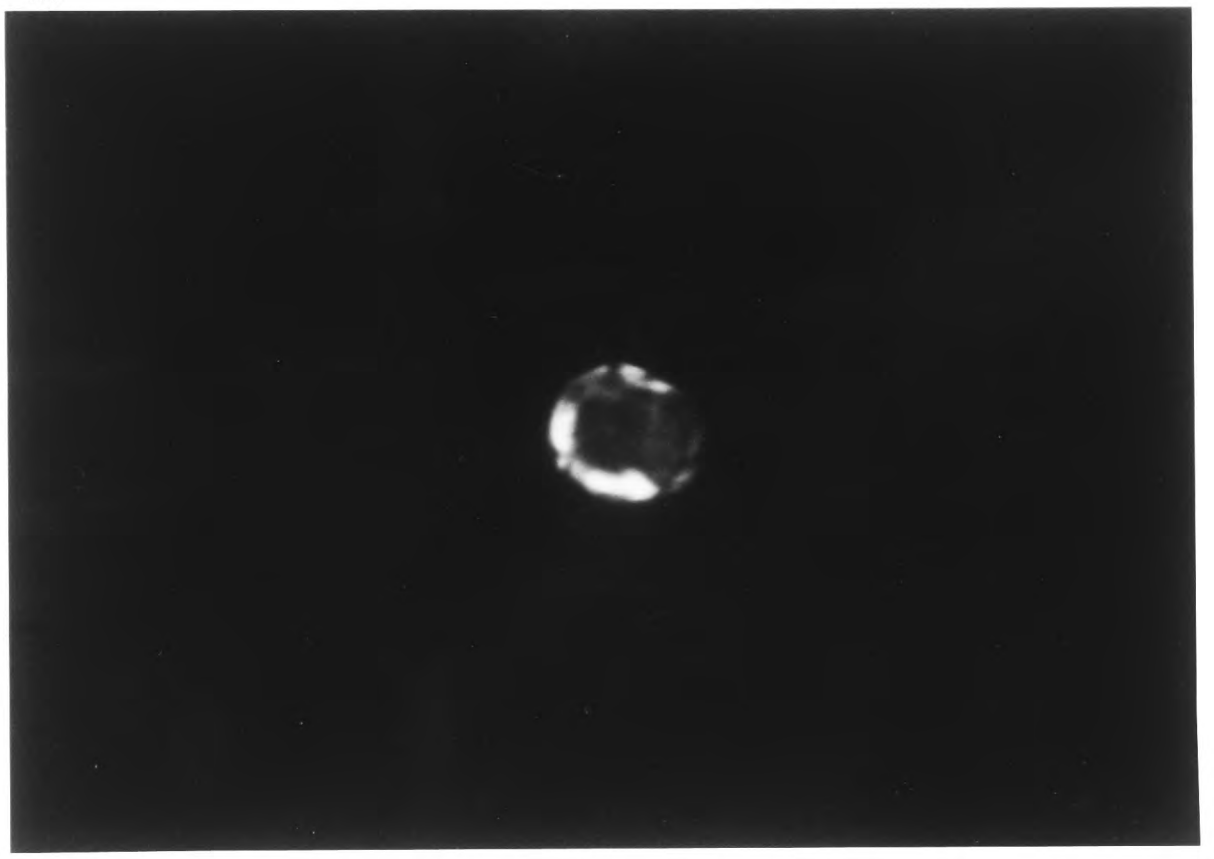

b

0.3µm

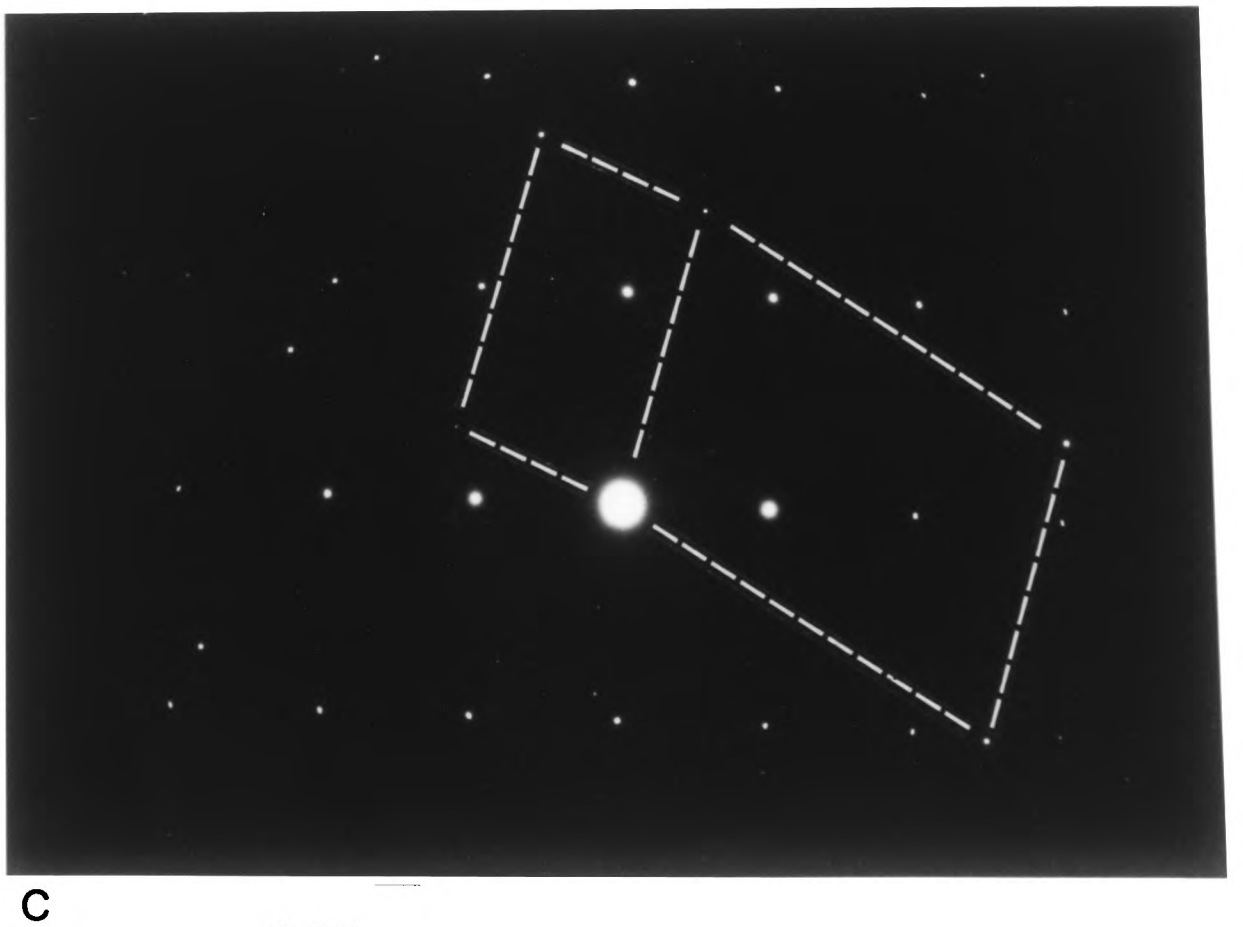

c

Figure 6.26

EDX spectra from heavy alloy aged at 900°C for 100 hours.

a) From 'precipitate' in the W-phase.

b) From surrounding W.

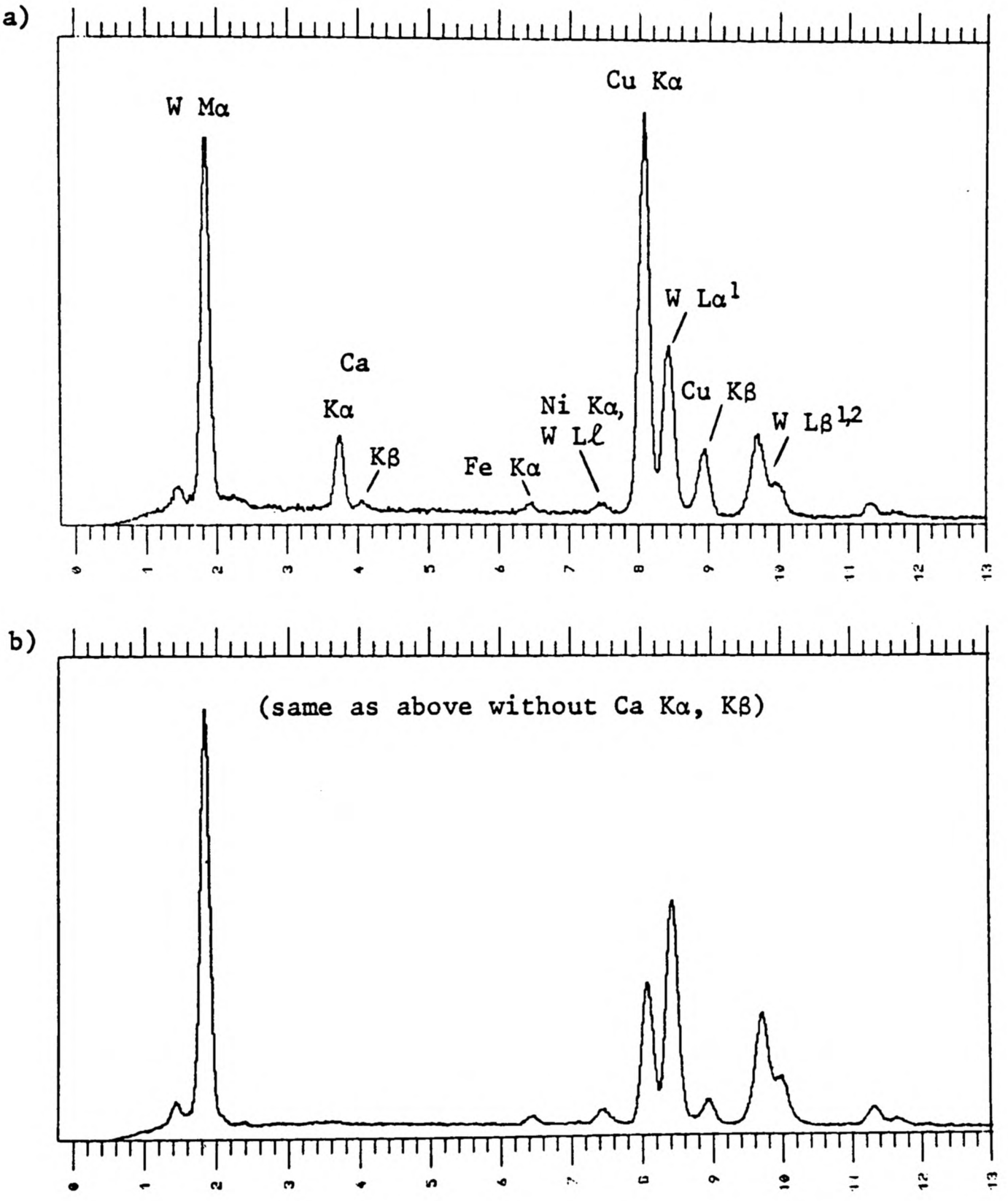

Figure 6.27

Maximum observed precipitation in the W-phase of the heavy alloy after different heat treatments ($\underset{\sim}{g}(200)$ and $s \simeq 0$).

a) 500°C for 100 hours.

b) 700°C for 100 hours.

c) 800°C for 100 hours.

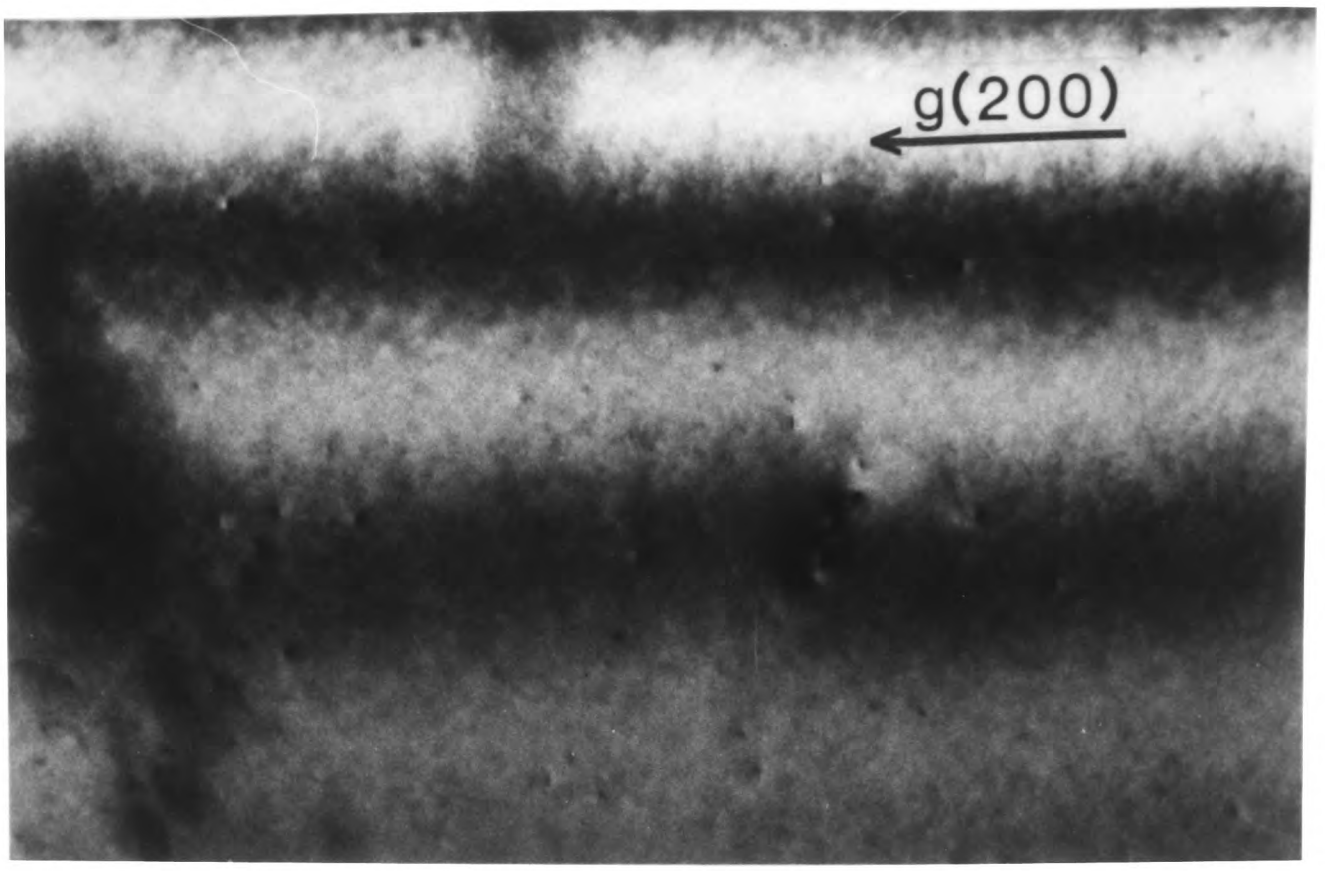

a

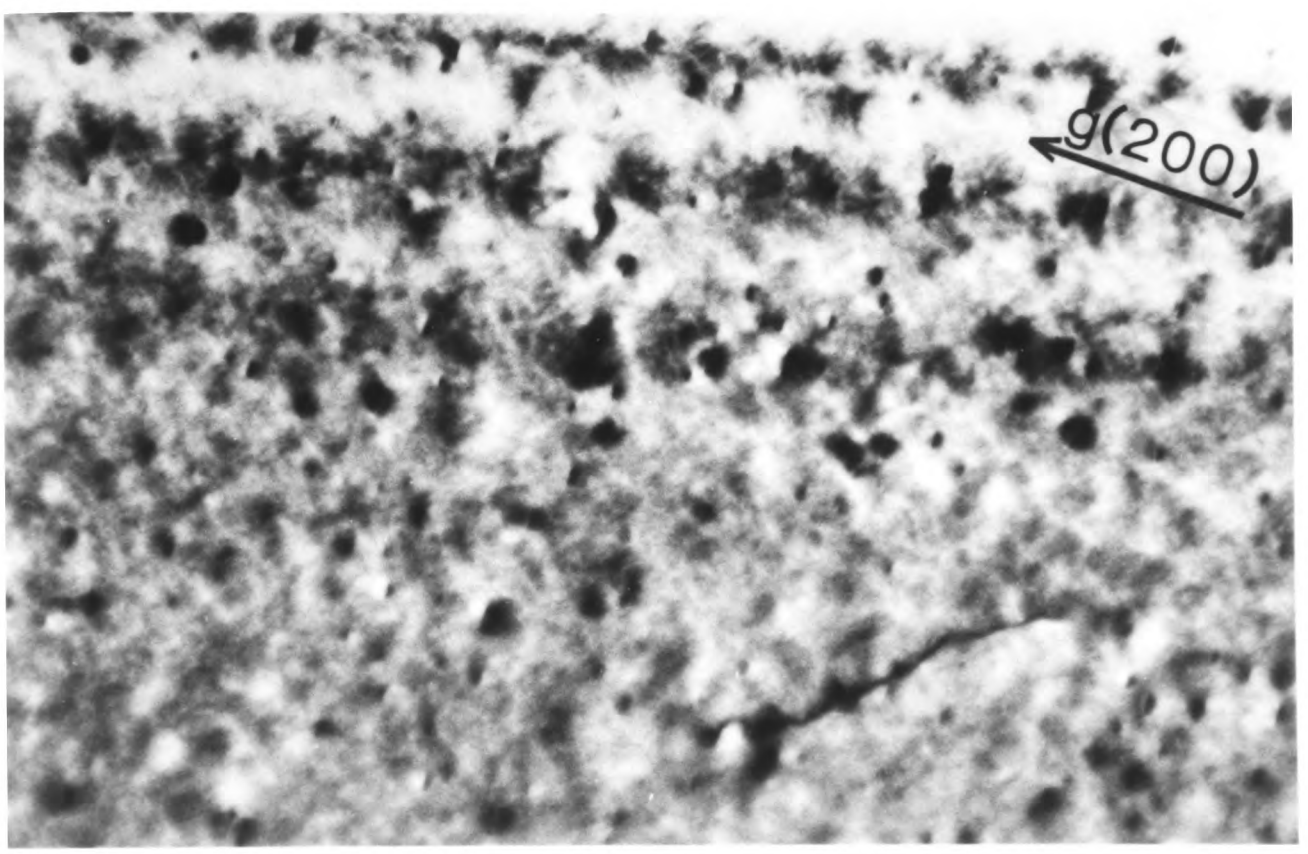

b

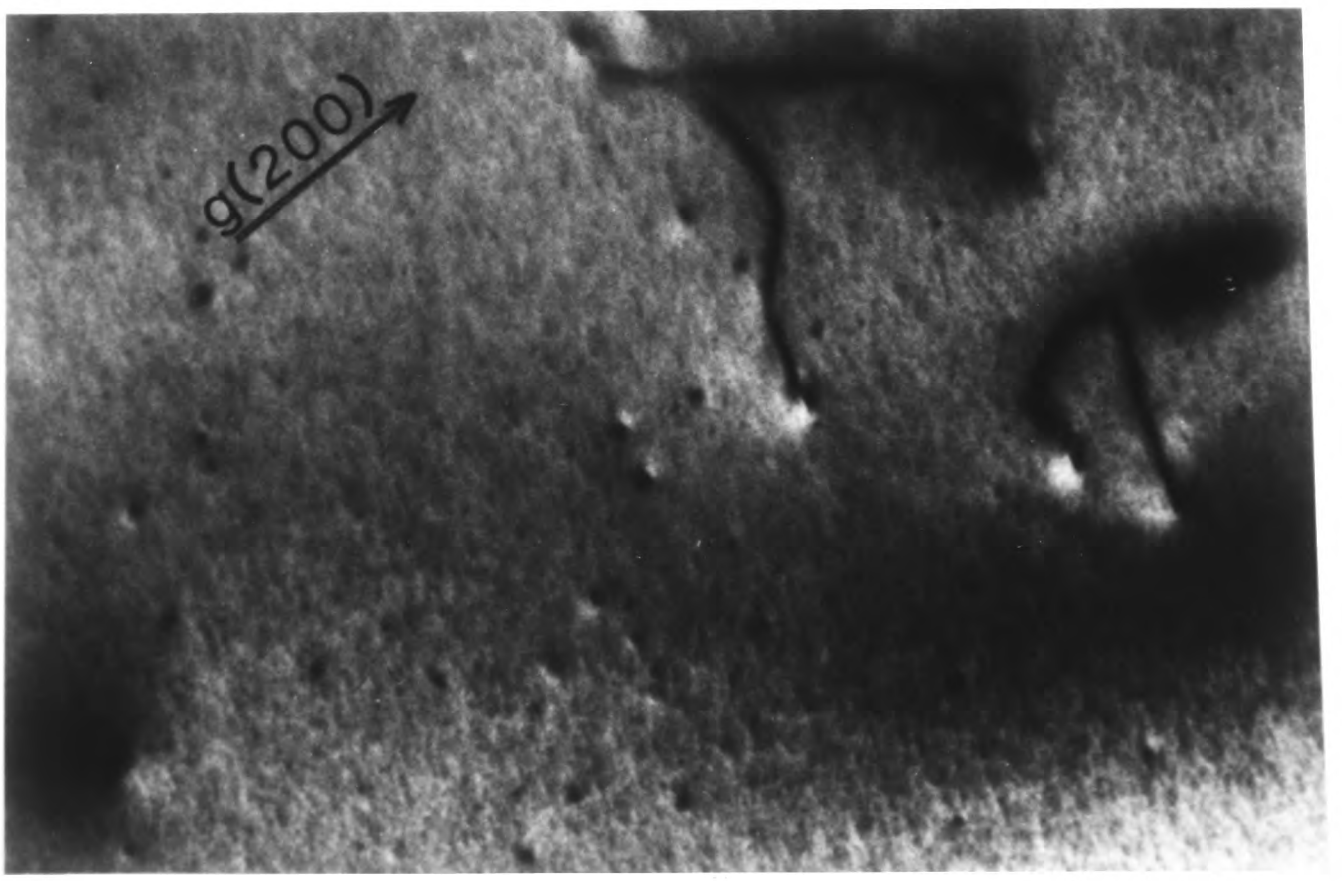

c

0.1μm

Figure 6.28

Time-temperature C-curve representing the appearance of precipitation in the W-phase of the undeformed heavy alloy.

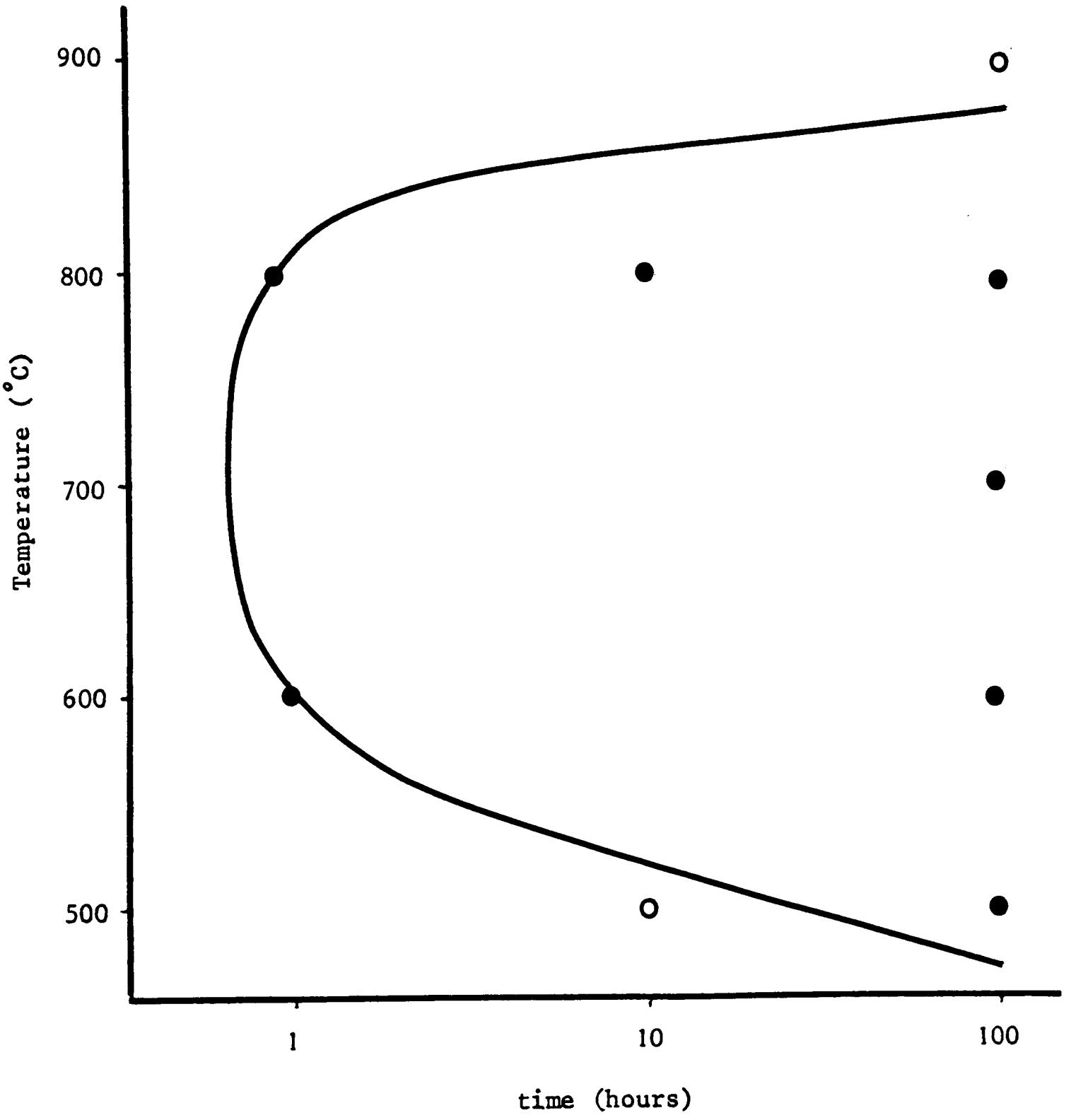

●- precipitate observed (however small an amount).

O- precipitate not observed.

Figure 6.29

Maximum observed precipitation in the W-phase of material aged at 600°C for 1 hour. The extent of precipitation after this heat treatment is essentially nil ($\underset{\sim}{g}(200)$ and $s \simeq 0$).

Figure 6.30

TEM micrograph of tungsten single crystal with ~ 14% reduction of area and aged at 700°C for 1 hour. No precipitation was visible ($\underset{\sim}{g}(200)$ and $s \simeq 0$).

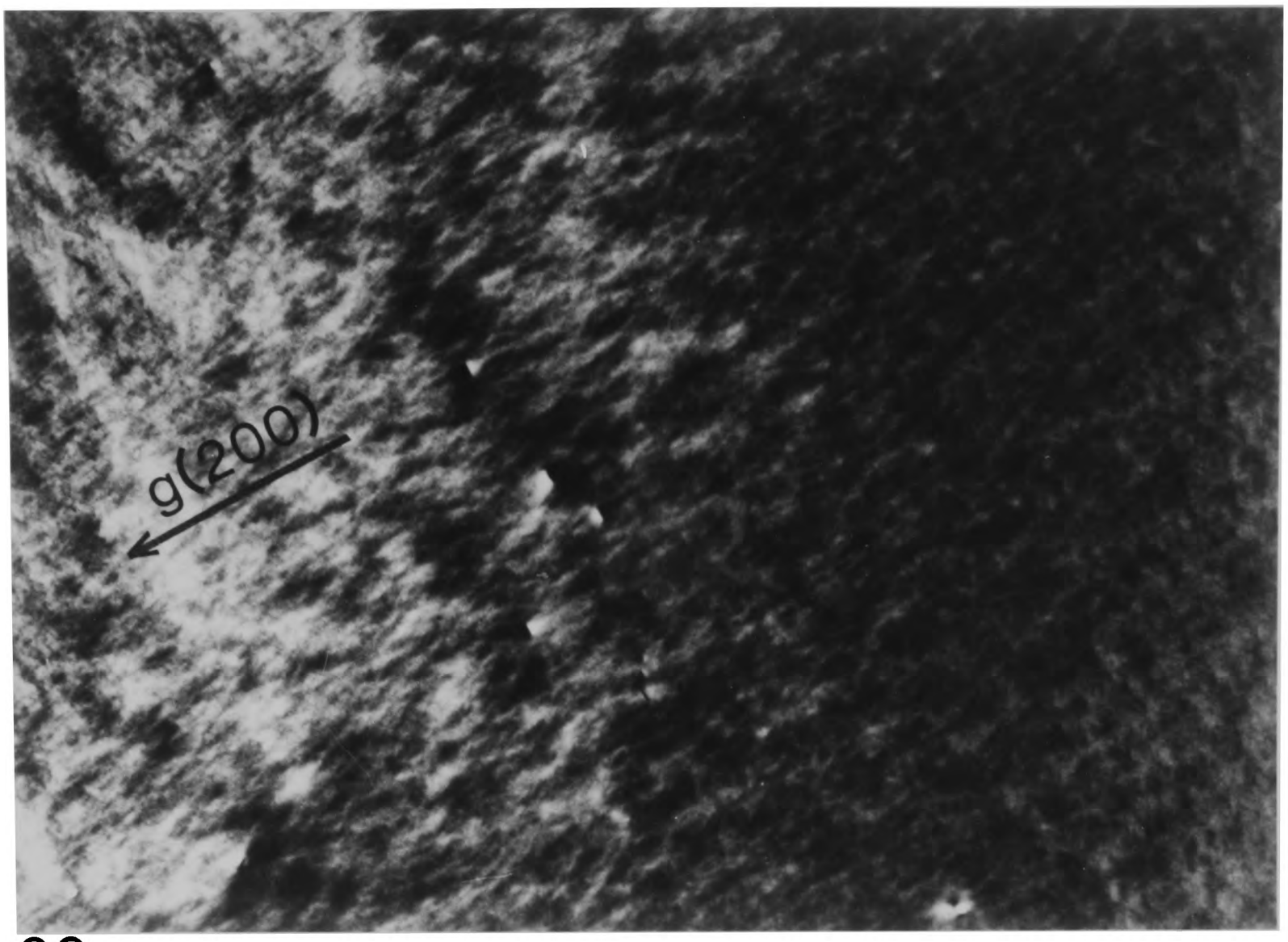

29

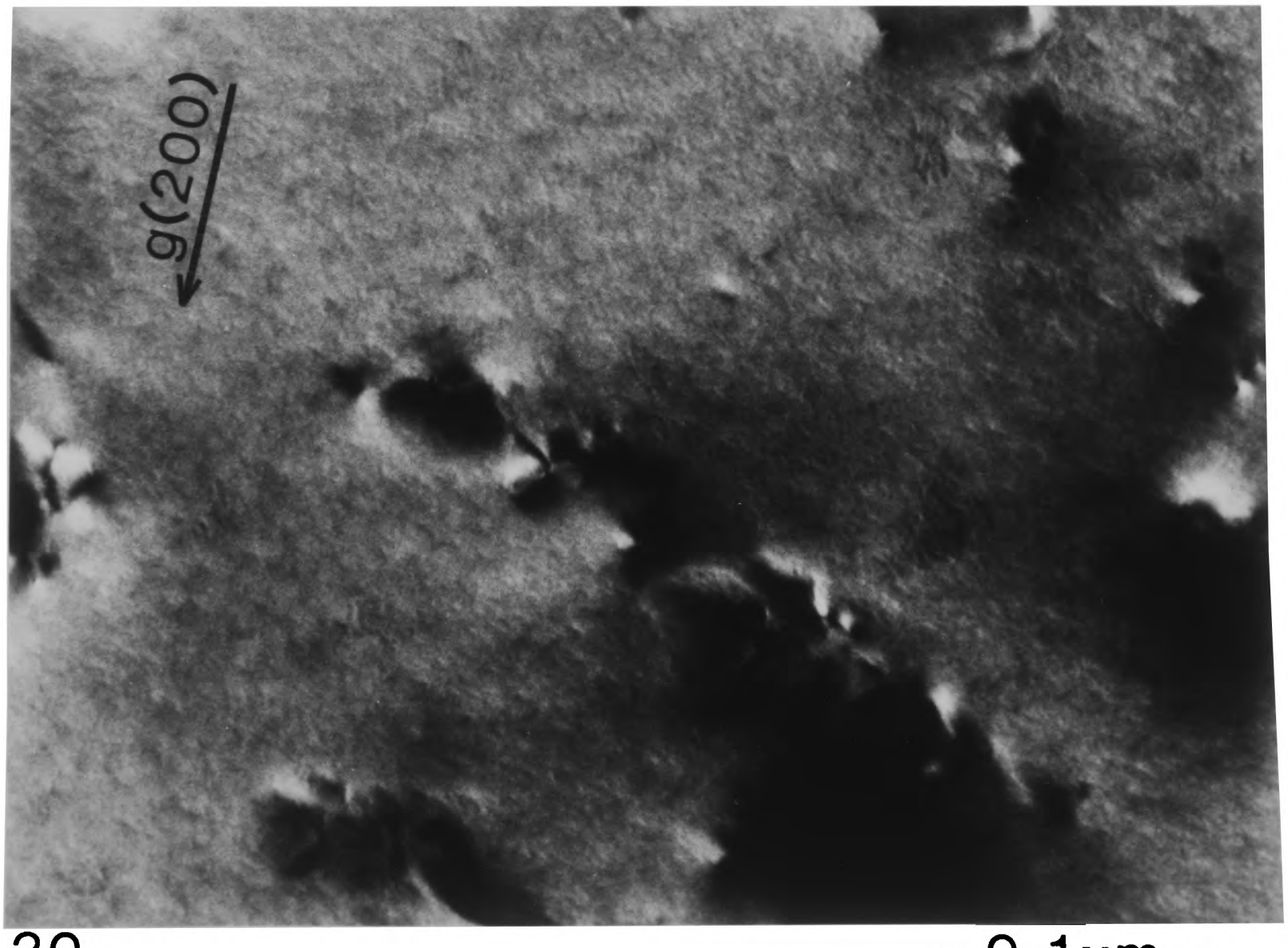

30

0.1μm

Figure 6.31

Microhardness results from tungsten single crystal with ~ 14% reduction of area by cold hydroextrusion (50g load, average of 10 indentations).

Before H.T.	Heat Treatment		After H.T.
VH(Kg/mm^2)	T(°C)	t(hrs)	VH(Kg/mm^2)
523 ± 44	500	1	490 ± 24
498 ± 25	500	10	488 ± 28
500 ± 27	500	100	477 ± 29
463 ± 37	600	1	474 ± 26
512 ± 27	600	10	512 ± 27
502 ± 20	600	100	474 ± 27
505 ± 29	700	1	477 ± 27
475 ± 29	700	10	486 ± 29
470 ± 23	700	100	481 ± 21
459 ± 26	800	1	491 ± 24
469 ± 29	800	10	471 ± 39
496 ± 40	800	100	464 ± 30

Chapter 7

DISCUSSION:
W-W GRAIN BOUNDARY PRECIPITATION AND
W-PHASE PRECIPITATION HARDENING

1. W-W Grain Boundary Precipitation

1.1. Precipitate Formation and Morphology

The observation of the fcc γ-phase grain boundary allotriomorph having an irrational orientation relationship with the bcc W grains is not unexpected. Hall, et al.[88] observed Cr-rich bcc precipitates in a Cu-rich fcc matrix with a range of orientation relationships varying from N-W to the K-S relationships, and Ryder and Pitsch[76] found the orientation relationship of ferrite precipitating from austenite in a Co-20Fe alloy to lie within an "orientation region". An intermediate orientation relationship is precisely what was observed between the allotriomorph and one W grain (see Fig. 6.8c). The relationship between the precipitate and the other W grain was thought to be near N-W but was not measured accurately.

A grain boundary allotriomorph having rational or near-rational orientation relationships with both adjacent grains would be expected to minimize the surface free energy. This, of course, would facilitate nucleation by lowering the critical free energy, ΔG^*. Thus, W grains oriented such that nuclei could have an orientation relationship in the N-W/K-S range with both adjacent grains would have an increased likelihood of precipitates nucleating on that boundary - all other factors being equal[89]. This might help explain the nonuniformity of precipitation observed.

Another possibility is chemical inhomogeneity of nickel and iron. If it is presumed that the precipitates form due to nickel and iron coming out of W-phase solution, and if the nickel and iron concentrations vary from

grain to grain, then grain boundary precipitates would be present or not present on individual boundaries accordingly. Further experimentation would be necessary to fully explain this aspect of the reaction.

Clearly, grain boundary diffusion is an important parameter in this type of precipitation, but the precise effect it has on the precipitate morphology is not obvious. In particular, is grain boundary diffusion responsible for a net loss or gain (or neither) of nickel and iron from the grain boundary? The four possible mechanisms of nickel and iron enrichment (and hence precipitation) at the grain boundary are sketched in Figure 7.1 and can be described as:

1) Nickel and iron diffusing from the interior of the W grains to the grain boundary and diffusing out of the grain boundary to the matrix region.
2) Nickel and iron diffusing from the interior of the W grains and from the matrix region into the grain boundary.
3) Nickel and iron only diffusing from the interior of the W grains to the grain boundary.
4) Nickel and iron only diffusing from the matrix region into the grain boundary.

As the SEM observations of W-W grain boundaries with precipitation show a difference in precipitate morphology between the center and the perimeter of the boundaries (which would be due to nickel and iron boundary transport) the third mechanism must be ruled out. Also, the fact that the 'perimeter' morphology is quite often seen to be a precipitate free zone(PFZ)(see Fig. 6.2) appears to preclude the possibility of nickel and iron from the matrix diffusing into the grain boundary to assist precipitation.

This last point, in the case of the fourth possible mechanism, can

be examined theoretically. If nickel and iron are transported only from the matrix region into the W-W grain boundary to precipitate γ-phase, there must be a driving force (i.e. a reduction in Gibbs free energy) for it to occur. According to classical nucleation theory, the change in free energy for precipitation of a second phase can be expressed as

$$\Delta G = \Delta g_c + \phi_{el} + \Delta g_s \qquad [1]$$

where Δg_c is the change in chemical free energy, ϕ_{el} is the elastic strain energy, and Δg_s is the change in surface free energy. As the matrix and the grain boundary precipitates are the same phase, there would be no reduction in chemical free energy ($\Delta g_c = 0$) by nickel and iron from the matrix region precipitating in a W-W grain boundary. Also, the elastic strain energy term will most surely increase ($\phi_{el} > 0$) with precipitation leaving only a reduction in surface free energy as a possible driving force (i.e. $\Delta g_s < 0$, and additionally, $|\Delta g_s| > |\phi_{el}|$).

Consider the most simple configuration for a grain boundary allotriomorph as shown in Figure 7.2. The expression for the change in surface free energy in this case† is

$$\Delta g_s = A_{W\gamma}\sigma_{W\gamma} - A_{WW}\sigma_{WW} \qquad [2]$$

where $A_{W\gamma}$ is the area of W-precipitate boundary, A_{WW} is the area of W-W grain boundary consumed, and $\sigma_{W\gamma}$ and σ_{WW} are the surface energies per unit area of W-precipitate and W-W boundaries, respectively. Clearly, the

---

† This treatment assumes $\sigma_{W\gamma}$ to be isotropic. In practice this is nearly never the case as faceting can reduce $\sigma_{W\gamma}$ locally *(90)*. This would mean the first term should be replaced by the more general expression

$$\sum_{n=1}^{k} A_n {}^n\sigma_{W\gamma}$$

where k is the number of boundary regions of different interfacial energy ${}^n\sigma_{W\gamma}$, and A_n is the area of each region. However, the essence and result of the above arguement remains unchanged for any grain boundary precipitate geometry or interfacial energies.

the condition

$$A_{W\gamma}\sigma_{W\gamma} < A_{WW}\sigma_{WW} \qquad [3]$$

is required for the $\Delta g_s < 0$ condition to be met. Examining the relationship between the two areas first - for the case of a very thin plate-like grain boundary precipitate the expression, $A_{W\gamma} \simeq 2A_{WW}$, would be a good approximation as two W-γ surfaces are created and one W-W surface destroyed. Generally, for real precipitate geometries the relation would have to be modified to

$$A_{W\gamma} \geq 2A_{WW}. \qquad [4]$$

The condition for static equilibrium is *(91)*

$$\sigma_{W\gamma} = \frac{\sigma_{WW}}{2\cos\theta} \qquad [5]$$

where $0^\circ < \theta < 90^\circ$ and is defined by the force diagram in Figure 7.2. Examining the first limiting case: as $\cos\theta \rightarrow 0$, $\sigma_{W\gamma} >> \sigma_{WW}$, and the expected precipitate geometry is shown in Figure 7.3. Of course, such a high $\sigma_{W\gamma}$ relative to σ_{WW} would preclude a reduction in surface free energy providing a driving force for precipitation. The second limiting case is: as $\cos\theta \rightarrow 1$, $\sigma_{W\gamma} = \frac{1}{2}\sigma_{WW}$, and the expected precipitate geometry is a thin plate as shown in Figure 7.4.

Therefore, the general case can be written as

$$\sigma_{W\gamma} \geq \tfrac{1}{2}\sigma_{WW} \qquad [6]$$

Combining expressions 4 and 6

$$A_{W\gamma}\sigma_{W\gamma} \geq A_{WW}\sigma_{WW} \qquad [7]$$

which does not fulfill the condition necessary for a reduction in surface free energy to provide a driving force for grain boundary precipitation (expression 3). It is interesting to note that if the $\sigma_{W\gamma}:\sigma_{WW}$ ratio is low enough the W-W grain boundary would be consumed entirely meaning there would be no discreet precipitates present, and the condition for static

equilibrium (equation 5) would no longer be applicable.

The preceding argument leads us to conclude that the fourth possible mechanism (Fig. 7.1d) for transport of nickel and iron to the boundary leading to precipitation is impossible. Likewise, this argument along with the fact that a PFZ is observed at the perimeter of many W-W grain boundaries containing precipitates appears to indicate that the second possible mechanism (Fig. 7.1b) is also implausible. Thus, it is tentatively concluded that γ-phase precipitation on W-W grain boundaries is due to nickel and iron coming out of supersaturated W-phase solution, and while grain boundary diffusion is obviously essential for the nucleation and growth of the γ-phase allotriomorphs, it also leads to some transport of nickel and iron to the matrix region.

1.2. Effect on Mechanical Properties

No systematic tests of the effect of this precipitate morphology on mechanical properties have been made. However, Brandon, et al.[19] associated W-W grain boundary precipitation with increased W-W boundary cohesion and, therefore, alloy ductility. Gero and Chaiat[23] also attribute improved ductility to the presence of these precipitates. These γ-phase precipitates would tend to reduce the total W-W grain boundary area which, as Muddle and Edmonds[44] suggest, may increase the impact resistance of the heavy alloy. However, further work is required to establish the change in mechanical properties afforded by this morphology.

2. W-Phase Precipitation Hardening

The observed defects are clearly precipitates because the only other possibility - dislocation loops - would not have $\underset{\sim}{R} = \underset{\sim}{b} = K\langle 100\rangle$ in a bcc metal, as explained in chapter 6 section 2.1.3.

2.1. Precipitate Identity

The EDX thin foil microanalysis of the small (~70Å) precipitates in the W-phase of the unworked material that was aged at 700°C for 100 hours showed no enrichment of iron (nickel was indeterminable). However, it must be remembered that this small precipitate was embedded in a W matrix (see Fig. 7.5) and therefore would make only a small contribution to the observed X-ray spectra relative to the W-phase. This obscuring effect could be minimized by going to thinner regions of the foil (e.g. $\lesssim$ 150Å), as was attempted, but the precipitates are difficult to locate because of the inferior imaging capability of the STEM and because of the very few precipitates in this region. Consequently, it is believed that this experiment does not conclusively show that the precipitates do not contain iron and/or nickel. This same situation could also account for the fact that no additional diffraction spots or fine structure were observed in the many electron diffraction patterns obtained.

The larger (~ 0.1μm) 'precipitates' observed after heat treatment at 900°C for 100 hours were shown to be only calcium-rich as compared with the surrounding W-phase. As calcium forms no compounds with tungsten[4] and inclusions containing calcium have been observed previously in the heavy alloy[22], albeit in the matrix region, it is believed that these 'precipitates' are, in fact, inclusions that bear no relationship to the precipitation observed at lower aging temperatures. The fact that they are very rarely observed also tends to support this view.

Because of the small precipitate size, the experimental results do not provide indisputable evidence of the identity of the precipitate phase. However, the fact that the W-phase definitely contains nickel and iron to the extent of 0.1 at% and 1.1 at%, respectively, and is seen to

precipitate these constituents at the W-W grain boundaries upon appropriate aging, leads to the inference, in the absence of conclusive data, that nickel and/or iron are responsible for the observed precipitation hardening. This will be presumed in the following sections.

2.2. Morphology and Kinetics

The absence of electron diffraction fine structure (e.g. streaking) from regions with small precipitates normally indicates that the precipitate shape is spherical. However, as mentioned above, it is believed that characteristic electron diffraction effects were not observed from the precipitates because of the low volume density of precipitate phase relative to the W matrix. Nevertheless, the fact that each precipitate has an associated tensile elastic displacement in the W-phase of only one $\langle 100 \rangle_W$ direction leads to a first interpretation that the precipitates are plates with a $\{100\}_W$ habit plane.

This interpretation appears sensible in that a Ni-Fe-W phase would certainly have lower elastic constants than the W matrix, and therefore a reduction in elastic strain energy would be afforded by a plate-like precipitate geometry for a coherent[92,93] or an incoherent[94,95] nucleus. Also, Lee, et al.[96] have shown for the case where the interfacial energy is boundary-orientation independent, that a strain energy to chemical free energy ratio $\gtrsim \frac{3}{4}$ is required for the critical nucleus shape to differ from a sphere. The fact that neither nickel or iron solubility in tungsten are thought to be profoundly temperature dependent[4] would be consistent with a small Δg_c and hence a potentially large $\phi_{el}:\Delta g_c$ ratio.

However, it would be more complete to consider all aspects of the precipitate structure and morphology to arrive at a theoretical configuration which would maximize the reduction in free energy upon transformation.

Such an examination would have to maximize $-\Delta G$ (which would also minimize ΔG^*, the critical free energy) with respect to the following:

Factor	Term in Eq.1 effected
Identity of matrix precipitate	Δg_c
- elastic constants	ϕ_{el}
Precipitate size	Δg_c, ϕ_{el}, Δg_s
Precipitate shape	ϕ_{el}, Δg_s
Boundary structure	ϕ_{el}, Δg_s
- interfacial energy	Δg_s
- degree of coherency	ϕ_{el}, Δg_s
- orientation relationship	ϕ_{el}, Δg_s
- habit plane	ϕ_{el}, Δg_s

A more detailed account of the theoretical aspects of this problem is presented by Christian[72]. Unfortunately, there is insufficient data to attempt a quantitative calculation for the present transformation.

It is interesting to consider the state of coherence of the precipitate. As mentioned previously, the $\underset{\sim}{R}$ = K<100> defects could not be dislocation loops with $\underset{\sim}{b} = \underset{\sim}{R}$ = K<100>. However, if the elastic coherency strains associated with precipitation became too high, then some of the misfit strain could possibly be alleviated by dislocation(s) being created at or being attracted to the interface. Conceivably, this may have happened at some point during the growth of the observed precipitates thereby leading to an interfacial edge-dislocation with Burgers vector $\underset{\sim}{b}$<100> encircling the perimeter of a plate-like precipitate.

The strain field of such a dislocation would certainly effect the contrast observed in a TEM image. Eyre, et al.[97] have calculated TEM images for $\underset{\sim}{b}$[100] edge-dislocation loops in bcc molybdenum that show what the authors call "type 4" contrast for $\underset{\sim}{g}$(200) diffraction conditions.

Type 4 contrast is a black/white lobe strain contrast with additional 'interface' structure. This particular 'interface' structure is, in fact, observed for $\underset{\sim}{g}(200)$ images of precipitates in the W-phase (see Fig. 6.21c).

To arrive at a very rough approximation of the "equivalent $\underset{\sim}{b}$" for these plate-like precipitates, it should be possible to use the calculations of Ashby and Brown[86] that relate the image width (as measured normal to the line-of-no-contrast) and the radius of the precipitate to '$\underset{\sim}{b}$', $\underset{\sim}{g}$, and the angle, θ, between the normal to the line-of-no-contrast and $\underset{\sim}{g}$. This relation is reproduced in graphical form in Figure 7.6. To test the accuracy of this calculation for small planar defects that display oscillatory black/white contrast with depth in the foil we can use the calculated image for a $\underset{\sim}{b}[100]$ edge-dislocation loop in Mo with $\underset{\sim}{g}(200)$ (see Fig. 1[97]). The measured image width is ~ 160Å, and r, $\underset{\sim}{g}$, ξ_g, and θ are approximately 24Å, 0.636Å^{-1}, 329Å, and zero, respectively. Using the values with the graph in Figure 7.6, $\underset{\sim}{b}[100]$ is found to be ~ 3.7Å. This compares with the actual value of $\underset{\sim}{b}\langle 100\rangle = a_{Mo} = 3.146$Å. The measured value is ~ 20% greater than the actual value - so it appears as if we can use the measured value for $\underset{\sim}{b}$ as an approximate upper limit.

Turning now to the precipitates observed in the W-phase - in particular in material that has been aged at 700°C for 100 hours (Fig. 6.21c). Using the same procedure as above with the fixed values: $\underset{\sim}{g}(200) = 0.632$Å^{-1}, $\xi_{200} = 222$Å, and θ = zero, and measuring r and the image width, the 'equivalent $\underset{\sim}{b}$' is found to be ~ 1.3 ± 0.3Å. This, of course, should be treated as an <u>approximate</u> upper limit. As $\underset{\sim}{b}\langle 100\rangle_W = a_W = 3.165$Å, it is concluded that there is not a $\underset{\sim}{b}\langle 100\rangle$ edge-dislocation loop around the perimeter of the precipitate and that the observed strain contrast is due to elastic coherency strains.

In principle, it should now be possible to estimate the thickness of

the precipitate as the 'equivalent $\underset{\sim}{b}$' can be approximated by εt, where $\varepsilon(=e^c)$ is the constrained strain normal to the precipitate and t is the precipitate thickness[86]. Unfortunately, no data exists that establishes the crystal structure of the precipitate or the orientation relationship it has with the W matrix, and given the fact our estimate of the 'equivalent $\underset{\sim}{b}$' is very approximate, it seems inappropriate to speculate further concerning the precipitate microstructure. Further work would be necessary to understand this aspect of the precipitate morphology more completely.

The sporadic distribution of precipitates from one W grain to the next in the undeformed material remains unexplained. One possible reason for this is if the nickel and/or iron supersaturation level was already generally low in the W-phase then just a slight decrease in the nickel and/or iron concentration in a particular grain would substantially reduce the chemical free energy change, Δg_c, for precipitation in that grain. This, of course, would raise the critical free energy, ΔG^*, thereby retarding nucleation.

It is interesting to note that this sporadic distribution is not observed in material that was cold worked prior to aging. In fact, precipitation is quite extensive after aging for only one hour in the range 600-750°C. It appears that the prior deformation has accelerated the nucleation kinetics. This can be best understood by examining the classical theory of time-dependent nucleation.

The general equation for the time-dependent nucleation rate† is

$$J(t) = J^s \exp(-\tau/t) \qquad [8]$$

where J^s is the steady-state nucleation rate, τ is the incubation time, and t is the time (there is no nucleation for $t \ll \tau$) and is illustrated in Figure 7.7. The steady-state nucleation rate is given by

---

† Time-dependent nucleation theory is much more thoroughly reviewed by Christian *(72)*, Russell *(98)*, and Aaronson and Russell *(99)*.

$$J^s = Z\beta C \qquad [9]$$

Where Z is the Zeldovich nonequilibrium factor (discussed more completely elsewhere [72,98,99]), β is the rate at which atoms join the critical nucleus, and C is the concentration of the critical nucleus. The various terms are quite complicated as they depend on the composition, shape, and surface energy of the critical nuclei[99]. However, if we assume that these factors and, additionally, Δg_c and the transformation temperature are the same for precipitation in both the deformed and undeformed alloys we can write the ratio of the time-dependent nucleation rates as

$$\frac{J^d(t)}{J(t)} = \frac{D^d N^d}{DN} \exp\left[\frac{\Delta G^* - \Delta G^{*,d}}{kT}\right] \exp\left[\frac{A}{t(D-D^d)}\right] \qquad [10]$$

steady-state term transient term

where D is the diffusivity†(which can be approximated by D_{Ni} or D_{Fe} for dilute nickel or iron solutions, respectively), N is the number of nucleation sites, k is Boltzmann's constant, T is absolute temperature, and A is a constant containing factors that are assumed to be constant.

If heterogeneous precipitation is occurring then $N^d/N < 1$[100]. In this case heterogeneous precipitation could only be occurring at point defect clusters as precipitation at dislocations is relatively negligible compared to apparent homogeneous precipitation (see Fig. 6.13b). Also, if precipitation was occurring preferentially at point defect clusters there may be a reduction in strain energy and hence in critical free energy. In this case, the condition

$$\frac{N^d}{N} \exp\left[\frac{\Delta G^* - \Delta G^{*,d}}{kT}\right] > 1 \qquad [11]$$

would have to be fulfilled for the heterogeneous nucleation rate in the deformed material to be greater than the homogeneous nucleation rate in the

---

† The proper diffusivity expression depends on the state of coherence of the nuclei and is discussed in more detail by Russell [101].

undeformed material.

Possibly more important to the relative nucleation rates is the effect of diffusivity, especially on the transient term. Clearly, $\tau \propto D^{-1}$ [72], so as the diffusion coefficient increases, the incubation time for nucleation decreases. Also, if $D^d > D$ the steady-state term of equation 10 would increase.

Certainly direct evidence confirming or denying the possibility of heterogeneous precipitation occurring at point defect clusters would be difficult to obtain. Because the experimental results tend to suggest a significant decrease in the incubation time for nucleation with prior deformation for a constant aging temperature (compare Fig. 6.13b with Fig. 6.29), it appears that prior alloy deformation induces a higher point defect concentration† thereby increasing volume diffusivity.

This is plausible only if the point defects (in this case, vacancies) created by plastic deformation have long enough lifetimes at the aging temperature[72]. Resistivity measurements of tungsten quenched from near the melting point showed that after aging at 550°C for 10 minutes there is no resistivity change - meaning the excess, quenched-in vacancies have not yet begun to anneal out[103]. Even after 30 minutes at this temperature the equilibrium concentration of vacancies has not been reached. Clearly, at the aging temperatures that induce precipitation hardening of the W-phase in prior deformed heavy alloy, excess (nonequilibrium) vacancies could last long enough to increase the diffusivity for at least some significant portion of an aging treatment lasting one hour. The incubation time for nucleation would then be reduced accordingly.

---

† For the mechanism of this process the reader is referred to Honeycombe[102].

2.3. Effect on Mechanical Properties

This study has shown that the precipitation hardening of the W-phase in undeformed material is responsible for small (~5%) but significant heavy alloy strengthening. This is qualitatively similar to results obtained previously (see chapter 2 section 2.4). Prior deformed material, exhibiting more uniform precipitation, is hardened considerably more by appropriate aging treatments. Additionally, precipitation at preexisting dislocations, while insignificant from a nucleation kinetics point of view, could help inhibit the onset of dislocation slip very effectively. Theoretical treatments of precipitation hardening have been reviewed by many authors *(e.g. 104,105,106)* and therefore will not be discussed here.

3. Relation Between W-W Grain Boundary Precipitation and W-phase Precipitation Hardening

As both reactions appear to involve the precipitation of nickel and/or iron from the W-phase, the appearance of the respective morphologies should be related with respect to aging temperature. This is, in fact, the case as the maximum precipitation in the W-phase is observed at ~ 700°C (all t = 100 hour anneals) while the maximum precipitation at the W-W grain boundaries is observed at higher temperatures (750-900°C). Additionally, W-W grain boundary precipitation was observed up to 1050°C while W-phase precipitation hardening was not found above 800°C.

This transition from bulk precipitation to a grain boundary precipitate morphology upon raising the aging temperature is characteristic of precipitation from supersaturated solid-solution and is discussed in more detail, although for the different case of precipitation of W from the γ-phase, in chapter 5 section 2. It is also worthy of note that both morphologies are sporadic and nonuniform - supporting the hypothesis that there are different nickel and/or iron concentrations from grain to grain.

Figure 7.1

Possible mechanisms for nickel and/or iron enrichment and transport to and along the W-W grain boundary. Arrows indicate direction of Ni,Fe diffusion. See text for full explanation.

a)

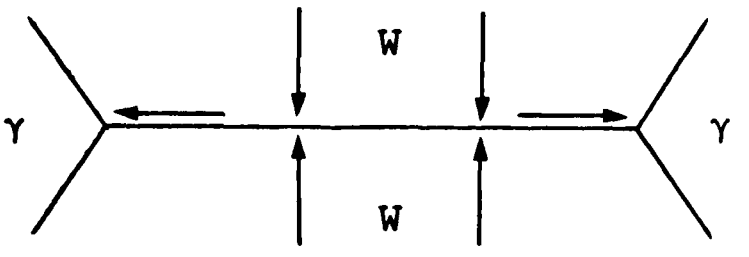

b)

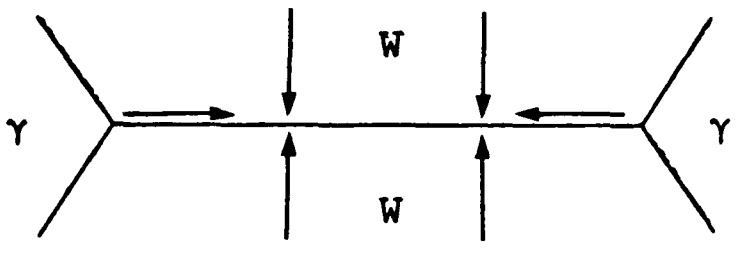

c)

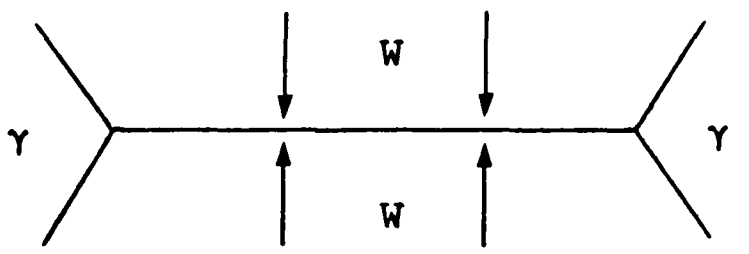

d)

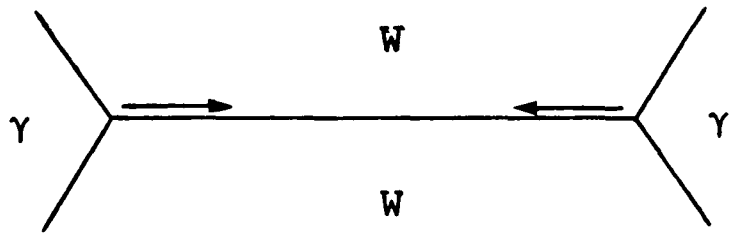

Figure 7.2

Grain boundary allotriomorph in static equilibrium after Clemm and Fisher[91].

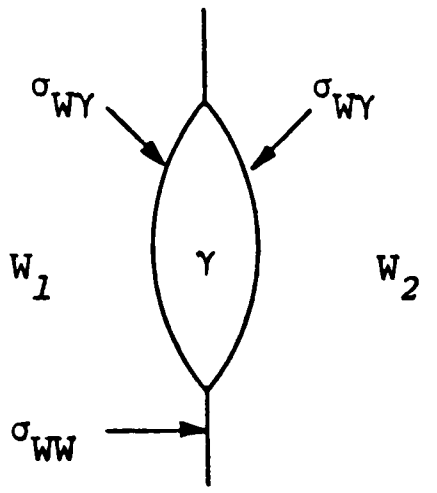

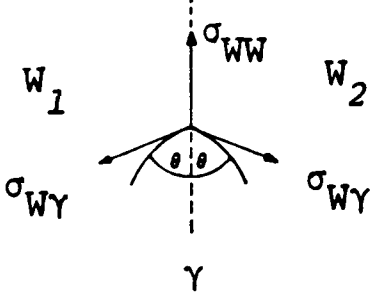

Figure 7.3

Expected grain boundary precipitate geometry when $\sigma_{WY} >> \sigma_{WW}$.

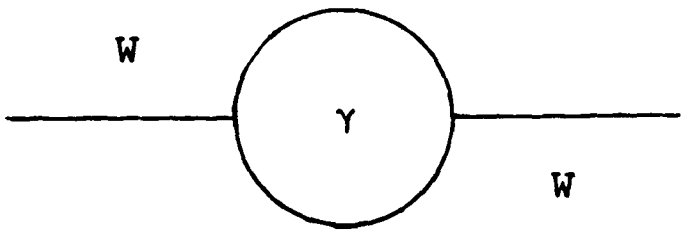

Figure 7.4

Expected grain boundary precipitate geometry when $\sigma_{WY} \approx \frac{1}{2}\sigma_{WW}$.

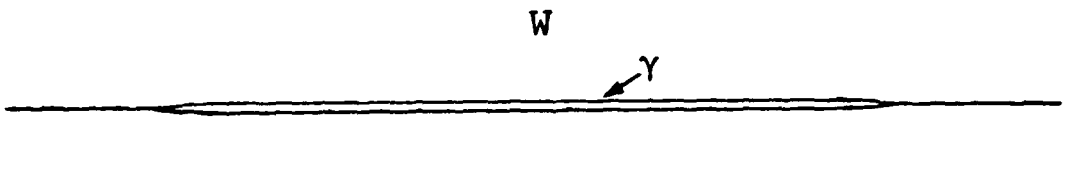

Figure 7.5

The configuration for microanalysis of a small precipitate embedded in a 'thin' foil.

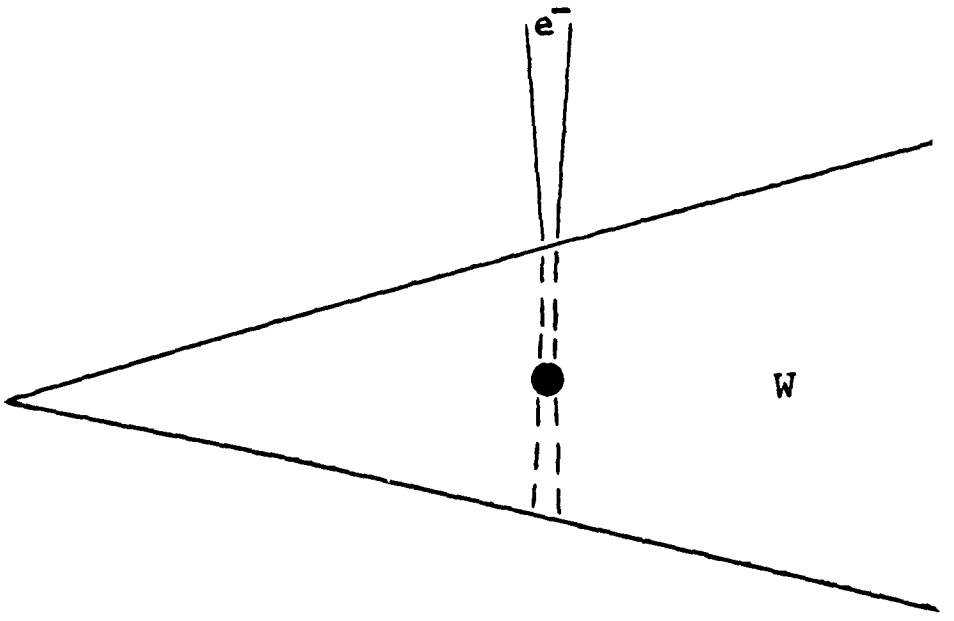

Figure 7.6

Summary of image width data for prismatic dislocation loops and plate-like precipitates. Foil taken as $5\xi_g$ thick, s = 0, and $\xi_g/\xi'_g = 0.1$ (after Ashby and Brown[86]).

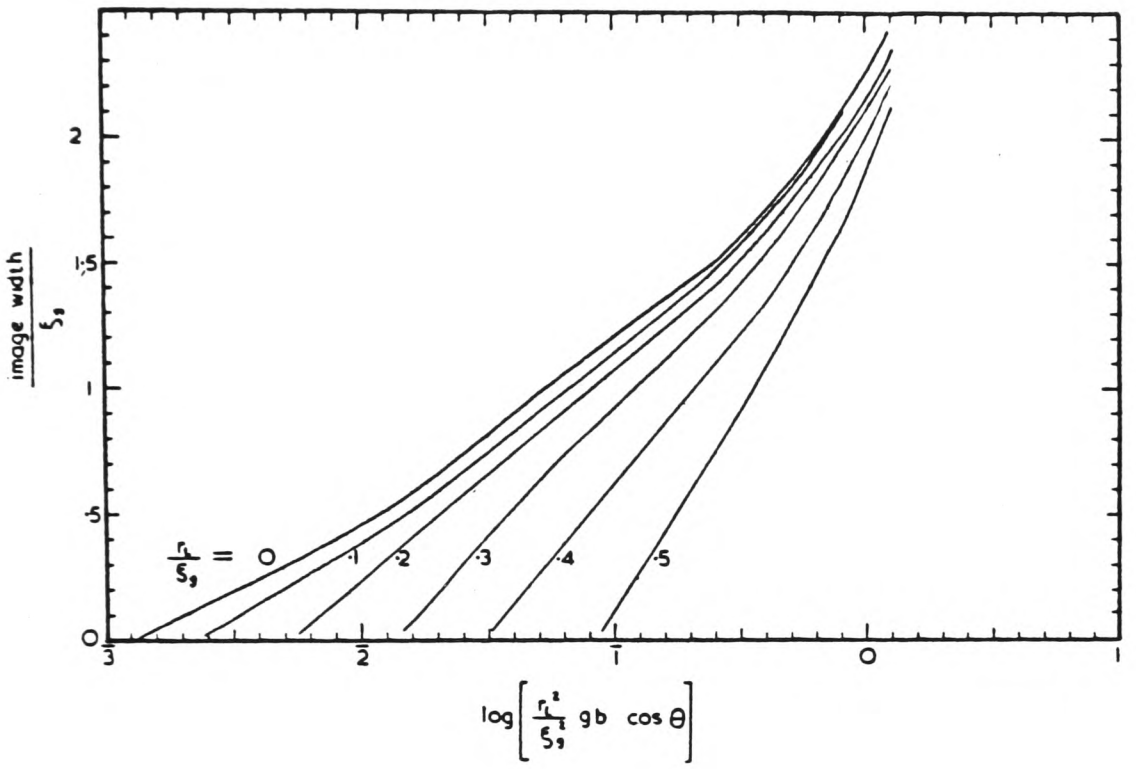

Figure 7.7

Number of particles nucleated per unit volume vs. time (after Russell [101]).

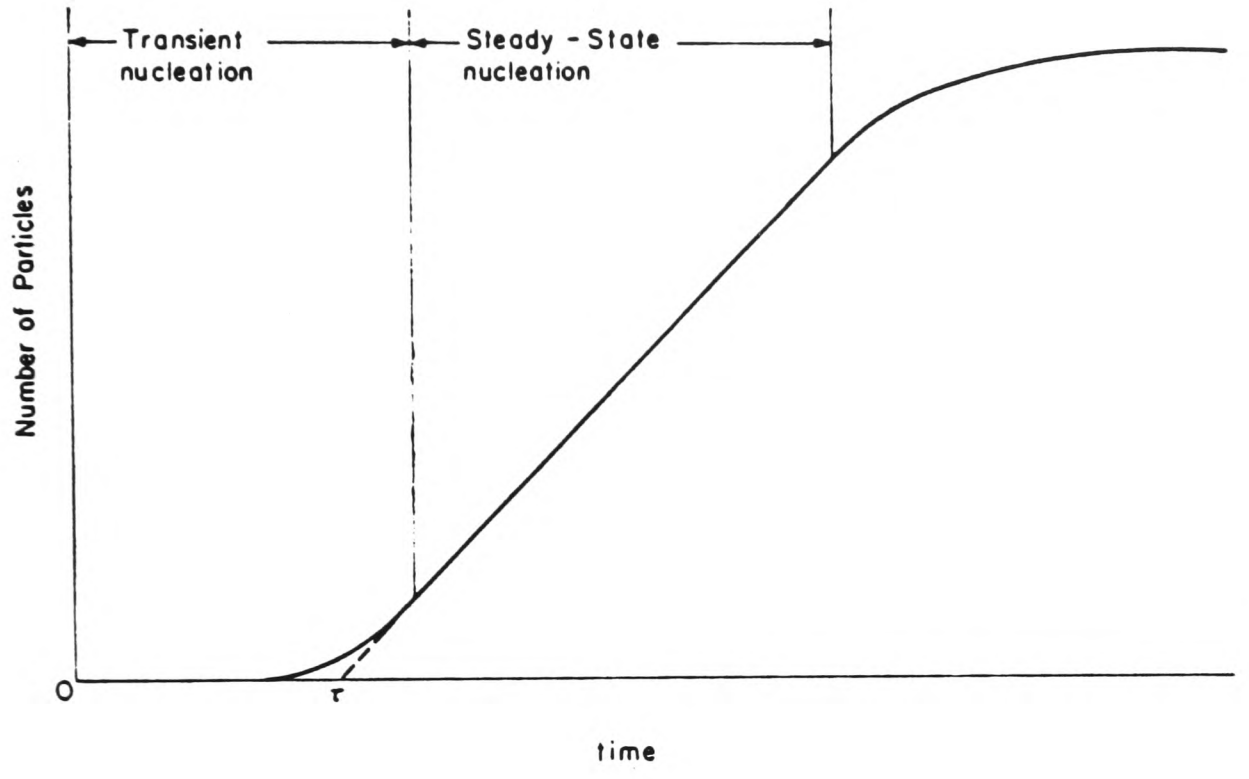

Chapter 8

SUMMARY

This research has investigated four precipitation reactions in the 90W-5Ni-5Fe heavy alloy. Ni-Fe-W matrix-composition alloys were also studied to further the understanding of two of these reactions. The main conclusions obtained from the work are given below.

1. Conclusions

1) An η-carbide was observed in a ~ 21.5W-38.5Ni-40Fe (0.10 wt%C) matrix-composition alloy. Electron diffraction evidence showed that a similar η-carbide forms at the W-γ and γ-γ boundaries in the heavy alloy upon solution treating at 1350°C and subsequent aging at 750-850°C for 100 hours. This morphology is expected to reduce the interphase boundary cohesion and hence cause alloy embrittlement.

2) The precipitation of W from a 19.2W-41.4Ni-39.4Fe matrix-composition alloy was found to progress from a discontinuous morphology at lower aging temperatures to predominantly grain boundary precipitation at higher aging temperatures. This was, in part, explained by considering the thermodynamics of the transformation.

3) Irregular and sporadic discontinuous precipitation of W in the matrix region of the heavy alloy was observed upon solution treating at 1350°C and subsequent aging at 750-850°C. The hypothesis that a γ-γ grain boundary (an infrequently observed feature as the γ grains are $\gtrsim$ 100μm) is necessary for the nucleation of this reaction was presented.

4) γ-phase allotriomorphs were observed at the W-W grain boundaries. The bcc/fcc orientation relationship was found to be in the K-S/

N-W region. It was argued that the allotriomorphs must form due to nickel and iron precipitating from the supersaturated W-phase.

5) Precipitation hardening was found to account for the observed alloy strengthening upon aging in the temperature range 500-750°C. Prior alloy deformation was seen to accelerate this reaction. TEM analysis showed the precipitates to be plate-like with a {100} habit plane (three variants) and are responsible for <100> tensile coherency strains in the W lattice. It is believed that the precipitates are nickel and/or iron rich.

2. Suggestions for Further Work

There is no doubt that there are many interesting aspects of the tungsten heavy alloys that are worthy of academic study, and, in fact, various suggestions for continued work on these precipitation reactions have been made throughout the text. The suggestions listed below, in the author's opinion, particularly require attention.

1) Correlate the formation of the interfacial η-carbide with alloy impurity (esp. carbon) content and processing parameters.
2) Establish the nucleation site(s) of the discontinuous precipitation of W in the γ-phase.
3) Establish whether or not a low-energy orientation relationship exists between the γ-phase allotriomorph and both adjacent grains by characterizing many precipitates.
4) Directly determine the chemical constituents of the small plate-like precipitates in the W-phase using FIM/atom probe.

BIBLIOGRAPHY

1. J.C. McLennan and C.J. Smithells, J. Sci. Instr., 12 (1935) 159.
2. G.H.S. Price, C.J. Smithells, and S.V. Williams, J. Inst. Metals, 62 (1938) 239.
3. E.C. Green, D.J. Jones, and W.R. Pitkin, Proc. Conf., Symposium on Powder Metallurgy, Iron and Steel Inst. Special Report 58 (1956) 253.
4. M. Hansen, Constitution of Binary Alloys, McGraw-Hill, NY, (1958).
5. D.V. Edmonds and P.N. Jones, Metall. Trans., 10A (1979) 289.
6. L.A. Konyukhova, Yu.A. Eiduk, and L.S. Vodop'yanova, Tsvet. Metally, No. 10 (1974) 57.
7. E.J. Votava, Planseeber. Pulvermet., 21 (1973) 79.
8. E.-T. Henig, H. Hofmann, and G. Petzow, Proc. 10th Plansee-Seminar, 2, (1981) 335, ed. H.M. Ortner.
9. H. Takeuchi, J. Jpn. Inst. Metals, 31 (1967) 1064.
10. R.V. Minakova, A.N. Piliankevich, O.K. Teodorovich, I.N. Frantsevich, and I.E. Shilanovskai, 2nd Int. Powder Metall. Conf., 2 (1966) 91.
11. R.V. Minakova, A.N. Piliankevich, O.K. Teodorovich, and I.N. Frantsevich, Poro. Metall., No.5(65), (1983) 73.
12. A. Kannappann, Report No. R70/71, Chalmers University of Technology, Gothenburg, (1971).
13. J.M. Walsh and M.J. Donachie, Metall. Trans., 4A (1973) 2854.
14. B.C. Muddle, Private Communications, (1980-1983), University of Illinois, Champaign - Urbana.
15. M.-L. Fiedler and H.H. Stadelmaier, Z. Metallkunde, 66 (1975) 402.
16. Ya.S. Umanskiĭ and N.T. Chebotarev, Izv. Akad. Nauk. SSSR, Ser. Fiz., 15 (1951) 24.

17. J. Leciejewicz, J. Less-Common Metals, 7 (1964) 318.

18. S.S. Kiparisov, L.S. Vodop'yanova, Yu.A. Eiduk, and Z.S. Iisakova Nauchn. Tr. Vses. Naucho - Issled. Proektn. Inst. Tugo. Met. Tverd. Splanov., 16 (1976) 280.

19. D.G. Brandon, E. Ariel, and J. Barta, Proc. 5th Int. Symp. Electron Microscopy and Str. of Materials, (1972) 849, ed. G. Thomas.

20. P.A. Verkhovodov, L.D. Konchakovskaya, A.P. Kresanova, R.V. Minakova, and I.V. Uvarova, Poro. Metall., No. 4 (196),(1979) 8.

21. I.N. Frantsevich, R.V. Minakova, and L.G. Bazhenova, 5th Polish Conf. on Powder Metall., 2 (1979) 221.

22. M. Hogwood, Private Communication, (1981) Royal Armaments Research and Development Establishment, Sevenoaks.

23. R. Gero and D. Chaiat, Materials Engr. Conf., Technion, (1981) 46, Haifa, Israel.

24. C. Lea, B.C. Muddle, and D.V.Edmonds, Metall. Trans., 14A (1983) 667.

25. A.G. Wehr, Ph.D. thesis, University of Missouri, Engr. - Metall., (1962).

26. D.J. Jones and P. Munnery, Powder Metall., 10 (1967) 156.

27. "The Effect of Post Sintering Mechanical and Thermal Treatments on the Microstructure and Properties of Liquid Phased (sic) Tungsten Alloys", Internal Report No. 2001/19, Royal Armaments Research and Development Establishment, Sevenoaks, (1980) 13pp.

28. E.I. Larsen and P.C. Murphy, Can. Min. and Metall. Bull., (April 1965) 413.

29. E. Ariel, J. Barta, and D.G. Brandon, Powder Metall. Int., 5 (1973) 126.

30. L. Ekbom, Scand. J. Metall., 5 (1976) 179.

31. V.N. Eremenko, Yu.V. Naidich, and I.A.Lavrinenko, Liquid-Phase Sintering, Consultants Bureau, NY, (1970).

32. E.G. Zukas and H. Sheinberg, Powder Tech., 13 (1976) 85.

33. Y. Masuda and R. Watanabe, Sintering Processes, Mat. Sci. Res., 13 (1980) 3, ed. G.C. Kuczynski.

34. R. Watanabe and Y. Masuda, Sintering Processes, Mat. Sci. Res., 13 (1980) 389, ed. G.C. Kuczynski.

35. R.H. Krock and L.A. Shepard, Trans. AIME, 227 (1963) 1127.

36. I. Roman and D. Jinchuck, Fatigue of Engr. Mater. and Str., 5 (1982) 71

37. K.-S. Churn and D.N. Yoon, Powder Metall., No. 4 (1979) 175.

38. W.A. Kaysser, O.J. Kwon, and G. Petzow, P/M-82 in Europe, Int. Powder Metall. Conf., (1982) 23.

39. G. Louis Powell, Analyt. Chem., 44 (1972) 2357.

40. F.E. Sczerzenie and H.C. Rogers, Proc. Int. Conf. Hydrogen Metall. (1973) 645, eds. I.M. Bernstein and A.N. Thompson.

41. Z. Guisen, L. Mingcheng, L. Zhongjie, and Y. Shuyan, Acta Metall. Sinica, 17 (1981) 39.

42. B. Lux, G. Jangg, and H. Danninger, U.S. Govt. Accession No. AD-A099799, (Feb. 1981) 85pp.

43. H.K. Yoon, S.H. Lee, S.-J.L. Kang, and D.N. Yoon, J. Mater. Sci., 18 (1983) 1374.

44. B.C. Muddle and D.V. Edmonds, Met. Sci., 17 (1983) 209.

45. K. Winkler and R. Vogel, Arch. Eisenhüttenwesen, 6 (1932) 165.

46. G.V. Raynor and V.G. Rivlin, Int. Metals Rev., 26 (1981) 213.

47. G.V. Raynor and V.G. Rivlin, Int. Metals Rev., 28 (1983) 122.

48. G.L. Kehl, The Principles of Metallographic Laboratory Practice, McGraw-Hill, NY, (1949).

49. Practical Scanning Electron Microscopy - Electron and Ion Microprobe Analysis, eds. J.I. Goldstein and H. Yakowitz, Plenum Press, NY, (1975).

50. A. Lasalmonie and J.W. Martin, Acta Metall., 22 (1974) 1449.

51. P. Hirsch, A. Howie, R.B. Nicholson, D.W. Pashley, and M.J. Whelan, Electron Microscopy of Thin Crystals, Krieger, NY, (1977).

52. G. Thomas and M.J. Goringe, Transmission Electron Microscopy of Materials, Wiley-Interscience, NY, (1979).

53. J.W. Edington, Practical Electron Microscopy in Materials Science, N.V. Philips, Eindhoven, (1975).

54. D.J.H. Cockayne, M.L. Jenkins, and I.L.F. Ray, Phil. Mag., 24 (1971) 1383.

55. P. Guyot, J. Microsc. (Oxford), 98 (1973) 180.

56. R.M. Allen and J.B. Vander Sande, Metall. Trans., 9A (1978) 1251.

57. D.J.H. Cockayne, I.L.F. Ray, and M.J. Whelan, Phil. Mag., 20 (1969) 1265.

58. D.J.H. Cockayne, J. Appl. Cryst., 8 (1975) 222.

59. D.J.H. Cockayne, J. Microsc. (Oxford), 98 (1973) 116.

60. D.J.H. Cockayne, Z. Naturforsch., 27a (1972) 452.

61. H. Diepers, Phys. Stat. Sol., 24 (1967) 235.

62. B.F. Buxton, J.A. Eades, J.W. Steeds, and G.M. Rackman, Phil. Trans. Roy. Soc., A281 (1976) 171.

63. J.W. Steeds and R. Vincent, J. Appl. Cryst., 16 (1983) 317.

64. J.A. Chandler, Practical Methods in Electron Microscopy, 5 (1977) North-Holland, ed. A.M. Glauert.

65. B.D. Cullity, Elements of X-ray Diffraction, Addison-Wesley, London, (1956).

66. T. Dingle, B.W. Griffiths, J.C. Ruckman, and C.A. Evans,Jr., Microbeam Analysis - 1982, (1982) 365, ed. K.F.J. Heinrich.

67. R. Gevers, A. Art, and S. Amelinckx, Phys. Stat. Sol., 3 (1963) 1563.

68. International Tables for X-ray Crystallography, 1 (1965) eds. N.F.M. Henry and K. Londsdale.

69. T. Dingle, Private Communication, (1983) Cambridge Mass Spectrometry Ltd., Cambridge.

70. C.B. Pollock and H.H. Stadelmaier, Metall. Trans., 1 (1970) 767.

71. H.I. Aaronson, Decomposition of Austenite by Diffusional Processes, (1962) 387, AIME, eds. V.F. Zackay and H.I. Aaronson.

72. J.W. Christian, The Theory of Transformations in Metals and Alloys, Pergamon, Oxford, (1975).

73. D.B. Williams and E.P. Butler, Int. Met. Rev., 26 (1981) 153.

74. D.A. Porter and J.W. Edington, Proc. Roy. Soc., 358A (1977) 355.

75. M.H. Ainsley, G.J. Cocks, and D.R. Miller, Met. Sci., 13 (1979) 20.

76. P.L. Ryder and W. Pitsch, Acta Metall., 14 (1966) 1437.

77. T.K. Kang, Dissertation, Universität Stuttgart (1981).

78. M. Hogwood, Private Communications, (1982-3) R.A.R.D.E., Sevenoaks.

79. K.W. Andrews, D.J. Dyson, S.R. Keown, Interpretation of Electron Diffraction Patterns, Hilger, London (1971).

80. D.V. Wilson and B. Russell, cited by J.D. Baird, Metall. Rev., 16 (1971) 1, Rev. No. 149.

81. G.D. Rieck, G.H.G. Vaessen, and D.L. Vogel, Trans. AIME, 242 (1968) 575.

82. M. Wilkins, Vacancies and Interstitials in Metals, (1969) 485, North-Holland, eds. A. Seeger, D. Schumacher, W. Schilling, and J. Diehl.

83. M. Rühle, Phys. Stat. Sol., 19 (1967) 263.

84. M. Rühle, Phys. Stat. Sol., 19 (1967) 279.

85. M.F. Ashby and L.M. Brown, Phil. Mag., 8 (1963) 1083.

86. M.F. Ashby and L.M. Brown, Phil. Mag., 8 (1963) 1649.

87. Powder Diffraction File Search Manual-Inorganic Materials, JCPDS, USA, (1979).

88. M.G. Hall, H.I. Aaronson, and K.R. Kinsma, Surf. Sci., 31 (1972) 257.

89. W.C. Johnson, C.L. White, P.E. Marth, P.K. Ruf, S.M. Tuominen, K.D. Wade, K.C. Russell, and H.I. Aaronson, Metall. Trans., 6A (1975) 911.

90. J.K. Lee and H.I. Aaronson, Acta Metall., 23 (1975) 799, 809.

91. P.J. Clemm and J.C. Fisher, Acta Metall., 3 (1955) 70.

92. F. Laszlo, J. Iron Steel Inst., 164 (1950) 5.

93. D.M. Barnett, J.K. Lee, H.I. Aaronson, and K.C. Russell, Scr. Metall., 8 (1974) 1447.

94. F.R.N. Nabarro, Proc. Roy. Soc., 175A (1940) 519.

95. E. Kröner, Acta Metall., 2 (1954) 302.

96. J.K. Lee, D.M. Barnett, and H.I. Aaronson, Metall. Trans., 8A (1977) 963.

97. B.L. Eyre, D.M. Maher, and R.C. Perrin, J. Phys. F: Metal Phys., 7 (1977) 1359.

98. K.C. Russell, Phase Transformations, (1970) 219, ASM, Metals Park, Ohio.

99. H.I. Aaronson and K.C. Russell, Proc. Int. Conf. Solid → Solid Phase Transformations, (1982) 101, AIME, eds. H.I. Aaronson, D.E. Laughlin, R.F. Sekerka, and C.M. Wayman.

100. R.B. Nicholson, Phase Transformations, (1970) 269, ASM, Metals Park, Ohio.

101. K.C. Russell, Acta Metall., 17 (1969) 1123.

102. R.W.K. Honeycombe, The Plastic Deformation of Metals, Edward Arnold, London, (1968).

103. K.-D. Rasch, R.W. Siegel, and H. Schultz, Phil. Mag., 41A (1980) 91.

104. L.M. Brown and R.K. Ham, Strengthening Methods in Crystals, (1971) 12, Elsevier, eds. A. Kelly and R.B. Nicholson.

105. J.W. Martin, Precipitation Hardening, Pergamon, Oxford (1968).

106. G.S. Ansell, Physical Metallurgy (1965) 887, North-Holland, ed. R.W. Cahn.